

INFORMATION TO USERS

The most advanced technology has been used to photograph and reproduce this manuscript from the microfilm master. UMI films the text directly from the original or copy submitted. Thus, some thesis and dissertation copies are in typewriter face, while others may be from any type of computer printer.

The quality of this reproduction is dependent upon the quality of the copy submitted. Broken or indistinct print, colored or poor quality illustrations and photographs, print bleedthrough, substandard margins, and improper alignment can adversely affect reproduction.

In the unlikely event that the author did not send UMI a complete manuscript and there are missing pages, these will be noted. Also, if unauthorized copyright material had to be removed, a note will indicate the deletion.

Oversize materials (e.g., maps, drawings, charts) are reproduced by sectioning the original, beginning at the upper left-hand corner and continuing from left to right in equal sections with small overlaps. Each original is also photographed in one exposure and is included in reduced form at the back of the book.

Photographs included in the original manuscript have been reproduced xerographically in this copy. Higher quality 6" x 9" black and white photographic prints are available for any photographs or illustrations appearing in this copy for an additional charge. Contact UMI directly to order.

U·M·I

University Microfilms International
A Bell & Howell Information Company
300 North Zeeb Road Ann Arbor MI 48106-1346 USA
313 761-4700 800 521-0600

Order Number 9026339

**Rectangular microstrip radiator for a multielement local
hyperthermia applicator**

Underwood, Harold Roger, Ph.D.

University of Illinois at Urbana-Champaign, 1990

U·M·I
300 N. Zeeb Rd.
Ann Arbor, MI 48106



**RECTANGULAR MICROSTRIP RADIATOR FOR A
MULTIELEMENT LOCAL HYPERTHERMIA APPLICATOR**

BY

HAROLD ROGER UNDERWOOD

**B.S., University of Illinois, 1984
B.A., Wheaton College, 1984
M.S., University of Illinois, 1986**

THESIS

**Submitted in partial fulfillment of the requirements
for the degree of Doctor of Philosophy in Electrical Engineering
in the Graduate College of the
University of Illinois at Urbana-Champaign, 1990**

Urbana, Illinois

UNIVERSITY OF ILLINOIS AT URBANA-CHAMPAIGN

THE GRADUATE COLLEGE

AUGUST 1989

WE HEREBY RECOMMEND THAT THE THESIS BY

HAROLD ROGER UNDERWOOD

ENTITLED RECTANGULAR MICROSTRIP RADIATOR FOR A MULTIELEMENT

LOCAL HYPERTHERMIA APPLICATOR

BE ACCEPTED IN PARTIAL FULFILLMENT OF THE REQUIREMENTS FOR

THE DEGREE OF DOCTOR OF PHILOSOPHY

Richard L. Magin

Director of Thesis Research

Anthony N. Trid

Head of Department

Committee on Final Examination†

Paul E. Meyer
L. J. Franke

Chairperson

† Required for doctor's degree but not for master's.

RECTANGULAR MICROSTRIP
RADIATOR FOR A MULTIELEMENT
LOCAL HYPERTHERMIA APPLICATOR

Harold Roger Underwood, Ph.D.
Department of Electrical and Computer Engineering
University of Illinois at Urbana-Champaign, 1990

Advances in printed circuit technology facilitate the design of thin, conformable, microstrip patch antenna arrays. Such multielement microwave antenna arrays can be advantageous for controlled heating of superficial malignancies during cancer therapy. This thesis reports a theoretical analysis and design verification of the rectangular microstrip radiator for a hyperthermia applicator.

Applicability of a cavity model approach for predicting near field patterns of a probe fed microstrip patch radiating in a lossy homogeneous medium is analyzed throughout a step-by-step development based on electromagnetic principles. A modal expansion technique and length correction factor slightly improve this model. Limitations of the simplifying assumptions and approximations in this model are tested by comparing numerical results of a single patch radiating in water with the measured results from an electric field probe. The measurement probe is an encapsulated miniature dipole designed for microwave transparent nonperturbing electric field measurement in biomedical media. Results show that safe and efficient performance of a microstrip patch as a biomedical radiator can be enhanced by a thin superstrate cover layer. Linear array patterns indicate that amplitude and phase variations can compensate for mutual coupling effects to adjust beam width and smoothness necessary in controlled hyperthermia heating.

DEDICATION

To the Author of life, who formed our beings and knows us better than we know ourselves, who understands the nature of our diseased condition, who stooped from His high position that we might know Him and that He would relate to us in every way, who gave His own life to solve our problem uniquely, efficiently and effectively. Today He offers us unending hope in the name of Jesus Christ.

ACKNOWLEDGEMENTS

I would like to thank several key people who shared expertise and personal support to make this project possible. Dr. Richard Magin, my advisor, helped me establish interdisciplinary contacts. These people collaborated with me and shared their knowledge and resources. I also thank Dr. Magin for the innovative ideas that made this project a unique research contribution. Dr. Andrew Peterson gave me assistance in the theoretical formulation of the EM problem during numerous consultations and on the manuscript. Dr. Steven Franke contributed advice on the microwave hardware and measurement system methods. Discussions with several antenna experts gave me additional insight: Dr. David Tanner, Mr. Hugh Smith, Dr. Stephen Wright and Dr. Y. T. Lo. I would also like to thank Dr. Paul Mayes and Dr. Paul Klock for suggestions on theoretical models, experimental measurements and for access to microwave lab equipment.

Bioacoustics Lab personnel also assisted me during this project. Billy McNeill crafted several pieces of experimental apparatus. Joe Cobb and Bob Cicone helped maintain and upgrade hardware and computing systems. Wanda Elliot kept account of our financial support and reminded us of our birthdays. Thanks to Dr. Floyd Dunn, Bioacoustics Laboratory Director, who was responsible for the quality and security of lab personnel and facilities.

Several other fellow students deserve a word of thanks: John McCarthy, Jay Alameda, Jim Kelton, Mohammed Ibbini, Emad Ebbini, Jim Drewniak, Dave Tammen and everyone from GradIV and TCBC.

Finally, I would like to especially thank my family who gave me continued encouragement often at critical times. I am indebted to my parents for their discipline and love that made my higher education possible.

TABLE OF CONTENTS

CHAPTER	PAGE
1	INTRODUCTION TO MICROWAVES AND HYPERTHERMIA 1
2	THEORETICAL MODELS OF MICROSTRIP PATCH ANTENNAS 12
3	EXPERIMENTAL MEASUREMENTS OF MICROSTRIP PATCH ANTENNAS IN WATER . . . 53
4	RESULTS: THEORY VERSUS EXPERIMENT 82
5	DISCUSSION OF RESULTS 100
6	CONCLUSIONS. 106
7	FURTHER INVESTIGATION. 109
	REFERENCES 112
	APPENDICES
A	ARRPAT2.FOR: NUMERICAL SIMULATION PROGRAM FOR PLANAR APPLICATORS. 118
B	MWPLAN.FOR: DATA ACQUISITION AND CONTROL PROGRAM FOR MICRO PDP-11 AND MILL-BASED SCANNER 137
C	SUPPLEMENTARY SIMULATED MICROWAVE POWER PATTERNS. 147
D	SUPPLEMENTARY MEASURED MICROWAVE POWER PATTERNS. 190
	VITA 198

CHAPTER 1

INTRODUCTION TO MICROWAVES AND HYPERTHERMIA

Light shines through darkness for us to see. It also energizes many of our life processes. Sunlight that shines on the earth generates photosynthetic energy. It also enables image recognition through visual object resolution. Artificially controlled generation and reflection of light provide an indirect means of communication over long distances. Those who expose themselves to direct sunlight for regulated periods often experience the therapeutic effects of its radiation. These benefits of light are familiar to all who can see or feel it.

Electromagnetic (EM) "light" waves often pass us unnoticed. The particular EM waves above the visible frequency spectrum of light (shorter wavelength) energetic enough to liberate ions are called ionizing radiation. Ionizing radiation includes ultraviolet (UV) light, X-rays and Gamma rays. Less energetic EM waves below the visible frequency spectrum of light (longer wavelength) include Infrared (IR), Microwave (MW) and Radiofrequency (RF) waves. Of these nonionizing types, it is the MW spectrum [1] that realizes much utilization among engineers for long-range (far field) communication and radar detection applications. Microwaves, however, also possess latent energy useful in close range (near field) biomedical applications (Fig. 1). This thesis evaluates a multielement microwave application device for controlled therapeutic heating.

1.1 Technology and Medical Needs

As they work to provide better medical care treatments, members of the medical profession continue to deal with difficult human health problems. Two basic kinds of medical need emerge: 1) diagnostic -- the detection and evaluation of disease or disorder and 2) therapeutic -- the regenerative or rehabilitative treatment. Several EM techniques have been applied for these applications.

1.1.1 Biomedical EM wave applications

The diagnostic and therapeutic applications of EM wave energy include imaging, detection, measurement and heating techniques. Certain noninvasive diagnostic and monitoring techniques depend on differences or changes in the EM properties of tissue as a function of dynamic physiological parameters such as blood flow, lung fluid (Impedance Plethysmography [2]) or respiratory volume [3]. Microwave radiometry relies on the black (or "gray") body principle of radiation [4]. Other diagnostic techniques involve the variation of measurable dielectric parameters in diseased compared to healthy tissues [5]. Biomedical imaging was originally attempted by application of EM scattering [6] and now shows promise as nuclear magnetic resonance (NMR) technology is adopted for Magnetic Resonance Imaging (MRI). The MRI technique has the ability to discriminate between tissues and the potential to detect tumors [7] in real time. Passing electric currents and EM radiation through human tissues to induce heating (diathermy) is an old therapeutic technique

used to treat a variety of ailments and diseases. Diathermic heating now includes the warming of human blood, the rapid elimination of hypothermia following open heart surgery and the thawing of other human tissues [3]. Although diathermy has had a history of successful application to a variety of musculoskeletal diseases and many other ailments [8], deep-seated heating has rarely been achieved without the painful side effect to the patient of skin and fat burns due to excessive surface heating. This can also be a problem in modern hyperthermia therapy.

Hyperthermia treatment is the delivery of therapeutic doses of heat by a technique such as diathermy for use during cancer therapy. A therapeutic dose typically at 42-45°C is directed to the tumor site to enhance the effects of radiation or chemotherapy. Controlled and selective heating is desirable to heat the tumor alone and leave the normal tissue unharmed. A water bolus can usually couple the energy from an applicator to the tissue and minimize the surface heating problem.

The relative value of a MW hyperthermia applicator in the medical clinic is thus related to its ability to heat a particular anatomical site in an efficient, safe and selective manner. During administration of hyperthermia therapy, oncologists like to use a controlled and if possible, noninvasive heating device. Externally induced heating can often be used to manage (e.g., control or eradicate) tumors during the course of cancer treatment. For this reason, biomedical engineers have attempted to improve upon the traditional diathermy technique by employing the controlled MW energy of a multielement array. It is hoped that this method can

come closer to the desired goal of hyperthermia therapy as a method of power deposition control that allows efficient delivery of a uniform thermal dose to the anatomical site of a malignancy.

To determine feasibility, working applicator prototypes were developed in this project to demonstrate operation under laboratory simulated biomedical conditions. In conjunction with the prototype, mathematical models were developed to predict performance. The value of the model is that it helps the design engineer evaluate the effect of varying critical design parameters and facilitates design optimization. Ideally, a good model can serve as a tool for the medical clinicians to aid in device selection and potential treatment planning. In addition, a particular hyperthermia applicator with known performance can be selected to match a particular patient need in terms of tumor site, geometry, size and depth.

1.1.2 EM hyperthermia applications

Although prognostic and quality assurance factors must be more carefully considered, clinical studies [9] continue to suggest positive benefits of heat (hyperthermia) applications for helping manage tumors during cancer therapy. Hyperthermia therapy ranges from whole body to localized anatomical treatment. In addition, ionizing radiation such as X-rays together with MW can combine to increase the probability of tumor regression [10]. One simplified explanation for this "synergistic" effect is that the malignant cells are both heat and radiation sensitive at different stages of the cell cycle. The combined modality produces an effective

"1,2-punch" which rapidly reduces the abnormal cell population. Early clinical trials suggest that hyperthermia as an adjuvant to radiation therapy increases the cure rate significantly [11]. However, results of recent multi-institutional experience have been mixed. Insufficient standardization throughout hyperthermia sessions among these institutions may account for this ambiguity. Nonuniform standards for evaluation inevitably occur due to unavailable patient control groups (patients chosen for trial treatments are often at an advanced stage of disease). Also, inadequately controlled heating is suspect. A recent study on head and neck treatments by Perez et al. [12] indicated that only properly designed, prospective, randomized clinical trials have the potential to show the efficacy of hyperthermia (currently unclear) combined with irradiation as an adjuvant to surgery or as a primary treatment in high-risk patients. On the other hand, treatments of recurrent carcinoma of the breast in the chestwall indicate a positive response between thermal dose and tumor rates by Perez et al. [13] indicating that hyperthermia does have a definite role in the management of these lesions.

1.2 Antenna Applicators for Hyperthermia

By shifting from the traditional diathermy frequency (2450 MHz to 915 MHz) to get deeper penetration [3] and by more innovative applicator design, EM hyperthermia may effectively continue to contribute to the role of hyperthermia in cancer therapy. For hyperthermia treatments that lack specific power deposition

control, the electronically phased antenna array is a promising prospect [14]. Using noninvasive microwave applications under microcomputer control with multipoint thermometry, real-time adjustments can be made during the course of therapy to tailor the power deposition pattern to the size and shape of the tumor. This kind of dynamic control also makes it possible to deal with the thermodynamic effects of blood perfusion which can be difficult to predict prior to treatment.

Ultrasound arrays now also effectively induce localized hyperthermia competing with microwave antenna arrays for deeper penetration and sharper focusing [15-17]. With a shorter wavelength and lower attenuation at typical operating frequencies, ultrasound energy penetrates deeper than MW energy and resolves a smaller focal region in unobstructed tissue regions. However, bone and air cavities present impedance mismatches that reflect and scatter ultrasound. Such obstructions can cause reflections that result in unwanted hot spots. Thus obstructed anatomical sites such as head, neck, chest, abdominal and pelvic regions remain prime candidates for microwave applications since more shallow penetration of microwaves limits and protects against excessive heating. Conceivably, ultrasound and microwave modalities could be used together to combine the advantage of each.

1.2.1 Microwave antenna radiators

Magin and Peterson have surveyed radiating antenna elements for MW hyperthermia [14]. They conclude that simple monopole

and dipole antennas produce regional or whole body heating better than local heating. However, direct contact antennas consisting of a waveguide, horn or cavity element can significantly restrict the region of energy deposition. A waveguide surface provides a natural shield to reduce leakage fields while the electric fields are distributed across the aperture to locate a more uniform but localized power deposition. Waveguide elements, however, often produce a bothersome central hot spot since the power is related to the square of the aperture field which peaks in its central region. This problem is diffused by arranging the radiators in a multisource configuration typical for regional heating (e.g., the MAPA [18]). The distribution of a multielement configuration allows amplitudes and phases of each individual element to be adjusted so as to concentrate (focus) the power with gain to a specific treatment region.

Closely packed surface types of phased arrays are possibly more suitable for localized superficial heating. Such arrays (e.g., rectangular, hexagonal) of aperture antennas retain the potential for amplitude and phase control as well as broad superficial heating. A dielectric loaded waveguide is useful for this type of multielement array to permit adequate aperture size scaling and impedance matching to biological media. However, waveguide materials make the overall size and weight of the array somewhat prohibitive. Applicator bulk can be conveniently eliminated by making use of antennas fabricated by new lightweight printed circuit technologies. Printed circuit antennas were first introduced by Munson [19] as a conformable high performance alternative for antennas arrays on missiles, rockets and satellites. In this thesis, a microstrip antenna

printed circuit radiator is evaluated for the biomedical application of hyperthermia during cancer therapy.

1.2.2 Printed-circuit radiators

Printed-circuit radiators are thin, lightweight, inexpensive to fabricate and potentially conformable to curved anatomical surfaces. An early notable one was the novel "bean-bag" applicator developed by Mendecki at RCA [20]. This consisted of a multiplicity of printed circuit dipoles underneath a dielectric powder filled bag. Elements were excited in phase at 2.45 GHz. I. J. Bahl and coworkers developed ring-type or loop microstrip radiators for heating local tissue volumes [21,22]. An important aspect of microstrip antenna (radiator) design was identified as the determination of the effective dielectric constant by the variational technique [23] to predict the effect of the load (lossy layers) [24]. It is the effective dielectric constant (ϵ_e) that determines the resonance dimensions (L,W) of a rectangular microstrip radiator at a given frequency.

1.2.3 Rectangular microstrip radiators

Microstrip radiators have recently been studied in terms of their design characteristics and suitability for biomedical heating. Tanabe et al. experimentally evaluated various microstrip patch shapes including circular, rectangular, triangular, radial, ring and spiral antennas [25]. This group concluded that a spiral antenna was best suited for a flexible array based on its uniform radiation pattern

and inherently broad bandwidth. Johnson et al. have introduced "low-profile" applicators of original shapes including a dielectric cover layer and ferrite material to get better matching, relative heating profiles and to allow optimization over a range of anatomical sites and frequencies [26]. Parsons evaluated the performance of a rectangular patch antenna for microwave diathermy at 2450 MHz [27]. Sandhu and Kolozsvary at Henry Ford Hospital constructed a linear array (700-900 MHz) for chest wall recurrences and very localized head and neck tumors [28]. They reported good agreement between theory and experiment in prediction of the resonant frequency. Near field effects were essentially eliminated using a 2 cm thick water bolus. A nonuniform heating pattern was produced that appeared to have some potential for clinical application. Other forms of microstrip slot resonators [29-31] have been proposed but results of multielement trials are not yet available.

Johnson et al. later tested the performance of compact applicators in a multiapplicator configuration for localized hyperthermia based on field penetration at 200 MHz [32]. The microstrip resonators used consisted of planar rectangular or circular patches sandwiched by dielectric layers with relative permittivity between 30 and 90. An important simplifying step in the analysis of these applicators was the assumption of "fictitious" magnetic edge dipoles whose strength is dependent on the magnitude of internal cavity fields related to the shape and mode of cavity resonance. A direct vector potential method is then used to compute the exact field radiated from these "fictitious" sources. The validity of this model, however, is limited to the validity of the lumped magnetic

current source approximation in replacing the "leaky" microstrip cavity. Johnson relies on previous experience with microstrip antennas [33] to justify this representation.

These examples show results of trials with microstrip applicators in the literature, but the exact connection between an equivalent source model using lumped magnetic current sources and the radiated fields in a lossy medium has not been thoroughly analyzed. The intention of Chapter 2 in this thesis is to describe and identify probable limitations of the choice of an equivalent source model for a rectangular microstrip antenna radiator in a lossy medium. The goal of Chapter 3 is to identify experimental methods and parameters relevant for evaluating microstrip applicator design characteristics. Chapter 4 compares theoretical versus experimental results of radiated field patterns for single element and linear array configurations in water. Chapter 5 discusses probable reasons for the discrepancy between theoretical and experimental results. Chapter 6 presents the conclusions of this investigation in terms of the analysis and measurement of a microstrip antenna array radiating in a lossy medium and the implications of using a rectangular microstrip radiator for the purpose of safer and more effective hyperthermia heating. Suggestions for further investigation are given in Chapter 7. Throughout this thesis, all figures and tables referenced in the text appear at the end of each chapter.

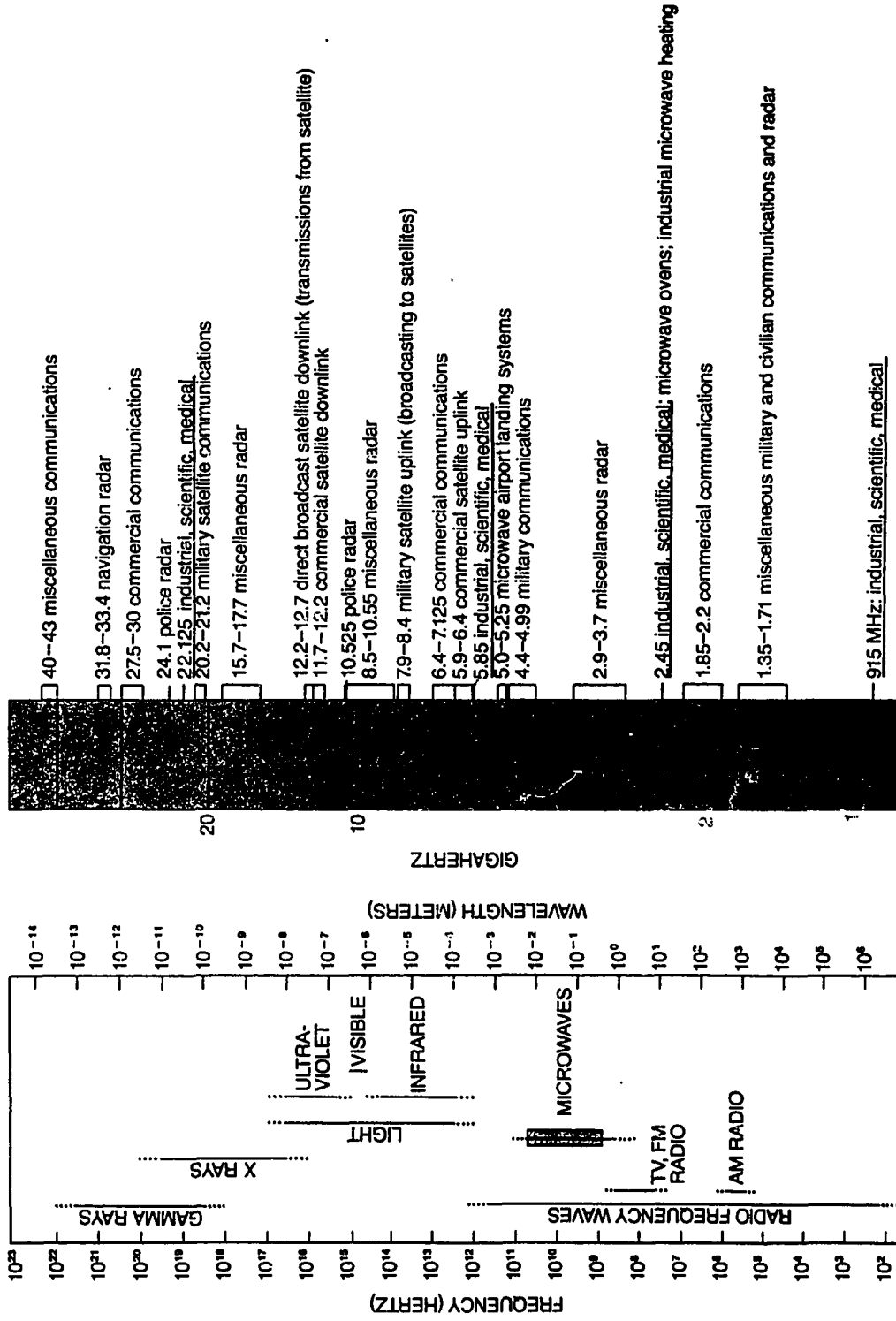


Figure 1.1. Microwave (MW) band of the electromagnetic (EM) spectrum indicating frequencies designated for industrial, scientific and medical (ISM) applications among others [1].

CHAPTER 2

THEORETICAL MODELS

OF MICROSTRIP PATCH ANTENNAS

A diagram of the microstrip patch antenna (Fig. 2.1) shows the dimensions (L,W) of the rectangular conductive region above a dielectric substrate backed by a ground plane. From the interior perspective of an observer at a point between the conductive layers, the patch looks like an infinite parallel plate waveguide. Yet from an exterior perspective, both the ground plane and the patch have finite dimensions. Usually, the ground plane is several times larger than the patch in a typical design. Thus the patch might resemble an ideal capacitor from this external perspective. However, since the dimensions of the patch are only a fraction of a wavelength, electric fields leak out the edges of the structure. If large enough in terms of wavelengths, the ground plane can be considered infinite relative to the patch. Thus it is this disproportionate structure that directs radiation of the fringing fields away from the patch. By characterizing and modeling the fringing fields, the behavior of the patch as a radiating antenna can be predicted.

2.1 Radiation Source Model

For the hyperthermia application, the model ideally should account for the behavior of radiated electric field power patterns near a multielement microstrip patch antenna array in a lossy medium (e.g., water). This fundamentally requires an appropriate equivalent source model for an individual microstrip radiator. In

addition, the theory should account for the effect of spacing between the elements as well as various geometric configurations of the array on the control and uniformity of the radiation patterns. Steps in the development of a rigorous equivalent source model should be based on actual physical characteristics of the antenna design and relevant principles of EM theory. Appropriate approximations are identified here that simplify the model and facilitate computation. Expected sources of error for alternative equivalent source models of a microstrip patch as a biomedical radiator will be identified in this chapter. A validity criterion for the cavity model of choice will be offered in Chapter 4 where theoretical and experimental results are compared.

2.1.1 Conceptual development

This section exposes some underlying details related to the choice of an equivalent source model of a rectangular microstrip patch excited by a probe feed and the steps in its development. A schematic representation of the microstrip patch shows a mathematical surface known as Huygens' surface that arises in the application of Huygens' principle [34]. Huygens' principle states that "each particle in any wave front acts as a new source of disturbance sending out secondary waves, and these secondary combine to form a new wave front." The Huygens' surface can be placed along boundary layers of the patch-substrate-groundplane composite with probe feed in three natural ways. Each of these surfaces is indicated (Fig. 2.2a) with the corresponding surface in the modified design

with a cover layer (Fig. 2.2b). The radiated fields from these composite structures are the same as those produced by certain equivalent sources located on the Huygens' surface. The concept of equivalent sources is discussed in detail by Harrington [35]. Application of the equivalence principle to each of these composites produces a unique equivalent source distribution. However, suitable simplifying approximations leave only two equivalent source models: one consisting of lumped magnetic line sources and one involving exclusively electric surface currents.

The first choice is a Huygens' surface (H1) that is chosen along the patch, substrate and the ground plane (Fig. 2.2a) in such a way to completely enclose the region directly beneath the patch delineating an interior and exterior region. By the equivalence principle, both electric ($\mathbf{J} = \mathbf{n} \times \mathbf{H}$) and magnetic ($\mathbf{M} = \mathbf{E} \times \mathbf{n}$) surface currents can substitute for the fields (excited by the probe) in the interior (cavity) region. A set of equivalent sources describing the exterior (radiated) fields consists of magnetic currents (\mathbf{M}_s) on the cavity side walls as the primary sources, some electric currents (\mathbf{J}_s) also on these side walls as well as on the top (\mathbf{J}_t) of the patch and on the ground plane (\mathbf{J}_g) near the edge of the patch. For a thin substrate (relative to a substrate wavelength) with a probe feed excitation, most electric surface currents (Fig. 2.3) are expected to be on the bottom of the patch ($\mathbf{J}_p = \mathbf{J}_b + \mathbf{J}_t \cong \mathbf{J}_b$) and small on the ground plane ($\mathbf{J}_g \cong 0$) beyond the edge of the patch [36].

It is a property of the equivalence principle that the fields remain the same even if the region beneath the Huygens' surface is altered. In this case, the interior region is replaced by a perfect

electric conductor (PEC). The PEC "shorts out" J_s , J_b and J_g leaving only M_s sources on the side walls. This approach takes advantage of the internal fields (approximated as cosinusoidal resonant cavity modes) to facilitate determination of the relative distribution of the magnetic current ribbon along these side walls. If the substrate dielectric layer is thin enough, it can be approximated to infinitesimal size. This effectively lumps the magnetic ribbon as a line source around the perimeter of the patch above an infinite flat ground plane. Thus, one significant error expected in near field predictions from the cavity model is the amount of scattering that would occur due to the exact distributed magnetic ribbon sources at the edges of a step discontinuity in the ground plane. The other is that the lumped magnetic sources have a distribution based on the internal fields approximated as cosinusoidal resonant modes. The magnitude of both of these errors is expected to be highly sensitive to the thickness of the patch (substrate) in wavelengths. In addition, errors insignificant in the far field are expected to remain significant within a wavelength (near field) of the patch antenna. The final step in this source model (Fig. 2.3) is to double the strength of the magnetic line sources by the image principle and remove the ground plane to allow calculation of the radiated fields using the homogeneous half-space Green's function.

A second choice for the Huygens' surface (H2) appears to be a theoretically attractive alternative (Fig. 2.2a). The surface H2 covers the flat region above the substrate layer. A step-by-step application of the equivalence principle can be performed as before. The difference is that on H2 the magnetic current ribbon occurs parallel

to the ground plane around the periphery of the patch with some associated electric current (J_r). The width and distribution of this ribbon ($M_r + J_r$) are determined by the extent of the fringing fields. Before approximation, this source model directly expresses the fields responsible for radiation. However, the exact width and distribution of the fringing fields are not easily determined. Interior fields can not be approximated as cavity modes and simply related to the unknown sources as on H1. However, the intensity of the fringing fields is expected to drop off away from the edge of the patch (Fig. 2.1b), thus a reasonable assumption is that $M_r + J_r$ is maximum at the patch edges. This approximation leads to an error comparable to the "shadow" effect of the ground plane "bump" present in H1. A good first-order approximation would be to concentrate the entire magnetic current ribbon at these edges. If a PEC backs H2 all along the boundary, an equivalent source problem is defined which leaves only M_r (shorts out J_r as before). Then, applying the image principle as before, this model reduces to the same primary equivalent magnetic sources as developed from H1. Since no approximation in this approach is necessary concerning the thickness of the substrate, the error arises largely from concentrating distributed sources at the edge of the patch along H2. However, the distribution of the lumped magnetic sources remains undetermined unless it is approximated as for H1. Since they reduce to the same lumped equivalent source model, no clear cut advantage exists between the choice of H1 or H2 in terms of accuracy.

Finally a third Huygens' surface (H3) can be identified (Fig. 2.2a). The surface H3 encloses the volume of the conducting patch

and the probe feed, covers the ground plane and shrinks down to infinitesimal size. Sources on H3 are the total electric source currents ($\mathbf{J} = \mathbf{J}_t + \mathbf{J}_b + \mathbf{J}_f + \mathbf{J}_g$) on the patch ($\mathbf{J}_p = \mathbf{J}_t + \mathbf{J}_b$), feed (\mathbf{J}_f) and ground plane (\mathbf{J}_g) (Fig. 2.3). The advantage of this approach is that it maintains specificity about the position of the primary sources (\mathbf{J}_p) above the ground plane to within the thickness of the patch conductor. There is no need to neglect any sources in this model and no approximations concerning the thinness of the dielectric substrate are necessary. Error in this model is confined to assuming the disposition of the feed current and electric sources on the patch. Since it retains information about the position of radiating sources above the ground plane and allows modal matching in the Fourier domain at the substrate/lossy dielectric medium interface, this approach has the potential for more accurate near field predictions in homogeneous media and for the solution to the field problem in multilayered (stratified) dielectric media. This approach has been used by Tanner [37] for patches embedded in stratified dielectric layers. Beyne and DeZutter [38] use it to determine the power deposition of a microstrip radiator in a layered biological medium.

Electric surface currents (\mathbf{J}_p) on H3 are limited by boundary conditions at the periphery of the patch and constrained in their relationship to the surrounding fields by Maxwell's equations. A rigorous solution of Maxwell's equations can be obtained using the method of moments described by Harrington [39]. For example, Beyne and DeZutter use subsectional bases and a point matching technique [38]. However these techniques often involve a great computational expense [37,38]. In practice, microstrip antenna

practitioners often fall back on the more efficient expedient embodied in the cavity model. In this approach, the electric currents on the patch (H3) are assumed to be those related to the fields in an ideal, closed cavity as previously discussed. Although approximate, the cavity model is effective at predicting accurate far field quantities [40]. In this thesis, the validity of the cavity model for near field prediction is investigated.

Compared to the electric surface current approach, the lumped magnetic current source model has the advantage of allowing radiated fields to be expressed by one-dimensional integrals through the vector potential method. Further mathematical simplification (Section 2.2.1) allows the radiated field components to be computed directly through finite line integrals of the edge magnetic current sources. For computational efficiency, this feature favors its application over surface current source approaches involving two-dimensional integrals in the planar and conformal antenna array formulations expressed here.

2.1.2 Simplifying assumptions and approximations

Three versions of the equivalent magnetic current source model were developed for the purpose of efficiently and more accurately predicting radiated fields from a microstrip patch: 1) a simple (2-edge) cavity-source (SC) model, 2) a complete (4-edge) cavity-source (CC) model and 3) a multimode cavity-source (MC) model. As previously noted, the cavity model approach is well-suited for application to microstrip patch radiators with a thin

substrate demonstrated by the close agreement between theory and experiment for input impedance and far field pattern prediction in air [40]. Since biomedical applications involve the near fields in lossy media, it was deemed necessary to expand the SC model often used to predict far field patterns in air by retaining a complete set of edge sources (CC model) and including multiple modes (MC model) excited by the probe feed to account for asymmetry observed in the pattern (see measurements in Chapter 3). Contour plots of total power (relative dB) in the E-plane for the first several centimeters away from the patch show the major differences between the predictions of these 3 source models (Figs. 2.6-2.8). The single element pattern compared to the experimental evidence serves as a basis for source model selection in formulations for planar and conformal arrays. Formulations for planar and conformal applicator types are presented in subsequent sections. Analytic expressions for each formulation were programmed in FORTRAN code using efficient algorithms to compute the required functions (e.g., trig., Bessel, integration). Each FORTRAN program includes input parameters that define operating frequency, antenna dimensions, array type and geometry; specify substrate curvature; identify medium permittivity; set observation plane orientation, size and sample increment; and budget an integration accuracy criterion.

A complete set of radiated electric field components can be calculated by any of these programs for a rectangular patch radiating into a lossy medium such as water. Patterns can be plotted in the E (x-z), H (y-z) and P (parallel x-y) planes for typical hyperthermia depths. In Chapter 4, calculated results are compared with measured

E-field power patterns for the case of a single rectangular patch on a planar substrate in order to assess the spatial range of validity for the cavity model. Independent element isolation in the microstrip antenna array applicators is also evaluated (Chapter 3) using transmission loss measurements as a function of element spacing. This provides a basis for choosing an array spacing where the neglect of mutual coupling in the model might be justifiable. Numerical computations were performed on a VAX 11/730 computer and an Intel 80386 microprocessor based personal computer (PC). Contours were plotted with NCAR Graphics distributed by the National Center for Atmospheric Research (Boulder, CO) and licensed by the University Corporation for Atmospheric Research (UCAR) on the VAX and simple x-y plots with Cricket Graph (Cricket Software, Malvern, PA) on a Macintosh PC (Apple Computer, Cupertino, CA).

The key assumptions and approximations of the cavity model can be summarized as follows:

- 1) Interior E-fields are normal to the conductive patch and ground plane surfaces; interior H-fields are transverse to these surfaces; all interior fields ($0 < x < L$; $0 < y < W$) are independent of the normal coordinate (z).

$$\mathbf{E}_i = z\mathbf{E}_z(x,y) \quad (2.1)$$

$$\mathbf{H}_i = x\mathbf{H}_x(x,y) + y\mathbf{H}_y(x,y) \quad (2.2)$$

- 2) The interior region can be approximated by a closed cavity whose side walls are perfect magnetic conducting (PMC) and top and bottom walls are perfect electric conducting (PEC) boundaries.

3) Lumped magnetic line sources replace distributed magnetic current ribbons above the ground plane as a simple source model for computing radiated fields in a homogeneous half-space.

These simplifying assumptions (1-3), consistent with the conceptual development of the cavity-source model (H1), allow the internal cavity modes to be expressed in terms of cosine functions. The error that is introduced by approximating the internal field orientation by Equations (2.1) and (2.2) is related to the thickness of the substrate and is minimized when the substrate is thin, relative to a medium wavelength. The fields can thus be related to the magnetic sources by the equivalence principle (Section 2.2.1).

A microstrip patch radiator also can include a protective superstrate lossless dielectric cover layer in its design. The function of a superstrate dielectric (cover) layer over a patch might be understood by analogy from the stripline structure. In the stripline structure, it changes the phase velocity by altering the effective dielectric constant and protects the conductive strip. With respect to propagating waves radiating from the patch antenna, even though the superstrate layer is much thinner than a typical quarter-wave matching layer (see Table 3.2). It effectively enhances the transmission of radiation into the high dielectric constant biological medium. Theoretically, since this layer occurs in the exterior region (Fig. 2.2b), it would invalidate use of the homogeneous half-space Green's function for calculating radiated fields from this structure. The lumped magnetic current source model can be retained if the necessary approximation is justified. A Green's function for the

layered geometry could properly model wave reflections and mode conversions occurring at the dielectric interface of the superstrate and the biological medium. However, it also introduces significant mathematical complexity to the model. When surface waves are negligible and the superstrate layer is thin enough, the cover layer might be modeled as "transparent" to the radiated fields. This is consistent with the substrate thinness approximation if the relative dielectric constant of both layers is the same. In this thesis, the applicability of the homogeneous half-space Green's function will be analyzed.

2.2 Radiation in Biological Media

The formulations for the fields radiated from planar and conformal applicators depend on the source model (discussed in the previous section) and assume the patch is radiating at resonance into a lossy homogeneous dielectric ($\hat{\epsilon} = \epsilon' - j\epsilon''$) medium. The assumption of a homogeneous water ($\hat{\epsilon} = 77 - j12$ is used here for distilled water at 915 MHz; see [41] for further reference data) medium as an idealized biological tissue model is a good one for initially predicting the expected electric field power deposited in tissues with high water content. It also satisfies the investigational need for a fluid medium in which predictions can be easily verified by measurements with a miniature nonperturbing E-field probe. The value of radiated E-field components predicted in a simple homogeneous medium is that they can be used to estimate how the power will transfer at a biological tissue interface such as a fat/muscle layer.

2.2.1 Formulation for planar applicators

Formulation of the radiated E-field components in rectangular (Cartesian) coordinates from a rectangular microstrip patch on a planar (flat) substrate begins by expressing the internal electric fields underneath the patch. The z-directed electric fields underneath a rectangular patch excited by a probe feed can be expanded in terms of modal functions [42] when the cavity model assumptions (Section 2.1.2) are valid. Thus, the complex internal fields can be expressed as

$$E_z(x,y) = j\omega\mu_0 \sum_{m=0}^{\infty} \sum_{n=0}^{\infty} \frac{\phi_{mn}(x,y)\phi_{mn}(x_0,y_0)}{\hat{k}^2 - k_{mn}^2} \frac{2L \sin(\frac{m\pi d}{2L})}{m\pi d} \quad (2.3)$$

where $\phi_{mn}(x,y) = \sqrt{\frac{\epsilon_{om}\epsilon_{on}}{LW}} \cos(\frac{m\pi x}{L}) \cos(\frac{n\pi y}{W})$

and $\hat{k}^2 = \epsilon_r(1-j\delta_e)k_0^2$; $k_0^2 = \omega^2/c^2$; $k_{mn}^2 = (m\pi/L)^2 + (n\pi/W)^2$;
 $\epsilon_{op} = 1$ for $p=0$, $\epsilon_{op} = 2$ for $p > 0$

where δ_e is the effective loss tangent of the dielectric substrate into which is lumped the total losses realized by the cavity due to individual dielectric, conductor and radiation losses [42]. Coefficients associated with the modal functions (ϕ_{mn}) are

$$E_z(x,y) = j\omega\mu_0 \sum_{m=0}^{\infty} \sum_{n=0}^{\infty} \hat{\alpha}_{mn} \phi_{mn}(x,y) \quad (2.4)$$

$$\hat{\alpha}_{mn} = \frac{\phi_{mn}(x_0, y_0) \operatorname{sinc}\left(\frac{m\pi d}{2L}\right)}{\hat{k}^2 - k_{mn}^2}$$

where

and d represents the "effective width" of a uniform strip of z -directed source current located at (x_0, y_0) . Use of the effective dimensions (L_e, W_e) can also extend the actual dimensions of the patch (L, W) to account for fringing fields. A first-order approximation (Hammerstad [43]) would be $L_e = L + 2h$ and $W_e = W + 2h$ (see Table 2.1).

Further simplification of the coefficients for the internal fields facilitates the analysis.

$$\begin{aligned} E_z^{mn}(x, y) &= \hat{A}^{mn} \cos(m\pi x/L) \cos(m\pi y/W) && \text{for } 0 < x < L; 0 < y < W \\ &= 0 && \text{elsewhere} \end{aligned} \quad (2.5)$$

$$\text{where } \hat{A}^{mn} = j\omega\mu_0 \hat{\alpha}_{mn} \sqrt{\frac{\epsilon_{0m}\epsilon_{0n}}{LW}}$$

is the complex amplitude factor for the m th mode at an arbitrary feed position (x_0, y_0) . Significance of the complex coefficients \hat{A}^{mn} can be determined in terms of the real number relative magnitude

$$A^{mn} = \frac{|\hat{A}^{mn}|}{\left[|\hat{A}_{\max}^{mn}| \right]}$$

However, in general, the complex coefficients \hat{A}^{mn} must be used in order to retain phase information.

After these coefficients have been determined for a given case, the Huygens' principle can be applied as previously discussed ($\mathbf{K}^{mn} = 2\mathbf{n} \times z\mathbf{E}_z$) to obtain the equivalent magnetic sources around the patch edges.

$$\begin{aligned} K_y^{mn}(x',y') &= \hat{A}^{mn} \cos(m\pi x'/L) \cos(n\pi y'/W) [\delta(x') - \delta(x' - L)] \\ &\quad \text{for } 0 < y' < W \\ &= 0 \quad \text{elsewhere} \end{aligned} \quad (2.6)$$

$$\begin{aligned} K_x^{mn}(x',y') &= -\hat{A}^{mn} \cos(m\pi x'/L) \cos(n\pi y'/W) [\delta(y') - \delta(y' - W)] \\ &\quad \text{for } 0 < x' < L \\ &= 0 \quad \text{elsewhere} \end{aligned} \quad (2.7)$$

where $x'x + y'y = r'$ is a source point relative to the origin ($z' = 0$) and $xK_x^{mn} + yK_y^{mn} = \mathbf{K}^{mn}$. As an example, consider the probe ($d=1$ mm) fed patch on Duroid 6010 at a position $x_0=0.10$, $y_0=W/2$ (see Fig. 2.1) with resonance dimensions $L=3.4$ cm and $W=2.5$ cm and thickness $h=0.25$ cm at the frequency $f=915$ MHz assuming $\delta_e=0$. The magnitude of the five most significant coefficients (relative to A^{10}) are: $A^{00}=0.64$, $A^{02}=0.08$, $A^{10}=1.0$, $A^{12}=0.14$, $A^{20}=0.16$ and $A^{22}=0.10$. Applying a 10% significance criterion, A^{00} , A^{10} , A^{12} , A^{20} and A^{22} are retained. Tables 2.1 and 2.2 summarize the effect on the complex coefficients of adding loss (δ_e), correcting for fringing fields (L_e, W_e) and using higher dielectric constant substrate material.

When only magnetic sources are involved, the complete electric fields can be derived from

$$\mathbf{E}(\mathbf{r}) = -\nabla \times \mathbf{F}(\mathbf{r}) \quad (2.8)$$

where $\mathbf{r} = xx + yy + zz$ is the field (observation) point position vector. In an unbounded homogeneous region, $\mathbf{F}(\mathbf{r})$ is expressed as

$$\mathbf{F}(\mathbf{r}) = \frac{1}{4\pi} \iiint_{-\infty}^{+\infty} \frac{1}{R} \mathbf{M}(\mathbf{r}') e^{-jkR} dx'dy'dz' \quad (2.9)$$

where $R = |\mathbf{r} - \mathbf{r}'|$, $k = \omega\sqrt{\mu\hat{\epsilon}}$

and $\mathbf{M}(\mathbf{r}') = \sum_{m=0}^{\infty} \sum_{n=0}^{\infty} \mathbf{K}^{mn}(x',y')$

Breaking \mathbf{F} into its two rectangular (Cartesian) components, simplifying the volume integral and considering only the dominant modes for Duroid 6010 applicators,

$$F_y = \sum_{m,n=0}^2 \sum_{l=1}^2 \hat{A}^{mn} (-1)^l \cos\left(\frac{m\pi x'_l}{L}\right) \int_0^W \frac{\cos\left(\frac{n\pi y'}{W}\right)}{R_{lx}} e^{-jkR_{lx}} dy' \quad (2.10)$$

where $R_{lx} = \sqrt{(x-x'_l)^2 + (y-y')^2 + z^2}$

at $x'_l = 0, L$ for $l = 1, 2$.

$$F_x = \sum_{m,n=0}^2 \sum_{l=1}^2 \hat{A}^{mn} (-1)^l \cos\left(\frac{n\pi y'_l}{W}\right) \int_0^L \frac{1}{R_{ly}} \cos\left(\frac{m\pi x'}{L}\right) e^{-jkR_{ly}} dx' \quad (2.11)$$

where $R_{ly} = \sqrt{(x-x')^2 + (y-y'_l)^2 + z^2}$

at $y'_l = 0, W$ for $l=1, 2$.

Taking the curl (Eq. (2.8)) inside the integrand (Eq. (2.9)), and applying derivatives to the appropriate F component by the cross-product rule, expressions for the complex electric field components become

$$E_x = \frac{\partial F_y}{\partial z} = z \sum_{m,n=0}^2 \sum_{l=1}^2 \hat{A}^{mn} (-1)^l \cos\left(\frac{m\pi x_1'}{L}\right) \int_0^W \frac{(1+jkR_{lx}) \cos(n\pi y'/W)}{R_{lx}^3} e^{-jkR_{lx}} dy' \quad (2.12)$$

$$E_y = -\frac{\partial F_x}{\partial z} = \sum_{m,n=0}^2 \sum_{l=1}^2 \hat{A}^{mn} (-1)^l \cos(n\pi y'/W) \int_0^L \frac{(1+jkR_{ly})}{R_{ly}^3} \cos\left(\frac{m\pi x_1'}{L}\right) e^{-jkR_{ly}} dx' \quad (2.13)$$

$$E_z = \frac{\partial F_x}{\partial y} - \frac{\partial F_y}{\partial x} = \sum_{m,n=0}^2 \sum_{l=1}^2 \hat{A}^{mn} (-1)^l (y-y_1') \cos(n\pi y'/W) \int_0^L (1+jkR_{ly}) \cos\left(\frac{m\pi x_1'}{L}\right) e^{-jkR_{ly}} dx' \quad (2.14)$$

$$+ \sum_{m,n=0}^2 \sum_{l=1}^2 \hat{A}^{mn} (-1)^l (x-x_1') \cos\left(\frac{m\pi x_1'}{L}\right) \int_0^W \frac{(1+jkR_{lx}) \cos(n\pi y'/W)}{R_{lx}^3} e^{-jkR_{lx}} dy'$$

These are the explicit expressions for each E-field component at an arbitrary point in a homogeneous lossy half-space using a multimode cavity source model (Fig. 2.7) accounting for the most significant modes (>10% of the fundamental) excited under a patch on Duroid 6010 by the probe feed. The simple array theory used in this investigation assumes an absence of mutual coupling between the array elements. This assumption is only justified for an array spacing indicated by measurements of transmission loss (S_{21}) as a function of array spacing (Chapter 3). Array patterns are predicted

by calculating the total fields by vectoral addition (the simple array factor does not apply in the near field).

$$\mathbf{E}(\mathbf{r}) = \sum_{n=1}^N \hat{I}_n \mathbf{E}_n(\mathbf{r}) \quad (2.15)$$

where $\mathbf{E} = x\mathbf{E}_x + y\mathbf{E}_y + z\mathbf{E}_z$, $\mathbf{E}_n(\mathbf{r})$ is the elementary contribution to the field arising from sources of the n th individual array element and $\hat{I}_n = I_n e^{j\phi(n)}$ is the complex coefficient accounting for the magnitude and phase of the excitation. Expressions (2.12)-(2.14) are numerically evaluated using a source point ($\mathbf{r}' = \mathbf{r}'_0 + \Delta \mathbf{r}'_n$) referenced to the central array element making this method suitable for computing the total electric fields in the near zone of the N element array. The validity of this method also depends on the assumption that individual elements are isolated from one another (mutual coupling negligible). A range of validity for this assumption is suggested by S-parameter data as a function of element spacing for 2 elements on a Duroid substrate (Fig. 3.3) and similarly can be performed for rectangular and hexagonal unit cell configurations (see also Table 3.4 for mutual coupling between elements in a linear array spaced 3 cm apart on MCT-85).

2.2.2 Formulation for conformal applicators

For conformal (curved substrate) applicators the EM field problem can be more efficiently expressed in cylindrical coordinates (Fig. 2.4). A suitable approach for modeling the applicator is to assume a completely enclosed cylinder around a lossy homogeneous

interior even though the conformal applicator actually has an angular extent of only a fraction (sector) of a cylinder. A complete cylinder assumption is valid as long as enough loss in the medium exists relative to the diameter of the cylinder (radius of curvature) to suppress reflections. For example, in water the attenuation constant is $\alpha_w = 0.13 \text{ Np/cm} = 1.1 \text{ dB/cm}$ (using $\hat{\epsilon} = 77 - j12$ and $\sigma = 0.61 \text{ mho/m}$ at 915 MHz). Thus, the penetration depth (distance the wave travels before the electric field intensity drops by $1/e$) is $\delta_w = 1/\alpha_w = 7.6 \text{ cm}$. For a 5 cm radius of curvature, this means that the wave attenuates 10 dB before it "sees" the opposite wall of the cylinder. For the chest region, a 15-20 cm applicator radius is reasonable. This gives at least 15-20 dB attenuation before waves meet the opposite wall. Also, the cylindrical ground plane sector must have enough angular extent compared to the extent of the array to minimize finite ground plane edge effects. A working assumption in lossy media such as water is that finite ground plane edge effects in both axial and circumferential directions are minimal by virtue of distance and attenuation.

Using the same simplifying approximations as in the planar case, the multimode cavity source model can be expressed for the conformal case as a source function in cylindrical coordinates.

$$G(\phi, z) = \phi E_\phi(a, \phi, z) + z E_z(a, \phi, z) \quad (2.16)$$

where $E_\phi(a, \phi, z) = C \ln(\delta(\phi + L/2a) + \delta(\phi - L/2a)) p(z, -W/2, W/2) \delta(\rho - a)$

and $E_z(a, \phi, z) = C \ln[\delta(z - W/2) \cos(a\pi\phi/L) - \delta(z + W/2) \cos(a\pi\phi/L)] \cdot p(\phi, -L/2a, L/2a) \delta(\rho - a)$

where a is the radius of curvature, L is the length and W is the width of the microstrip patch. In this case, the length of the patch is oriented in the circumferential direction. The source function for an axially oriented patch can be expressed analogously.

By formulating the problem in the Fourier transform domain, general expressions for the fields within the interior region of the cylinder can be matched with the source function to systematically solve for the unknown coefficients. In this formulation, the convention $i = \sqrt{-1}$ is used and j becomes an index for the set of cylindrical variables (ρ, ϕ, z) . The double Fourier transform is expressed as

$$g_m(k_z) = \mathcal{F}\{G(\phi, z)\} = \phi g_{\phi m}(k_z) + z g_{zm}(k_z) \quad (2.17)$$

where

$$g_{jm}(k_z) = \frac{1}{2\pi^2} \int_{-\infty}^{\infty} \int_{-\pi}^{\pi} E_j(a, \phi, z) e^{im\phi} d\phi e^{ik_z z} dz \quad (j = \phi, z)$$

After integration and algebraic simplification, the expressions become

$$g_{\phi m}(k_z) = \frac{C \ln W}{2\pi^2} \cos\left(\frac{mL}{2a}\right) \text{sinc}\left(\frac{k_z W}{2}\right) \quad (2.18)$$

$$g_{zm}(k_z) = \frac{2i C \ln\left(\frac{a\pi}{L}\right) \sin\left(\frac{k_z W}{2}\right)}{\pi^2 \left(\left(\frac{a\pi}{L}\right)^2 - m^2\right)} \cos\left(\frac{mL}{2a}\right) \quad (2.19)$$

When only the fundamental (TM_{01}) mode is assumed, the source coefficient C^{1n} is normalized to the peak internal field of the cavity ($C^{10} = 2E_0$).

J.R. Wait formulates EM radiation from cylindrical structures [44] using Hertzian vector potentials. Both electric (zU) and magnetic (zV) vector potentials can conveniently express fields in the interior region of a conducting cylinder under the assumption of z invariance [45]. Waves in a lossy medium can be expressed by modified Bessel functions of complex argument ($I_m(z)$) with associated undetermined coefficients.

$$U_m = A_m(k_z)I_m(\nu\rho) \quad (2.20)$$

$$V_m = B_m(k_z)I_m(\nu\rho) \quad (2.21)$$

in the spectral domain where $\nu = ik_\rho$ and $I_m(z) = i^{-m}J_m(iz)$. The propagation constant (γ) of the medium is

$$\gamma = \sqrt{i\omega\mu(\sigma + j\omega\epsilon)} = ik \quad (2.22)$$

$$\text{where } k^2 = -\nu^2 + k_z^2 = k_\rho^2 + k_z^2 \quad (2.23)$$

Identifying the expressions for the electric field components that obey Maxwell's equations from these vector potentials,

$$E_{\phi m}(\rho) = -(mk_z/\rho)A_m I_m(\nu\rho) + i\omega\mu\nu B_m I_m'(\nu\rho) \quad (2.24)$$

$$E_{zm}(\rho) = -\nu^2 A_m I_m(\nu\rho) \quad (2.25)$$

Now A_m and B_m are determined by matching at the source.

$$\mathbf{E}_m(a, k_z) = \mathbf{g}_m(k_z) \quad (2.26)$$

These equations are solved by simple substitution.

$$A_m(k_z) = \frac{4iE_0 \left(\frac{a\pi}{L}\right) \sin\left(\frac{k_z W}{2}\right) \cos\left(\frac{mL}{2a}\right)}{-v^2 I_m(va) \pi^2 \left(\left(\frac{a\pi}{L}\right)^2 - m^2\right)} \quad (2.27)$$

$$B_m(k_z) = \frac{\left(\frac{m}{a}\right) k_z A_m(k_z) I_m(va) + \left(\frac{E_0}{\pi^2}\right) W \cos\left(\frac{mL}{2a}\right) \operatorname{sinc}\left(\frac{k_z W}{2}\right)}{i\omega\mu v I_m'(va)} \quad (2.28)$$

where the recurrence formula for the derivative of the modified Bessel function is $I_m'(z) = (I_{m-1}(z) + I_{m+1}(z))/2$ [46]. Complete expressions for the fields at an arbitrary field point in the interior region can thus be formulated by the inverse Fourier transform,

$$E_\rho(\rho, \phi, z) = \int_{-\infty}^{\infty} \sum_{m=-\infty}^{\infty} \left[ik_z v A_m I_m'(v\rho) + \frac{m\mu\omega}{\rho} B_m I_m(v\rho) \right] e^{-i(m\phi + k_z z)} dk_z \quad (2.29)$$

$$E_\phi(\rho, \phi, z) = \int_{-\infty}^{\infty} \sum_{m=-\infty}^{\infty} \left[\frac{-mk_z}{\rho} A_m I_m(v\rho) + i\omega\mu B_m I_m'(v\rho) \right] e^{-i(m\phi + k_z z)} dk_z \quad (2.30)$$

$$E_z(\rho, \phi, z) = \int_{-\infty}^{\infty} \sum_{m=-\infty}^{\infty} \left[v^2 A_m I_m(v\rho) \right] e^{-i(m\phi + k_z z)} dk_z \quad (2.31)$$

where the summations are carried out over modes m and the integrals over k_z . Further simplification of these expressions allows

more practical and efficient computation. Symmetry simplifications and finite bounding of the infinite series, subject to a practical error criterion, are the first steps. Total fields can be computed from array configurations applying elemental field addition as for planar arrays (Eq. (2.15)) but here need a vector translation and transformation in accordance with the cylindrical coordinate convention adopted to suit conformal applicator geometry.

2.3 Techniques for Numerical Computation

Suitable computational tools necessary to calculate results of these theories were chosen on the basis of accuracy, efficiency and accessibility of resources at the Electrical Engineering Annex at the University of Illinois.

2.3.1 Computer hardware system

Initial FORTRAN programs were coded and executed on a VAX-11/730 system. Programs HEXPAR, ARRPAT, ARRPAT2 computed an array of 2500 field points on this system in less than 1 hour of CPU time. Results of the calculation were represented by contour and surface plotting routines using NCAR graphics. Program CYLARR, for the conformal applicator, initially required excessive computation times of several CPU hours on the VAX due to computation of the double inverse Fourier transforms involving Bessel functions and thus was ported to a faster machine. An Intel 80386 microprocessor based PC was able to cut the execution time for CYLARR by a factor of 2 or 3.

2.3.2 Computational algorithms

Numerical algorithms used to attack these problems were selected and derived on the advice of members of the EM and antenna laboratory at the University of Illinois, with the aid of various mathematical subroutine libraries (such as IMSL) and functions mostly intrinsic to VAX/VMS and MS-DOS systems. A Romberg integration routine (A. F. Peterson) functioned as the FORTRAN integration tool for both the planar and cylindrical applicator programs. The Romberg method refines the estimate of an integral over defined limits to a desired accuracy between 0.00001 and 1.0. The minimum and maximum number of function evaluations can be set with enough flexibility to handle smooth or highly oscillatory, rapidly varying functions if necessary. Each complex integrand is split into real and imaginary functional parts declared external in the calling routine.

2.3.3 Software programs

For planar applicators, the FORTRAN programs HEXPAR, ARR PAT and ARR PAT2 were used to calculate the radiated fields from arrays of rectangular microstrip patch antennas. Program ARR PAT2 has the most developed model (MC) that allows specification of coefficients for the dominant TM_{mn} cavity modes of a given patch design. These coefficients are derived from information about the substrate thickness and feed position (Section 2.1.2). Program ARR PAT includes all four edge sources (CC) but assumes the

TM₀₁ mode excited only. Program HEXPAR has the simplest source model (SC) including only the two primary edge radiating sources. A listing of ARR PAT2 that incorporates all 3 models is given in Appendix A.

For conformal applicators, CYLARR uses the CC model assuming TM₀₁ mode excitation. The program makes a series of subroutine calls at each point in the domain of integration in order to evaluate complex coefficients over a sufficient number of modes (m) in polar angle ϕ to achieve desired accuracy (meet the specified error criterion). The modified Bessel function of complex argument (MMBZIN in IMSL version 9.0) is included in these calculations. Subroutine MMBZIN handles real and imaginary parts of the argument as separate inputs along with the highest order (n) required for evaluation. Outputs are vectors of length n containing the real and imaginary parts of the modified Bessel function. As the number of calls to MMBZIN increases significantly with increasing radius of curvature, the computation time increases accordingly.

As a computation time saver, a "look-up" table was created that consists of a matrix of Bessel function values over a discrete set of arguments in the range $0 < k_{z\max}\rho < k_{z\max}a$. This cuts computation time by a factor of 2 or 3. However, this reduction comes at the expense of some increased error since arguments of the integrand usually fall between the discretely tabulated Bessel values and require interpolation. Interpolation error can be decreased by increasing the total number of tabulated Bessel values.

2.4 Numerical Results

In this section, samples of the numerical results calculated by HEXPAR, ARRPAT, ARRPAT2 and CYLARR for a single 2.5 x 3.4 cm patch radiating into distilled water are presented for analysis. A rectangular patch of this size is resonant at 915 MHz on Duroid 6010 (see Table 3.3). The complete set of radiated electric field components calculated for each individual source model in the E, H and P planes from this patch radiating in water are exposed by contour plots given in Appendix C. For quantitative comparison, the calculated beam pattern characteristics of each cavity-source model have been tabulated (Tables 2.3, 2.4).

2.4.1 Planar case

An examination of contour plots for the radiated electric field components predicted by the cavity-source models for a single planar patch confirms certain expected characteristics (see Fig. 2.5) at each step in the development from the simple SC model to the multimode MC model. For example, radiated electric fields from the SC source model show $E_y = 0$ throughout the half-space while the E_z -field pattern contains a null through the center of the patch (along $x=0$ in Figs. C.1b, C.3b, C.5b and C.7b). The primary transverse component (E_x) peaks at the center of the patch (along $x=0$ in Figs. C.3a, C.5a, C.7a). The CC source model exhibits radiated fields that have nulls in E_y through the center of the patch (along $x=0$ and $y=0$

in Figs. C.10b, C.13b, C.16b, C.19b) and in E_z as before (along $x=0$ in Figs. C.11a, C.14a, C.17a) where E_x peaks (along $x=0$ in Figs. C.13a, C.16a, C.19a).

The multimode MC model exhibits marked asymmetry in the radiated fields which can be understood by the addition of modal source components represented in Figure 2.5. This behavior is caused by the asymmetric location of the feed point. At the feed edge of the patch, the magnetic sources add to produce a greater contribution to the field whereas at the opposite edge, sources cancel to reduce the contribution. This can be observed most clearly by the patterns of the primary transverse component (E_x) in P planes (Figs. C.24a, C.27a, C.30a) and in the E-plane (Fig. C.33a). Total power patterns in the P plane also exhibit this offset peak toward the feed as expected (Figs. C.26, C.29 and C.32). The Y-axis symmetry alone is retained in the MC model as exhibited by the single null in E_y through the center of the patch (along $y=0$ in Figures C.24b, C.27b and C.30b). The normal component now peaks at the opposite edge of the patch from the feed as exhibited in Figures C.28a, C.31a. The implication of this can be observed by contours of the relative normal to transverse component power ratios (R_{zt}) in Figures C.25b, C.28b and C.31b. These plots show a peak where $R_{zt} > 0$ dB indicating that a potential hot spot could occur at this position when heating muscle through a fat layer. However, the problem is lessened at increasing distances away from the radiator and because the R_{zt} peak occurs away from the total power peak where primary heating occurs.

Comparing the total power contours (relative dB) in the E-plane for the SC model versus the CC model (Fig. 2.6), it is clear that the most distinguishable differences occur in the first 1 cm of axial depth for the case of this 2.5 x 3.4 cm patch where the fields are dying off rapidly. Beyond approximately $z=3.0$ cm, the fields from a patch of this dimension appear functionally equivalent in this homogeneous medium. Calculations of the MC model for this case (Fig. 2.7b) show a pronounced asymmetry in the field patterns near the patch that distinguishes it from the SC and CC models. This can be explained as before by the addition of modes at the feed edge as opposed to cancelation at the opposite edge (Fig. 2.5). Thus the magnetic source pair now radiates in a manner similar to a single dipole into the far field (6-10 cm) where a less directive beam (and larger beamwidth) than predicted by the SC or CC model is observed. Patterns for linear, rectangular and hexagonal arrays of rectangular patches (assuming no mutual coupling) can also be calculated but are beyond the scope of this thesis.

2.4.2 Conformal case

The total relative dB power contours for a single patch (2.5 x 3.4 cm) oriented circumferentially on a conformal cylindrical sector applicator with a small radius of curvature ($a=5.0$ cm) are shown in Fig. 2.7b. This result compared to radiated fields obtained from the patch on a planar substrate shows the additional beam concentration obtained with a curved (conformal) substrate. The curved ground plane effectively acts as a reflector to direct the radiation toward a

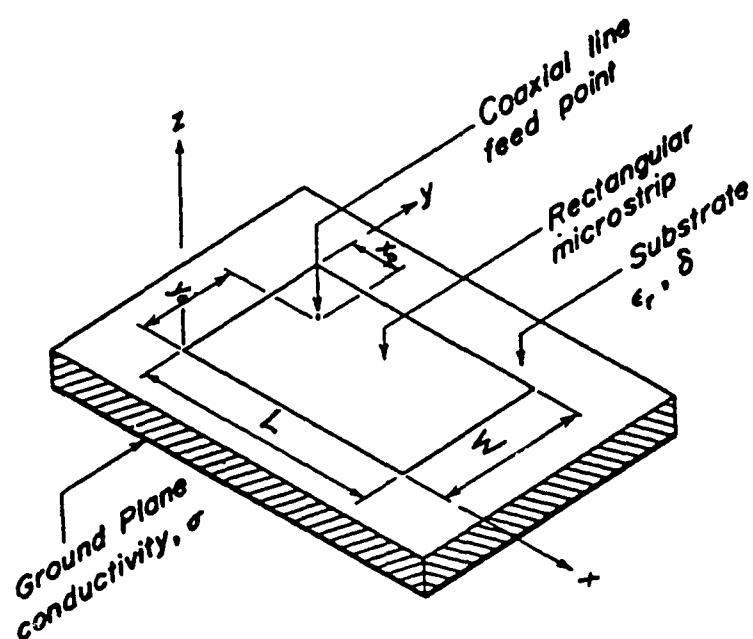
central point. The complete set of electric field components for this case is given in Appendix C (Figures C.38-C.42). Field components are referenced to the cylindrical coordinate system of Figure 2.4. Patterns from linear, hexagonal and rectangular arrays assuming negligible mutual coupling can also be predicted by CYLARR for conformal applicators of larger radius of curvature if the computation time can be afforded. This task could be facilitated by a supercomputer.

2.5 Summary

In this chapter, the cavity-source model has been formulated for use with the rectangular microstrip radiators on planar and conformal substrates. Modal matching coefficients were used to account for the position of feed excitation under the patch which results in some pattern asymmetry. The fringing field correction factor and dielectric constant significantly affect the relative magnitudes of these coefficients while the effective loss tangent appears to affect them minimally. A complete (CC) set of lumped equivalent magnetic source currents is retained to increase the accuracy of prediction in the near field. Two sources of expected error intrinsic to the model are the cosinusoidal internal field assumption dependent on the actual thickness of the substrate relative to a wavelength and the "shadow" effect or blockage of the edge sources not accounted for in the flat ground plane approximation. Further improvements in the model are unlikely without an approach involving distributed instead of lumped sources.

Finally, the source model is used in the formulation for calculating fields for arrays on both planar and conformal substrates. Numerical results are faster to compute for the planar than the conformal applicators. Results of calculated electric field power patterns for a single element graphed by contour plots exhibit characteristics consistent with what is expected from the lumped source models based on duality, symmetry, and vector field addition considerations. Thus, a comparison of these patterns with experimental measurement results in the near field should lead to a better understanding of the range of validity for these models for a rectangular patch radiating into water.

a)



b)

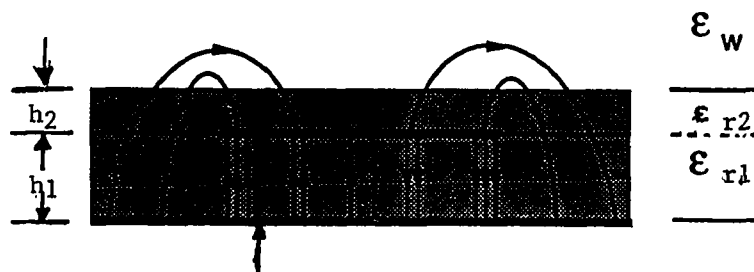


Figure 2.1. Rectangular microstrip patch a) on a simple dielectric substrate [42] with dimensions (L, W) and probe feed position (x_0, y_0) referenced to a rectangular coordinate system at the corner and b) with substrate (ϵ_{r1}) and superstrate (ϵ_{r2}) layers (h_1, h_2) thick) with fringing fields roughly represented.

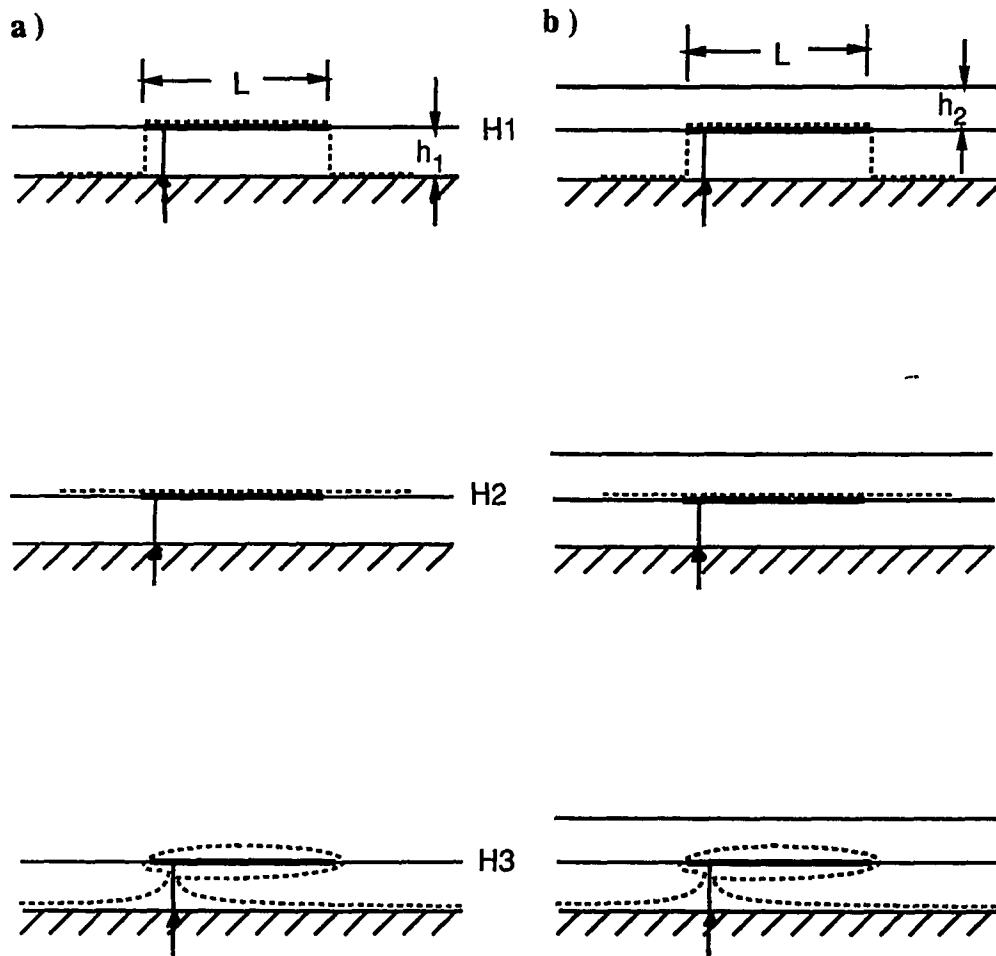


Figure 2.2. Huygen's surfaces [34] for a rectangular microstrip patch
 a) dielectric substrate only;
 b) dielectric substrate and superstrate (cover) layers.

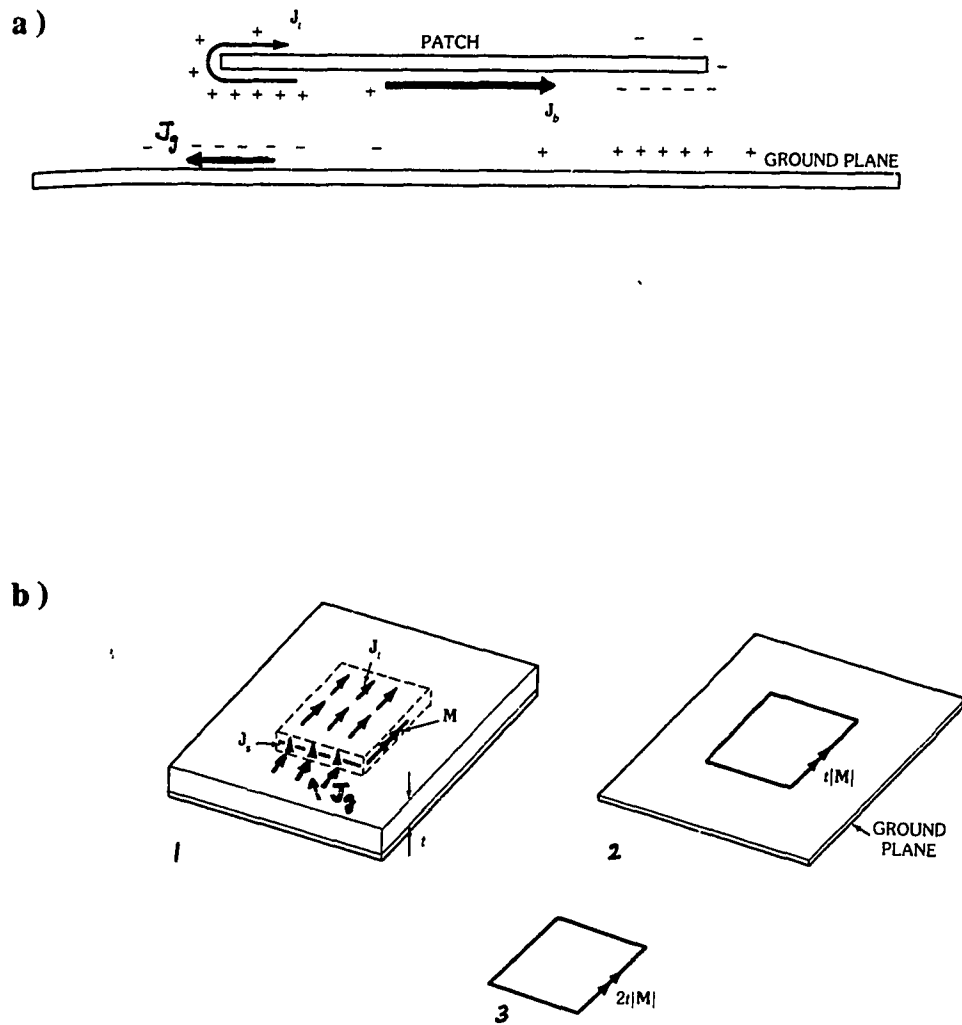


Figure 2.3. Microstrip patch currents [36] a) with electric surface currents due to charge flow on patch and ground plane conductors; b) after steps to the radiating lumped equivalent magnetic line source currents from the cavity model.

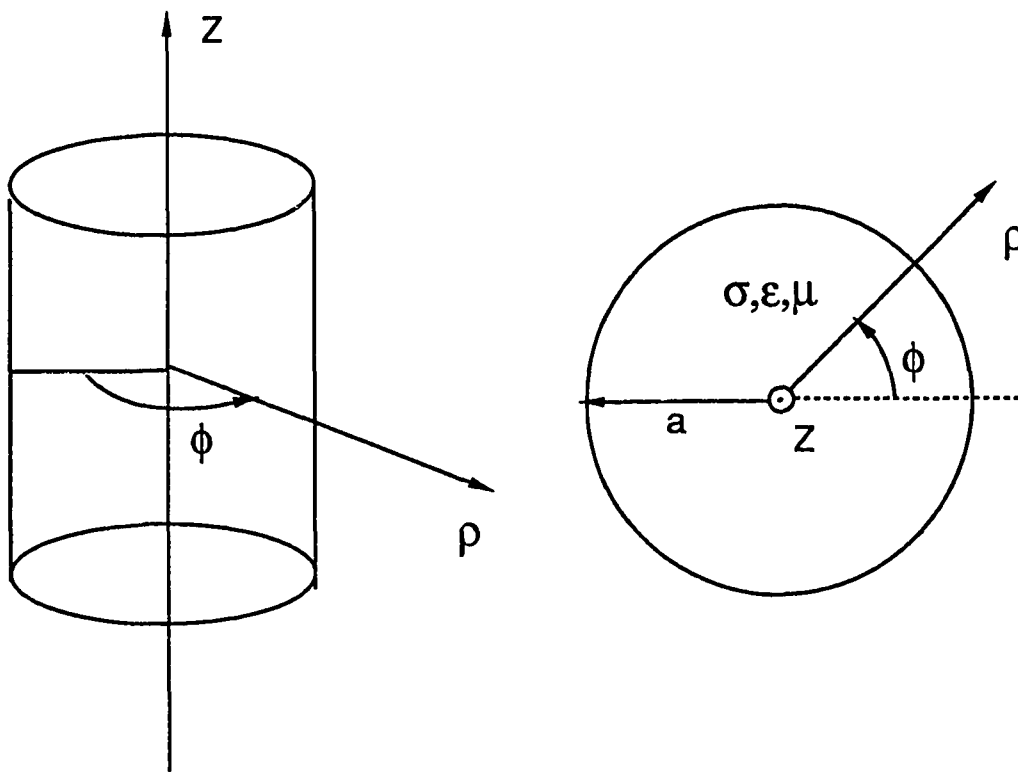


Figure 2.4. Cylindrical coordinate system after J. R. Wait [47,48] for a PEC/dielectric cylinder with a homogeneous lossy dielectric interior.

PATCH EQUIVALENT SOURCES

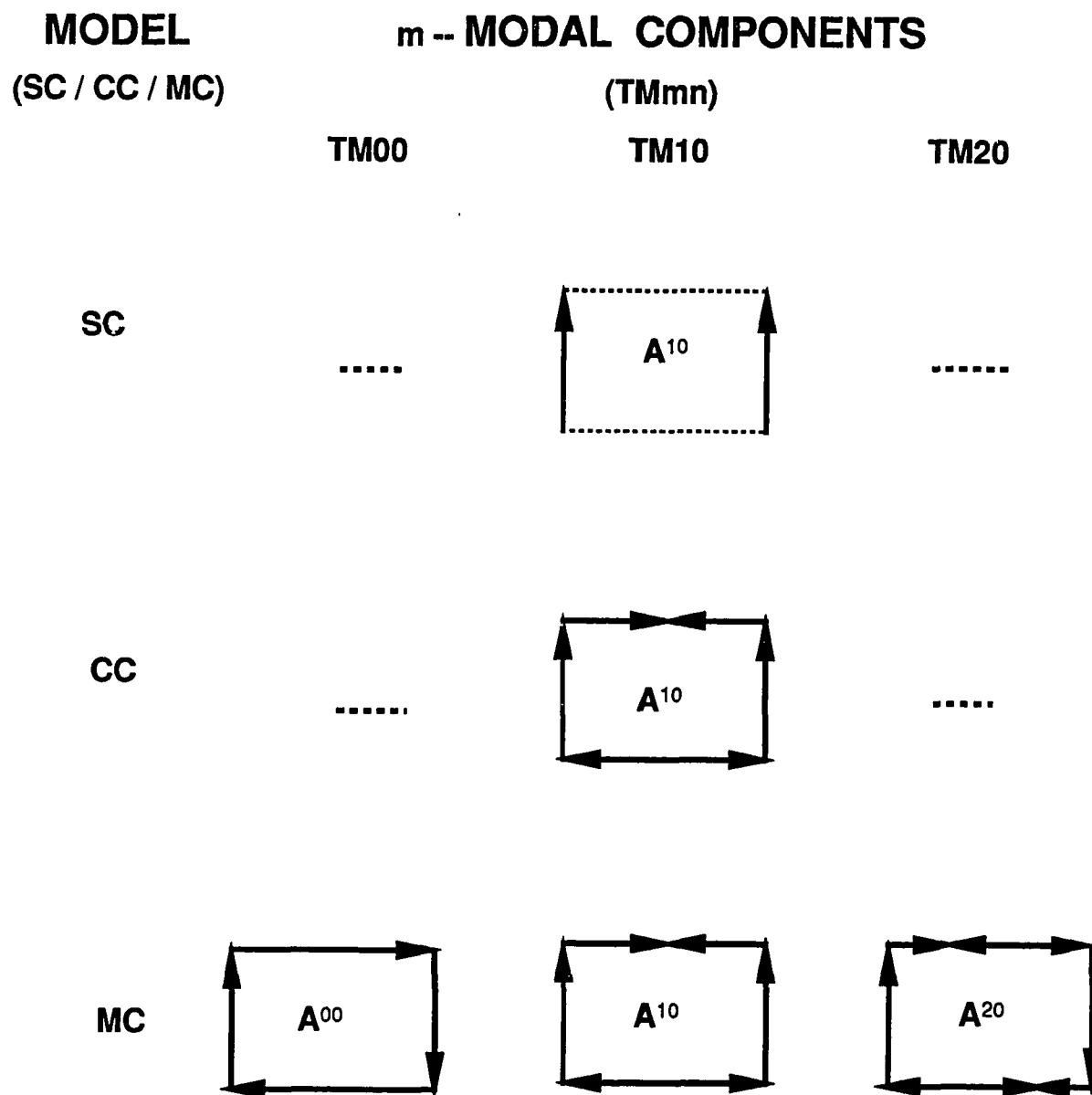


Figure 2.5. Equivalent magnetic current sources for the simple (SC) cavity-source model, complete (CC) cavity-source model and the first 3 m-modal components of the multimode (MC) cavity-source model.

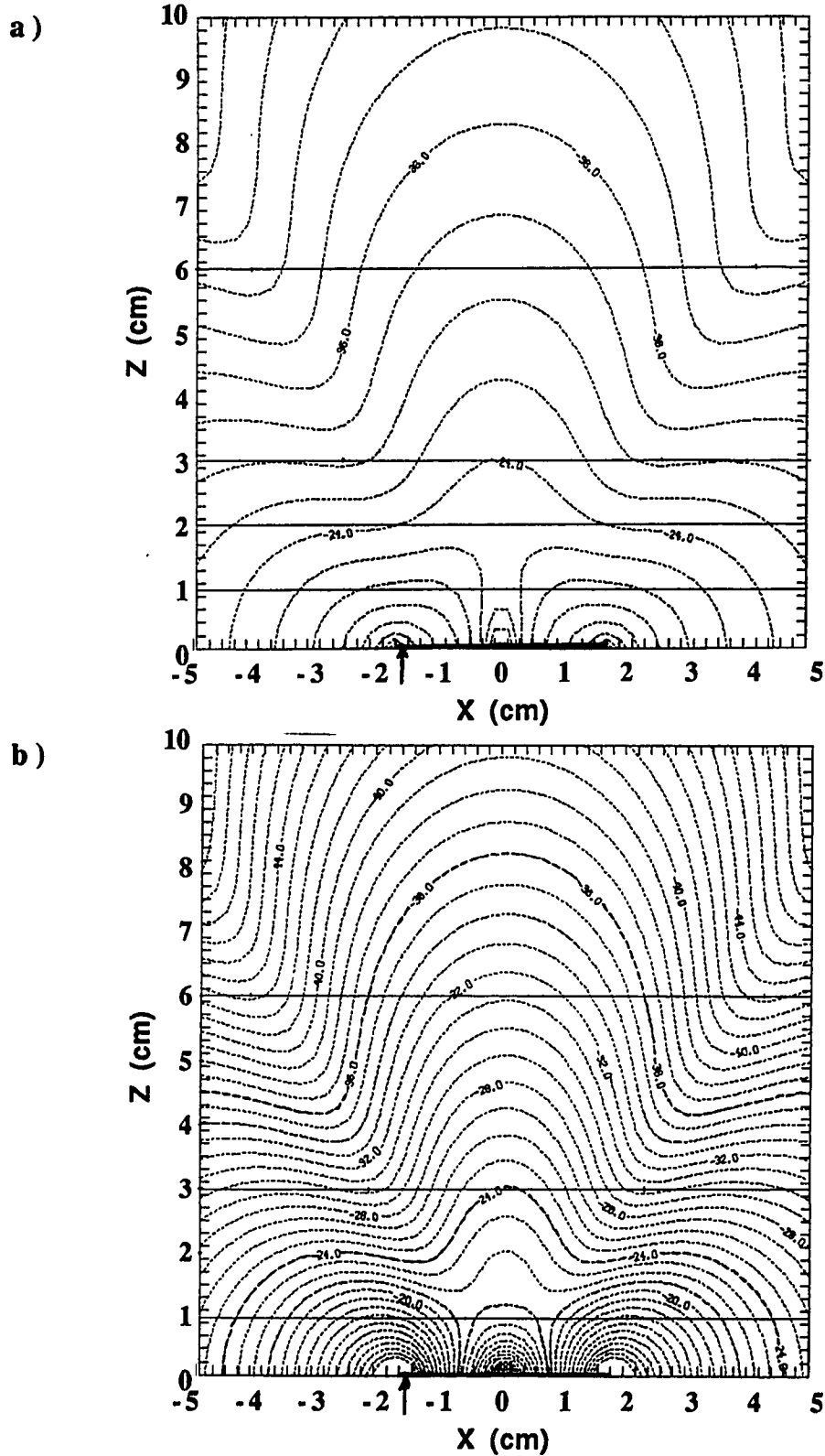


Figure 2.6. Total power $P_T \sim |E|^2$ (relative dB) contours calculated in the E-plane ($y=W/2$) of a planar 2.5×3.4 cm patch radiating in water
 a) SC model (HEXPAR) b) CC model (ARRPAT).

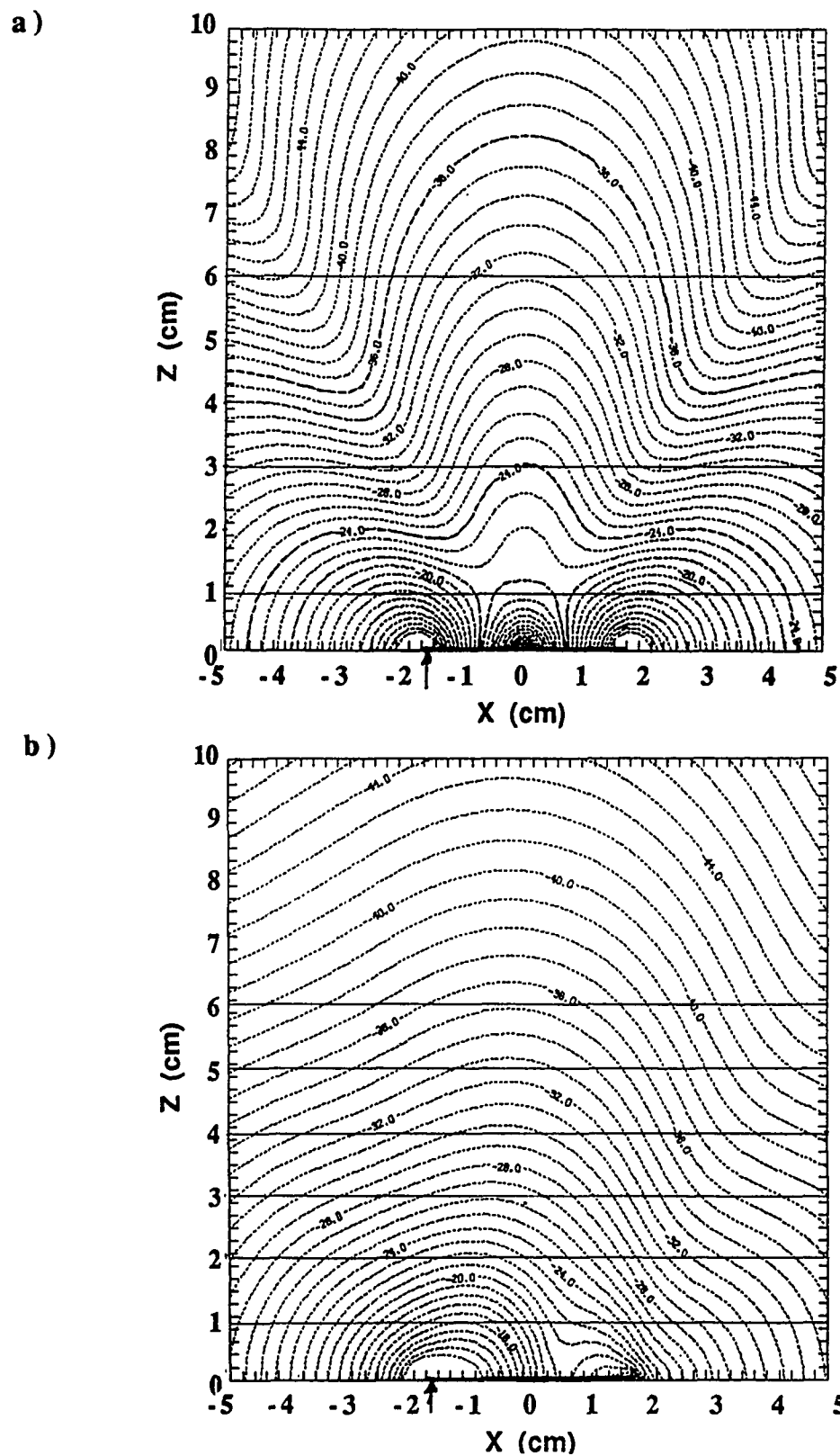


Figure 2.7. Total power $P_T \sim |E|^2$ (relative dB) contours calculated in the E-plane ($y=W/2$) of a planar 2.5×3.4 cm patch radiating in water
 a) CC model b) MC model with $A^{00}=0.56$, $A^{10}=1.0$ and $A^{20}=0.11$.

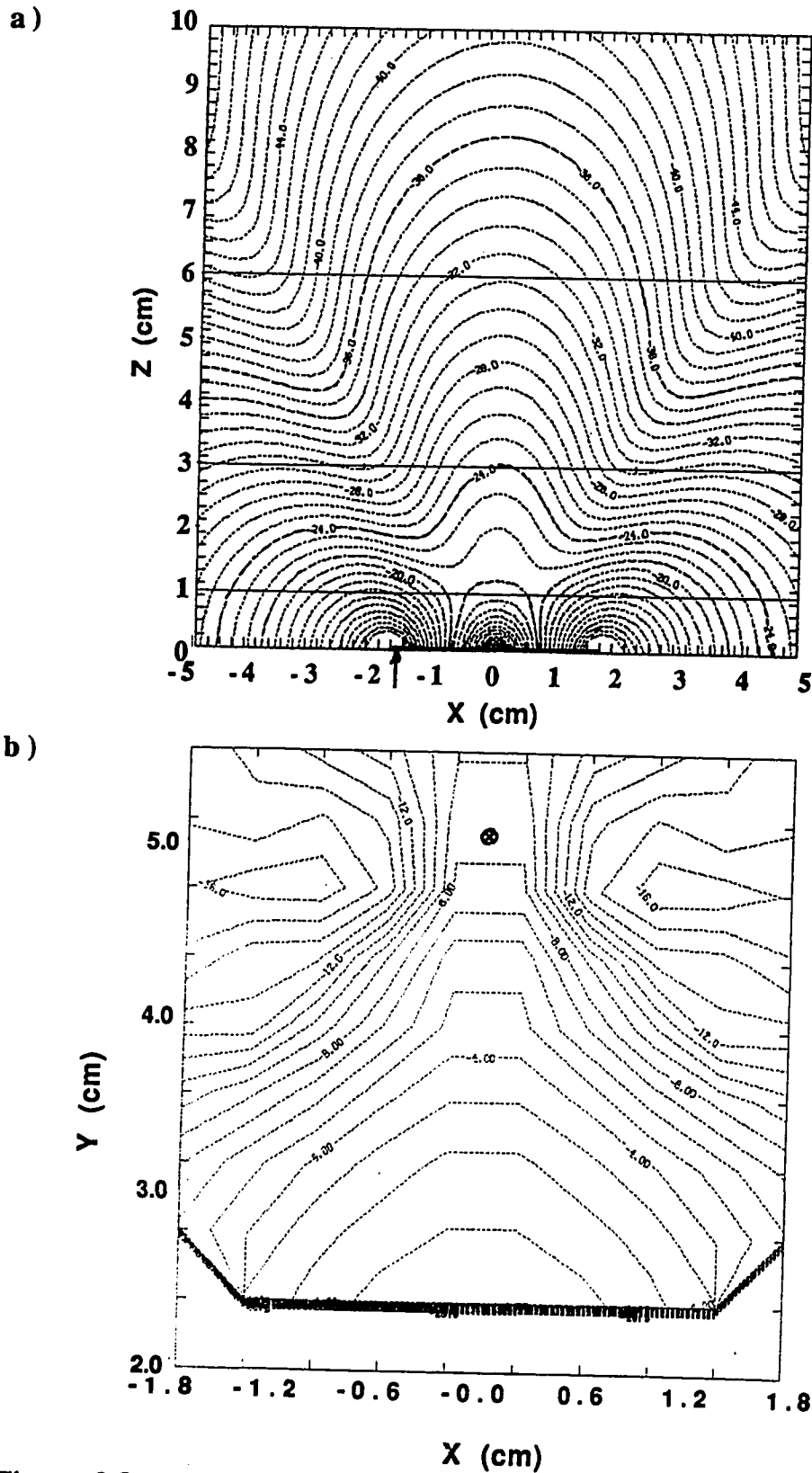


Figure 2.8. Total power $P_T \sim |E|^2$ (relative dB) contours calculated in the E-plane of a 2.5 x 3.4 cm patch radiating in water a) CC model (ARRPAT) b) CC model (CYLARR: radius of curvature $a = 5.0$ cm).

Table 2.1 Electric field component beam characteristics for a 3.4 x 2.5 cm patch radiating in water as calculated by simple (SC), complete (CC) and multimode (MC) cavity-source models in parallel x-y (P-planes) from results represented graphically in Appendix C: the peak power component in each plane is indicated by relative dB values (*) referenced to the primary transverse power component (P_x) at $z=1$ cm; for each model, respectively, multiple 3 dB beam regions in a given plane are indicated {*}.

Depth Z-plane (cm)	Model Type	Peak Power Component			3dB Beam Region	
		P_x (dB)	P_y (dB)	P_z (dB)	Xwidth (cm)	Ywidth (cm)
1.0	SC	-7.1(0)	---	---	1.3{2}	1.9{2}
		---	---	-9.1(-2.0)	0.9{2}	2.2{2}
	CC	-7.1(0)	---	---	1.3{2}	1.9{2}
		---	-10.8(-3.7)	---	2.8{4}	1.1{4}
	MC	---	---	-9.8(-2.7)	---	---
		-2.2(0)	---	---	1.2	1.8
---	---	-5.5(-3.3)	---	---	---	
---	---	---	-1.4(+0.8)	0.8	0.9	
3.0	SC	-13.5(-6.5)	---	---	2.2	3.4
		---	---	-22.8(-15.7)	1.3{2}	3.6{2}
	CC	-13.6(-6.5)	---	---	2.2	3.4
		---	-22.2(-15.1)	---	2.4{4}	2.4{4}
	MC	---	---	-22.1(-15.0)	1.8{4}	3.1{4}
		-12.7(-10.5)	---	---	4.2	2.9
---	---	-16.4(-14.2)	---	3.1{2}	2.4{2}	
---	---	---	-16.1(-13.9)	2.8	1.8	
6.0	SC	-20.8(-18.6)	---	---	3.3	5.4
		---	---	-34.1(-31.9)	2.0{2}	6.1{2}
	CC	-20.8(-18.6)	---	---	3.3	5.4
		---	-32.2(-30.0)	---	---	---
	MC	---	---	-32.5(-30.3)	0.4-3.2{2}	>10.0{2}
		-20.6(-18.4)	---	---	2.7	3.0
---	---	-26.3(-24.1)	---	3.2{2}	2.4{2}	
---	---	---	-27.1(-24.9)	2.4	3.2	

Relative magnitudes of MC coefficients approximated as $A^{mn} = \hat{A}^{mn}$:
 $A^{00} = 0.56$, $A^{10} = 1.0$ and $A^{20} = 0.11$.

Table 2.2 Total power electric field beam characteristics for a 3.4 x 2.5 cm microstrip patch radiating in water as calculated by 3 cavity-source models in the E and H planes at 3 depths--based on results represented graphically in Appendix C: peak total power levels in each plane (*) are referenced to the total power level $P_T \sim |E|^2$ at $z=1$ cm to indicate the relative dropoff at depth; predicted values are also indicated for the half-power beam width (HPBW) and first null beam width (FNBW).

Depth z (cm)	Model Type	Reference Peak Level (dB)	Beamwidth		Plane E/H (x/y)	Side Lobe Level
			HPBW (cm)	FNBW (cm)		SLL (dB)
1.0	SC	-17(0)	2.5	1.0	x	+5
		-22(-5)	2.2	>10	y	(none)
	CC	-17(0)	1.1	1.3	x	+5
		-22(-5)	2.1	>10	y	(none)
	MC	-15(0)	2.2	>10	x	(none)
		-19(-4)	2.5	>10	y	(none)
3.0	SC	-24(-7)	2.6	5.1	x	-7
		-24(-7)	3.4	>10	y	(none)
	CC	-24(-7)	2.4	4.4	x	-5
		-24(-7)	3.4	>10	y	(none)
	MC	-26(-11)	4.3	>10	x	(none)
		-26.5(-11.5)	3.9	>10	y	(none)
6.0	SC	-31(-14)	3.6	7.8	x	-12
		-31(-14)	5.4	>10	y	(none)
	CC	-31(-14)	3.6	8.25	x	-12
		-31(-14)	5.4	>10	y	(none)
	MC	-35(-20)	5.3	>10	x	(none)
		-35(-20)	5.3	>10	y	(none)

Relative magnitudes of MC coefficients approximated as $A^{nm} = \hat{A}^{nm}$:
 $A^{00} = 0.56$, $A^{10} = 1.0$ and $A^{20} = 0.11$.

Table 2.3 Complex amplitude coefficients of the resonant cavity modes for the z-directed internal electric fields of the closed ideal cavity as a function of substrate dielectric constant ($\epsilon_{r1} = 10.2$), effective loss tangent (δ_e) and fringing field dimensional correction factor ($\Delta W = \Delta L = 2h = 0.50$ cm).

Substrate Constant	Dielectric ϵ_{r1}	Effective Loss Tangent δ_e	Patch Dimension		Mode Number mn	Amplitude Coeff. Complex Rel. Mag.		A^{mn}
			W (cm)	L (cm)		Real $\{\hat{A}^{mn}\}$	Img $\{\hat{A}^{mn}\}$	
10.2	10.2	0	2.54	3.40	00	0	2230	0.64
					02	0	290	0.08
					10	0	-3480	1.00
					12	0	504	0.14
					20	0	-541	0.16
					22	0	358	0.10
					00	-22.3	2230	0.64
02	0.2	290	0.08					
10	-27.3	-3480	1.00					
12	0.3	504	0.14					
20	-0.7	-541	0.16					
22	0.1	358	0.10					
10.2	10.2	0.1	2.54	3.40	00	-220.8	2208	0.64
					02	1.9	290	0.08
					10	-271.1	-3459	1.00
					12	2.9	504	0.14
					20	-6.7	-541	0.16
					22	1.5	358	0.10
					00	-220.8	2208	0.64
02	1.9	290	0.08					
10	-271.1	-3459	1.00					
12	2.9	504	0.14					
20	-6.7	-541	0.16					
22	1.5	358	0.10					
10.2	10.2	0	3.04	3.90	00	0	1625	0.38
					02	0	312	0.07
					10	0	-4276	1.00
					12	0	514	0.12
					20	0	-464	0.11
					22	0	317	0.07
					00	0	1625	0.38
02	0	312	0.07					
10	0	-4276	1.00					
12	0	514	0.12					
20	0	-464	0.11					
22	0	317	0.07					
10.2	10.2	0.01	3.04	3.90	00	-16.2	1624	0.38
					02	0.3	312	0.07
					10	-58.6	-4275	1.00
					12	0.4	514	0.12
					20	-8	-464	0.11
					22	0.2	317	0.07
					00	-16.2	1624	0.38
02	0.3	312	0.07					
10	-58.6	-4275	1.00					
12	0.4	514	0.12					
20	-8	-464	0.11					
22	0.2	317	0.07					
10.2	10.2	0.1	3.04	3.90	00	-160.8	1608	0.38
					02	3.0	312	0.07
					10	-575.0	-4197	1.00
					12	4.2	514	0.12
					20	-7.8	-464	0.11
					22	1.8	317	0.07
					00	-160.8	1608	0.38
02	3.0	312	0.07					
10	-575.0	-4197	1.00					
12	4.2	514	0.12					
20	-7.8	-464	0.11					
22	1.8	317	0.07					

Table 2.4 Complex amplitude coefficients of the resonant cavity modes for the z-directed internal electric fields of the closed ideal cavity as a function of substrate dielectric constant ($\epsilon_{r1} = 85$), effective loss tangent (δ_e) and fringing field dimensional correction factor ($\Delta W = \Delta L = 2h = 0.50$ cm).

Substrate Constant ϵ_{r1}	Dielectric Constant	Effective Loss Tangent δ_e	Patch Dimension		Mode Number mn	Amplitude Coeff. Complex Rel. Mag. A^{mn}		
			W (cm)	L (cm)		Real $\{A^{mn}\}$	Img $\{A^{mn}\}$	Rel. Mag.
85	0	0	2.54	3.40	00	0	1284	0.01
					02	0	217	0.00
					10	0	99200	1.00
					12	0	395	0.00
					20	0	-833	0.01
					22	0	306	0.00
85	0.01	0.01	2.54	3.40	00	-12.8	1284	0.01
					02	0.2	217	0.00
					10	-33723	85973	1.00
					12	0.3	395	0.00
					20	-2.9	-833	0.01
					22	0.2	306	0.00
85	0.1	0.1	2.54	3.40	00	-127.1	1271	0.05
					02	1.9	217.2	0.01
					10	-23747	6054	1.00
					12	3.1	395	0.02
					20	-28.7	-832	0.03
					22	2.0	306	0.01
85	0	0	3.04	3.90	00	0	670	0.23
					02	0	288	0.10
					10	0	2951	1.00
					12	0	453	0.15
					20	0	-557	0.19
					22	0	219	0.07
85	0.01	0.01	3.04	3.90	00	-6.7	667	0.23
					02	0.6	288	0.10
					10	-73	2949	1.00
					12	0.9	453	0.15
					20	-4	-557	0.19
					22	0.3	219	0.07
85	0.1	0.1	3.04	3.90	00	-66.3	663	0.23
					02	6.2	288	0.10
					10	-690	2780	1.00
					12	8.7	453	0.16
					20	-39.9	-554	0.19
					22	3.1	219	0.08

CHAPTER 3

EXPERIMENTAL MEASUREMENTS OF MICROSTRIP PATCH ANTENNAS IN WATER

3.1 Materials and Methods

3.1.1 Measurement systems

For validating and testing the limits of the cavity-source model and evaluating the effect of design parameter variations such as substrate and superstrate thickness, dielectric constant and array element spacing on the performance of a microstrip antenna applicator for hyperthermia therapy, two measurement systems were utilized. First, a network analyzer was used to measure Return Loss (S_{11}) and Transmission Loss (S_{21}) for water submerged antenna array radiators in the operating frequency range of interest. Second, a 3-axis scanner was used to characterize 3D radiated E-field power patterns in a water tank. The scanning system served to collect electric field pattern measurement data along linear (1D) axial and transverse scan paths or 2D regions such as the principal E (x-z), H (y-z) (Balanis [49]) and P (parallel x-y) planes of interest. These measurement data provide information about the effectiveness of a particular applicator design in achieving E-field distributions suitable for hyperthermia heating. Reflection and Transmission Loss measurements as a function of frequency supply information about the impedance match quality of an antenna radiator and mutual element coupling. Antenna input match and mutual coupling have implications in terms of energy transfer efficiency over a specified

bandwidth and the degree of independent element isolation (and hence control) that can be expected from a given array element spacing. Finally, phase and amplitude adjustments can be tested to investigate focusing possibilities necessary to concentrate energy for local and deep heating.

A complete 3-axis scanning system (Fig. 3.1) consists of 3 step motors connected to a mechanical 3-axis positioner. Step motors are controlled by software on a microcomputer system that performs linear (1D) and planar (2D) raster scans in a user specified direction. The microcomputer sends control signals through a digital-to-analog (D/A) converter and the associated hardware controller in such a way to carry out a scan according to user specified length, width, orientation and sample spacing. Data acquisition is also performed by the microcomputer. Electric field power detected by the measurement probe is converted to dc voltage by a diode square law detector and sampled by an analog-to-digital (A/D) converter.

The measurement probe consists of a small, insulated or encapsulated dipole. For crude square law detection measurements, the leads of a diode can be used to form a diode-dipole (DD) probe where the dipole is approximately half-wavelength in water (2 cm) and connected to a coaxial transmission line. However, this allows only half-wavelength resolution and limits measurements to transverse E-field components so that the coax does not perturb the field. If field variations are small enough and sample averaging can be tolerated, then this type of probe can suffice for measuring transverse field components. However, a miniature, nonperturbing, microwave transparent measurement (MND) probe [51] enables

higher resolution, smaller field perturbation and "sees" the normal component of the E-field radiated from the source.

In the Bioacoustics Research Laboratory (BRL) at the University of Illinois at Urbana-Champaign, microwave field measurements were performed on a modified mill-based scanner system under DEC PDP-11 microcomputer control [50]. Data acquisition for microwave power scans was performed by the FORTRAN program MWPLAN (Appendix A). Both crude DD and miniature MND probes were used as the detectors. The MND probe (Fig. 3.2) has a 3 mm wide encapsulated tip with an electrodeposited nickel dipole oriented at 57 degrees to the probe axis. A beam lead zero-bias Schottky diode (HSCH 5330, Hewlett Packard, San Jose, CA) bonded with conductive epoxy (Chomerics, Woburn, MA) in the gap between electrodeposited nickel dipole elements converts the antenna to a square law detector. The probe outputs a mV dc voltage proportional to mW/cm^2 . A pair of fine closely spaced resistive leads deposited on a narrow substrate (Ohmegaply, Omega, Culver City, CA) gives the probe its microwave transparent nonperturbing quality. The lead pair actually acts as a lossy transmission line that low-pass filters by attenuating microwave frequency signals [51]. The DD probe uses an HP HSCH 3486 zero bias Schottky diode insulated with a coating of nail polish and connected to high carbon polymer wire (Polymer Corporation, Reading, PA) leads to effectively increase its microwave transparent characteristic over a coax cable. The DD probe is not as precise as the MND probe for E-field component resolution but it is easier to fabricate and less fragile. It works well for rough measurements. The mV dc output signal from either probe requires amplification to

scale it to the 0-10 v 12-bit A/D range. This is accomplished by a high input impedance adjustable high-gain (multistage) dc amplifier.

The water tank for this system has usable inside dimensions of 50 x 38 x 25 cm (20 x 15 x 10 in). This was judged to be large enough for measurements of a single patch and small scale arrays of a few elements. Maximum travel distance is maintained by limit switches that keep the miniature electric field probe from touching the tank walls. Although some metallic pipes that carry water for heating and cooling exist on the bottom of the tank, these were considered far enough from the source that attenuation of water should sufficiently damp out any potential scattering.

An HP8408 Network Analyzer performed Return Loss (S_{11}) and Transmission Loss (S_{21}) measurements for the water submerged antenna radiators. The HP 8408 makes automatic S-parameter measurements with the aid of Accuracy Enhancement Software (Jose Schutt-Aine, EM Laboratory, University of Illinois). Plastic tubs (6 x 9 x 18 in; 8 x 12 x 24 in) full of distilled water were used to submerge the antenna applicator during measurements. Subminiature (SMA) connectors were employed with 50 ohm RG 58/U cables to connect to the probe fed patches on the applicator substrate. Type APC-7 to SMA and N-type adapters were also used to connect the device under test (DUT) to the HP 8408.

3.1.2 Applicator Design

Conductive and nonconductive (dielectric) materials are required to construct a microstrip antenna array applicator. The

substrate consists of a thin ($h/\lambda_s \ll 1$) sheet of low loss ($\sigma_s/\omega\epsilon \ll 1$) dielectric with dimensions large enough to handle the size of the desired antenna array. Ideally, the extent of the array is enough to cover the area of a typical treatment region. The number of array elements also affects the degree of focusing possible for energy concentration (gain) at deeper anatomical sites. Once the total number of antenna elements in the array has been chosen, the size of the array (thus size of the substrate) can be determined. The largest substrate dimension depends on the maximum number of elements (N) desired in each direction, the resonant element length ($l = \lambda_e/2$) and the array element spacing ($d_s = a\lambda_w$ where typically $0.5 < a < 1.5$). An effective wavelength (λ_e) is a function of the effective dielectric constant

$$\lambda_e = \frac{\lambda_0}{\sqrt{\epsilon_e}} \quad (3.1)$$

The effective dielectric constant (ϵ_e) is a nontrivial function of the substrate dielectric constant (ϵ_{r1}) and thickness (h_1); superstrate dielectric constant (ϵ_{r2}) and thickness (h_2); complex medium permittivity (ϵ_m) and the width (W) of the patch radiator.

$$\epsilon_e = f(W, h_1, h_2, \epsilon_{r1}, \epsilon_{r2}, \epsilon_m) \quad (3.2)$$

Using the variational technique of Yamashita and Mittra [23], it is possible to calculate this function via the charge to determine the capacitance with dielectric layers present (C) versus free space (C_0).

This computation of C and C_0 is facilitated by a moment method integration technique.

An alternative approach to obtaining ϵ_e for design purposes is to extract it from an experimental measurement technique. A microstrip line technique uses a stripline of known physical length and width on a substrate in a test tank with a matched termination. Walls of the tank are enclosed, sealed and filled with typical dielectric layers. Since the electrical length of the line is $\beta l = (2\pi l/\lambda)$, if the line is $2-3\lambda$ long, a Return Loss (S_{11}) vs. frequency plot in the operating range of interest will show maximums corresponding to line lengths $l = n\lambda/2 = nc/2f$. Two successive maximums are separated by $\Delta\beta l = \beta_H l - \beta_L l = \pi$. A relationship for ϵ_e can be derived in terms of these parameters.

$$\epsilon_e = (c/2L(f_H - f_L))^2 \quad (3.3)$$

This method was tried but gives only approximately refined estimates of the effective dielectric constant within the expected boundaries $\epsilon_{r1} < \epsilon_e < |\epsilon_w|$ since the presence of a lossy medium complicates the return loss versus frequency information. Thus, a cut and try method was used to determine the resonance length ($l = \lambda_e/2$) of a rectangular patch on a given substrate in water. This can be carried out by measuring the Return Loss (S_{11}) of the patch in water over a wide frequency range to identify the resonance. Rough approximations of ϵ_e can be used to estimate the overall array size on a given substrate material.

To properly function as a substrate for the microstrip patch, the dielectric material must have a conducting ground plane on one surface. On Duroid substrates (Tables 3.1-3.3), electrodeposited copper (1 ounce) works as a good conducting surface. One side of the dielectric sheet is exposed with a suitable etchant such as Printed Circuit (Ferric Chloride) Etching Solution (GC Electronics, Rockford, IL). Copper electrical tape (Scotch Brand, 3M, St. Paul, MN) also works to cover one side of an exposed dielectric sheet. A groundplane for the MCT-85 substrate (Tables 3.1-3.5) was constructed by this method [52]. Solder fillets were added along the overlapping edges of the copper strips to insure electrical contact and eliminate possible resistance pathways from the conducting surface to make it a better conducting groundplane.

Omni/Spectra SMA stripline launchers (Compucon, Des Plaines, IL) acted as feed connectors to bring the MW power from the N(male)-SMA(male) RG-58 50 Ω coaxial cable (Pasternack Enterprises, Irvine CA) through the ground plane to the copper tape (3M) microstrip patch via a probe feed (Fig. 3.3). The probe feed fits an accommodating hole drilled in the substrate at a position determined by the array geometry. The tip was trimmed flush with the substrate surface allowing electrical solder connection to the copper patch as well as flush contact of a superstrate covering layer.

3.1.3 S-parameter measurements

S-parameter measurements, as noted previously, supply information about the quality of microstrip applicator design for

single and multiple element configurations. For example, return loss ($L_R = |S_{11}|^2 = -20 \log|\Gamma|$ dB where 1 refers to the self-input of a microstrip patch element) versus frequency measurements identify the resonance and match quality (dB) of a single patch. This method, for example, was used to show the advantage of a thin superstrate cover layer in the design of a patch on a low K (Duroid 6010) substrate when radiating into water (Fig. 3.4). When this method is used iteratively along with incremental changes in the patch dimensions (e.g., length L) it allows the resonance dimensions (L,W) to be determined at the design frequency (915 MHz). This happens to be an easier and more direct approach for finding ϵ_e than the approach described in Section 3.1.2. Results of resonance length (L) determination and subsequent ϵ_e calculation for various substrate and superstrate applicator designs are compiled for a single patch radiating into air (Table 3.2) and radiating into water (Table 3.3). An effective dielectric constant is also calculated for comparison by Schneider's [53] empirical relationship (see also Hammerstad [43]).

$$\epsilon_e = \left(\frac{\epsilon_r + 1}{2}\right) + \left(\frac{\epsilon_r - 1}{2}\right)\left(1 + \frac{12h}{W}\right)^{-\frac{1}{2}} \quad (3.4)$$

A modified form (ϵ_e^*) of Schneider's expression is used here as a rough approximation for biomedical media such as water.

$$\epsilon_e^* = \left(\frac{\epsilon_r + |\epsilon_w|}{2}\right) + \left(\frac{\epsilon_r - |\epsilon_w|}{2}\right)\left(1 + \frac{12h}{W}\right)^{-\frac{1}{2}} \quad (3.5)$$

where $|\epsilon_w| = 78$ for water. In conjunction with this, inequalities are used to establish a range of expected values for applicators with substrate and superstrate layers.

Results of effective dielectric constant determination from measurement of the half-wavelength patch resonance frequency in air (Table 3.1) show good agreement against calculations based on Schneider's relation (Eq. (3.4)) with the inequalities for low K substrates. However, experimental results with the MCT-85 substrate disagree widely from Equation (3.4). In water, the rough approximation based on Schneider (3.5) gives estimates close to the experimentally measured results. Agreement can be obtained in most cases for the dual-layered applicators when inequalities are used to establish the upper or lower limits of the value. However, enough error is observed for the Duroid 6010 1-layer and MCT-85 2-layer cases to suggest cautious use of Eq. (3.5) except as a rough approximation.

A 2-port measurement such as insertion loss ($L_1 = |S_{21}|^2 = -20 \log(T_{21})$ dB where 2 refers to the input of an antenna element neighboring the antenna belonging to input 1) versus frequency serves to assess the mutual coupling between 2 adjacent elements in an array. Table 3.4 gives some insertion loss data for a 3-element linear array on MCT-85 radiating into water. A resonance shift is suggested by the data for a 3 cm spacing as indicated by values at 1012 MHz.

For a lower dielectric constant applicator, the mutual coupling factor ($|S_{21}|^2$ dB) as a function of spacing is indicated in Figure 3.5. This applicator consists of a patch between Duroid 6010 ($\epsilon_r = 10$)

substrate and superstrate layers radiating into water. Also indicated here by the dotted line is that the experimental data follow a trend which leads to the expected value of 0 dB at $d=3.4$ cm where the elements would be butted together (touching).

3.2 Design Example: Rectangular Microstrip Patch

As an example, consider the design of a single rectangular patch with a probe feed on a dielectric substrate at 915 MHz for radiation into water compared to the typical design for radiation into air. It is assumed that the optimum orientation of the feed for matching the rectangular antenna to 50 ohms as well as exciting primarily the "quasi" TM_{01} mode underneath the patch is just inside the center of one short edge of the $\lambda_e/2$ resonant patch as it is for air; thus, the feed excites the fields underneath the patch where the fields are a maximum at the "open circuit" edge. One long dimension (L) is maintained as the resonance length while the short dimension (W) is kept less than the length to reduce the possibility of higher order n-modes. Primarily, low dielectric constant ($\epsilon_r \leq 10$) substrates are used for antennas radiating into air. For radiating into water, the intuitive motivation for a higher dielectric constant substrate is twofold. First, it more closely matches the relative permittivity of water so that, except for a difference in scale and the presence of loss in the medium, the antenna should act more like it does in air. Second, the reduction in scale ($\lambda_e = \lambda_0/\sqrt{\epsilon_e}$) means a smaller antenna size advantageous for precise control desired in arrays for hyperthermia application. The low dielectric constant

substrate Duroid 6010 works better in an applicator design for water when a superstrate layer is included (Fig. 3.4) although it gives less size reduction for array elements than the MCT-85 substrate. The effective dielectric constant for a particular choice of dielectric materials and layers can be roughly calculated or measured using one of the methods previously mentioned. Then the antenna radiator on the substrate is immersed in water and return loss is measured with the network analyzer as a function of frequency. The resonance frequency of the patch is assumed to be where the return loss maximum occurs. Fine tuning can be done by trimming the length of the patch until this maximum occurs at or near the desired resonance frequency. Figure 3.4 shows a patch tuned close to 915 MHz.

Absence of a sharp peak in the return loss plot indicates a poor match between the patch antenna and water. Sometimes this is as simple a problem as a poor solder connection between the feed and the patch conductor. Otherwise, the patch resonance length has been misjudged or the dielectric constant poorly chosen. For the case of the Duroid 6010 material, a thin superstrate layer on top of the patch conductor helps to draw out the fringing fields to successfully match the radiator into water in spite of the drastic dielectric discontinuity. However, this layer is much thinner than the typical quarter-wavelength matching layer.

3.3 E-field Measurement Probe Characteristics

A set of experiments was performed on the MND probe to characterize its response over a range of incident (radiated) field power and frequency. Figure 3.6 indicates a linear response for probe output voltage versus radiated power from a rectangular C-band (WR-187; 1.872" x 0.872") dielectric filled waveguide converted and matched to water at 915 MHz. In this case, the probe measured the primary transverse component of radiated power from the waveguide source at a depth of 10 cm. Figures 3.7 and 3.8 show normal and transverse components measured from microstrip applicators that indicate linearity over a broad range of input power. These high-power experiments illustrate the power handling capability of microstrip applicators for typical and radiated power levels required to induce a typical thermal dose for hyperthermia therapy. Frequency response data were also collected for the MND probe using the rectangular waveguide source by holding the radiated power constant as the source frequency varied. Data plotted in Figure 3.9 indicate that the probe is relatively insensitive to frequency variations (drift) around 915 MHz. For a 10 MHz range of frequency (915 +/- 5 MHz), the output response changes less than 1 dB. The data indicate that the probe has a 1.5 dB bandwidth of 60 MHz (880 - 940 MHz) where the response peaks at 900 MHz (0 dB).

To test the reliability of the probe against the possibility of perturbation by its physical presence in the fields under measurement, a comparison was made between measurements of the MND and DD probes. Since these two probes have different size,

shape and construction, any significant amount of perturbation should show up as a difference in the measured pattern observed by the probe. As a case for comparison, the primary transverse power component radiated from a microstrip patch on MCT-85 was measured by both probes over a common range 3 cm wide ($-1.5 < x < 1.5$ cm) in the transverse direction and 2.5 cm deep ($1.5 < z < 4.0$ cm) in the axial direction. Since these E-plane cuts (Figure D.5) show no significant discrepancies in the contour patterns between these two probes of different size, no clear evidence is provided to suggest significant perturbations by either the MND or the DD probe in this range. Also, other tests with the MND probe were performed by measuring the radiated fields in water for the rectangular dielectric filled waveguide as a "reference" source. The measured and theoretical patterns are in reasonable enough agreement to suggest that the MND probe can be trusted to characterize other sources under the same conditions in a nonperturbing and reliable manner.

3.4 Measurement Results

Contour plots of electric field power radiated from microstrip patches as measured by an MND probe in water are included in Appendix D. These contour plots illustrate the radiated electric field components in the E, H and P (parallel) planes several cm in front of a 3.4 x 2.5 cm patch on Duroid 6010 with substrate and superstrate layers (Figures D.1-D.4 and D.6) and a 1.8 x 1.0 cm patch on MCT-85 substrate alone (Figures D.5 and D.7). Figure D.7 shows radiated fields in the E-plane from a 3-element linear array on MCT-85

spaced 3 cm apart where amplitudes and phases of each element are unadjusted. Quantitative results of these measurements in terms of beam characteristics at $z=1.0, 3.0$ cm depths are compiled in Table 3.6. These can be compared with the corresponding results of relative component levels and 3 dB regions given by the theory for the cavity-source models in Table 2.1 and Table 2.2. Direct theory versus experiment comparisons of linear E and H plane cuts for patches resonant on MCT-85 are given in Chapter 4.

Some basic significant features of the measurement data can be easily observed. Perpendicular E and H-plane cuts for the 3 radiated field components indicate that the primary power component ($P_{xp} = 10.1$ dB) radiated from the 3.4×2.5 cm patch is in the x-direction as expected (Figure D.1). The beam is slightly narrower and more directional in the E-plane than the H-plane as should be expected at least in the far field since $L > W$. The normal component is small ($P_{zp} = +4.0$ dB) in the central H-plane ($x=L/2$) as expected due to cancellation (Figure D.2) and its peak safely below the primary transverse component in the E-plane ($P_{zp} = +8.0$ dB). The asymmetry observed in the normal component pattern has a characteristic double peak in the transverse direction. Although the recorded reference position indicates that the peak of greater amplitude occurs on the feed side of the patch, this is against all other E-plane scan data (e.g., Figure 4.3) collected from such a probe fed patch that indicate the peak of greater amplitude opposite the feed side. This suggests a measurement error. The patterns of Figure D.1a and D.2a also appear to be shifted approximately -5 mm off center possibly due to a systematic error. Figure D.3 shows that the secondary

transverse (P_y) component radiated from the patch is several dB below the primary (P_x) component as expected.

Cuts in the parallel (x - y) plane from the same size patch are shown in Figure D.4 at $z=1.0$ and $z=3.0$ cm. These contours represent the primary transverse radiated component. At $z=1.0$ cm, the pattern appears somewhat more complicated with the presence of two nulls at diagonally opposite corners and a nonuniform central beam region. At $z=3.0$ cm, the beam region becomes more uniform and appears broader in the y -direction. It is clear that the peak region occurs in these parallel planes at both depths on the feed side of the patch.

Primary power component patterns radiated from an MCT-85 patch (Figure D.5a) exhibit uniform beam contours similar to the Duroid patch (Figure D.1a) but scaled down in size and less directive as expected due to smaller resonance dimensions. Figure D.6a exhibits comparable features to D.4b although it is at a slightly greater depth ($z=3.8$ cm). Figure D.6b, however, holds few distinguishable features and thus its reliability is questionable. Finally, Figure D.7 shows E-plane scan contours from an unadjusted amplitude, 3-element linear array on MCT-85 and is valuable as broad background reference data for the linear cuts selected in Chapter 4 to make direct theory versus experiment comparisons.

3.5 Summary

In this chapter, experimental methods and equipment used to aid the design, evaluation and testing of microstrip patch radiators in

water have been described. The quality of measurement devices and techniques have been assessed. One and two-port S-parameters were related to the impedance match quality and mutual coupling of antenna radiators. Some typical results were given. Results of effective dielectric constant determination were given for various layered applicator types in water versus air. Finally, radiated electric field power pattern measurement results were presented for a patch on low and high K substrates. The basic significant features of these patterns were identified in preparation for Chapter 4 where cases are selected for comparison with the theory.

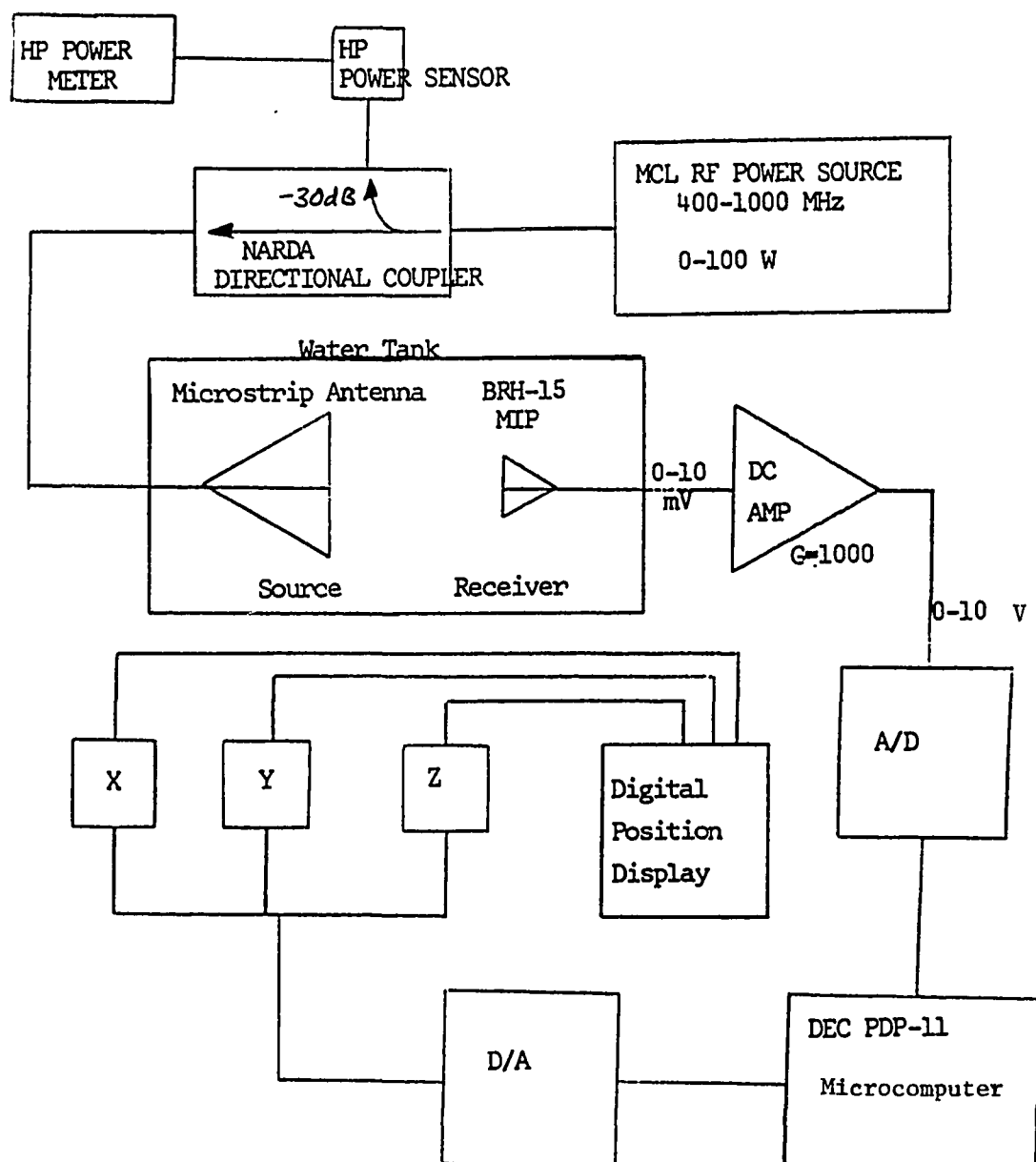


Figure 3.1. Measurement system block diagram.

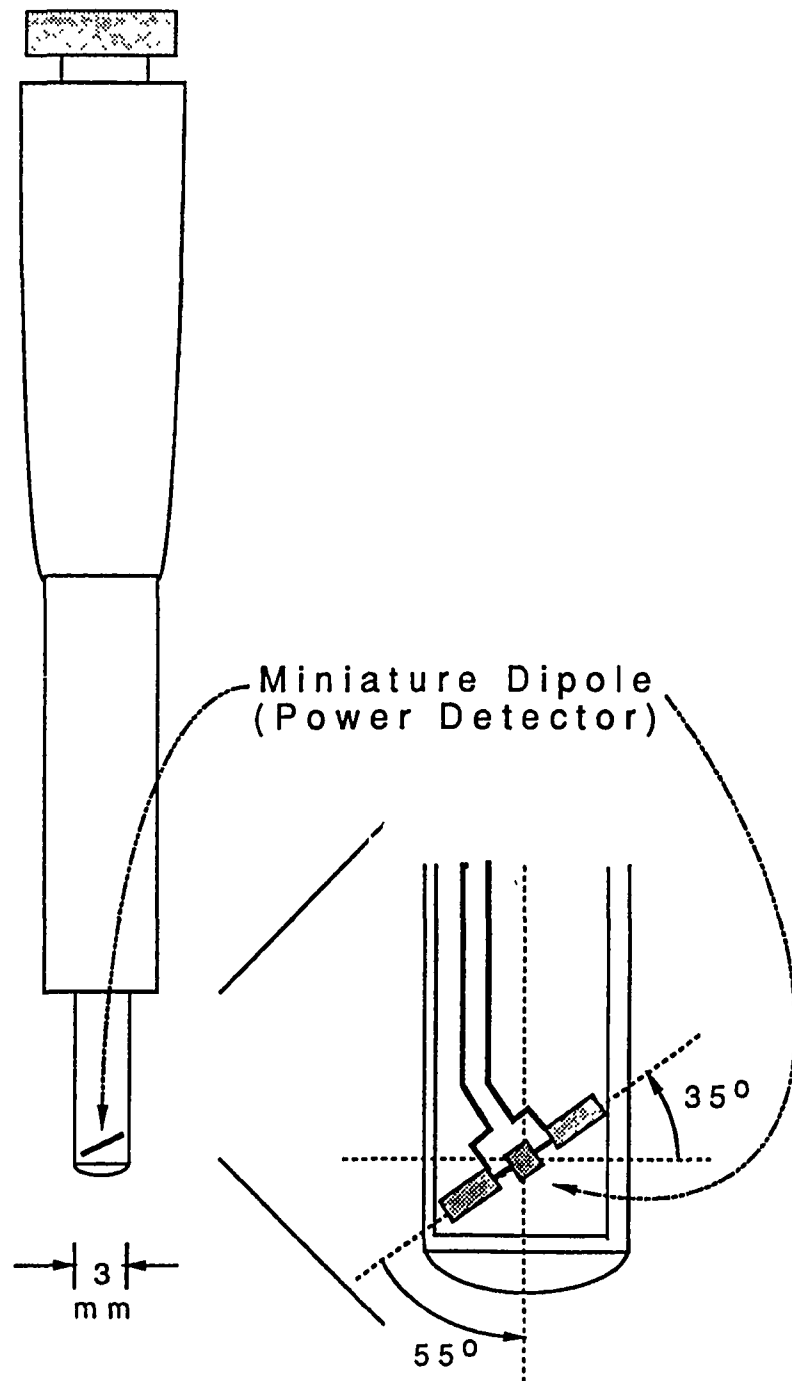


Figure 3.2. Miniature dipole (MND) E-field probe with expanded view of the encapsulated tip.

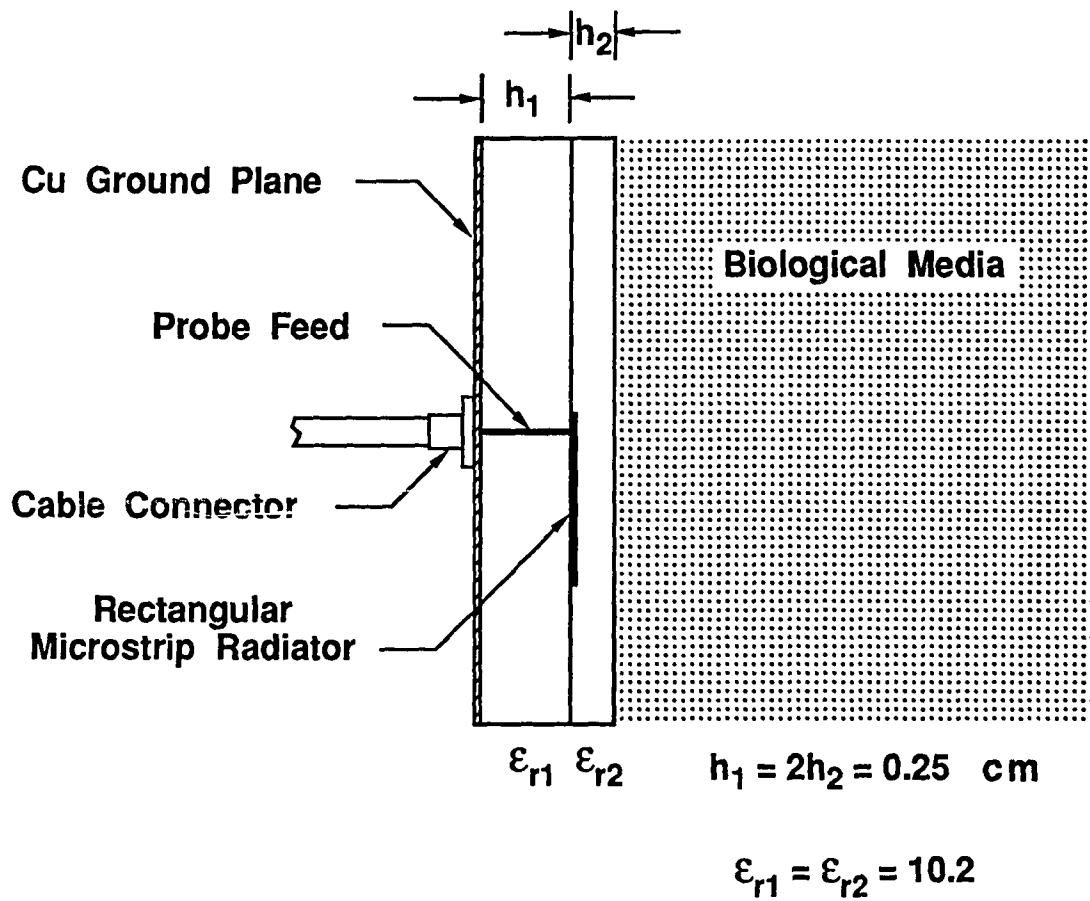


Figure 3.3. Applicator design for a probe fed microstrip patch on a Duroid 6010 dielectric substrate with superstrate (cover) layer.

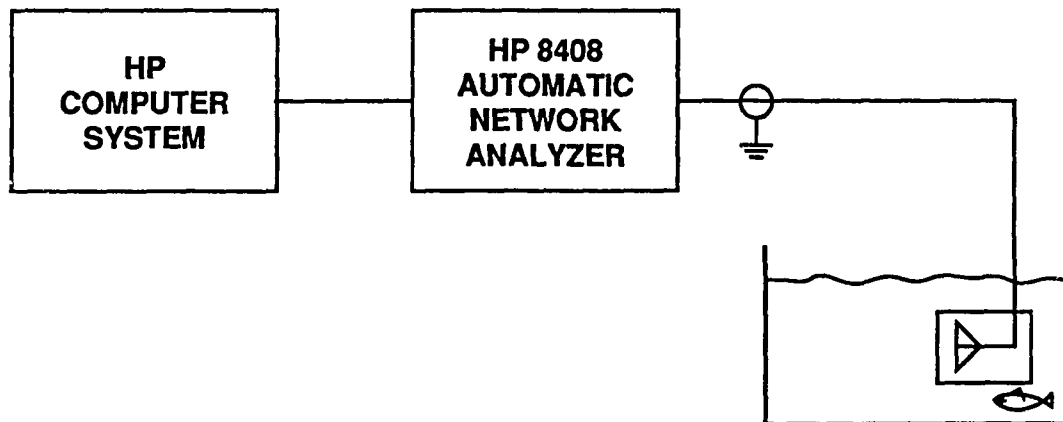
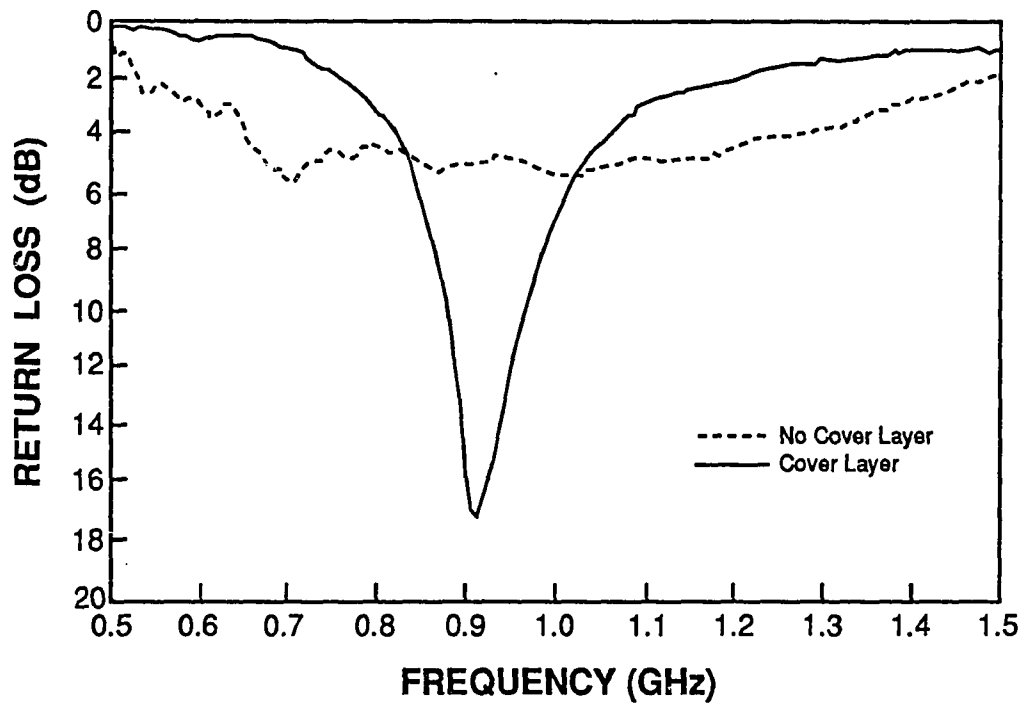


Figure 3.4. Improved match at 915 MHz for a Duroid 6010 applicator with cover layer radiating into water as indicated by return loss ($L_R = |S_{11}|^2$ dB) versus frequency measurements.

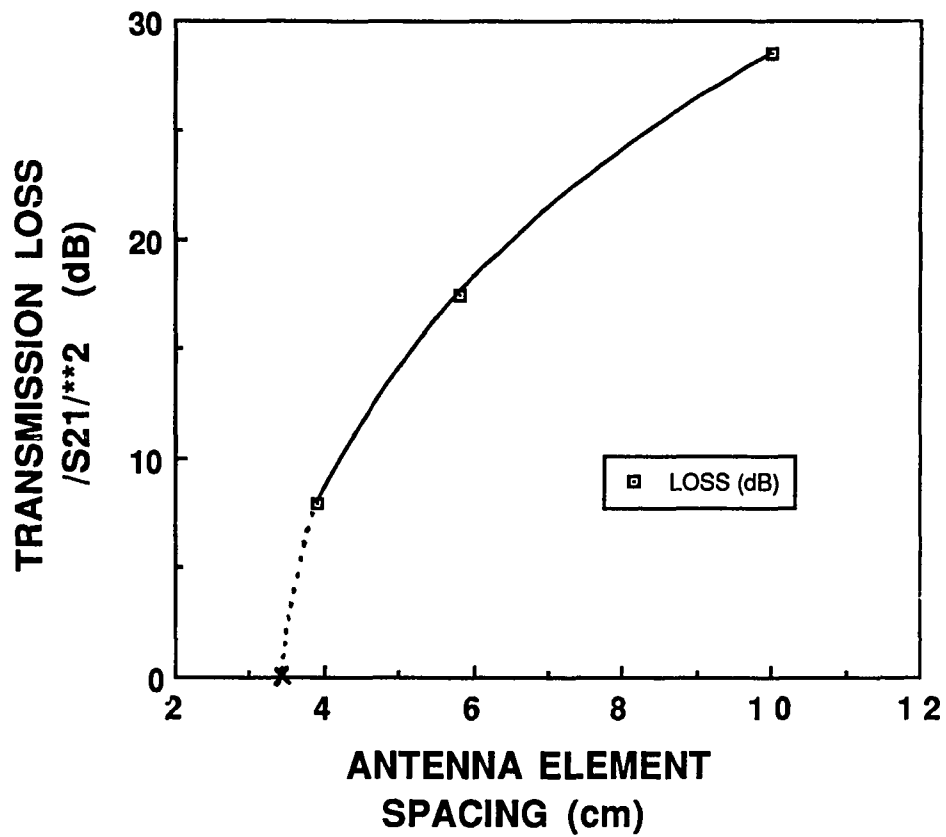


Figure 3.5. Mutual coupling between 2 rectangular microstrip patch elements on a Duroid 6010 substrate/superstrate applicator as measured by transmission loss versus antenna element spacing □ -measured values; x-expected value for butted elements

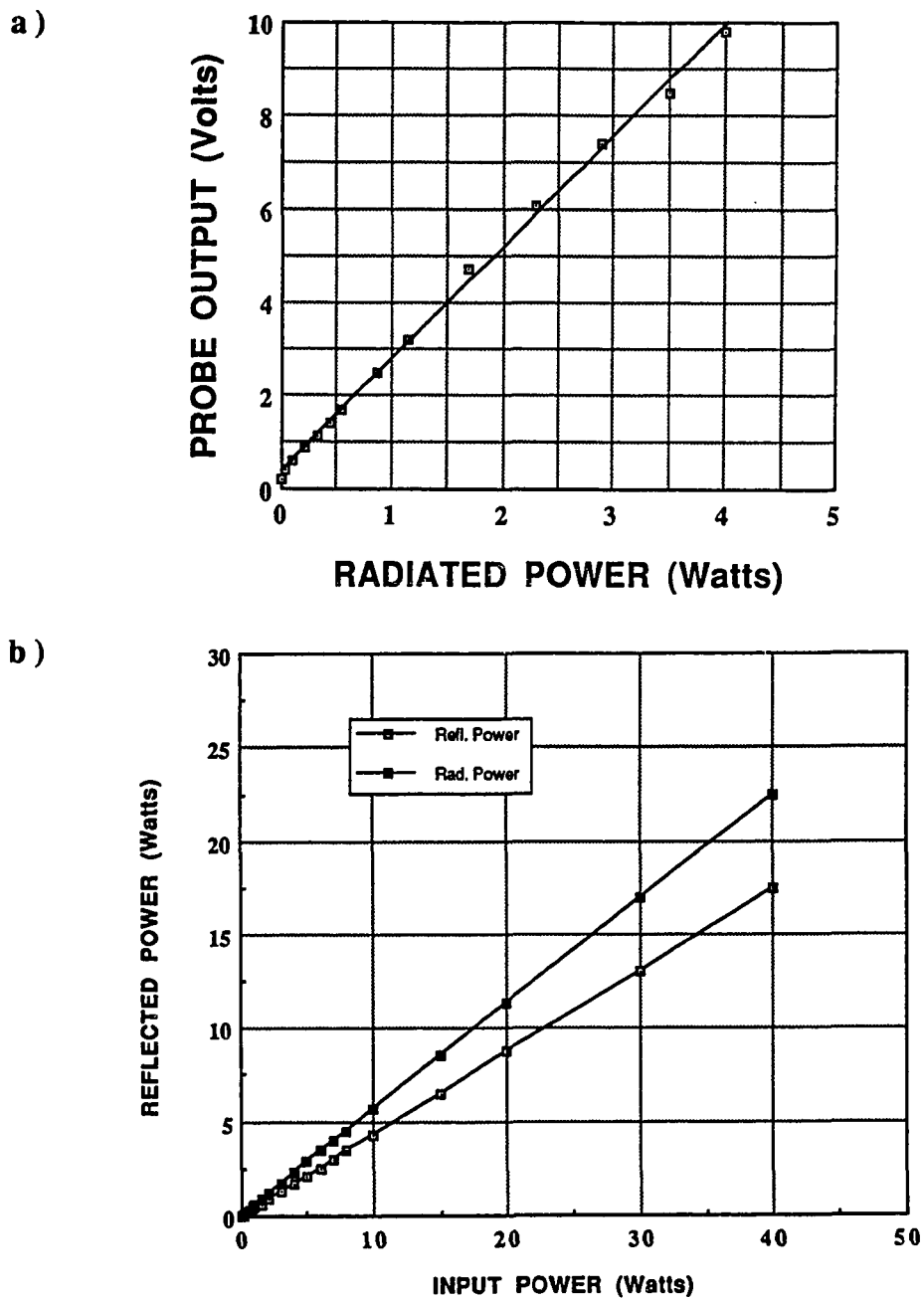


Figure 3.6. Miniature dipole (MND) probe calibration at 915 MHz with a rectangular dielectric filled C-band waveguide in water
a) probe output linearity versus radiated microwave power;
b) radiated and reflected microwave power versus input power.

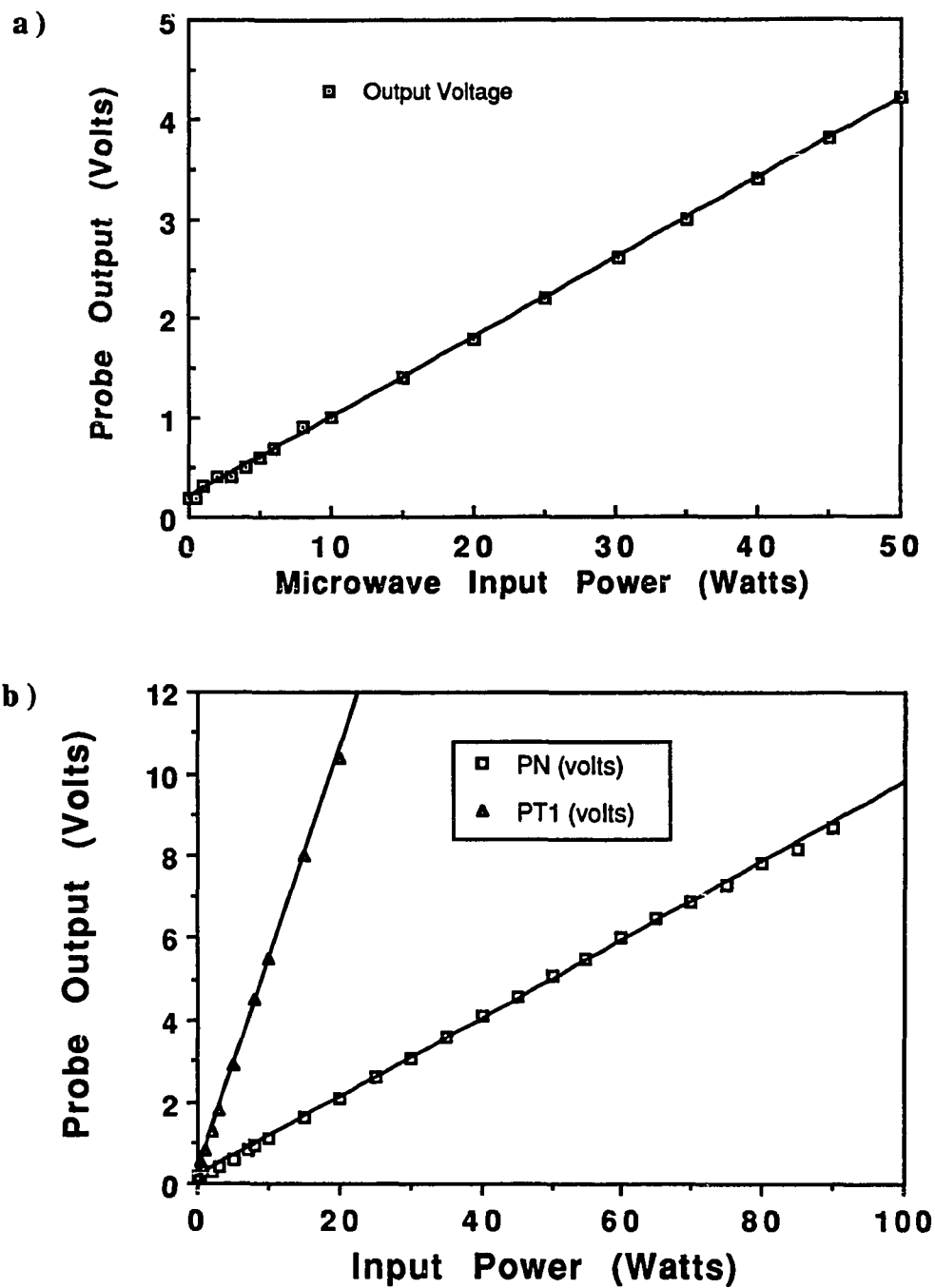


Figure 3.7. High-power performance at 915 MHz of a single rectangular microstrip patch radiating in water as measured by an MND probe at a depth of 15 cm for a) Duroid 6010; b) MCT-85.

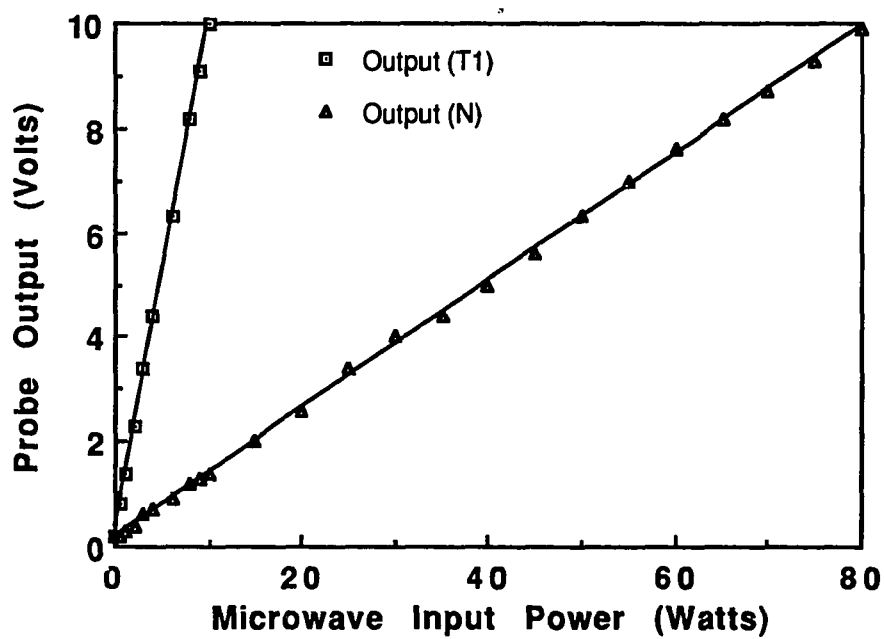


Figure 3.8. High-power performance at 915 MHz of a 3-element linear array of rectangular microstrip patches radiating in water as measured by an MND probe 15 cm from the MCT-85 substrate.

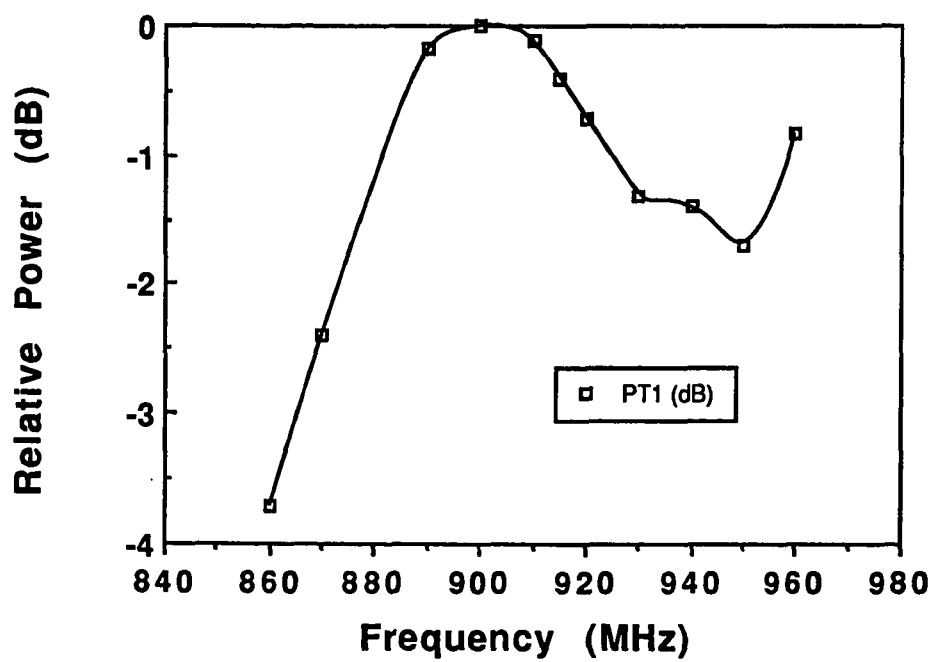


Figure 3.9. Frequency response of a miniature dipole (MND) E-field probe measuring the primary component from a rectangular dielectric filled waveguide source radiating fixed output power.

Table 3.1. Dielectric substrate materials for a hyperthermia applicator: sources, constants and specifications.

Source	Substrate	Dielectric		Specifications	
		Constant (ϵ_r)	Dimensions (in.)	Thickness (in./cm)	
Rogers (Chandler, AZ)	Duroid 5870	2.3	9 x 12	0.062/0.16	
	6010	10.2	10 x 10	0.100/0.25 0.050/0.12	
Emerson & Cumming (Canton, MA)	HI K 500 F	30	9 x 12	0.250/0.64	
Trans-Tech (Gaithersburg, MD)	MCT-85	85	6 x 6	0.100/0.25	

Table 3.2 Experimentally determined resonance length (L) and effective dielectric constant (ϵ_e) for a rectangular microstrip patch on dielectric applicator types in AIR: Return Loss (S_{11}) versus frequency method.

Material	Thickness		Width-to-Height Ratio (W/h ₁)	Effective Dielectric Constant (ϵ_e)		Resonance Length L (cm)
	Substrate h ₁ (cm)	Superstrate h ₂ (cm)		(1)	(2)	
Durioid 5870	0.156	---	16	2.1	2.1	11.3
	0.156	0.156	16	2.1-2.3	2.1	11.2
6010	0.250	---	10	8.5	9.2	5.4
	0.250	0.125	10	8.5-10	9.6	5.3
	0.250	0.250	10	8.5-10	9.9	5.2
Durioid 6010/ Hi K 500 F	0.250	0.635	10	8.5-30	12	4.8
MCT-85	0.250	---	10	7.1	28	3.1
	0.250	0.250	10	71-85	51	2.3

$$(1) \quad \epsilon_e = \left(\frac{\epsilon_r + 1}{2}\right) + \left(\frac{\epsilon_r - 1}{2}\right) \left(1 + \frac{12h}{W}\right)^{-\frac{1}{2}}$$

(Schneider's formula [53])

$$(2) \quad \epsilon_e \cong \left(\frac{\lambda_0}{2L}\right)^2$$

Table 3.3 Experimentally determined resonance length (L) and effective dielectric constant for a rectangular microstrip patch on dielectric applicator types in WATER: Return Loss (S₁₁) versus frequency method.

Material	Thickness		Width-to-Height Ratio (W/h ₁)	Effective Dielectric Constant (ε _e)		Resonance Length L (cm)
	Substrate h ₁ (cm)	Superstrate h ₂ (cm)		(1*)	(2)	
Duriod 5870	0.156	---	16	12	---	---
	0.156	0.156	16	12-2.3	5.8	6.8
6010	0.250	---	10	22	30	3.0
	0.250	0.125	16	22-10	23	3.4
	0.250	0.250	10	22-10	12	4.7
Duriod 6010/ Hi K 500 F	0.250	0.635	10	30-8.5	18	3.9
MCT-85	0.250	---	10	83	83	1.8
	0.250	0.250	10	83-85	67	2.0

$$(1*) \quad \epsilon_e^* = \frac{(\epsilon_r + \epsilon_w)}{2} + \frac{(\epsilon_r - \epsilon_w)}{2} \left(1 + \frac{12h}{W}\right)^{-\frac{1}{2}}$$

(rough approximation based on
Schneider's formula)

$$(2) \quad \epsilon_e \equiv \left(\frac{\lambda_0}{2L}\right)^2$$

Table 3.4 Applicator design characteristics for 1 or 2 rectangular microstrip radiators on MCT-85 dielectric substrate in water at 915 MHz

Dielectric Substrate	Thickness Superstrate	Resonance Length (1 patch)	Effective Dielectric Constant	Return Loss (1 patch)	Insertion Loss (2 patches)
h_1 (cm)	h_2 (cm)	L (cm)	$\epsilon_e = (\lambda_0/2L)^2$	L_R (dB)	L_I (dB)
0.250	0.000	1.8	83	13	18
0.250	0.250	2.0 (2.2)	67.4 (55.4)	12 (15)	35 (18)

(*) values at 1012 MHz due to mutual coupling

Table 3.5 Theory versus experiment comparisons of E-plane beam characteristics for a 3-element linear array of rectangular microstrip patches (probe-fed) spaced 3 cm apart on MCT-85 at 915 MHz radiating in water

Axial Depth Z (cm)	Experimental Pattern (Pattern synthesis by amplitude (A) or phase (P) adjustment)		E-plane Beam Parameters			
			HPBWidth Th/Exp (cm)	R_{zx}^* Ratio Th/Exp (dB)	FBWidth Th/Exp (cm)	R_{zx}^* Ratio Th/Exp (cm)
1.0	unadjusted	A,P	2.2/4.2	+11/-4.0	10/10	+11/+5
3.0	unadjusted	A,P	7.4/5.0	+1.0/-7.0	10/10	+3.0/+1.5
3.0	Beam Concentration P for focus at z=3 cm unadjusted	A	2.0/3.0	-12/-5.5	10/10	-2.0/-4.0
3.0	Beam Broadening A adjustment unadjusted	P	7.4/7.8	1.0/-9.0	10/10	+3.0/+4.0

*

$$R_{zx} = -20 \log\left(\left[\frac{|E_z|}{|E_x|}\right]_p\right)$$

Table 3.6 Radiated electric field pattern characteristics as measured by MND probe in water for a 2.5 x 3.4 cm patch on Duroid 6010 (2L) with 0.4 Watts input power: relative power level values (*) referenced to primary transverse (T1) component (where $P_x \sim |E_x|^2$) at z=1 cm (T2-secondary transverse component, N-normal component).

Peak Power Component			Depth Z (cm)	Plane E/H (x/y)	3dB Beam Region	
Px(T1) (dB)	Py(T2) (dB)	Pz(N) (dB)			Xwidth (cm)	Ywidth (cm)
10.1(0)	---	---	1.0	x	2.6	---
8.3(-1.8)	---	---	1.0	y	---	3.3
---	5.4(-4.7)	---	1.0	x	2.3	---
---	4.8(-5.3)	---	1.7	y	---	2.7
---	---	8.8(-1.3)	1.0	x	1.8,0.6	---
---	---	2.2(-7.9)	1.0	y	---	3.5
7.4(-2.7)	---	---	3.0	x	2.7	---
5.8(-4.3)	---	---		y	---	4.8
---	1.6(-8.5)	---		x	3.0	---
---	2.8(-7.3)	---		y	---	>3.3
---	---	3.1(-7.0)		x	2.1	---
---	---	0.2(-9.9)		y	---	4.9

CHAPTER 4

RESULTS: THEORY VERSUS EXPERIMENT

This chapter compares the electric fields predicted by the cavity-source models for a rectangular microstrip patch discussed and presented in Chapter 2 with the microwave power patterns measured experimentally as discussed in Chapter 3. The comparison leads to further insight concerning the reliability and predictability of these radiated field patterns and limits the characterization by a validity criterion. Experimental cases selected for measurement data collection were considered in terms of the practicality of the antenna array prototype as a potentially useful hyperthermia applicator and the physical limitations of the measurement system to collect suitable data. To best illustrate calculated versus measured results, data sets are selected along 1D scans in the primary E and H planes as well as the axial z-direction from the rectangular patch radiator. As a first step, the case of radiation from a single element is analyzed. Then the case of radiation patterns measured from a 3-element linear array configuration is compared with theory since this configuration is a basic building block of rectangular and hexagonal arrays. Although other conceivable multielement array configurations comprised of a larger number of elements can be simulated and tested by these methods, they are left for further study. This thesis concentrates on the fundamental analysis of the choice of a rectangular microstrip radiator for controlled biomedical heating in an array.

4.1 Single Element Patterns

Figure 4.1 shows the electric field power in water including the primary transverse ($PT1 \sim P_x \sim /E_x/2$) and normal ($PN \sim P_z \sim /E_z/2$) components radiating in the axial direction away from a single rectangular microstrip patch designed for resonance on a MCT-85 substrate. For the purpose of theory versus experiment comparisons in the axial direction, power levels have been normalized (0 dB) to the peak of the primary transverse component while the relative normal-to-transverse component power ratio has been held constant. The CC source model predicts smoothly decaying electric fields beyond $z=1$ cm where the normal component which is down 6 dB from the transverse component at $z=0.5$ cm decays more rapidly than the transverse component. Measurement data agree initially with the theory (at $z=1$ cm) for the low normal-to-transverse electric field ratio. However, the theory predicts that the normal component should decay much more rapidly than the experimentally measured data indicate. One possible explanation for this discrepancy is that the CC source model breaks down near the patch. Some error also comes from interference due to wave reflections between source and receiver close to the patch. It is also possible that attenuation loss in the water is less than expected so that actual reflections are not completely damped out from tank walls and cooling pipes. The evidence for overestimation of the loss factor comes from the

measured transverse component which decays more slowly than predicted by the CC source model.

The MC source model used for the patch on MCT-85 substrate at 915 MHz with fringing field correction factor includes 5 major modal coefficients as listed in Table 2.4 to account for the probe feed. Axial variation of normal and transverse components is similar to the prediction of the CC source model except that the normal-to-transverse ratio is much greater close to the patch. This can be explained by the contributions of the $n=0$ and $n=2$ modes at $x=L/2$ where the $n=1$ mode is null (see Figure 2.5). If the peak transverse component of the measured data is normalized to the corresponding peak transverse component of the theory (at 1 cm), the normal components agree only at a depth of approximately 1.5 cm. From this point, the data indicate that the normal component decreases much more slowly than the MC source model predicts. Thus, neither the MC nor the CC source model agrees with measurement data for the normal-to-primary-transverse component power ratio over the entire axial range but the CC source model appears to do better close to the patch ($z < 1.0$ cm). Both MC and CC source models do equally well at predicting the primary transverse power component pattern in the axial direction except that the medium attenuation appears to be overestimated.

Transverse scan pattern comparisons in the E-plane (Figs. 4.2, 4.3) exhibit some correlating features. At a depth of $z=1$ cm (Fig. 4.2), the double-peaked normal component pattern predicted by the CC source model is substantiated by measurement data except that the measurement data have some unpredicted asymmetry due to

the absence of the probe feed expansion in the CC source model. The primary transverse component power level is greater than 3 dB higher than the normal component power level as indicated both in the theory and experimental patterns with the CC source model. This suggests safe heating potential at this depth. The MC source model makes an improvement over the CC source model by predicting the shape and magnitude of asymmetry observed in normal component measurements but underestimates the overall broadness of the beam at this depth.

Moving out to $z=3$ cm axially from the microstrip patch radiator, the main beam features in the E-plane (Fig. 4.3) are smoother in both theory and experiment. The primary transverse component shape is predicted almost perfectly by either the MC or CC source model. The MC model also predicts the major asymmetric features of the normal component at this depth. The peak of greater amplitude in the normal component at both $z=1$ and $z=3$ cm clearly occurs at the side of the patch opposite the feed.

To check the significance of Hammerstad's [43] fringing field correction factor ($\Delta W=\Delta L=2h$) and the effective loss tangent (δ_e) in the extended MC source model, patterns were plotted for comparison in the E-plane at $z=3.0$ cm (Figure 4.4). In the first case, a comparison was made between the pattern predicted with ($W_e=W+\Delta W$, $L_e=L+\Delta L$) and without ($W_e=W$, $L_e=L$), the fringing field correction factor. The result of this test in Figure 4.4a shows that this dimensional correction factor account for the additional asymmetry in the normal component pattern and improves the agreement with experimental data. Since the inclusion of this factor

also makes sense to account for deviations from cosinusoidal resonance underneath the patch, it is retained for the second comparison. In the second case, a comparison was made between the patterns predicted with significant effective loss ($\delta_e=0.1$) versus no effective loss ($\delta_e=0$). The result of this test in Figure 4.4b shows that the effective loss in this case is relatively insignificant for this case and thus can be ignored. This explains the choice of coefficients indicated earlier in this section.

In the H-plane of the MCT-85 patch (Figs. 4.5,4.6), it is clear that the beamwidth indicated by measurements at 1 cm is underestimated by both the CC and MC models. In addition, the MC model overpredicts the peak magnitude of the normal component in the central region of the beam. However, an improvement is again observed at the 3 cm depth. The MC source model predicts the shape and levels of both transverse and normal components reasonably well. Only the beamwidth is slightly underpredicted. Symmetry in both the theoretical and experimental results exhibited here further substantiates the hypothesis that asymmetry in the E-plane is arising from the probe feed.

A common figure for antennas used to delineate between the near and far field radiation regions is the far field distance factor $r_{ff} = 2D^2/\lambda$. When this factor is specialized for a patch, where the effective aperture width is $D=\lambda_e/2$, it becomes

$$r_{ff}^p = \frac{2(\lambda_e/2)^2}{\lambda_0\sqrt{|\epsilon_w|}} = \frac{\lambda_0\sqrt{|\epsilon_w|}}{2\epsilon_e} \quad (4.1)$$

which for MCT-85 (1L) is $r_{ff}^p = 1.7$ cm (with $\epsilon_e = 83$ and $10h = 2.5$ cm) and for Duroid 6010 (2L) it is $r_{ff}^p = 6.3$ cm (with $\epsilon_e = 23$ and $10h = 3.75$ cm). If the far field factor is considered as a criterion to estimate the expected limitation of agreement for the cavity source model, it indicates that good agreement can be expected only for field points beyond 6.3 cm for Duroid 6010 (2L) patches. This would be a severe limitation for the applicators made from the Duroid 6010 dielectric substrates since penetration depth for microwaves in biological tissue is only 3.0 cm at 915 MHz. However, a criterion based on the thickness is less restrictive ($10h = 3.75$ cm for Duroid 6010-2L). For MCT-85, both the far field ($r_{ff}^p = 1.7$ cm) and the thickness ($10h = 2.5$ cm) criteria are less prohibitive for hyperthermia pattern predictions. Figures 4.3b and 4.6b indicate that good agreement between relative component levels and pattern shape does occur with the MC model at 3.0 cm for a patch on MCT-85. This is consistent with either the far field or thickness criterion for this substrate.

4.2 Multielement Array Patterns

Linear, rectangular and hexagonal geometries were considered for multielement array applicator designs (Fig. 4.7). Due to space and time limitations, the results of the 3-element linear array patterns (Fig. 4.8-4.10) were selected for presentation in this section. However, the unit cell arrangements for rectangular and hexagonal array geometries would be the next step to establish a basis for design with these geometries. The 3-element linear array

can be considered as a basic building block for rows in the rectangular array. Array patterns of any of these geometries can be predicted by ARR PAT2 using the MC model assuming individual element isolation (mutual coupling negligible).

Axial ($x=W/2$; $y=L/2$) patterns (Fig. 4.8) illustrate the normal and transverse components away from the 3-element linear array as a function of depth in water. Comparing the focused case (Fig. 4.8b) to the unfocused case (Fig. 4.8a), the normal component gives evidence that more power is being deposited away from the surface of the applicator peaks at $z=2.5$ cm compared to 1.2 cm and the primary transverse component drops off 1.8 dB (focused case) versus 2.3 dB (unfocused case) from $z=2$ to $z=3$ cm.

Measurement data in transverse E-plane scans for this 3-element array at $z=3$ cm show an example of beam broadening (Fig. 4.9b) versus beam concentration (Fig. 4.10b). Initially, the radiated field pattern is asymmetric due to mutual coupling effects between array elements which are excited equally by a signal of uniform amplitude and phase (Figs. 4.9a, 4.10a). The theory is shown for comparison in each case using the CC source model first with uniform phase and amplitude (Figs. 4.9, 4.10a), then phased for a focus on the axis in the $z=3$ cm plane (Fig. 4.10b). To achieve beam broadening or smoothing by overcoming mutual coupling effects, ARRA variable attenuators (Bay Shore, NY) were adjusted to equalize the radiated power from each element. In this case, the 3 dB beamwidth becomes ~ 8 cm compared to the original 5 cm (Fig. 4.9). If the relative phases are adjusted (MICROLAB/FXR trombone line stretchers, Livingston, NJ) between elements to maximize the

power on the axis at 3 cm depth, the 3 dB beamwidth becomes distinctly narrower ~ 3 cm compared to the original 5 cm (Fig. 4.10). These examples show that some significant beam shaping can be achieved by this simple 3-element linear array. The primary transverse component is better predicted by the CC source model than the normal component here. The radiated field patterns from this 3 element linear array give additional evidence of the mutual coupling previously evident in Insertion Loss (S_{21}) for the two elements on MCT-85 (Table 3.4). In a clinical system, a dynamic closed-loop feedback control method could help create the desired beam shape. For example, a multipoint thermometry system feeds back continuous temperature information to gauge the course of therapy. Thus, when an applicator is radiating, a temperature difference (error) signal could be used to adjust the amplitude and phase factors and thereby control the heating pattern.

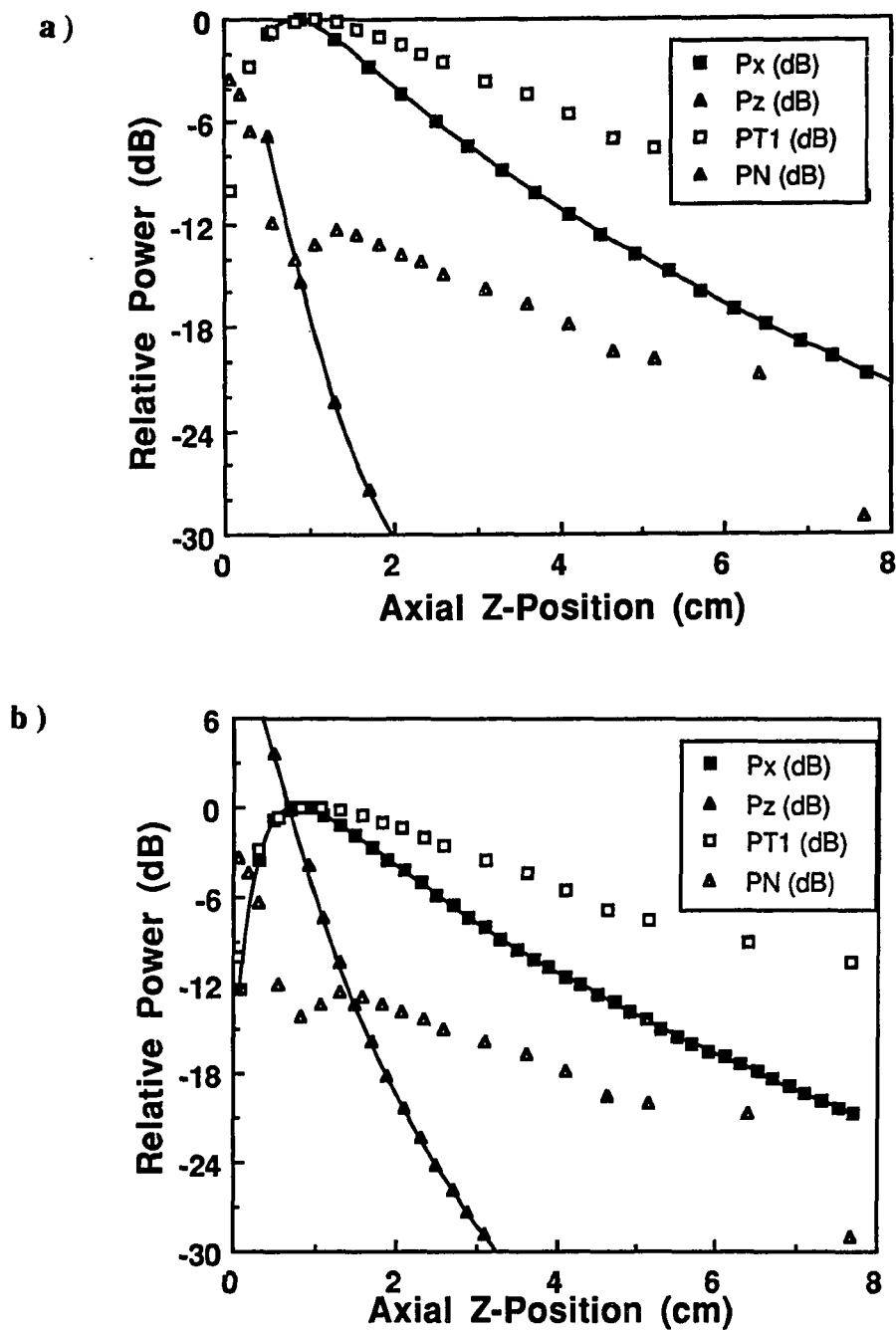


Figure 4.1. Calculated (■ ▲) versus measured (□ Δ) axial power in water including the primary transverse (P_x , PT1) and normal (P_z , PN) electric field components radiated from a 1.0 x 1.8 cm microstrip patch resonant on a MCT-85 dielectric substrate a) CC source model ($A^{10}=1.00$) b) MC source model ($A^{00}=0.23$, $A^{02}=0.10$, $A^{10}=1.00$, $A^{12}=0.15$ and $A^{20}=0.19$).

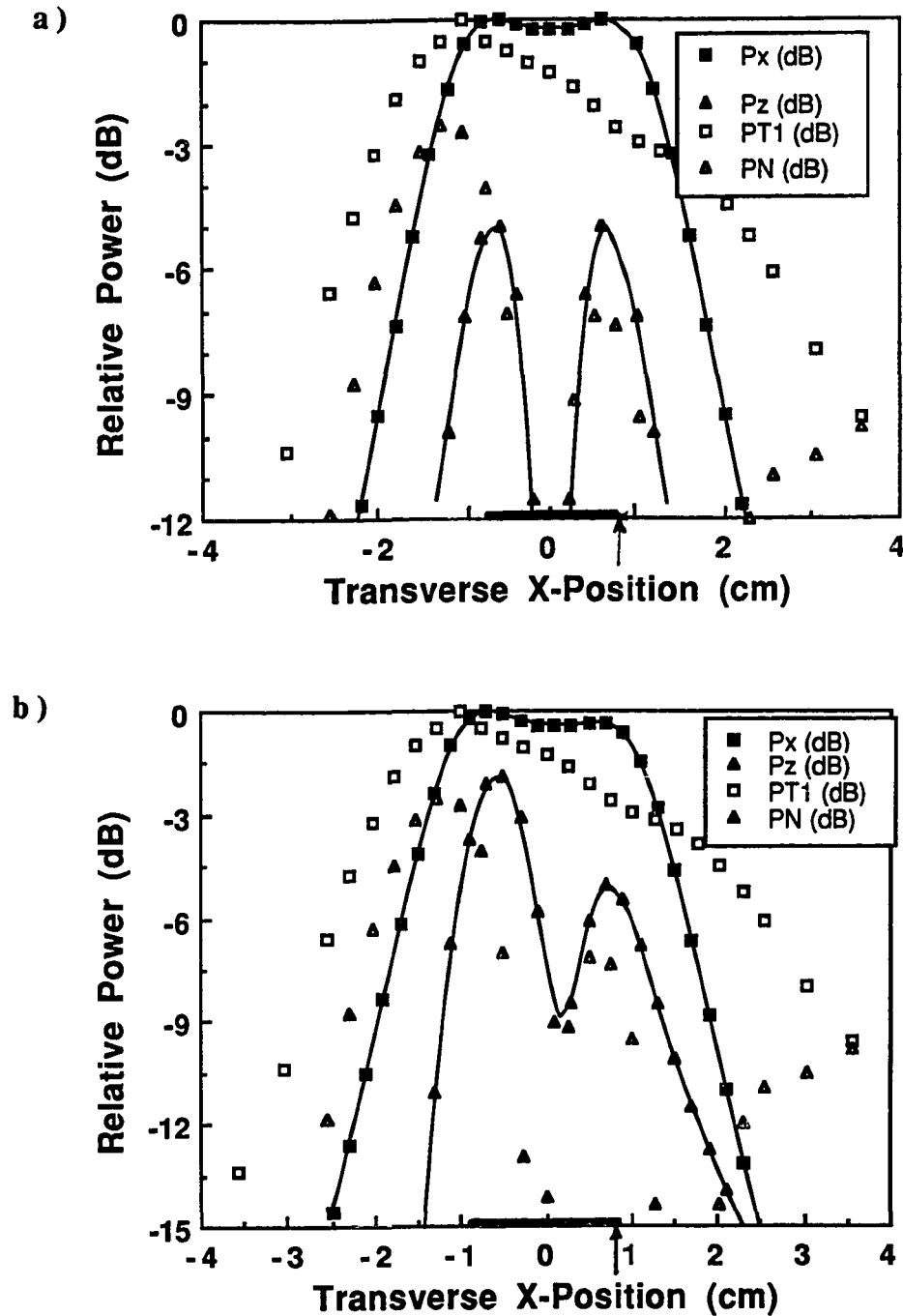


Figure 4.2. Calculated (■ ▲) versus measured (□ Δ) transverse power patterns in water including primary transverse (P_x , PT_1) and normal (P_z , PN) electric field components in the E-plane ($y=W/2$) at $z=1$ cm from a 1.0×1.8 cm microstrip patch on a MCT-85 substrate a) CC source model ($A^{10}=1.00$) b) MC source model ($A^{00}=0.23$, $A^{02}=0.10$, $A^{10}=1.00$, $A^{12}=0.15$ and $A^{20}=0.19$).

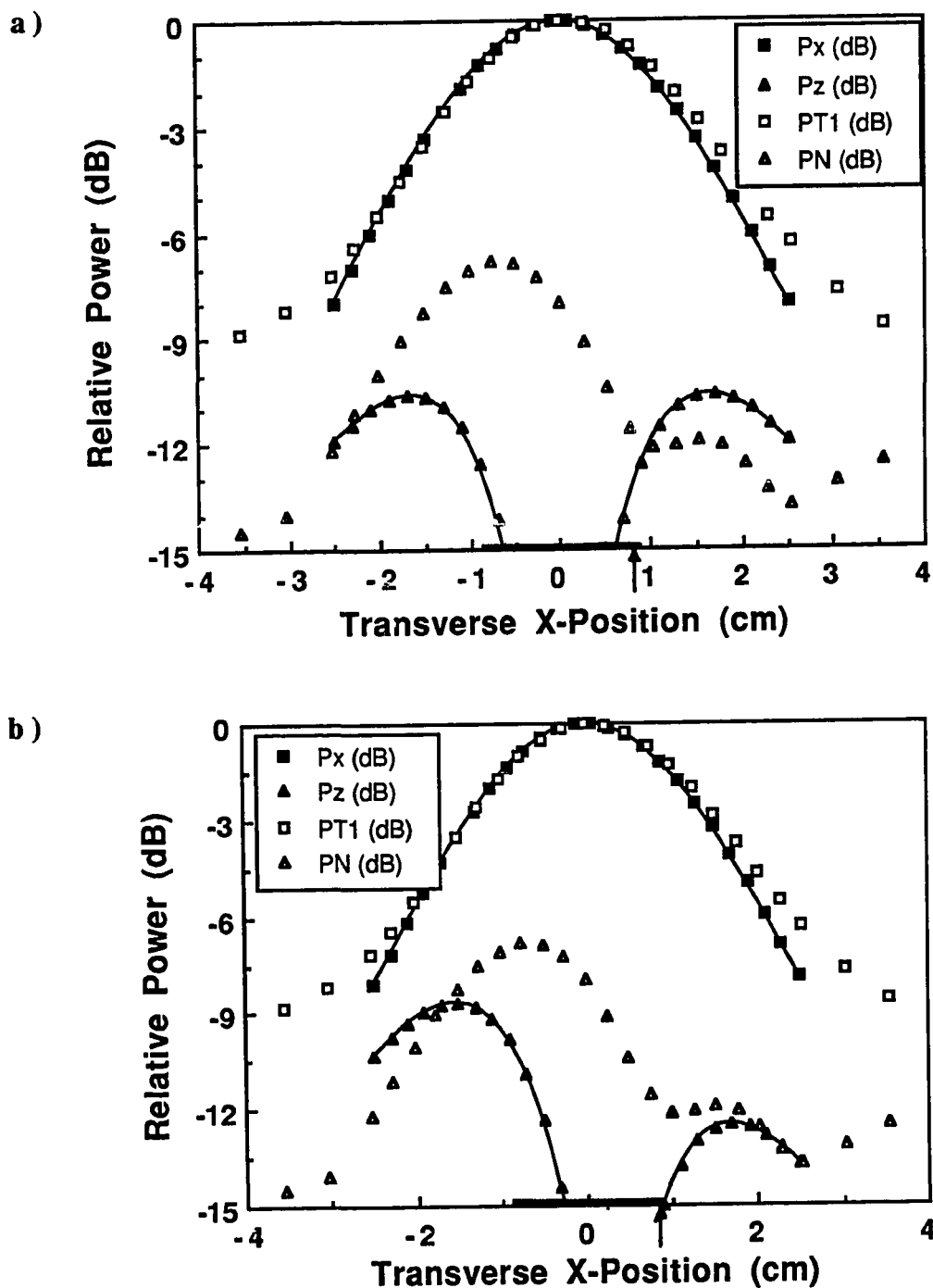


Figure 4.3. Calculated (■ ▲) versus measured (□ Δ) transverse power patterns in water including primary transverse (P_x , $PT1$) and normal (P_z , PN) electric field components in the E-plane ($y=W/2$) at $z=3$ cm from a 1.0×1.8 cm microstrip patch on a MCT-85 substrate a) CC source model ($A^{10}=1.00$) b) MC source model ($A^{00}=0.23$, $A^{02}=0.10$, $A^{10}=1.00$, $A^{12}=0.15$ and $A^{20}=0.19$).

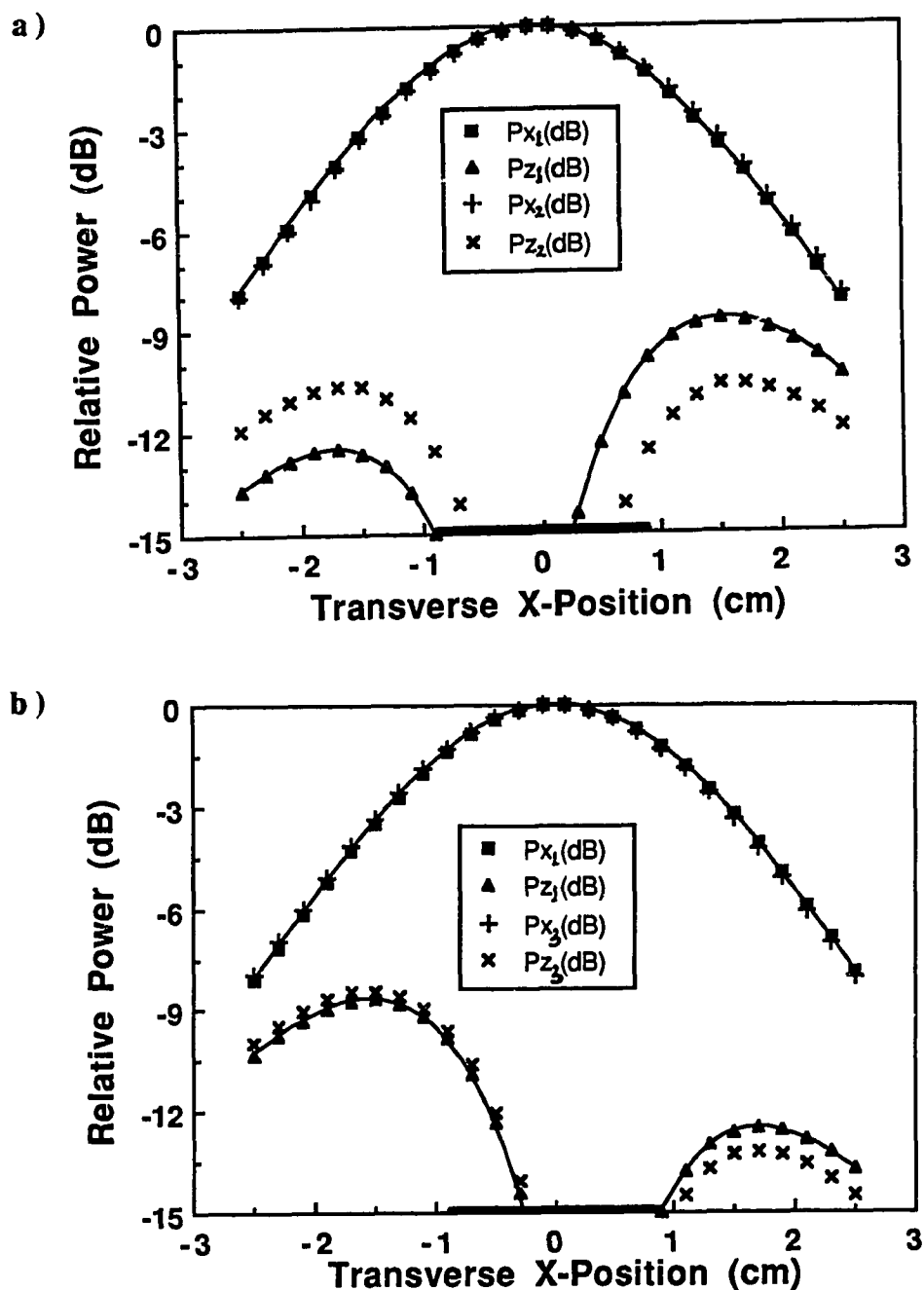


Figure 4.4. Calculated transverse power patterns in water including primary transverse (\blacksquare +) and normal (\blacktriangle x) electric field components in the E-plane ($y=W/2$) at $z=3$ cm with A^{mn} from Table 2.4 for MCT-85 substrate with fringing field correction factor ($\Delta W=\Delta L=0.5$ cm) and no effective loss tangent (P_{x1} , P_{z1}) versus pattern a) (P_{x2} , P_{z2}) with no correction factor ($\Delta W=\Delta L=0$) and b) (P_{x3} , P_{z3}) with significant effective loss tangent ($\delta_e=0.1$).

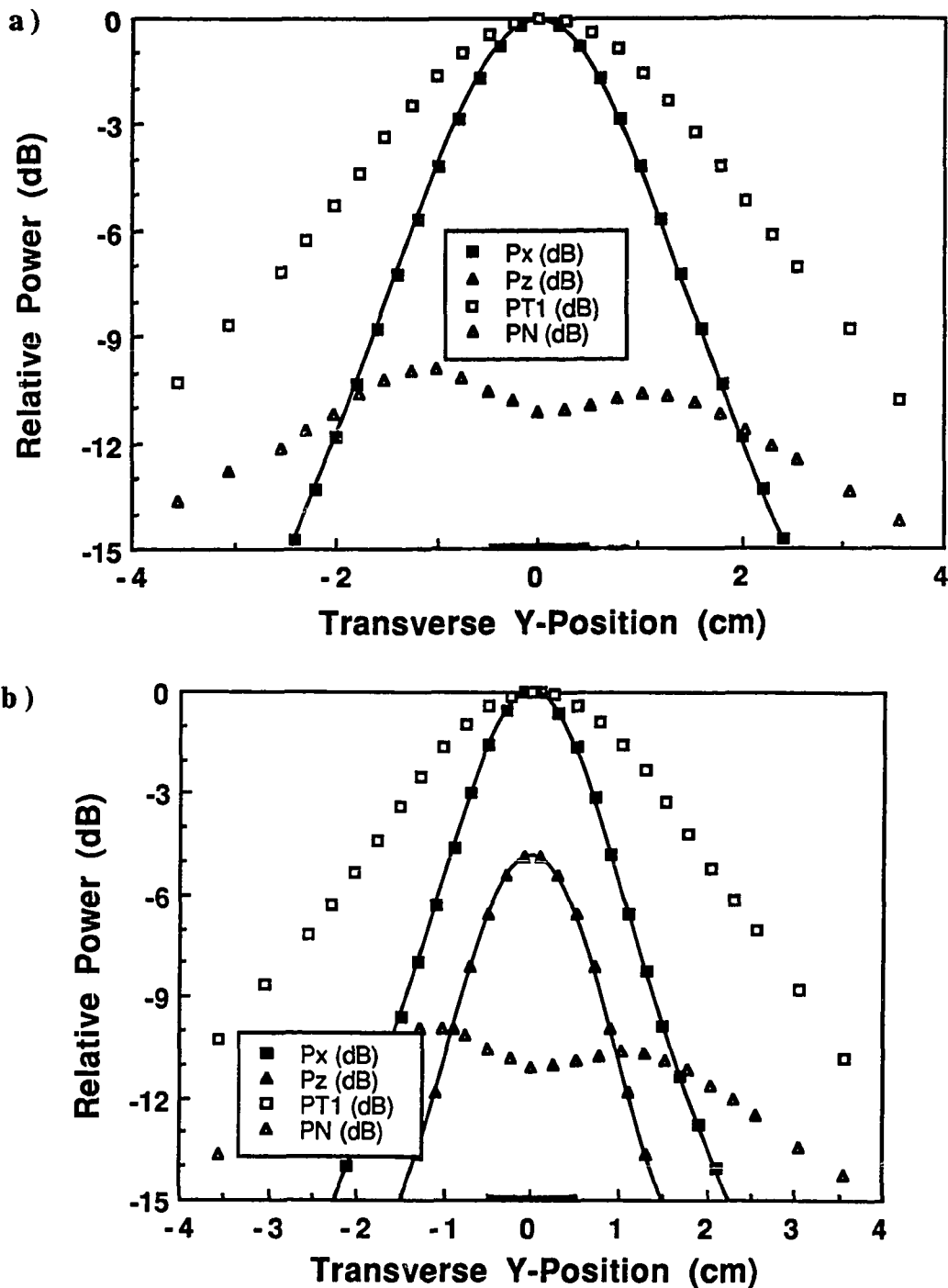


Figure 4.5. Calculated (■ ▲) versus measured (□ Δ) transverse power patterns in water including primary transverse (P_x , PT_1) and normal (P_z , PN) electric field components in the H-plane ($x=L/2$) at $z=1$ cm from a 1.0×1.8 cm microstrip patch on a MCT-85 substrate a) CC source model ($A^{10}=1.00$) b) MC source model ($A^{00}=0.23$, $A^{02}=0.10$, $A^{10}=1.00$, $A^{12}=0.15$ and $A^{20}=0.19$).

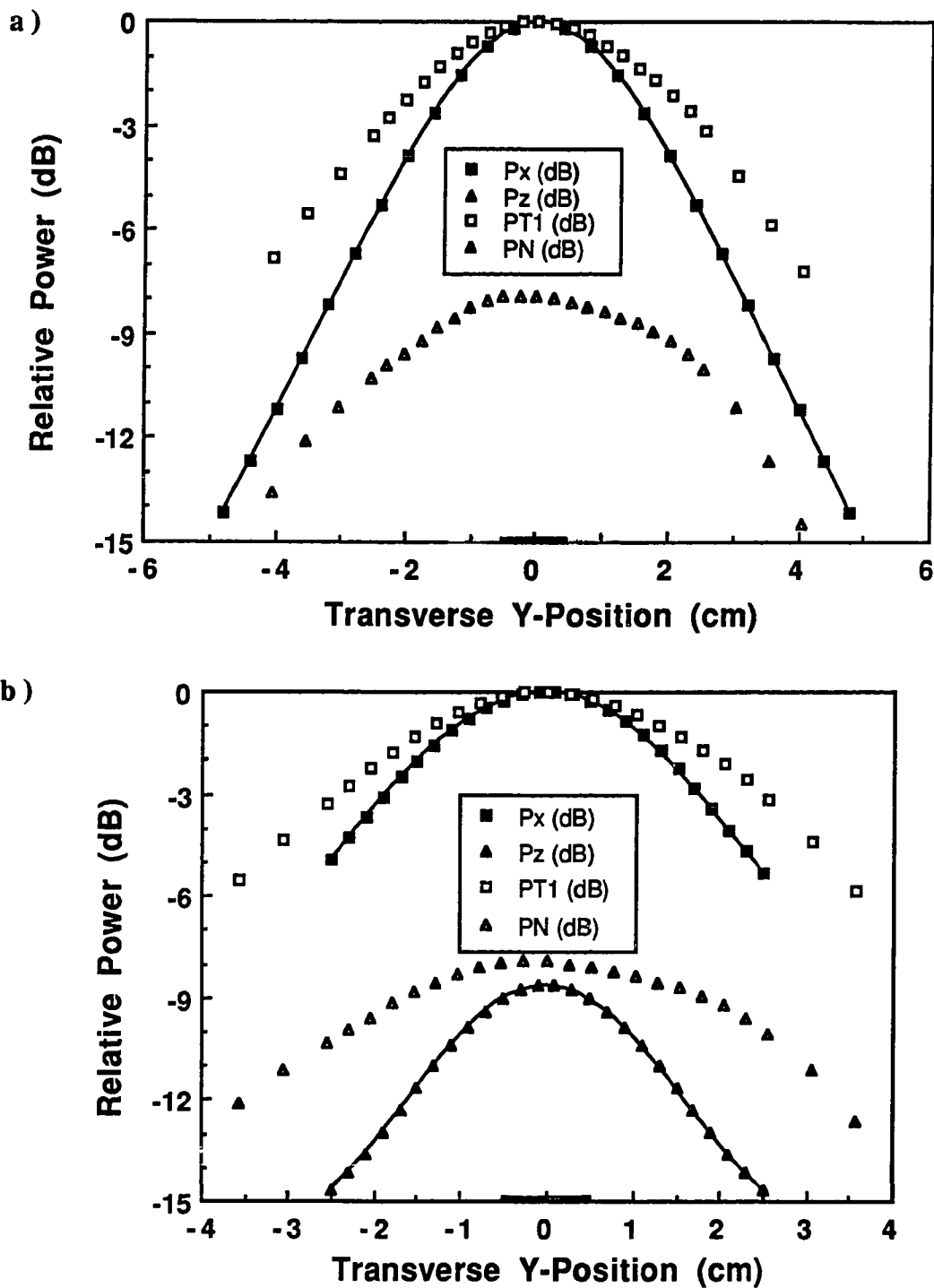


Figure 4.6. Calculated (■,▲) versus measured (□, Δ) transverse power patterns in water including primary transverse (P_x , $PT1$) and normal (P_z , PN) electric field components in the H-plane ($x=L/2$) at $z=3$ cm from a 1.0×1.8 cm microstrip patch on a MCT-85 substrate a) CC source model ($A^{10}=1.00$) b) MC source model ($A^{00}=0.23$, $A^{02}=0.10$, $A^{10}=1.00$, $A^{12}=0.15$ and $A^{20}=0.19$).

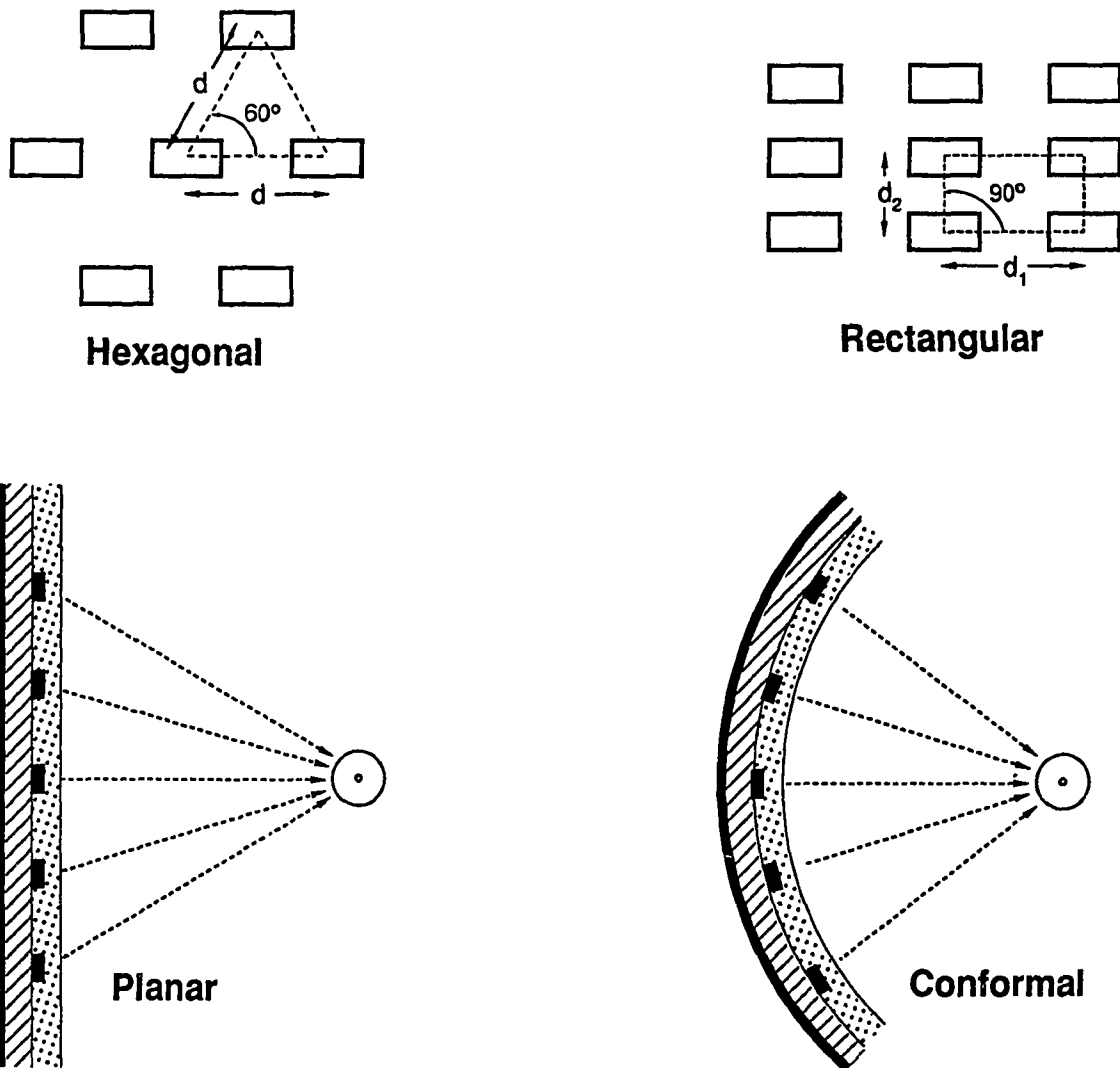


Figure 4.7. Rectangular and hexagonal arrays of rectangular microstrip patches on a planar or a conformal substrate from Magin and Peterson [14].

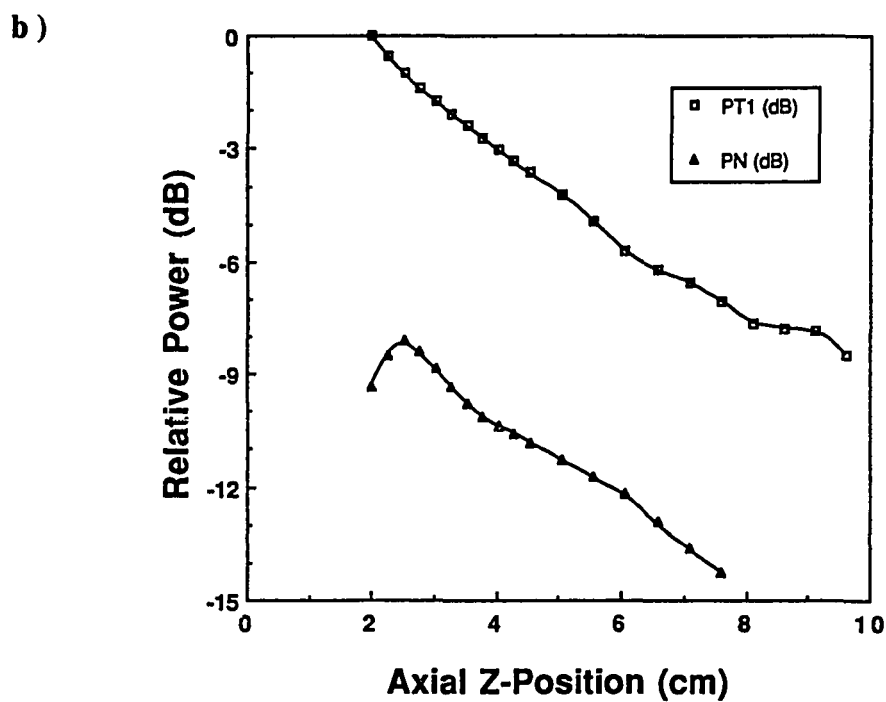
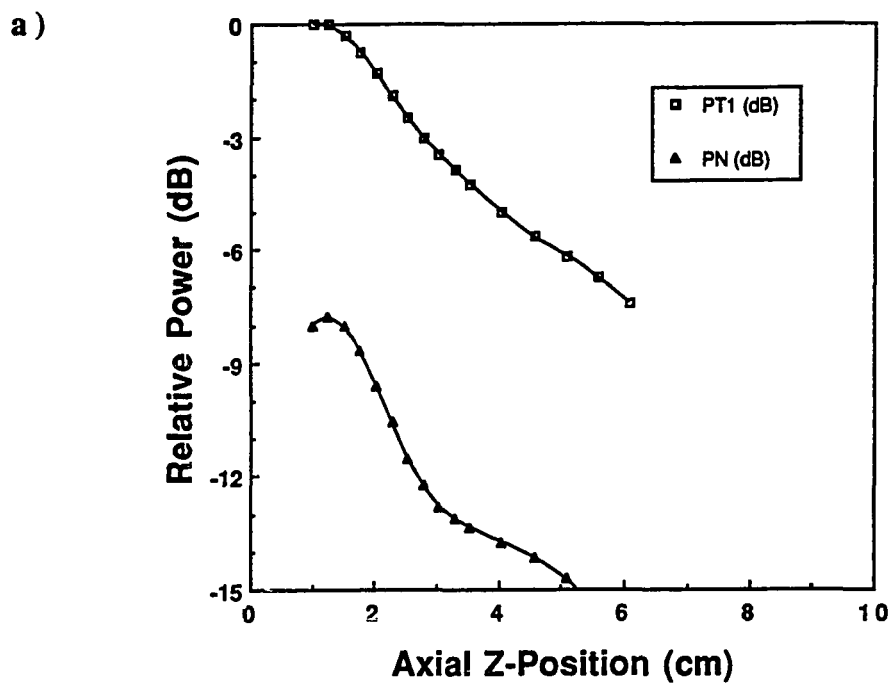


Figure 4.8. Measured axial power pattern in water for a 3-element linear array of rectangular microstrip patches radiating with unadjusted amplitude and a) uniform phase; b) phased for axial focus at 3 cm.

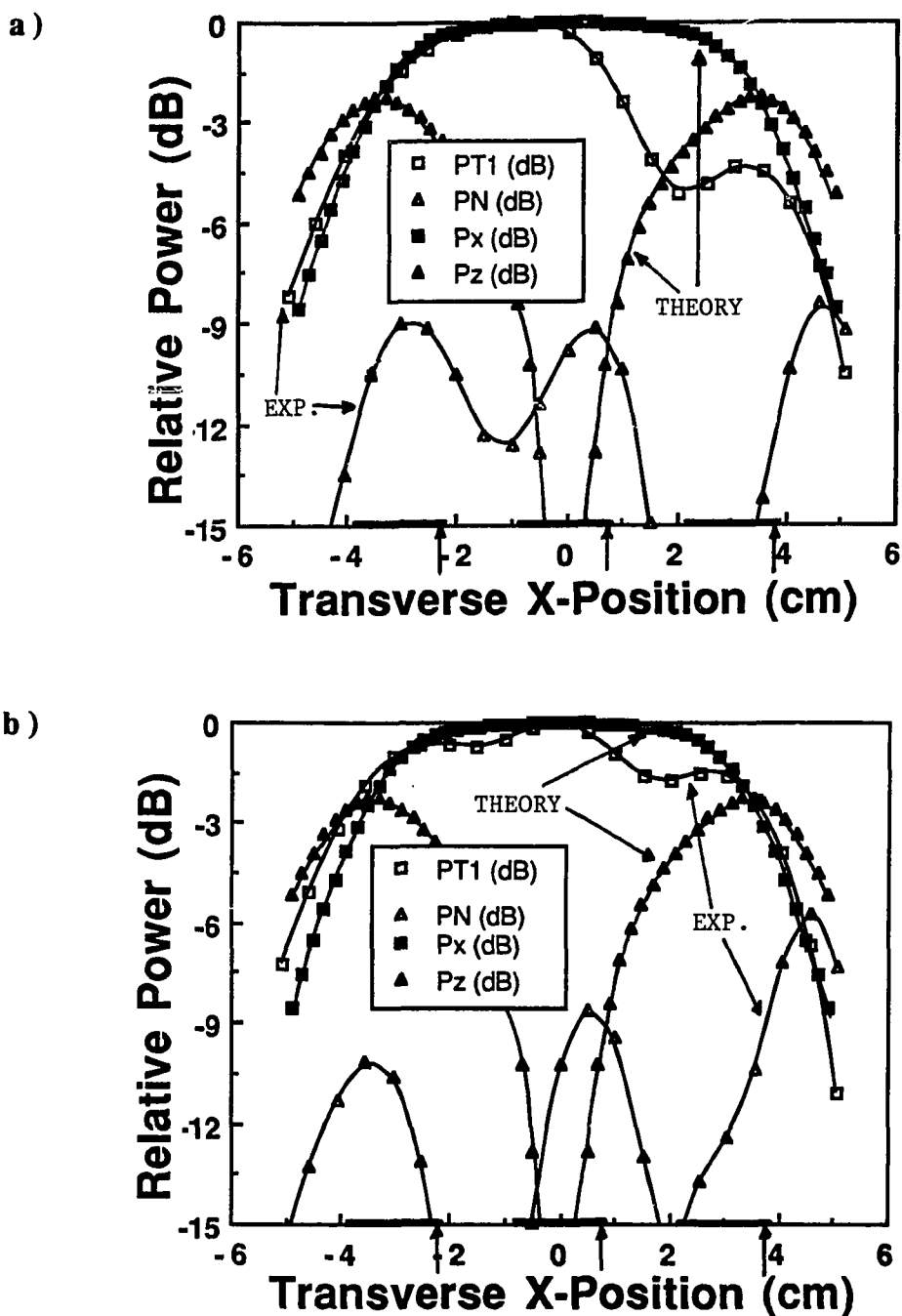


Figure 4.9. Calculated (■▲) versus measured (□△) transverse power patterns in water including primary transverse (P_x , PT1) and normal (P_z , PN) electric field components in the E-plane ($y=W/2$) at $z=3$ cm from a 3-element linear array of 1.0×1.8 cm patches on MCT-85 using the CC source model and a) unadjusted amplitude; b) adjusted amplitude (beam broadening).

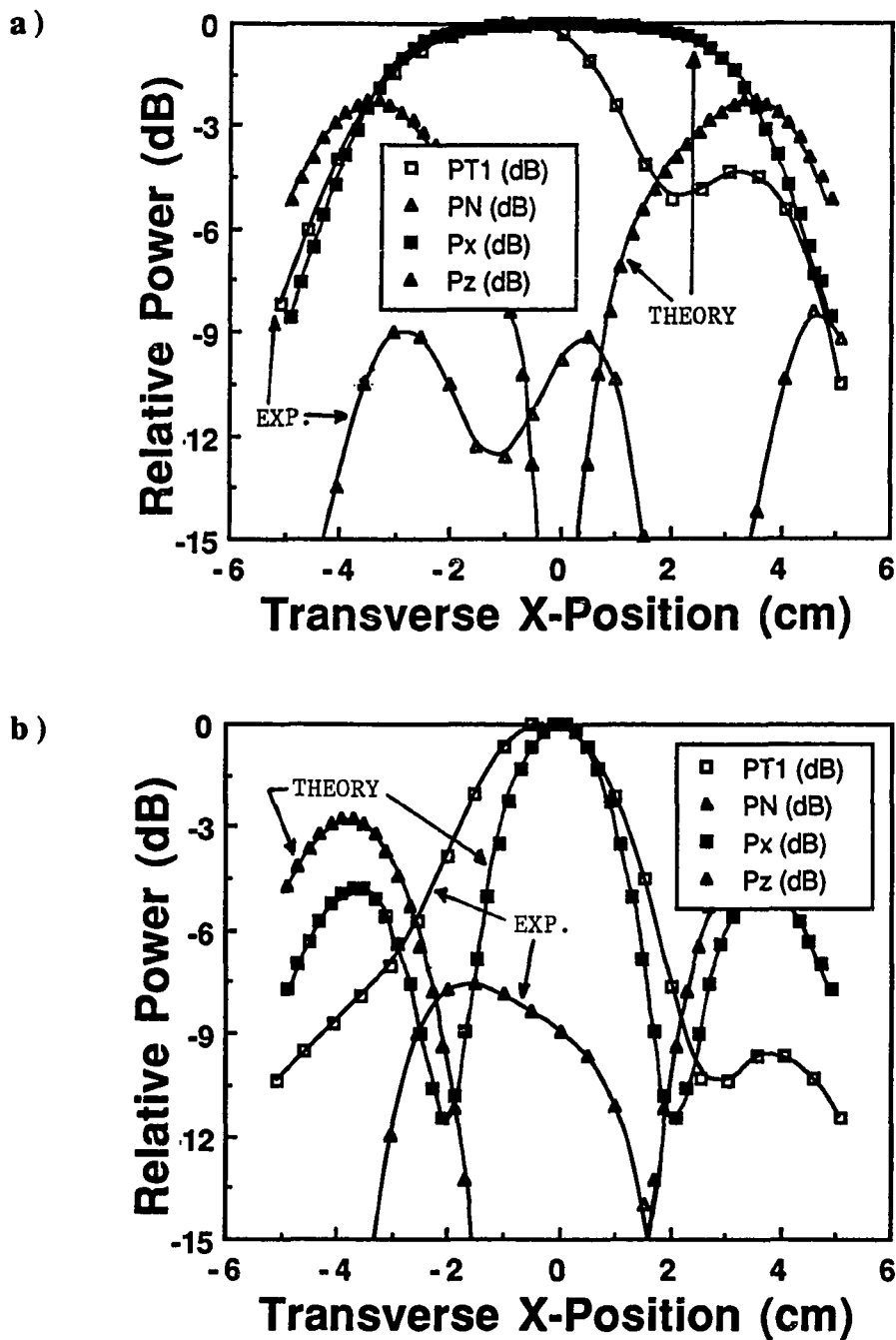


Figure 4.10. Calculated (■▲) versus measured (□Δ) transverse power patterns in water including primary transverse (P_x , PT1) and normal (P_z , PN) electric field components in the E-plane ($y=W/2$) at $z=3$ cm from a 3-element linear array of 1.0×1.8 cm patches on MCT-85 using the CC source model and a) unadjusted phase; b) phased for a focus (beam concentration).

CHAPTER 5

DISCUSSION OF RESULTS

5.1 Analysis of Theory

The cavity source models that provide a simple and efficient means of calculating radiated far fields from a microstrip patch in air exhibit some weaknesses in predicting the near zone fields in a homogeneous medium. This is an expected tradeoff in accuracy in exchange for simplicity and efficiency. To improve the model, a modal matching technique based on probe-feed current excitation position identifies coefficients for the MC source model. Inclusion of these additional modes serves to better represent the pattern asymmetry observed in measurements. However, a discrepancy between the predicted normal-to-transverse component power ratio (Figure 4.6b) persists. Although the cavity model does not completely predict the behavior of the radiated field pattern near the patch, it does predict major power patterns of the beam outside the extreme near field region.

Two major sources of error in the cavity source model have been identified (Section 2.1.1). The first is the internal field approximation based on cosinusoidal resonant modes in a closed ideal cavity. The second is the flat ground plane approximation backing the lumped equivalent magnetic sources. In the first case, the walls of the cavity are actually impedance boundaries rather than perfect magnetic conductors. The idealized modes may lead to some error in the distribution of the lumped magnetic current sources. In

the second case, the approximation neglects the actual ground plane bump coupled with a ribbon width distribution of the magnetic sources. The approximation thus ignores some scattering effects due to the more complex physical structure that may be significant. This error, however, should prove to be less significant for substrates very thin relative to a wavelength.

The question of conductive losses in the cavity was addressed by varying the loss tangent factor in the MC model. Changes in the loss tangent were found to have negligible effect on the E-plane pattern at $z=3.0$ cm (Fig. 4.4b) and little effect on the A^m_n coefficients for either the $\epsilon_r=10$ or $\epsilon_r=85$ substrates (Tables 2.3 and 2.4). The fringing field correction factor does, however, introduce significant additional asymmetry into the predicted E-field pattern toward the direction indicated by the measurements. This is one indirect way of compensating for the error in the cosinusoidal mode approximation.

Coefficients obtained for the MC model were based on a 2D width of excitation current and retained by a 10% significance criterion. These assumptions are good enough to evaluate the feed contribution as a refinement to the cavity model. Further refinements in the cavity model are unlikely to lead to significant improvements.

Finally, mutual coupling due to surface wave modes and induced currents are not expressed in the cavity model array theory. Thus, the array theory is valid only for array spacings wide enough to justifiably assume isolation. If the requirements for hyperthermia dictate smaller spacing for compactness and beam shaping, they

must be assessed experimentally. Mutual coupling for a given configuration can be used to determine the effective amplitude excitation of neighboring elements.

5.2 Experimental Error Analysis

Much effort has been applied in the design and arrangement of experimental measurement equipment in this project to insure reliability and accuracy of measurement data. Although an acceptable resolution size for measurements was obtained, a certain degree of uncertainty remains which could be reduced by a more complete characterization of the measurement probe. The MND E-field probe initially used for measurements was a Narda BRH-15 (3-axis) probe whose characteristics have been documented by Bassen and Smith [51]. Since the Schottky diode bonded at the tip of these probes tends to be fragile, an in-house version of the MND probe was constructed to replace it when the BRH-15 version failed. The MND probe has a single channel with a tip width of ~ 3 mm (Fig. 3.2). A flat frequency response varying less than 1.5 dB over the range 880-960 MHz and a linear output voltage versus radiated source power incident on the probe were indicated in Chapter 3. In addition, a comparison between the measurements made by the MND probe for the primary radiated component in the E-plane of a patch and the DD probe (~ 2 cm length dipole) in the same range of the source (Fig. D.5) indicated no evidence of significant perturbation of the fields under measurement. Since the approximate calibration factor (sensitivity) of the MND probe is presently known only for water,

relative dB measurements at low power were used to characterize radiation patterns from the source. The sensitivity factor of the MND probe might eventually be useful to help determine the input power levels required to generate the specific absorption rate (SAR) distribution in water necessary for thermal doses needed in hyperthermia therapy. However, other simpler methods of measuring SAR might be employed.

Another potential source of systematic error in the experimental method is the small tank size. Although tank size was expected to be sufficiently large for measurements of radiated fields from a single small patch on MCT-85 substrate centered in the tank, larger patches (Duroid 6010, 5870) and arrays submerged in the tank may not have enough clearance to eliminate tank wall reflections that can cause standing wave interference. This problem might be avoided by using a larger tank, putting microwave absorber on the walls or increasing the loss in water (e.g., by using saline). Distilled water is lossy to microwaves but the attenuation is not enough to completely eliminate reflection interference from a small tank. If the attenuation factor of distilled water is as much as 1 dB/cm (see Section 2.2.2), then a patch centered in the tank $2-3 \lambda$ (~ 10 cm) from the tank floor could see reflections that should be attenuated by at least 20 dB. By this calculation, any power levels seen in the measurements near or below this level are expected to have a significant uncertainty due to possible interference from reflected waves. A simple experimental method that measures the dielectric constant and loss factor of water could further quantify this error. Metallic heating pipes on the bottom of the tank of the

BRL Mill-based scanner, for example, are potentially significant scatterers. Also, the water/air interface is reflective. For example, reflections could account for the error between theory and experiment in the normal component of the axial field pattern (Fig. 4.1) at significant depth ($z > 6$ cm). Some transverse electric field component power may convert to normal component power by reflection at the pipes.

An experiment was performed to investigate the significance of tank wall and pipe reflection interference errors. The MND probe was positioned at an axial distance 5 cm from the surface of a single rectangular microstrip patch centered in the tank to minimize reflections. The patch received an input power of 5.0 W that produced a 4.0 mV response at the probe measuring the normal component. When a conducting metal sheet was placed on the bottom of the tank without any other change, the signal decreased to 3.0 mV. This evidence suggests that reflections are a factor at this depth causing cancellation interference in the case of the metallic plate. When the probe was moved out to an axial distance of 10 cm the probe output dropped to 0.5 mV without the metal plate. When the plate was reintroduced, the signal increased to 0.8 mV. When the plate was removed and a Plexiglass dielectric plate introduced, the signal dropped to 0.3 mV. Although these data are insufficient to draw broad conclusions, they suggest that reflections in the tank are somewhat significant and may explain some of the discrepancy between theoretical and experimental component patterns at a depth away from the patch. Accounting for tank wall reflections and the

complex permittivity (loss tangent) of the water properly might increase agreement significantly.

Measurements very close to the patch (2 or 3 times the diameter of the encapsulated MND probe) are not expected to be as reliable as measurements away from the patch. Within a wavelength of the source, perturbation of the fields due to the probe and standing wave interference are more likely to have a significant effect. However, the small tip and high resistance leads (microwave transparent) of the MND probe should minimize this effect. As an independent test, the MND probe was used to make pattern measurements of the E-field components from a dielectric filled rectangular waveguide as a reference source. The fact that the polarity and pattern of the major field components were measured as expected by the MND probe provides further evidence of the trustworthiness of the microstrip patch antenna measurements. The performance of the MND probe was compared to the DD probe for a particular E-plane cut which indicated no significant discrepancies. An assessment of probe response near and far from the source could be studied by comparing it to other references such as the DD or commercial probes.

CHAPTER 6

CONCLUSIONS

6.1 Applicator Design

A rectangular microstrip patch can be matched to lossy media by appropriate design techniques. Low dielectric constant substrates such as Duroid 5870 and 6010 require a superstrate layer to enhance the match, whereas a high dielectric constant substrate such as MCT-85 can match well as a single substrate layer. The drawback with a superstrate is the increased mutual coupling of elements in an array. Mutual coupling is also a factor for compact arrays on the high dielectric constant substrate. Mutual coupling, however, can be compensated by amplitude and phase control on each individual element. The microstrip array applicator should be more convenient to use than bulkier waveguide applicators but must be tested further in a multichannel system.

6.2 Radiated Fields

Both theory and experiment indicate a safe range of effective heating by microstrip applicators when designed for an impedance match into a lossy medium such as water. A 1 cm thick water bolus for coupling and cooling is necessary, but the radiated field pattern in a homogeneous medium indicates that beyond 1 cm the primary power component is exclusively in the transverse direction. This should minimize overheating at fat/muscle boundary layers. More

evaluation of the heating potential can be made by thermographic techniques and layered tissue phantoms.

With an array of microstrip patches, the radiated field pattern can be controlled by amplitude and phase variations. The transverse beam pattern from a 3-element linear array exhibits significant beam broadening (smoothing) and on-axis beam concentration (focus). A 2D array of larger extent is thus expected to have 2D shaping and steering capabilities.

6.3 Theoretical Model

The cavity model can serve as a guide for predicting the shape of the power components of the radiated fields from a rectangular microstrip patch. Transverse patterns show good agreement between theory and experiment at hyperthermia depths (1-3 cm). Additional modes included in the model, based on feed position and fringing field correction, help explain the pattern asymmetry. However, results of axial pattern analysis with the cavity model warrant cautious use for field locations very near the patch. Array theory using the cavity model does not include mutual coupling effects. Those effects can be included only by effective amplitude adjustment based on experimental measurement.

6.4 Experimental Measurements

The miniature E-field probe served as a reliable means of characterizing the radiated fields from a microstrip patch and arrays with considerable resolution. Applicator prototypes of low and high

dielectric constant material were constructed easily and tested in a water tank. Scanner hardware, data acquisition and control worked adequately to permit 3D mapping of the fields from single element patch radiators and some small linear arrays. The size of the tank prohibited characterizing larger arrays.

CHAPTER 7

FURTHER INVESTIGATION

This chapter outlines some major ideas for future investigation related to the design, analysis and measurement of a rectangular microstrip radiator as a multielement microwave hyperthermia applicator.

7.1 Theoretical Model

Further refinements of the cavity-source (MC) model are unlikely to increase its accuracy for predicting fields radiated from a patch in a homogeneous or layered medium. Since major radiation characteristics can be ascertained by the model, other basic array configurations should be analyzed including those on the conformal substrate. These should be interpreted in the light of corresponding experimental cases. For accurately predicted fields radiated from array structures and layered dielectric media, mutual coupling must be carefully taken into account and a distributed equivalent source model is probably necessary. Examples of such an approach are available [36,37] and might be further specialized for these applicators.

7.2 Experimental Measurements

Improved measurements could come from refinements in the E-field probe design to make it smaller and less fragile. A more complete calibration should be made of the existing E-field probe to

determine its sensitivity factor, directionality and degree of perturbation in the fields under measurement. Studies on the MND probe characteristics could be carried out with a rectangular waveguide reference source and more thoroughly documented with a comparison of the predicted results. The measurement system could become more efficient at data collection by streamlining the software control of data sampling (e.g., eliminating pauses). However, this should be weighed against the need for reliable probe positioning without vibrations and signal artifacts. The tank size should be increased. Program MWPLAN should be upgraded (translated and converted) to run on a PC (e.g., IBM AT for use with the mill-based scanner). Data storage should be facilitated so that the format is easily readable for plotting contours with available software.

A method of direct measurement of the loss factor of the fluid medium should be devised. Since this is an important factor both for practical measurements and interpreting the pattern results, the loss factor could be studied as an independent variable by varying the concentration of saline in the tank water. The temperature effect might also be investigated.

7.3 Design Optimization

Further optimization of microstrip applicators could be pursued in terms of match quality, load insensitivity, array element isolation and array geometry so as to maximize control and beam-shaping (uniform or focused) possibilities. However, the existing prototypes

should first be tested with a multichannel system using tissue phantom and animal experiments to evaluate their potential. Models that take into account the dielectric layers could also be used to optimize the thickness of the substrate and superstrate layers for the purpose of matching with load insensitivity, low mutual coupling and small element size. The effect of spacing and antenna orientation on mutual coupling and pattern addition should be more thoroughly studied.

Other microstrip patch element geometries such as circular, ring or annular might be tested for multielement arrays. The rectangular patch was chosen in this study for its relative ease in design, construction and analysis.

7.4 Hyperthermia

As previously mentioned, thermographic studies performed for the microstrip applicators from simple, single element to array configurations would serve to more directly evaluate its potential for hyperthermic heating. This would lead to layered tissue phantom, animal experiments and if efficacy is demonstrated, use on humans in the clinic during cancer therapy.

REFERENCES

- [1] K. R. Foster and A. W. Guy, "The microwave problem," *Scientific American*, vol. 255, no. 3, September 1986.
- [2] M. F. Iskander and C. H. Durney, "Electromagnetic techniques for medical diagnosis: a review," *Proceedings IEEE*, vol. 68, pp. 126-132, 1980.
- [3] C. C. Johnson and A. W. Guy, "Nonionizing electromagnetic wave effects in biological materials and systems," *Proceedings IEEE*, vol. 60, pp. 692-718, June 1972.
- [4] P. C. Meyers, N. L. Sadowsky and A. H. Barrett, "Microwave thermography: principles, methods and clinical applications," *Journal of Microwave Power*, vol. 14, no. 2, pp. 105-115, June 1979.
- [5] K. E. Lonngren, "An application of microwaves to medical research," in *Summary of the 4th Annual IMPI Symposium*, University of Alberta, Edmonton, Canada, May 21-23, p. 91, 1969.
- [6] L. E. Larson and J. H. Jacobi, "Microwave scattering parameter imagery of an isolated canine kidney," *Medical Physics*, vol. 6, pp. 394-403, 1979.
- [7] P. C. Lauterbur, "Medical imaging by nuclear magnetic resonance zeugmatography," *IEEE Transactions on Nuclear Science*, vol. NS-26, pp. 2808-2811, 1979.
- [8] S. Licht, Ed., *Therapeutic Heat and Cold*. Baltimore, MD: Waverly, p. 958.
- [9] C. Povilat, Ed., *Radiation Oncology Center Scientific Report*. St. Louis, MO: Mallinckrodt Institute of Radiology, Washington University Medical Center, 1987-1988.
- [10] C. A. Perez, "Rationale for clinical application of hyperthermia or combined with irradiation or cytotoxic drugs in cancer therapy," In: G. H. Nussbaum, Ed., *Physical Aspects of Hyperthermia*. Medical Physics Monograph No. 8, American Institute of Physics, pp. 63-89, 1982.

- [11] J. H. Kim and E. W. Hahn, "Clinical and biological studies of localized hyperthermia," *Cancer Research*, vol. 39, pp. 2258-2262, 1979.
 - [12] C. A. Perez, B. N. Enami, T. J. Pajak, N. B. Hornback and P. Kasdorf, "Prognostic factors in clinical application of irradiation and heat: relevance of irradiation dose and fractionation: MIR and RTOG experience," in [9], p. 292.
 - [13] C. A. Perez, B. N. Enami, R. R. Kuske, N. B. Hornback, T. J. Pajak and P. Kasdorf, "Irradiation and hyperthermia in the treatment of recurrent carcinoma of the breast in the chest wall: MIR and RTOG experience," in [9], p. 282.
 - [14] R. L. Magin and A. F. Peterson, "Noninvasive microwave phased arrays for local hyperthermia: a review," *International Journal of Hyperthermia*, vol. 5, no. 4, pp. 429-450, July-August 1989.
 - [15] P. P. Lele, "Induction of deep, local hyperthermia by ultrasound and electromagnetic fields," *Radiation and Environmental Biophysics*, vol. 17, pp. 205-217, 1980.
 - [16] J. B. Marmor, D. Pounds, T. B. Postic and G. M. Hahn, "Treatment of superficial human neoplasms by local hyperthermia induced by ultrasound," *Cancer*, vol. 43, pp. 188-197, 1979.
 - [17] P. M. Corry, K. Jabboury, E. P. Armour and J. S. Kong, "Human cancer treatment with ultrasound," *IEEE Transactions on Sonics and Ultrasonics*, vol. SU-31, no. 5, September 1984.
 - [18] P. F. Turner, "Mini-annular phased array for limb hyperthermia," *IEEE Transactions on Microwave Theory and Techniques*, vol. MTT-34, no. 5, pp. 508-512, May 1986.
 - [19] R. E. Munson, "Conformal microstrip antennas and microstrip phased arrays," *IEEE Transactions on Antennas and Propagation*, vol. AP-22, pp. 74-78, January 1974.
 - [20] J. Mendecki, E. Friedenthal, C. Botstein, F. Sterzer and R. Paglione, "Therapeutic potential of conformal applicators for induction of hyperthermia," *Journal of Microwave Power*, vol. 14, p. 139-144, June 1979.
-

- [21] I. J. Bahl, S. S. Stuchly and M. A. Stuchly, "A new microstrip radiator for medical applications," *IEEE Transactions on Microwave Theory and Techniques*, vol. MTT-28, no. 12, pp. 1464-1468, December 1980.
- [22] I. J. Bahl, S. S. Stuchly, J. J. Lagendijk and M. A. Stuchly, "Microstrip loop radiators for medical applications," *IEEE Transactions on Microwave Theory and Techniques*, vol. MTT-30, no. 7, pp. 1090-1093, July 1982.
- [23] E. Yamashita and R. Mittra, "Variational methods for the analysis of microstrip lines," *IEEE Transactions on Microwave Theory and Techniques*, vol. MTT-16, pp. 251-256, April 1968.
- [24] I. J. Bahl and S. S. Stuchly, "Analysis of a microstrip covered with a lossy dielectric," *IEEE Transactions on Microwave Theory and Techniques*, vol. MTT-28, pp. 104-109, February 1980.
- [25] E. Tanabe, A. McEuen, C. S. Norris, P. Fessenden and T. V. Samulski, "A multielement microstrip antenna for local hyperthermia," *IEEE Transactions on Microwave Theory and Techniques-Symposium Digest*, pp. 183-185, 1983.
- [26] R. H. Johnson, J. R. James, J. W. Hand, J. W. Hopewell and P. R. C. Dunlop, "New low-profile applicators for local heating of tissues," *IEEE Transactions on Biomedical Engineering*, vol. BME-31, no. 1, pp. 28-37, January 1984.
- [27] K. M. Parsons, "Evaluation and performance of rectangular patch antennas for microwave diathermy at 2450 MHz," M.S. thesis, University of Maryland, 1980.
- [28] T. S. Sandhu and A. J. Kolozsvary, "Conformal hyperthermia applicators," *International Symposium on Hyperthermic Oncology*, J. Overgaard, Ed., pp. 671-674, 1984.
- [29] I. J. Bahl, S. S. Stuchly and M. A. Stuchly, "New microstrip slot radiator for medical applications," *Electronic Letters*, vol. 16, no. 19, pp. 731-732, 1982.
- [30] Y. X. Wang, "Coplanar waveguide short-gap resonator for medical applications," *IEEE Transactions on Microwave Theory and Techniques*, vol. MTT-33, no. 12, pp. 1310-1312, Dec. 1985.
-

- [31] Y. X. Wang, "Slot-line coupler for medical applications," *Electronics Letters*, vol. 20, no. 22, pp. 939-940, 25th October, 1984.
 - [32] R. H. Johnson, G. Andrasic, D. L. Smith and J. R. James, "Field penetration of arrays of compact applicators in localized hyperthermia," *International Journal of Hyperthermia*, vol. 1, no. 4, pp. 321-336, 1985.
 - [33] J. R. James, P. S. Hall and C. Wood, *Microstrip Antennas: Theory and Design*, Stevenage, U. K.: Peter Peregrinus, 1981.
 - [34] E. C. Jordan and K. G. Balmain, *Electromagnetic Waves and Radiating Systems*, 2nd Edition. Englewood Cliffs, New Jersey: Prentice-Hall, Inc., 1968, p.488.
 - [35] R. F. Harrington, *Time-Harmonic Electromagnetic Fields*. New York: McGraw-Hill, 1961.
 - [36] Y. T. Lo and S. W. Lee, Eds., *ANTENNA HANDBOOK: Theory, Applications, and Design*. New York: Van Nostrand Reinhold Company Inc., 1988.
 - [37] D. R. Tanner, "Numerical methods for the electromagnetic modeling of microstrip antennas and feed systems," Ph.D. dissertation, Department of Electrical and Computer Engineering, University of Illinois, Urbana, IL, 1988.
 - [38] L. Beyne and D. De Zutter, "Power deposition of a microstrip applicator radiating into a layered biological structure," *IEEE Transactions on Microwave Theory and Techniques*, vol. 36, no. 1, January 1988.
 - [39] R. F. Harrington, *Field Computation by Moment Methods*. Malabar, FL: Robert E. Krieger Publishing Co., 1982.
 - [40] Y. T. Lo, D. Solomon and W. F. Richards, "Theory and experiment on microstrip antennas," *IEEE Transactions on Antennas and Propagation*, vol. AP-27, no. 2, pp. 137-145, March 1979.
-

- [41] E. C. Burdette, F. L. Cain and J. Seals, "In vivo probe measurement technique for determining dielectric properties at VHF through microwave frequencies," *IEEE Transactions on Microwave Theory and Techniques*, vol. MTT-28, no. 4, pp. 414-427, April 1980.
 - [42] W. F. Richards, Y. T. Lo and D. D. Harrison, "An improved theory for microstrip antennas and applications," *IEEE Transactions on Antennas and Propagation*, vol. AP-29, no. 1, pp. 38-46, January 1981.
 - [43] E. O. Hammerstad, "Equations for microstrip circuit design," *Proceedings of the European Microwave Conference*, Hamburg Germany, pp. 268-272, September 1975.
 - [44] J. R. Wait, *Electromagnetic Radiation from Cylindrical Structures*. Elmsford, NY: Pergamon, 1959 (reprinted 1985).
 - [45] J. R. Wait, *Electromagnetic Wave Theory*. New York: Harper and Row, Chapter 6, 1985.
 - [46] M. Abramowitz and I. E. Stegun, Eds., *Handbook of Mathematical Functions*. National Bureau of Standards, AMS-55, Washington, D. C.: U. S. Government Printing Office, 1972.
 - [47] J. R. Wait, "Excitation of an enclosed lossy cylinder by an aperture source," *IEEE Transactions on Microwave Theory and Techniques*, vol. MTT-35, no. 2, February 1987.
 - [48] J. R. Wait, "General solution for excitation by slotted aperture source in conducting cylinder with concentric layering," *IEEE Transactions on Microwave Theory and Techniques*, vol. MTT-35, no. 3, March 1987.
 - [49] C. A. Balanis, *Antenna Theory, Analysis and Design*. New York, NY: Harper and Row, 1982, p. 20.
 - [50] S. T. Vaughn, "Automation of ultrasound dosimetry experiment," M.S. thesis, Department of Electrical and Computer Engineering, University of Illinois, Urbana, IL, p. 13, 1980.
-

- [51] H. I. Bassen and G. S. Smith, "Electric field probes--a review," *IEEE Transactions on Antennas and Propagation*, vol. AP-31, no. 5, pp. 710-718, September 1983.

 - [52] T. P. Benson, "The design of a microwave phased array hyperthermia system," M.S. thesis, Department of Electrical and Computer Engineering, University of Illinois, Urbana, IL, p. 20, 1985.

 - [53] M. V. Schneider, "Microstrip lines for microwave integrated circuits," *Bell System Technical Journal*, vol. 48, pp. 1421-1444, May-June 1969.
-

APPENDIX A
ARRPAT2.FOR: NUMERICAL SIMULATION
PROGRAM FOR PLANAR APPLICATORS

This appendix contains the FORTRAN code of ARRPAT2.FOR. The program ARRPAT2 computes electric field components in a lossy homogeneous medium from an array of rectangular microstrip patch antennas using the cavity model with optional improvements. All input parameters are requested at the beginning of the program. Then the fields are calculated at each grid point. Finally, the numerical data are scaled and formatted for output. All necessary subroutines and functions are included. Examples of output data are contained in Appendix C for a single microstrip patch.

```

C      ARRPAT2. This program calculates the radiated
C      near fields from a planar array of rectangular
C      microstrip patch radiators in a homogeneous
C      lossy medium. The algorithm sums the contribution
C      of each source at an individual field
C      (observation) point by calculating the integral
C      expression for each E-field component. The integral
C      is evaluated numerically with a ROMBERG integration
C      routine.
C
C      Each rectangular microstrip patch is treated
C      as a resonant cavity (following Lo [40]) with dominant
C      TM00 modes excited only. In the simple
C      model, each array element has 2 equivalent magnetic
C      current sources without the opposing sources along the
C      long edges. As an alternative, a more complete model
C      can be employed to increase the accuracy of near field
C      calculations. The complete model retains the equivalent
C      magnetic sources on all four edges of the patch.
C
C      Written by: Harold R. Underwood
C      Date: July 1986 (HEXPAR)
C
C      simple cavity/simple source model
C
C      Modified: March 1988 (ARRPAT)
C
C      complete equivalent source model
C
C      Modified: Oct. 1988 (ARRPAT2)
C
C      dominant TM00 modes included
C
C      PROGRAM ARRPAT2
C      COMPLEX A(5,5),Ex(10,50),Cy(10,50),Ez(10,50),COEF(19),Ct
C      REAL MEx(10,50),MEy(10,50),MEz(10,50),RE(10,50),MF(10,50)
C      REAL MEt(10,50)
C      REAL R1(15),XAR(19),YAR(19)
C      REAL FI,MU,EPS0
C      REAL DELX,DELY,EPSr,CPS1,FRED,L,W,UDIS,UL,UW,RERR,SCALE,SZ
C      REAL EPS,tr,t1,OMEGA,PMAX,SIGMA
C      REAL Rex,Rey,Rzc,Rzs,Imx,Imy,Izc,Izs,RMAG
C      INTEGER AG,ANMZ,HM,LM,HN,LN,NM,OP,PHAS,SYM,TBF
C      EXTERNAL Rex,Rey,Rzc,Rzs,Imx,Imy,Izc,Izs,RMAG
C
C      COMMON X,Y,Z,Kr,l1,L,W,M,N,PI,XARRAY,YARRAY
C
C      PI = 3.14159265
C      MU = 4.0*PI*1.0E-7
C      EPS0 = 8.85E-12
C
C      OPEN(UNIT=8,FILE='ARROUT',STATUS='unf nown',FORM='UNFORMATTED')
C      OPEN(UNIT=9,FILE='ARRINP',STATUS='unf nown')
C      OPEN(UNIT=10,FILE='ATBOUT',STATUS='unf nown')
C
C      USE READ (UNIT=5,*) FOR BATCH JOBS WITH INPUT DATA
C      IN THE COMMAND FILE

```

```

C
C USE READ (UNIT=6,*) TO INPUT DATA INTERACTIVELY FROM
  THE TERMINAL
C
C   -- -- -- -- Array Geometry -- -- --
C
PRINT *, 'ARRAY GEOMETRY'
PRINT *, ' ALL UNITS SHOULD BE IN CENTIMETERS.'
PRINT *
PRINT *, 'SPECIFY AN ARRAY GEOMETRY:'
PRINT *
PRINT *, '      1) HEXAGONAL'
PRINT *, '      2) RECTANGULAR'
PRINT *, '      3) LINEAR'
READ (6,*) AG
IF (AG .GE. 2) GOTO 2
WRITE (9,*) 'HEXAGONAL ARRAY OF RECTANGULAR MICROSTRIP'
WRITE (9,*) '          PATCHES'
WRITE (9,*)
PRINT *
PRINT *, 'ENTER NUMBER OF HEXAGONAL ARRAY ELEMENTS:'
PRINT *, '(1,7,17,19)'
READ (6,*) NAE
WRITE (9,*) NAE, ' ELEMENTS'
WRITE (9,*)
C
PRINT *
PRINT *, 'GIVE THE LENGTH OF ONE SIDE OF THE UNIT'
PRINT *, 'EQUILATERAL TRIANGLE.'
READ (6,*) UDIS
WRITE (9,*) UDIS, ' (cm) SPACING'
WRITE (9,*)
GOTO 4
2
CONTINUE
IF (AG .EQ. 3) THEN
  WRITE (9,*) 'LINEAR ARRAY OF RECTANGULAR MICROSTRIP'
  WRITE (9,*) '          PATCHES'
  WRITE (9,*)
  PRINT *
  PRINT *, 'ENTER NUMBER OF LINEAR ARRAY ELEMENTS.'
  PRINT *, '(1,2,3)'
ELSE
  WRITE (9,*) 'RECTANGULAR ARRAY OF RECTANGULAR MICROSTRIP'
  WRITE (9,*) '          PATCHES'
  WRITE (9,*)
  PRINT *
  PRINT *, 'ENTER NUMBER OF RECTANGULAR ARRAY ELEMENTS.'
  PRINT *, '(1,2,3,4,9,16)'
ENDIF
READ (6,*) NAE
WRITE (9,*) NAE, ' ELEMENTS'
WRITE (9,*)
C
PRINT *, 'GIVE THE UNIT LENGTH (X-DIRECTION) OF THE'
PRINT *, 'ARRAY ELEMENT SPACING (UL).'
READ (6,*) UL
IF (AG .EQ. 2) THEN
  PRINT *, 'GIVE THE UNIT WIDTH (Y-DIRECTION) OF THE'
  PRINT *, 'ARRAY ELEMENT SPACING (UW).'
ENDIF

```

```

WRITE (9,*) LW, ' BY ',UL, ' cm SPACING'
WRITE (9,*)
PRINT *
. NTFINUL

PRINT *, 'ENTER TYPE OF PHASING.'
PRINT *
PRINT *, '1) ALL ELEMENTS IN PHASE'
PRINT *, '2) ELEMENTS PHASED FOR A SPECIFIED FOCUS'
PRINT *, '3) INDEPENDENT ARBITRARY PHASES'
READ (6,*) PHAS
IF (PHAS .EQ. 3) THEN
  PRINT *, 'INPUT COEFFICIENTS FOR THE RELATIVE EXCITATION'
  PRINT *, 'OF THE ',NAE, ' RECTANGULAR ELEMENTS OF THE ARRAY.'
  PRINT *
L 157  C 1 1ns Indent          b:\fortran\arrpat2.f77
      DO 8 I=1,NAE
        PRINT *, 'ELEMENT #',I
        READ (6,*) COEF(I)
        PRINT *, I,COEF(I)
      8  CONTINUE
      ELSEIF (PHAS .EQ. 2) THEN
        CALL FOCUS (XAR,YAR,NAE,fr,COEF)
      ELSE
        DO 14 I=1,NAE
          COEF(I)=1.0
        14  CONTINUE
      ENDIF
C
C -----Patch Geometry-----
C
PRINT *
PRINT *, 'ENTER DIMENSIONS OF THE RECTANGULAR PATCH:'
PRINT *, 'L,W (LENGTH,WIDTH).'
READ (6,*) L,W
WRITE (9,*) 'PATCH DIMENSIONS ARE ',W, ' BY ',L, ' cm '
WRITE (9,*)
C
C -----Cavity Model-----
C
PRINT *
PRINT *, 'ENTER CAVITY-SOURCE MODEL TYPE FOR THE'
PRINT *, 'ARRAY ELEMENT (1=SIMPLE, 2=COMPLETE).'
READ (6,*) MODTYP
PRINT *, 'MODTYP =', MODTYP
IF (MODTYP .EQ. 1) THEN
  WRITE (9,*) 'SIMPLE CAVITY-SOURCE MODEL'
  WRITE (9,*)
ELSE
  WRITE (9,*) 'COMPLETE CAVITY-SOURCE MODEL'
  WRITE (9,*)
ENDIF
PRINT *
PRINT *, 'ENTER THE LOWEST MODE NUMBERS (n,m)'
PRINT *, 'INCLUDED IN THE SOURCE MODEL'
READ (6,*) LN,LM
PRINT *, 'ENTER THE HIGHEST MODE NUMBERS (n,m)'
PRINT *, 'INCLUDED IN THE SOURCE MODEL'
READ (6,*) HN,HM

```

```

C
NM = HM - LM + 1
NN = HN - LN + 1
C
WRITE (9,*) NN*NM, POSSIBLE MODES ARE INCLUDED IN THE MODE
WRITE (9,*) 'THE LOWEST MODE IS n,m =',LN,LM
WRITE (9,*) 'THE HIGHEST MODE IS n,m =',HN,HM
WRITE (9,*)
DO 27 J=LN+1,HN+1
  DO 25 I=LM+1,HM+1
    PRINT *, 'COMPLEX COEFFICIENT OF MODE:',J-1,I-1
    PRINT *, 'A (REAL,IMAGINARY) ='
    PRINT *, '(IF INSIGNIFICANT ENTER (0,0))'
    READ (6,*) A(J,I)
    PRINT *, 'J,I,A(J,I)',J,I,A(J,I)
25  CONTINUE
27  CONTINUE
C
-----Medium Parameters-----
C
PRINT *, 'MEDIUM PARAMETERS.'
PRINT *
PRINT *, 'ENTER THE OPERATING FREQUENCY (MHz).'
READ (6,*) FREQ
WRITE (9,*) 'OPERATING FREQUENCY IS ',FREQ,' MHz'
WRITE (9,*)
PRINT *
PRINT *, 'SPECIFY REAL AND IMAGINARY PARTS OF'
PRINT *, 'RELATIVE EPSILON.'
READ (6,*) EPSr,EPSi
OMEGA = 2.0*PI*FREQ*1.0E+6
SIGMA = -OMEGA*EPSi*EPS0
EPS = EPSr*EPS0
CK = OMEGA*CSORT(MU*EPS*CMPLX(1.0,-SIGMA/(OMEGA*EPS)))
CF = CK/100.
fr = REAL(CK)
fi = AIMAG(CK)
WRITE (9,*) 'RELATIVE PERMITTIVITY IS ',EPSr,EPSi
WRITE (9,*) 'CONDUCTIVITY IS',SIGMA
WRITE (9,*) 'COMPLEX PROPAGATION CONSTANT K IS ',CK
WRITE (9,*)
PRINT *, 'COMPLEX WAVENUMBER IS:',kr,fi
C
-----Observation Points-----
C
PRINT *, 'IS ANTENNA PATTERN X AND Y SYMMETRIC?'
PRINT *, '(1 = YES)'
READ (6,*) SYM
IF (SYM.NE.1) GOTO 30
WRITE (9,*) 'FIELD PATTERN IS X AND Y SYMMETRIC:'
WRITE (9,*) 'ON QUADRANT COMPUTED ONLY.'
30 CONTINUE
PRINT *
PRINT *, 'SPECIFY OBSERVATION PLANE ORIENTATION.'
PRINT *, ' 1) PARALLEL (TRANSVERSE)'
PRINT *, ' 2) PERPENDICULAR (AXIAL)'
READ (6,*) OP

```

```

PRINT *
PRINT *, 'LINEAR (PRIMARY PLANE) CUT?'
PRINT *, '      1) E-PLANE'
PRINT *, '      2) H-PLANE'
PRINT *, '      3) A-AXIAL'
PRINT *, '      4) NO'
READ (6,*) LPC
IF (LPC .EQ. 2) GOTO 50
PRINT *
PRINT *, 'THE FIELD IS SAMPLED IN A PLANE A DISTANCE'
PRINT *, 'Z = ZO FROM THE ANTENNA. ENTER THIS DISTANCE.'
READ (6,*) ZO
PRINT *, ZO
PRINT *
PRINT *, 'ENTER X-OFFSET VALUE (X=XO) FOR H-PLANE CUT:'
READ (6,*) XO
PRINT *, XO
PRINT *
PRINT *, 'THE OBSERVATION POINTS ARE ARRANGED IN AN'
PRINT *, 'ARRAY NX BY NY. ENTER NX,NY.'
READ (6,*) NX,NY
PRINT *, NX,NY
PRINT *
PRINT *, 'THE OBSERVATION POINTS ARE SPACED IN THE'
PRINT *, 'X-DIRECTION BY AN INTERVAL DELTA-X AND DELTA-Y'
PRINT *, 'IN THE Y-DIRECTION. ENTER DELTA-X,DELTA-Y.'
READ (6,*) DELX,DELY
PRINT *, DELX,DELY
WRITE (9,*) 'PARALLEL OBSERVATION PLANE: Z=',ZO
WRITE (9,*) NX,' BY ',NY,' ARRAY ',DELX,DELY,' cm INCREMENTS'
WRITE (9,*) (NX-1)*DELX,' BY ',(NY-1)*DELY,' cm WINDOW'
WRITE (9,*)
GOTO 80
50 CONTINUE
PRINT *
PRINT *, 'ENTER THE Y-VALUE FOR THIS CONSTANT Y-PLANE'
PRINT *, 'CUT PERPENDICULAR TO THE ANTENNA.'
READ (6,*) YO
PRINT *
PRINT *, 'ENTER THE MINIMUM SAMPLING DISTANCE FROM'
PRINT *, 'THE ANTENNA.'
READ (6,*) SZ
PRINT *
PRINT *, 'THE OBSERVATION POINTS ARE ARRANGED IN AN'
PRINT *, 'ARRAY NX BY NZ. ENTER NX,NZ.'
READ (6,*) NX,NZ
PRINT *
PRINT *, 'THE OBSERVATION POINTS ARE SPACED'
PRINT *, 'BY INTERVALS DELTA-X AND DELTA-Z'
PRINT *, 'ENTER DELTA-X, DELTA-Z.'
READ (6,*) DELX,DELZ
WRITE (9,*) 'PERPENDICULAR OBSERVATION PLANE: Y=0'
WRITE (9,*) NX,NZ,' ARRAY ',DELX,DELZ,' cm INCREMENTS'
WRITE (9,*) (NX-1)*DELX,' BY ',(NZ-1)*DELZ,' cm WINDOW'
WRITE (9,*) 'INITIAL Z= ',SZ,' cm'
80 CONTINUE
PRINT *, 'DO YOU WANT FIELD COMPONENTS AUTO-NORMALIZED?'
PRINT *, '(1=YES 2=NO)'
READ (6,*) ANMZ
IF (ANMZ .NE. 2) GOTO 90

```

```

PRINT *, 'SCALE FACTOR FOR FIELD NORMALIZATION (dB):'
READ (6,*) SCALE
WRITE (9,*) 'SCALE FACTOR=',SCALE,' (dB)'
20 CONTINUE

-----Integration Accuracy-----

PRINT *,
PRINT *, 'ENTER DESIRED ACCURACY OF INTEGRATION.'
READ (6,*) RERR
PRINT *, RERR

C -----Output File Type-----
C

PRINT *
PRINT *, 'OUTPUT FILE TYPE:'
PRINT *, '          1) BINARY UNFORMATTED'
PRINT *, '          2) TAB FORMAT'
READ (6,*) TBF

C -----
C

CALL LOCATE (AG,NAE,UDIS,UL,UW,XAR,YAR)
IF (PHAS .NE. 2) GOTO 100
CALL FOCUS (XAR,YAR,NAE,Fr,COEF)
100 CONTINUE
IF (OP .EQ. 2) GOTO 310

C ***LOOP THROUGH GRID OF OBSERVATION POINTS***
C 1) PARALLEL PLANE
C

IF (SYM .NE. 1) GOTO 110
NX1 = (FLOAT(NX)+1.5)/2.
NV = (FLOAT(NY)+1.5)/2.
GOTO 120
110 CONTINUE
NX1 = NX
NV = NY
120 CONTINUE
Z=Z0
Y=-FLOAT(NY-1)*DELY/2.+W/2.
DO 300 J=1,NV
PRINT *, 'Y=',Y
WRITE (9,*) 'Y=',Y
X=X0-FLOAT(NX-1)*DELX/2.+L/2.
DO 200 I=1,NX1

C
C COMPUTE ELECTRIC FIELD COMPONENTS AT P(X,Y,Z)
C

EX(I,J)=(0.,0.)
EY(I,J)=(0.,0.)
EZ(I,J)=(0.,0.)

C
C ***LOOP THROUGH ARRAY ELEMENTS AND SUM CONTRIBUTIONS***
C

DO 150 P=1,NAE
XARRAY=XAR(P)
YARRAY=YAR(P)

```

```

DO 145 N=LN,HN
DO 140 M=LM,HM
  IF (CABS(A(N+1,M+1)) .NE. 0) THEN
    Ex(I,J)=Ex(I,J)-2.0*A(N+1,M+1)*CMPLX(ROM1D(Rr, 0.,W,
    & RERR,15,3,R1,IER),ROM1D(Imx,0.,W,
    & RERR,15,3,R1,IER))*COEF(P)
    Ez(I,J)=Ez(I,J)+2.0*A(N+1,M+1)*CMPLX(ROM1D(Rzs,0.,W,
    & RERR,15,3,R1,IER),ROM1D(Izs,0.,W,
    & RERR,15,3,R1,IER))*COEF(P)
C
C
    IF (MODTYP .EQ. 1) GOTO 130
C
    Ey(I,J)=Ey(I,J)-2.0*A(N+1,M+1)*CMPLX(ROM1D(Rey,0.,L,
    & RERR,15,3,R1,IER),ROM1D(Imy,0.,L,
    & RERR,15,3,R1,IER))*COEF(P)
    Ez(I,J)=Ez(I,J)+2.0*A(N+1,M+1)*CMPLX(ROM1D(Rzc,0.,L,
    & RERR,15,3,R1,IER),ROM1D(Izc,0.,L,
    & RERR,15,3,R1,IER))*COEF(P)
C
C
130    CONTINUE
    ENDIF
140    CONTINUE
145    CONTINUE
150    CONTINUE
    X=X+DELX
200    CONTINUE
    Y=Y+DELY
300    CONTINUE
    IF (DP .NE. 2) GOTO 505
310    CONTINUE
C
C    2) PERPENDICULAR PLANE
C
    NX1 = NX
    NV = NZ
    Y=Y0
    Z=SZ
C
DO 500 J=1,NZ
  PRINT *, 'Z= ',Z
  X=-FLOAT(NX-1)*DELX/2.0 + L/2.
  DO 400 I=1,NX
C
C    COMPUTE ELECTRIC FIELD COMPONENTS AT P(X,Y,Z)
C
    Ex(I,J)=(0.,0.)
    Ey(I,J)=(0.,0.)
    Ez(I,J)=(0.,0.)
C
C    ***LOOP THROUGH ARRAY ELEMENTS AND SUM CONTRIBUTIONS***
C
DO 350 P=1,NAE
  XARRAY=XAR(P)
  YARRAY=YAR(P)
DO 345 N=LN,HN
DO 340 M=LM,HM
  IF (CABS(A(N+1,M+1)) .NE. 0) THEN

```

```

      Ex(I,J)=Ex(I,J)-2.0*A(N+1,M+1)*CMPLX(ROM1D(Re , , 126
&          RERR,15,3,R1,IER),ROM1D(Imx ,O ,W,
&          RERR,15,3,R1,IER))*COEF(P)
      Ez(I,J)=Ez(I,J)+2.0*A(N+1,M+1)*CMPLX(ROM1D(Rzc ,O ,J,
&          RERR,15,3,R1,IER),ROM1D(Izs ,O ,W,
&          RERR,15,3,R1,IER))*COEF(P)
      IF (MODTYP .EQ. 1) GOTO 330
C
      Ey(I,J)=Ey(I,J)-2.0*A(N+1,M+1)*CMPLX(ROM1D(Rey ,O ,J,
&          RERR,15,3,R1,IER),ROM1D(Imy ,O ,L,
&          RERR,15,3,R1,IER))*COEF(P)
      Ez(I,J)=Ez(I,J)+2.0*A(N+1,M+1)*CMPLX(ROM1D(Rzc ,O ,L,
&          RERR,15,3,R1,IER),ROM1D(Izc ,O ,L,
&          RERR,15,3,R1,IER))*COEF(P)
330      CONTINUE
      ENDIF
340      CONTINUE
345      CONTINUE
350      CONTINUE
      X=X+DELX
400      CONTINUE
      Z=Z+DELZ
500      CONTINUE
C
505      CONTINUE
C
C      CONVERT DATA TO RELATIVE DB
C
      XMAX=0.
      YMAX=0.
      ZMAX=0.
      PMAX=0.
      PRINT *, 'NV= ',NV
      DO 520 J=1,NV
        DO 510 I=1,NX1
          MEx(I,J)=CABS(Ex(I,J))
          MEy(I,J)=CABS(Ey(I,J))
          MEz(I,J)=CABS(Ez(I,J))
          MEt(I,J)=SQRT(MEx(I,J)**2 + MEy(I,J)**2)
          MP(I,J)=(MEx(I,J)**2.0+MEy(I,J)**2.0+MEz(I,J)**2.0)
          XMAX=AMAX1(XMAX,MEx(I,J))
          YMAX=AMAX1(YMAX,MEy(I,J))
          ZMAX=AMAX1(ZMAX,MEz(I,J))
          PMAX=AMAX1(PMAX,MP(I,J))
510      CONTINUE
520      CONTINUE
      Exp = 20.0*ALOG10(XMAX)
      Eyp = 20.0*ALOG10(YMAX + 1.0E-20)
      Ezp = 20.0*ALOG10(ZMAX)
      PRINT *, 'Exp = ',Exp
      PRINT *, 'Eyp = ',Eyp
      PRINT *, 'Ezp = ',Ezp
      WRITE (9,*) 'PEAK Ex = ',Exp,' (dB)'
      WRITE (9,*) 'PEAK Ey = ',Eyp,' (dB)'
      WRITE (9,*) 'PEAK Ez = ',Ezp,' (dB)'
      IF (ANMZ .NE. 2) GOTO 350

```

```

DO 540 J=1,NV
  DO 530 I=1,NX1
    RE(I,J)=10.0*ALOG10(MEz(I,J)/MEt(I,J)+1.0E-20)
    MEx(I,J)=20.0*ALOG10(MEx(I,J)+1.0E-20) + SCALE
    MEy(I,J)=20.0*ALOG10(MEy(I,J)+1.0E-20) + SCALE
    MEz(I,J)=20.0*ALOG10(MEz(I,J)+1.0E-20) + SCALE
    MP(I,J)=10.0*ALOG10(MP(I,J)/PMAX+1.0E-20)
530   CONTINUE
540   CONTINUE
      GOTO 580
550   CONTINUE
DO 570 J=1,NV
  DO 560 I=1,NX1
    RE(I,J)=10.0*ALOG10(MEz(I,J)/MEt(I,J)+1.0E-20)
    MEx(I,J)=20.0*ALOG10(MEx(I,J)/XMAX + 1.0E-20)
    MEy(I,J)=20.0*ALOG10(MEy(I,J)/(YMAX+1.0E-20) + 1.0E-20)
    MEz(I,J)=20.0*ALOG10(MEz(I,J)/ZMAX + 1.0E-20)
    MP(I,J)=10.0*ALOG10(MP(I,J)/PMAX + 1.0E-20)
560   CONTINUE
570   CONTINUE
580   CONTINUE

    IF (N=1 .GT. 50) THEN
      ILAST=50
    ELSE
      ILAST=NX1
    ENDIF
    IF (TB .EQ. 1) THEN
      DO 600 J=1,NV
        WRITE (8) (MEx(I,J),MEy(I,J),MEz(I,J),I=1,ILAST)
        WRITE (8) (RE(I,J),MP(I,J),I=1,ILAST)
        WRITE (8) (MEx(I,J),MEy(I,J),MEz(I,J),I=51,NX1)
        WRITE (8) (RE(I,J),MP(I,J),I=51,NX1)
600     CONTINUE
C
C     TAB FORMATTED OUTPUT FILE FOR SPREADSHEET
C
    ELSEIF (LPC .EQ. 1) THEN
      X=-FLOAT(NX1-1)*DELX/2.0
      DO 700 I=1,NX1
        WRITE (10,*) (' ',X,' ',MEx(I,J),' ',MEz(I,J),J=1,NV)
        X=NINT((X+DELX)*10.)/10.
700     CONTINUE
        PRINT *
        PRINT *, 'DATA FILE NAMED ARROUTn'
        PRINT *
    ELSEIF (LPC .EQ. 2) THEN
      Y=-FLOAT(NY-1)*DELY/2.
      DO 750 J=1,NV
        WRITE (10,*) (' ',Y,' ',MEx(I,J),' ',MEz(I,J),I=1,NX1)
        Y=NINT((Y+DELY)*10.)/10.
750     CONTINUE
    ELSEIF (LPC .EQ. 3) THEN
      Z=SZ
      DO 780 J=1,NV
        WRITE (10,*) (' ',Z,' ',MEx(I,J),' ',MEz(I,J),I=1,1)
        Z=NINT((Z+DELZ)*10.)/10.
780     CONTINUE
    ENDIF

```

```

          STOP
          END
C
C -----
C
SUBROUTINE LOCATE (AG,NAE,UDIS,UL,UW,XAR,YAR)
  REAL XAR(19),YAR(19)
  REAL UDIS,UL,UW
  INTEGER AG
  PI=3.14159265
  ***COMPUTE LOCATIONS OF ARRAY ELEMENTS***
C
  PRINT *, 'AG,NAE =',AG,NAE
  XAR(1)=0.
  YAR(1)=0.
C
C   1) HEXAGONAL ARRAY WITH THE CENTRAL ELEMENT (#1)
C      AT THE ORIGIN
C
  IF (AG .GE. 2) GOTO 50
  IF (NAE.LE.1) GOTO 45
C
C           LOCATIONS ON RING 1 OF 7-ELEMENT HEXAGONAL ARRAY
C
  DO 20 I=2,7
    XAR(I)=UDIS*COS(FLOAT(I-2)*PI/3.0)
    YAR(I)=UDIS*SIN(FLOAT(I-2)*PI/3.0)
  20 CONTINUE
  IF (NAE.LE.7) GOTO 45
C
C           LOCATIONS ON RING 2 OF 19-ELEMENT HEXAGONAL ARRAY
C
  DO 30 J=8,13
    XAR(J)=2.0*UDIS*COS(FLOAT(J-8)*PI/3.0)
    YAR(J)=2.0*UDIS*SIN(FLOAT(J-8)*PI/3.0)
  30 CONTINUE
  DO 40 I=14,19
    XAR(I)=2.*UDIS*COS(PI/6.)*COS((FLOAT(I-14)/3.+1./6.)*PI)
    YAR(I)=2.*UDIS*COS(PI/6.)*SIN((FLOAT(I-14)/3.+1./6.)*PI)
  40 CONTINUE
  IF (NAE .GT. 17) GOTO 45
C
C           ADJUST FOR LOCATIONS OF 17-ELEMENT HEX ARRAY
C
  DO 42 I=8,9
    XAR(I)=XAR(I+1)
    YAR(I)=YAR(I+1)
  42 CONTINUE
  DO 44 I=10,17
    XAR(I)=XAR(I+2)
    YAR(I)=YAR(I+2)
  44 CONTINUE
  45 CONTINUE
  DO 46 I=1,NAE
    PRINT *, '1,XAR,YAR=',I,XAR(I),YAR(I)
  46 CONTINUE
  RETURN
  50 CONTINUE

```

```

L
C      ) RECTANGULAR (OR LINEAR) ARRAY CENTERED AT THE ORIGIN
C      WITH ELEMENT #1 IN THE CORNER OF THE
C      THIRD QUADRANT
C
C      IF (NAE .EQ. 1) GOTO 70
C      IF (NAE .GE. 4) GOTO 58
C
C 52  CONTINUE
C      IF (NAE .EQ. 2) THEN
C          XAR(1)=-UL/2.
C          XAR(2)=UL/2.
C          YAR(2)=0.
C      ELSEIF (NAE .EQ. 3) THEN
C          DO 55 I=1,3
C              XAR(I)=(I-2)*UL
C              YAR(I)=0.
C 55  CONTINUE
C      ENDIF
C      RETURN
C 58  CONTINUE
C
C      LOCATIONS OF 4, 9 OR 16-ELEMENT ARRAY
C
C      YAR(1)=- (NAE**.5- 1)*ULW/2.0
C      DO 65 J=1, NAE**.5
C          XAR(1)=- (NAE**.5-1)*UL/2.0
C          DO 60 I=1, NAE**.5
C              I=I+(J-1)*NAE**.5
C              XAR(I)=XAR(1)+((I-1)*UL)
C              YAR(I)=YAR(1)+((J-1)*ULW)
C              PRINT *, 'XAR =', XAR(I), 'YAR=', YAR(I)
C 60  CONTINUE
C 65  CONTINUE
C 70  CONTINUE
C      RETURN
C      END
C
C      -----
C
C      SUBROUTINE FOCUS(X,Y,NAE,BETA,V)
C
C      COMPLEX V(19)
C      REAL X(19),Y(19),R(19),PHI(19)
C      REAL XF,YF,ZF,BETA
C      PRINT *
C      PRINT *, 'SPECIFY COORDINATES OF FOCAL POINT (X,Y,Z). '
C      READ (6,*) XF,YF,ZF
C      WRITE (9,*) 'FOCAL POINT (XF,YF,ZF) =',XF,YF,ZF,' (cm)'
C      DO 100 I=1,NAE
C          R(I) = SQRT((XF-X(I))**2 + (YF-Y(I))**2 + ZF**2)
C          PHI(I) = BETA*R(I)
C          V(I) = CMPLX(COS(PHI(I)),SIN(PHI(I)))
C          PRINT *, I, V(I)
C          WRITE (9,*) I,V(I)
C 100  CONTINUE
C      RETURN
C      END

```



```

55  DO 55 I = 1,2
      RMAG = RMAG(XP,YP)
      CT = ((EO*Z)/(4.*PI))*(1.+CJ*CK*R1x)*CEXP(-CJ*CK*R1x)
      CT = CT+COS(M*PI*XP/L)*COS(N*PI*YP/L)
      CI = CI + CT
      X1 = L
      EO = -EO
55  CONTINUE
C
      Imx = AIMAG(CI)
C
      RETURN
      END
C
C
C
C
      REAL FUNCTION Rey(XP)
C
      COMPLEX CI,CJ,CK,CT
      REAL Rr,l1,L,W,PI,Rly
      REAL RMAG
      INTEGER M
C
      EXTERNAL RMAG
C
      COMMON X,Y,Z,Rr,l1,L,W,M,N,PI,XARRAY,YARRAY
C
      CI = (0.,0.)
      CJ = (0.,1.)
      CK = CMPLX(Rr,l1)
      CT = (0.,0.)
C
      EO = 1.
      YF = 0.
C
      DO 60 I = 1,2
          Rly = RMAG(XP,YP)
          CT = ((EO*Z)/(4.*PI))*(1.+CJ*CK*Rly)*CEXP(-CJ*CK*Rly)
          CT = CT*COS(M*PI*XP/L)*COS(N*PI*YP/W)/Rly**2
          CI = CI + CT
          YF = W
          EO = -EO
60  CONTINUE
C
      Rey = REAL(CI)
C
      RETURN
      END
C
C
C
C
      REAL FUNCTION Imy(XP)
C
      COMPLEX CI,CJ,CK,CT
      REAL Rr,l1,L,W,PI,Rly
      REAL RMAG
      INTEGER M

```

```

C
C      EXTERNAL RMAG
C
C      COMMON X,Y,Z,t,r,t1,L,W,M,N,PI,XARRAY,YARRAY
C
C      CI = (0.,0.)
C      CJ = (0.,1.)
C      CI = CMPLX(t,r,t1)
C      CT = (0.,0.)
C
C      E0 = 1.
C      YP = 0.
C
C      DO 65 I = 1,2
C          R1y = RMAG(XP,YP)
C          CT = ((E0*Z)/(4.*PI))*(1.+CJ*CI*R1y)*CEXP(-CJ*CI*R1y)
C          CT = CT*COS(M*PI*XP/L)*COS(N*PI*YP/W)/R1y**3
C          CI = CI + CT
C          YP = W
C          E0 = -E0
65  CONTINUE
C
C      Imy = AIMAG(CI)
C
C      RETURN
C      END
C
C      REAL FUNCTION Rzc(XP)
C
C      COMPLEX CI,CJ,CI
C      REAL t,r,t1,L,W,PI,R1y
C      REAL RMAG
C      INTEGER M
C
C      EXTERNAL RMAG
C
C      COMMON X,Y,Z,t,r,t1,L,W,M,N,PI,XARRAY,YARRAY
C
C      CI = (0.,0.)
C      CJ = (0.,1.)
C      CI = CMPLX(t,r,t1)
C
C      E0 = 1.
C      YP = 0.
C
C      DO 70 I = 1,2
C          R1y = RMAG(XP,YP)
C          CT = ((E0*(Y-YP))/(4.*PI))*(1.+CJ*CI*R1y)*CEXP(-CJ*CI*R1y)
C          CT = CT*COS(M*PI*XP/L)*COS(N*PI*YP/W)/R1y**3
C          CI = CI + CT
C          YP = W
C          E0 = -E0
70  CONTINUE
C
C      Rzc = REAL(CI)
C
C      RETURN
C      END

```

```

(
C
REAL FUNCTION Izc(XP)
C
COMPLEX CJ,CJ,CI,CT
REAL Kr,t1,L,W,PI,Rly
REAL RMAG
INTEGER M
C
EXTERNAL RMAG
C
COMMON X,Y,Z,t,r,t1,L,W,M,N,PI,XARRAY,YARRAY
C
CI = (0.,0.)
CJ = (0.,1.)
CI = CMPLX(Kr,t1)
CT = (0.,0.)
C
EO = 1.
YP = 0.
C
DO 75 I = 1,2
  Rly = RMAG(XP,YP)
  CT = ((EO*(Y-YP))/(4.*PI))*(1.+CJ*CI*Rly)*CEXP(-CJ*CI*Rly)
  CI = CT*COS(M*PI*XP/L)*COS(N*PI*YP/W)/Rly**2
  CJ = CT + CI
  YP = W
  EO = -EO
75 CONTINUE
C
Izc = AIMAG(CI)
C
RETURN
END
C
C
C
REAL FUNCTION Rzs(YP)
C
COMPLEX CI,CJ,CI,CT
REAL Kr,t1,L,PI,Rlx
REAL RMAG
C
EXTERNAL RMAG
C
COMMON X,Y,Z,t,r,t1,L,W,M,N,PI,XARRAY,YARRAY
C
CI = (0.,0.)
CJ = (0.,1.)
CI = CMPLX(Kr,t1)
CT = (0.,0.)
C
EO = 1.
XP = 0.
C
DO 80 I = 1,2
  Rlx = RMAG(XP,YP)
  CT = ((EO*(X-XP))/(4.*PI))*(1.+CJ*CI*Rlx)*CEXP(-CJ*CI*Rlx)
  CI = CT*COS(M*PI*XP/L)*COS(N*PI*YP/W)/Rlx**2
  CI = CI + CT

```

```

      XP = L
      EO = -EO
80  CONTINUE
C
C     Rzs = REAL(CI)
C
C     RETURN
C     END
C
C
C     REAL FUNCTION Izs(YP)
C
C     COMPLEX CI,CJ,CK,CT
C     REAL Ir,Ii,L,PI,Rlx
C     REAL RMAG
C
C     EXTERNAL RMAG
C
C     COMMON X,Y,Z,Ir,Ii,L,W,M,N,PI,XARRAY,YARRAY
C
C     CI = (0.,0.)
C     CJ = (0.,1.)
C     CK = CMPLX(Ir,Ii)
C     CT = (0.,0.)
C
C     EO = 1.
C     XP = 0.
C
C     DO 85 I = 1,2
C       Rlx = RMAG(XP,YP)
C       CT = ((EO*(X-XP))/(4.*PI))*(1.+CJ*CK*Rlx)*CEXP(-CJ*CK*Rlx)
C       CT = CT*COS(M*PI*XP/L)*COS(N*PI*YP/W)/Rlx**3
C       CI = CI + CT
C       XP = L
C       EO = -EO
85  CONTINUE
C
C     Izs = AIMAG(CI)
C
C     RETURN
C     END
C
C     FUNCTION TO COMPUTE MAGNITUDE OF THE DISTANCE FROM
C     THE SOURCE ((XARRAY-XP),(YARRAY-YP),0) TO THE OBS.
C     POINT (X,Y,Z)
C
C     REAL FUNCTION RMAG(XP,YP)
C
C     REAL Ir,Ii,L,W,PI,X,Y,Z,XARRAY,YARRAY,XP,YP
C
C     COMMON X,Y,Z,Ir,Ii,L,W,M,N,PI,XARRAY,YARRAY
C
C     RMAG = SQRT((X-XARRAY-XP)**2 + (Y-YARRAY-YP)**2 + Z*Z)
C
C     RETURN
C     END
C

```

```

C
C
C      -----Romberg Integration Routine-----
C
C      FUNCTION ROMID(F,A,B,RERR,MAXP,MINP,R,IER)
C
C      This function returns an estimate of the integral of
C      'f' over the interval (a,b) by Romberg integration
C
C      'f'      an external function of the form 'f(x)'
C              (must be declared 'external' in the calling
C              program)
C      'rerr'   the desired relative accuracy (must be between
C              0.00001 and 1.0)
C      'maxp'   specifies the maximum number of function
C              evaluations as (1+2**(maxp-1))
C      'minp'   specifies the minimum number of function
C              evaluations as (1+2**(minp-1))
C              --sometimes Necessary if the integrand
C              oscillates several times within the interval.
C      'r'      an array of length 'maxp' (workspace provided
C              by the main routine). On return, contains the
C              last row of the Romberg extrapolation array.
C      'ier'   on return is set to zero if accuracy is met
C              on return is 1 if rerr is out of range
C              on return is 2 if maxp = 1 or minp = maxp
C              on return is 3 if accuracy is not met
C
C      Author: A. F. Peterson UIUC ECE Dept
C
C      Revised: April 16, 1986
C
C      REAL R(MAXP)
C      IF ((MAXP .LT. 1) .OR. (MINP .GT. MAXP)) THEN
C          IER=2
C          ROMID=0.
C          GOTO 30
C      ENDIF
C      IF ((RERR .LT. 0.00001) .OR. (RERR .GT. 1.0)) THEN
C          IER=1
C          ROMID=0.
C          GOTO 30
C      ENDIF
C      IER=0
C      SUM=0.5*(F(A)+F(B))
C      R(1)=SUM*(B-A)
C      N=1
C
C      REFINE ESTIMATE OF INTEGRAL USING TRAPEZOIDAL RULE
C
C      DO 20 I=2,MAXP
C          RLAST=R(1)
C          DEL=(B-A)/FLOAT(N)
C          X=A-0.5*DEL
C          DO 10 J=1,N
C              SUM=SUM+F(X+DEL*FLOAT(J))
C              N=N*2
C          R(I)=0.5*DEL*SUM

```

```

C
C      COMPUTE ROMBERG EXTRAPOLATION ARRAY
C
      W=4.0
      DO 15 J=2,I
        R(I+1-J)=(W*R(I+2-J)+R(I+1-J))/(W+1.0)
        W=4.0*W
15    CONTINUE
C
      ROM1D=R(I)
      IF (I .LT. MINP) GO TO 20
C
C      CHECK INTEGRAL ESTIMATE
C
C      IF ESTIMATE IS VERY SMALL, RETURN
C      (TAKES CARE OF THE CASE WHERE THE INTEGRAND VANISHES,
C      BUT MAY BE INACCURATE IF THE FIRST FEW SAMPLED POINTS
C      ARE ALL ZERO COINCIDENTALLY AND 'MINP' IS NOT SET
C      HIGH ENOUGH.)
C
C      IF CHANGE IN ESTIMATE IS WITHIN DESIRED RANGE, RETURN
C
      IF (ABS(ROM1D) .LT. 1.0E-20) RETURN
      IF (ABS((ROM1D-RLAST)/ROM1D) .LT. RERR) RETURN
20    CONTINUE
      IER=3
C
C      ERROR
C
30    PRINT *, 'ERROR IN ROM1D -- IER = ',IER
      RETURN
      END

```

APPENDIX B

MWPLAN.FOR: DATA ACQUISITION AND CONTROL

PROGRAM FOR MICRO PDP-11

AND MILL-BASED SCANNER

This appendix contains the FORTRAN code of MWPLAN.FOR. The program MWPLAN is written for a DEC Micro PDP-11 to control the BRL mill-based scanner and acquire electric field data from a miniature dipole probe submersed in a water tank. Both linear (1D) and planar (2D) scans are possible for a specified grid size and spacing. Sample output is contained in Appendix D in graphical form.

```

c MWSCAN.FORTRAN
c
c THIS PROGRAM WILL SCAN A MICROWAVE FIELD IN A
c WATER TANK ON THE BRL MILL-BASED SCANNING SYSTEM
c (ROOM 228)
c
c
c LINK WITH MOVSUB,BPSUB,ATD2
c
      integer*2 isctp, idir, ipts, ibuf, idisk, iplan
      integer*2 itot, jpts, kpts, iopt, ifile(7), iax(2)
      real plin(50), p2d(50, 50)
      real width, xwid, ywid, zwid, xpos, ypos, zpos
c
      real dist, kinc, jwid, kwid, ktot
      character *14 v0000000000000002
      equivalence (v0000000000000002, ifile)
# 16 "mwplan.for"
      write(unit=5, fmt=10)
c
c ENTER PARAMETERS FOR SCAN
c
# 17 "mwplan.for"
      10 format(///,10x,20hMICROWAVE POWER-SCAN,///)
c
c LINEAR SCAN PARAMETERS
c
# 21 "mwplan.for"
      20 continue
# 25 "mwplan.for"
      write(unit=5, fmt=30)
      30 format(/4x,34h SCAN TYPE: 1=LINEAR,2=PLANAR(2-D),)$)
      read(unit=*, fmt=*) isctp
      if (isctp - 2) 40, 100, 20
      40 continue
      write(unit=5, fmt=45)
      45 format(/4x,30h ENTER SCAN ORIGIN: X,Y,Z (CM),)$)
      read(unit=5, fmt=*) xpos, ypos, zpos
      write(unit=5, fmt=50)
      50 format(/4x,26h TOTAL WIDTH OF SCAN (MM):,$)
      read(unit=5, fmt=*) width
      write(unit=5, fmt=60)
      60 format(/4x,36h ENTER SCAN DIRECTION: (1=X,2=Y,3=Z),)$)
      read(unit=5, fmt=*) idir
      write(unit=5, fmt=70)
      70 format(/4x,31h TOTAL NUMBER OF SAMPLE POINTS:,$)
      read(unit=*, fmt=*) ipts
      write(unit=5, fmt=80)
      80 format(/4x,42h NUMBER OF SAMPLES AVGD PER POINT (<1000):,$)
      read(unit=*, fmt=*) ibuf
      write(unit=5, fmt=90)
      90 format(/4x,35h CENTER PROBE AT MINIMUM SCAN DEPTH)

```

```

c
# 47 "mwplan.for"
    pause '    PRESS <CR> TO BEGIN SCAN'
c
# 49 "mwplan.for"
    call lscan(idir, width, ipt, ibuf, plin)
# 51 "mwplan.for"
    write(unit=5, fmt=95)
    95 format(/4x,29h SAVE SCAN OR BEGIN NEW SCAN?,/,
    &26h(1=SAVE,2=NEW SCAN,3=QUIT),%)
    read(unit=*, fmt=*) iopt
    97 if (iopt - 2) 1000, 20, 2999
    100 continue
    write(unit=5, fmt=102)
    102 format(/4x,39h SCAN PLANE: 1=E(X-Y),2=H(X-Z),3=P(Y-Z),%)
    read(unit=*, fmt=*) iplan
c
c    P-PLANE (Y-Z) SCAN PARAMETERS
c
# 60 "mwplan.for"
    if (iplan - 2) 400, 500, 104
# 64 "mwplan.for"
    104 continue
    iax(1) = 2
    iax(2) = 3
    write(unit=5, fmt=105)
    105 format(/4x,28h P-PLANE ORIGIN: X,Y,Z (CM):,%)
    read(unit=5, fmt=*) xpos, ypos, zpos
    write(unit=5, fmt=110)
    110 format(/4x,21h WIDTH OF YSCAN (MM):,%)
c
# 72 "mwplan.for"
    read(unit=5, fmt=*) ywid
c
# 74 "mwplan.for"
    jwid = ywid
# 76 "mwplan.for"
    write(unit=5, fmt=120)
    120 format(/4x,21h WIDTH OF ZSCAN (MM):,%)
c
# 78 "mwplan.for"
    read(unit=5, fmt=*) zwid
# 80 "mwplan.for"
    dist = zwid / 2.
c
# 81 "mwplan.for"
    kwid = zwid
# 83 "mwplan.for"
    write(unit=5, fmt=130)
    130 format(/4x,30h TOTAL NUMBER OF YSCAN POINTS:,% )
    read(unit=*, fmt=*) jpts
    write(unit=5, fmt=140)
    140 format(/4x,30h TOTAL NUMBER OF ZSCAN POINTS:,% )
    read(unit=*, fmt=*) kpts
    145 continue
    write(unit=5, fmt=150)
    150 format(/4x,34h NUMBER OF SAMPLES AVGD PER POINT:,% )

```

```
c
# 92 "mwplan.for"
    read(unit=*, fmt=*) ibuf
c
# 94 "mwplan.for"
    itot = jpts * kpts
# 96 "mwplan.for"
    write(unit=5, fmt=160) itot
160 format(/4x,28h TOTAL POINTS IN SCAN PLANE:,i4)
    write(unit=5, fmt=170)
170 format(/4x,25h PUT PROBE AT SCAN CENTER)
c
c    MOVES MILLBASE TO INITIAL SCAN POSITION
c
# 100 "mwplan.for"
    pause '    PRESS <CR> TO BEGIN SCAN'
# 104 "mwplan.for"
    call bklsh(iax(2), - dist)
c
# 105 "mwplan.for"
    call bklsh(iax(1), - (jwid / 2.))
c
# 107 "mwplan.for"
    kinc = float(kwid / (kpts - 1))
c
c    PERFORMS 1D LINEAR SCAN
c
# 109 "mwplan.for"
    do 200 k = 1, kpts
c
c    STORES DATA POINTS IN ARRAY
c
# 113 "mwplan.for"
    call lscan(iax(1), jwid, jpts, ibuf, plin)
# 117 "mwplan.for"
    do 180 j = 1, jpts
        p2d(j,k) = plin(j)
c
# 119 "mwplan.for"
    180 continue
c
c    REVERSE DIRECTION AND RESUME SCAN
c
# 121 "mwplan.for"
    call bklsh(iax(2), kinc)
c
# 125 "mwplan.for"
    jwid = - jwid
c
c    RETURN TO SCAN CENTER
c
# 127 "mwplan.for"
    200 continue
```

```

c
# 131 "mwplan.for"
      ktot = (kwid - dist) + kinc
# 133 "mwplan.for"
      call bklsh(iax(2), - ktot)
c
# 134 "mwplan.for"
      call bklsh(iax(1), jwid / 2.)
# 136 "mwplan.for"
      write(unit=5, fmt=210)
210 format(/4x,34h SAVE SCAN DATA OR BEGIN NEW SCAN?,/,/4x,
      &27h (1=SAVE,2=NEW SCAN,3=QUIT),%)
      read(unit=*, fmt=*) iopt
c
# 140 "mwplan.for"
220 if (iopt - 2) 1000, 20, 2999
c
c E-PLANE (X-Y) SCAN PARAMETERS
c
# 142 "mwplan.for"
400 continue
# 146 "mwplan.for"
      iax(1) = 2
      iax(2) = 1
      write(unit=5, fmt=410)
410 format(/4x,28h E-PLANE ORIGIN: X,Y,Z (CM):,%)
      read(unit=5, fmt=*) xpos, ypos, zpos
      write(unit=5, fmt=420)
420 format(/4x,21h WIDTH OF YSCAN (MM):,%)
c
# 153 "mwplan.for"
      read(unit=5, fmt=*) ywid
c
# 155 "mwplan.for"
      jwid = ywid
# 157 "mwplan.for"
      write(unit=5, fmt=430)
430 format(/4x,21h WIDTH OF XSCAN (MM):,%)
c
# 159 "mwplan.for"
      read(unit=5, fmt=*) xwid
# 161 "mwplan.for"
      dist = 0.
c
# 162 "mwplan.for"
      kwid = xwid
# 164 "mwplan.for"
      write(unit=5, fmt=440)
440 format(/4x,30h TOTAL NUMBER OF YSCAN POINTS:,%$)
      read(unit=*, fmt=*) jpts
      write(unit=5, fmt=450)
450 format(/4x,30h TOTAL NUMBER OF XSCAN POINTS:,%$)
      read(unit=*, fmt=*) kpts
      goto 145

```

```

c
c H-PLANE (X-Z) SCAN PARAMETERS
c
# 171 "mwplan. for"
500 continue
# 175 "mwplan. for"
    iax(1) = 3
    iax(2) = 1
    write(unit=5, fmt=510)
510 format(/4x,28h H-PLANE ORIGIN: X,Y,Z (CM):,$)
    read(unit=5, fmt=*) xpos, ypos, zpos
    write(unit=5, fmt=520)
520 format(/4x,21h WIDTH OF ZSCAN (MM):,$)
c
# 182 "mwplan. for"
    read(unit=5, fmt=*) zwid
c
# 184 "mwplan. for"
    jwid = zwid
# 186 "mwplan. for"
    write(unit=5, fmt=530)
530 format(/4x,21h WIDTH OF XSCAN (MM):,$)
c
# 188 "mwplan. for"
    read(unit=5, fmt=*) xwid
# 190 "mwplan. for"
    dist = 0.
c
# 191 "mwplan. for"
    kwid = xwid
# 193 "mwplan. for"
    write(unit=5, fmt=540)
540 format(/4x,31h TOTAL NUMBER OF ZSCAN POINTS:,$)
    read(unit=*, fmt=*) jpts
    write(unit=5, fmt=550)
550 format(/4x,31h TOTAL NUMBER OF XSCAN POINTS:,$)
    read(unit=*, fmt=*) kpts
c
# 199 "mwplan. for"
    goto 145
c
c SAVE MEASUREMENT DATA TO DISKETTE
c
# 201 "mwplan. for"
1000 continue
# 205 "mwplan. for"
    write(unit=5, fmt=1100)
1100 format(43h ENTER DISKETTE FILENAME (EX: .DU1:FILE.DAT),/,
    &50h AN EXISTING FILE BY THE SAME NAME WILL BE ERASED.)
    read(unit=5, fmt=1200) (ifile(i),i = 1, 7)
1200 format(7a2)
    open(unit=4, file=v0000000000000002, status=
    &'UNKNOWN', err=1210)

```

```

# 211 "mwplan. for"
      goto 1300
1210 write(unit=5, fmt=1250)
1250 format(21h UNABLE TO OPEN FILE. ,/,
      &68h ENTER 1 TO TRY
      & END: , $)
# 215 "mwplan. for"
      read(unit=5, fmt=*) idisk
      if (idisk - 1) 2999, 1000, 2999
1300 continue
      if (isctp - 2) 2000, 1320, 2000
1320 continue
      write(unit=4, fmt=1350) xpos, ypos, zpos
      write(unit=5, fmt=1350) xpos, ypos, zpos
1350 format(3(2x, f8.4))
      write(unit=4, fmt=1380) jpts, kpts, jwid, kwid
      write(unit=5, fmt=1380) jpts, kpts, jwid, kwid
1380 format(2(2x, i2), 2(f8.4))
      do 1450 k = 1, kpts
      do 1400 j = 1, jpts
      write(unit=4, fmt=1500) p2d(j, k)
1400 continue
1450 continue
1500 format(f8.4)
      close(unit=4, err=3000)
      write(unit=5, fmt=1600)
1600 format(/4x, 20h (1=NEW SCAN, 2=QUIT), $)
      read(unit=5, fmt=*) iopt
      if (iopt - 2) 20, 2999, 2999
2000 continue
      write(unit=4, fmt=2050) xpos, ypos, zpos
      write(unit=5, fmt=2050) xpos, ypos, zpos
2050 format(3(f8.4, 2x))
      write(unit=4, fmt=2100) ipt, width
      write(unit=5, fmt=2100) ipt, width
2100 format(2x, i2, 2x, f8.4)
      do 2200 j = 1, ipt
      write(unit=4, fmt=2250) plin(j)
2200 continue
2250 format(f8.4)
      close(unit=4, err=3000)
      write(unit=5, fmt=2300)
2300 format(/4x, 20h (1=NEW SCAN, 2=QUIT), $)
      read(unit=*, fmt=*) iopt
      if (iopt - 2) 20, 2999, 2999
2999 continue
      stop
3000 stop ' PROBLEM CLOSING FILE. NO FILE SAVED. '
c
# 256 "mwplan. for"
      end

```

```

c
c      THIS ROUTINE PERFORMS A LINEAR SCAN IN THE 1=X,
c      2=Y OR 3=Z DIRECTION (IDIR) OVER A DISTANCE (WIDTH)
c      IN MM FOR A TOTAL NUMBER OF MEASUREMENT POINTS (IPTS)
c      AVERAGED AT EACH POSITION BY (IBUF) SAMPLES. THE
c      MEASUREMENT DATA IS STORED IN THE ARRAY PLIN(50).
c
c      subroutine lscan(idir, width, ipts, ibuf, plin)
c      integer*2 adbuf(4096), iadch, igain, idir, ipts, ibuf
c
c      INITIALIZES TO BEGIN A SCAN:
c
c      ICHAN      ADDRESS OF D/A FOR OUTPUT PULSE
c
c      IGAIN      GAIN SET PARAMETER
c
c      IADCH      A/D CHANNEL
c
c      IADCSR     CODE FOR GAIN/CHANNEL/SINGLE SAMPLE
c
c      real dist, wait, width, dinc, plin(50)
# 279 "mwplan.for"
c      ichan = 65000
c      igain = 3
c      iadch = 0
c      iadcsr = ((8 * igain) + 256) + 3
c
c      MOVES PROBE TO INITIAL POSITION OF SCAN
c
c      DIST=WIDTH/2.
c      CALL BKLSH(IDIR, -DIST)
c
c      CALCULATES SCAN INCREMENT (DINC)
c
# 283 "mwplan.for"
c      init = 1
c
c      ***MAIN LOOP***
c
# 292 "mwplan.for"
c      dinc = float(width / (ipts - 1))
c
c      SENDS OUTPUT PULSE TO TURN ON POWER SOURCE
c
# 296 "mwplan.for"
c      do 200 j = 1, ipts
# 300 "mwplan.for"
c      call ipoke(ichan, 2048)
c
c      SAMPLES MICROWAVE POWER (VOLTS)
c
# 301 "mwplan.for"
c      store = 0

```

```
c
c TURNS OFF POWER SOURCE
c
# 305 "mwplan.for"
      call atd2(adbuf, igain, iadch)
c
c IGNORES INITIAL 5 SAMPLES (SKIP TRANSIENT)
c AND SUMS THE REST (STORE)
c
# 309 "mwplan.for"
      call ipoke(ichan, 0)
# 314 "mwplan.for"
      do 50 i = 5, ibuf
        store = store + adbuf(i)
c
c AVERAGES THE "STEADY STATE" VALUES
c
# 316 "mwplan.for"
      50 continue
c
c CONVERTS BIT EQUIVALENT TO VOLTS (VAL)
c
# 320 "mwplan.for"
      temp = store / (ibuf - 5)
c
c STORES VALUE IN ARRAY
c
# 324 "mwplan.for"
      val = (10 * temp) / 4096
c
c CONVERTS BIT EQUIVALENT TO INTEGER
c
# 328 "mwplan.for"
      plin(j) = val
c
c PRINTS POSITION AND MEASUREMENT DATA ON SCREEN
c
# 332 "mwplan.for"
      itemp = ifix(temp)
# 336 "mwplan.for"
      call readms
      write(unit=5, fmt=90) i
      90 format(1x, 3hIY=, a2)
      write(unit=5, fmt=100) x, y, z
      100 format(1x, 12hPOSITION: X=, f8. 4, 4h   Y=, f8. 4, 4h   Z=, f8. 4)
      write(unit=5, fmt=150) itempo, val
```

```
c
c MOVES PROBE TO NEXT SCAN POINT
c
# 342 "mwplan.for"
150 format(10x,5hBITS=,i8,10h      VOLTS=,f8.3)
# 346 "mwplan.for"
      call bk1sh(idir, dinc)
c
c SUBTRACTS LAST INCREMENT
c
# 347 "mwplan.for"
200 continue
c
c MOVES MILLBASE TO ZERO
c
cC      DTOT = DIST + DINC
c
cC      CALL BKLSH(IDIR,-DTOT)
c
# 351 "mwplan.for"
      call bk1sh(idir, - dinc)
# 359 "mwplan.for"
      return
      end
```

APPENDIX C
SUPPLEMENTARY SIMULATED
MICROWAVE POWER PATTERNS

This appendix contains the electric field component power contours calculated by ARRPAT2 in a lossy homogeneous (water) medium. The scans are made in perpendicular (E,H) and parallel (P) planes at typical therapeutic depths with respect to the rectangular (2.5 x 3.4 cm) microstrip patch source in the $z=0$ plane at 915 MHz. The 0 dB reference value is indicated with respect to the peak power at $z=1.0$ cm. Size and feed position of the patch is also illustrated.

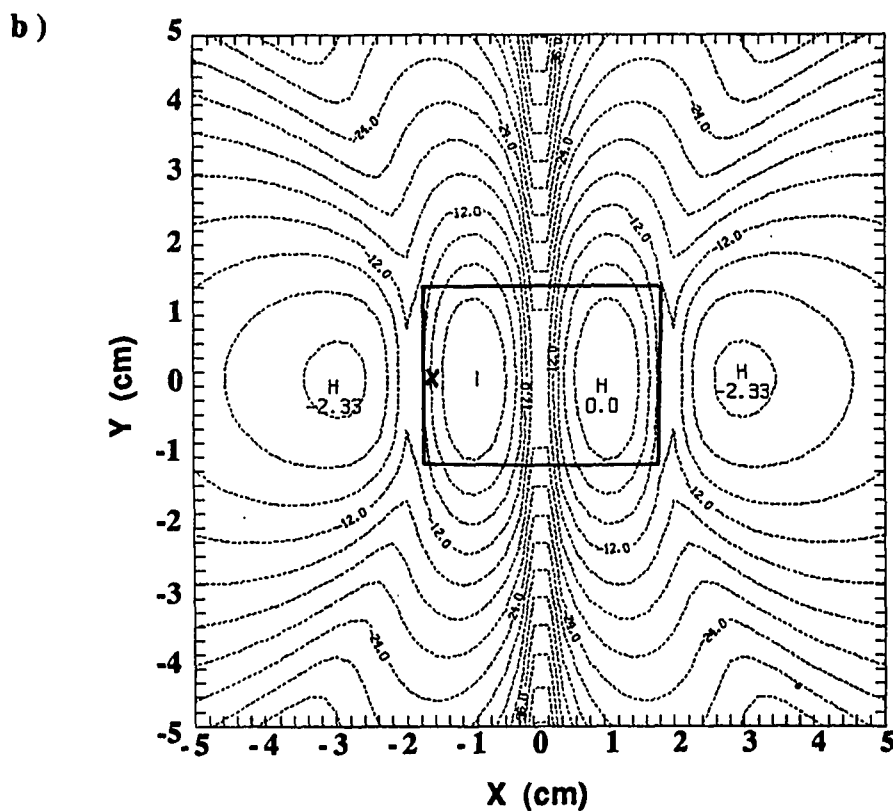
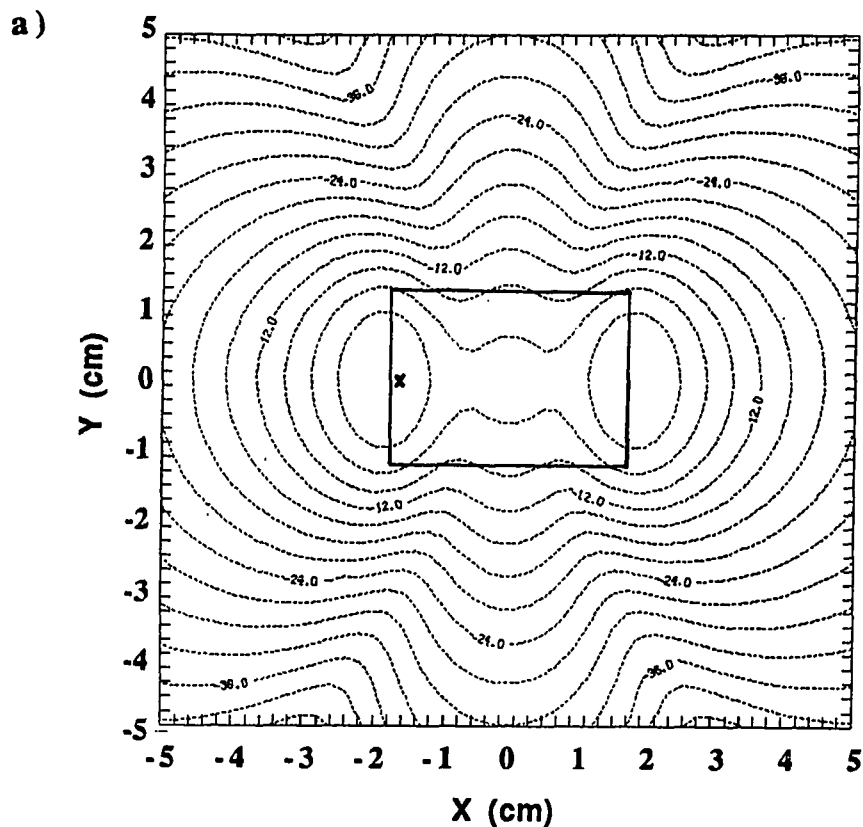


Figure C.1. Relative power (dB) contours predicted by SC model in the $z=1.0$ cm plane a) transverse component: $P_x \sim |E_x|^2$ ($P_{xp} = -7.1$ dB), b) normal component: $P_z \sim |E_z|^2$ ($P_{zp} = -9.2$ dB).

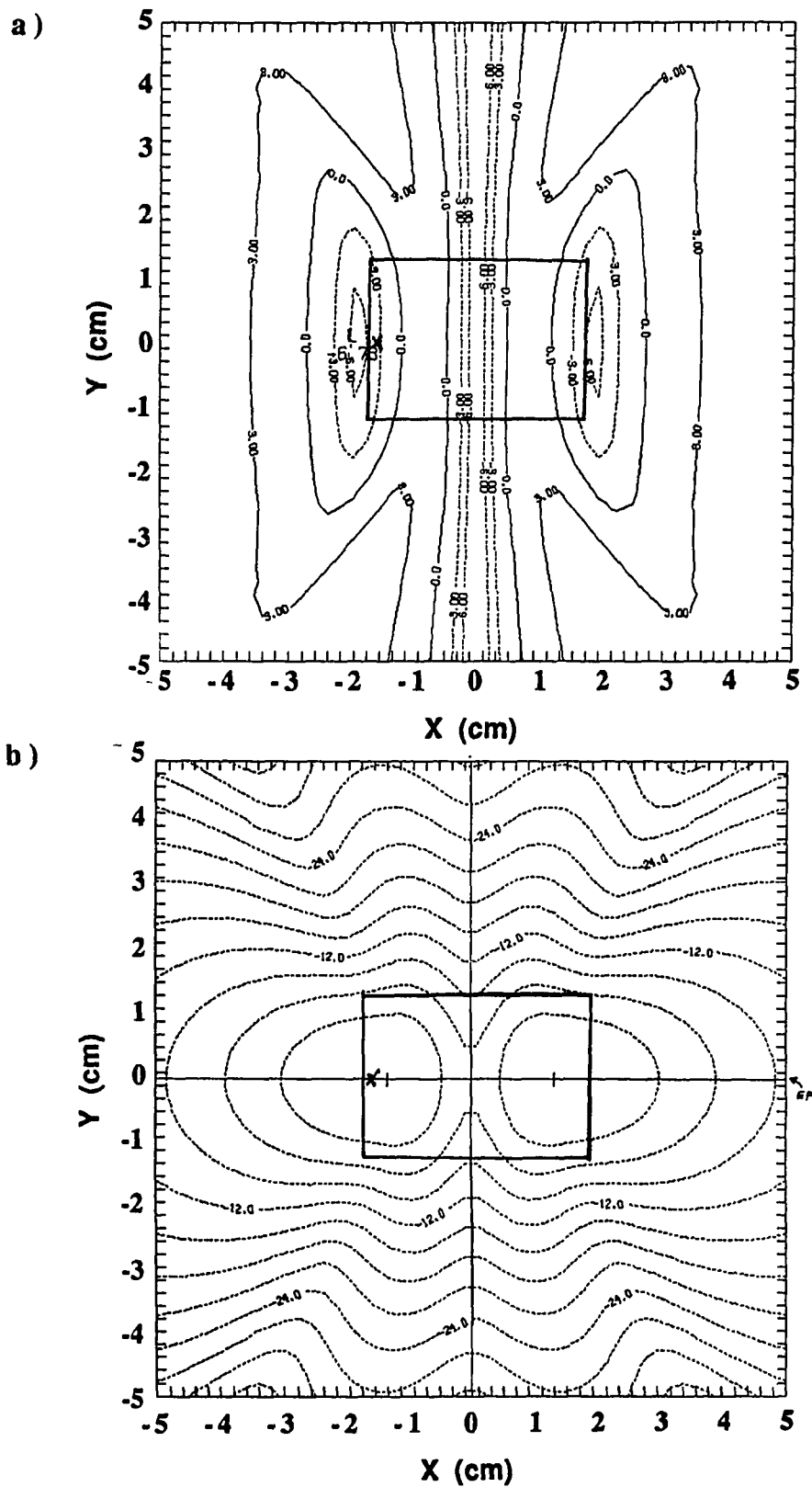


Figure C.2. Relative power (dB) contours predicted by SC model in the $z=1.0$ cm plane a) normal-to-transverse ratio: $R_{zx}=10\log(|E_z|/|E_x|)$, b) total E field: $P_T=|E|^2=(|E_x|^2+|E_z|^2)$.

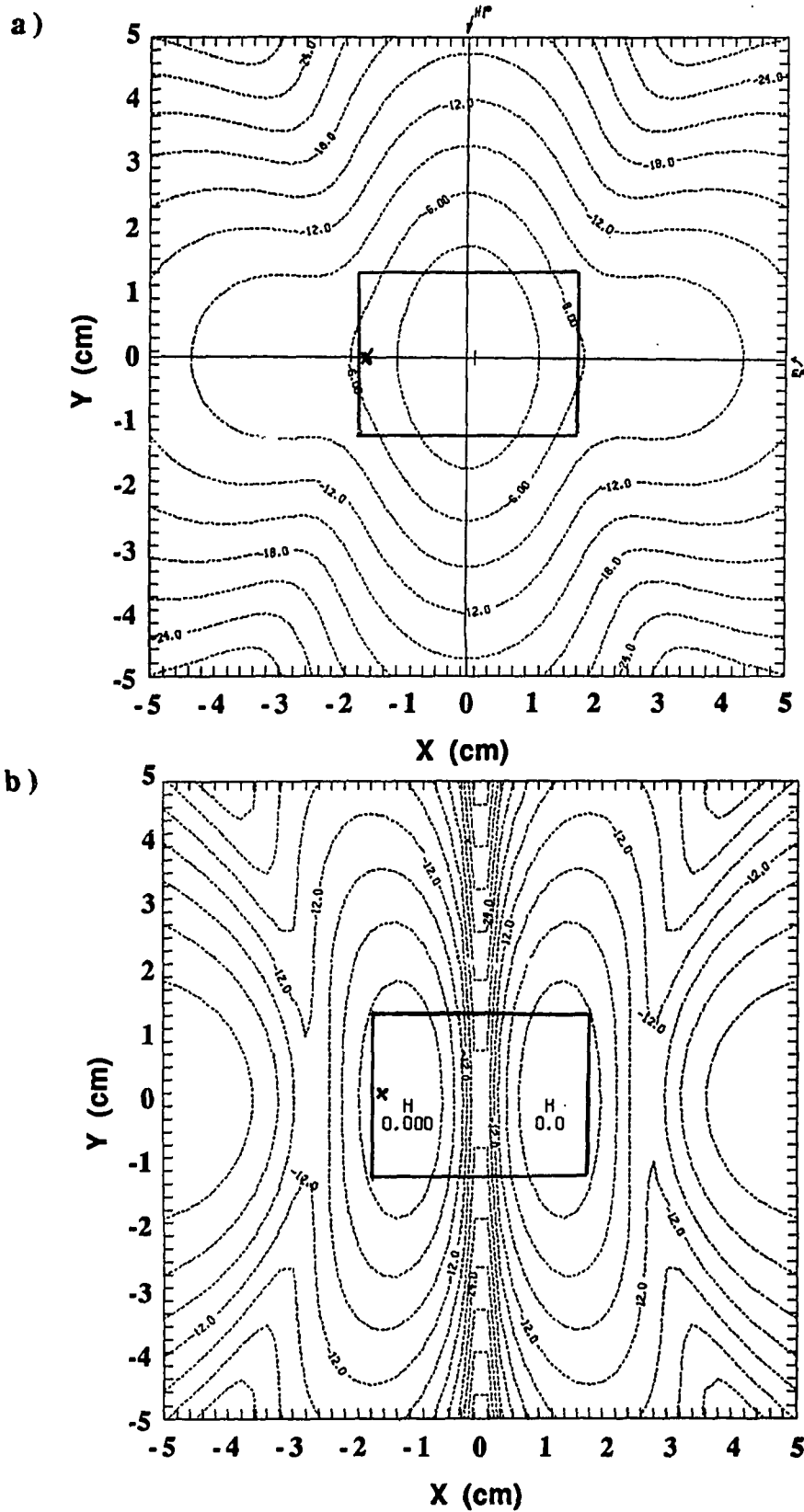


Figure C.3. Relative power (dB) contours predicted by SC model in the $z=3.0$ cm plane a) transverse component: $P_x \sim |E_x|^2$ ($P_{xp}=-13.6$ dB), b) normal component: $P_z \sim |E_z|^2$ ($P_{zp}=-22.8$ dB).

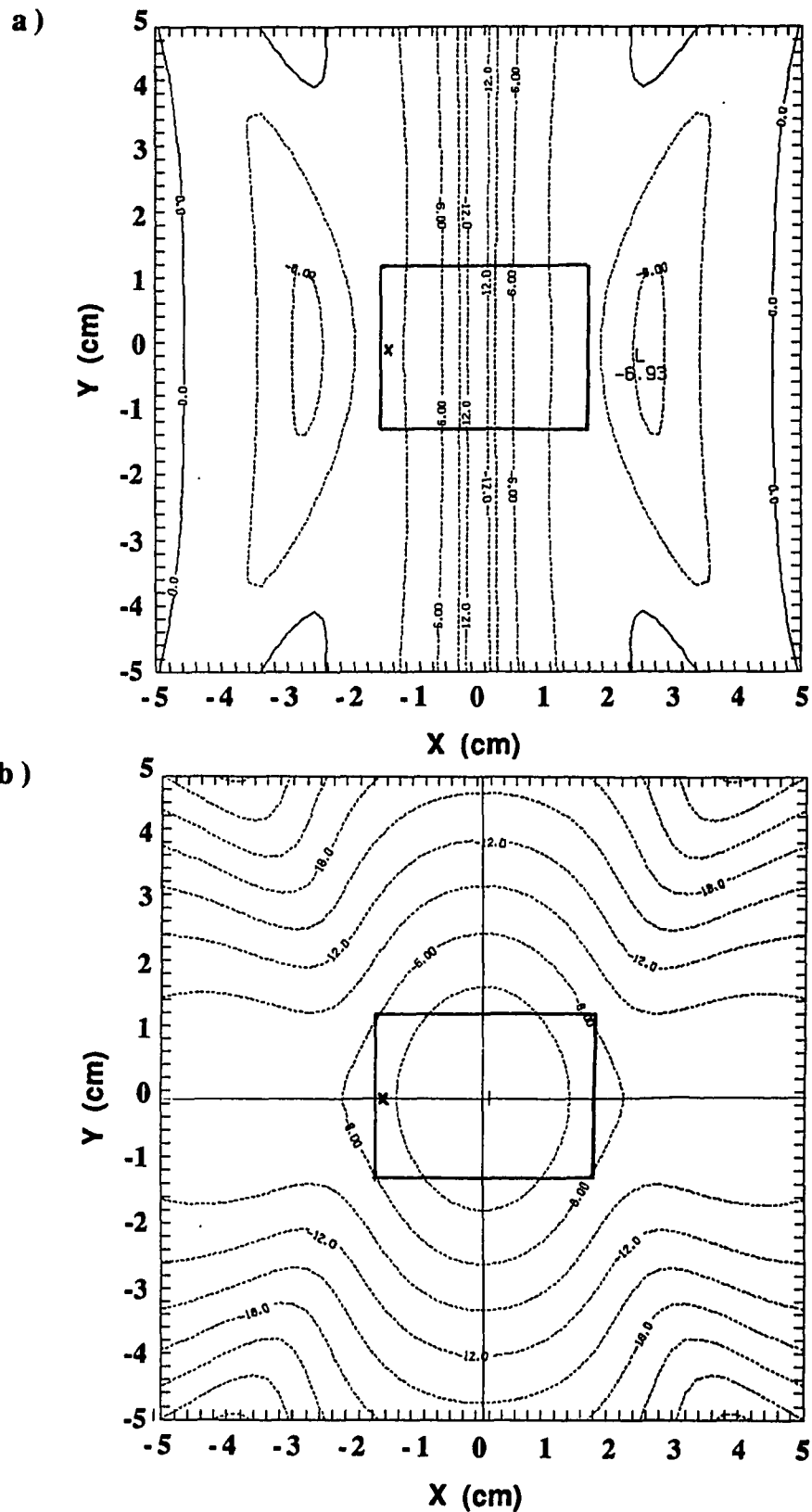


Figure C.4. Relative power (dB) contours predicted by SC model in the $z=3.0$ cm plane a) normal-to-transverse ratio: $R_{zx}=10\log(|E_z|/|E_x|)$, b) total E field: $P_T \sim |E|^2=(|E_x|^2+|E_z|^2)$.

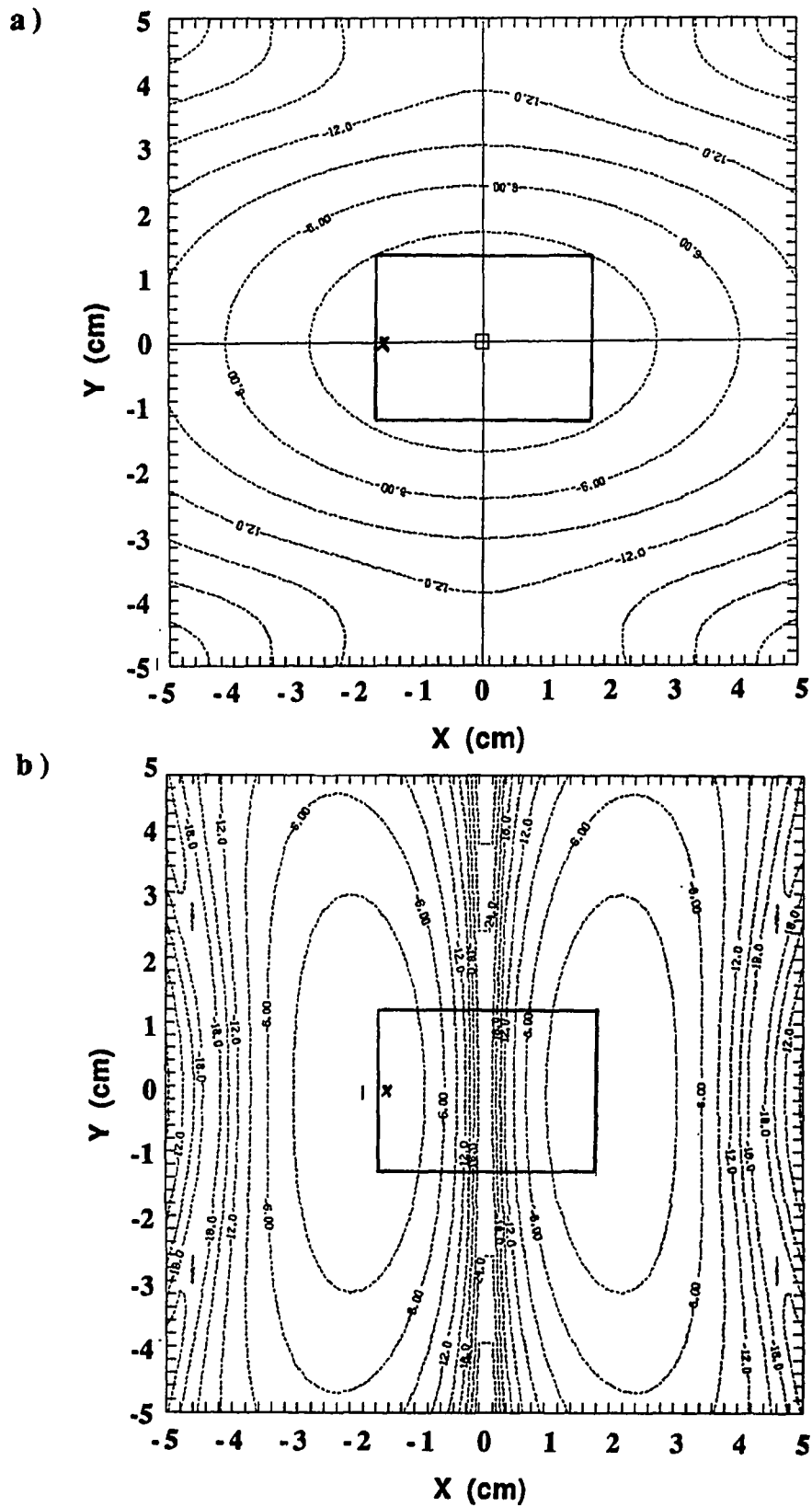


Figure C.5. Relative power (dB) contours predicted by SC model in the $z=6.0$ cm plane a) transverse component: $P_x \sim |E_x|^2$ ($P_{xp}=-20.8$ dB), b) normal component: $P_z \sim |E_z|^2$ ($P_{zp}=-34.1$ dB).

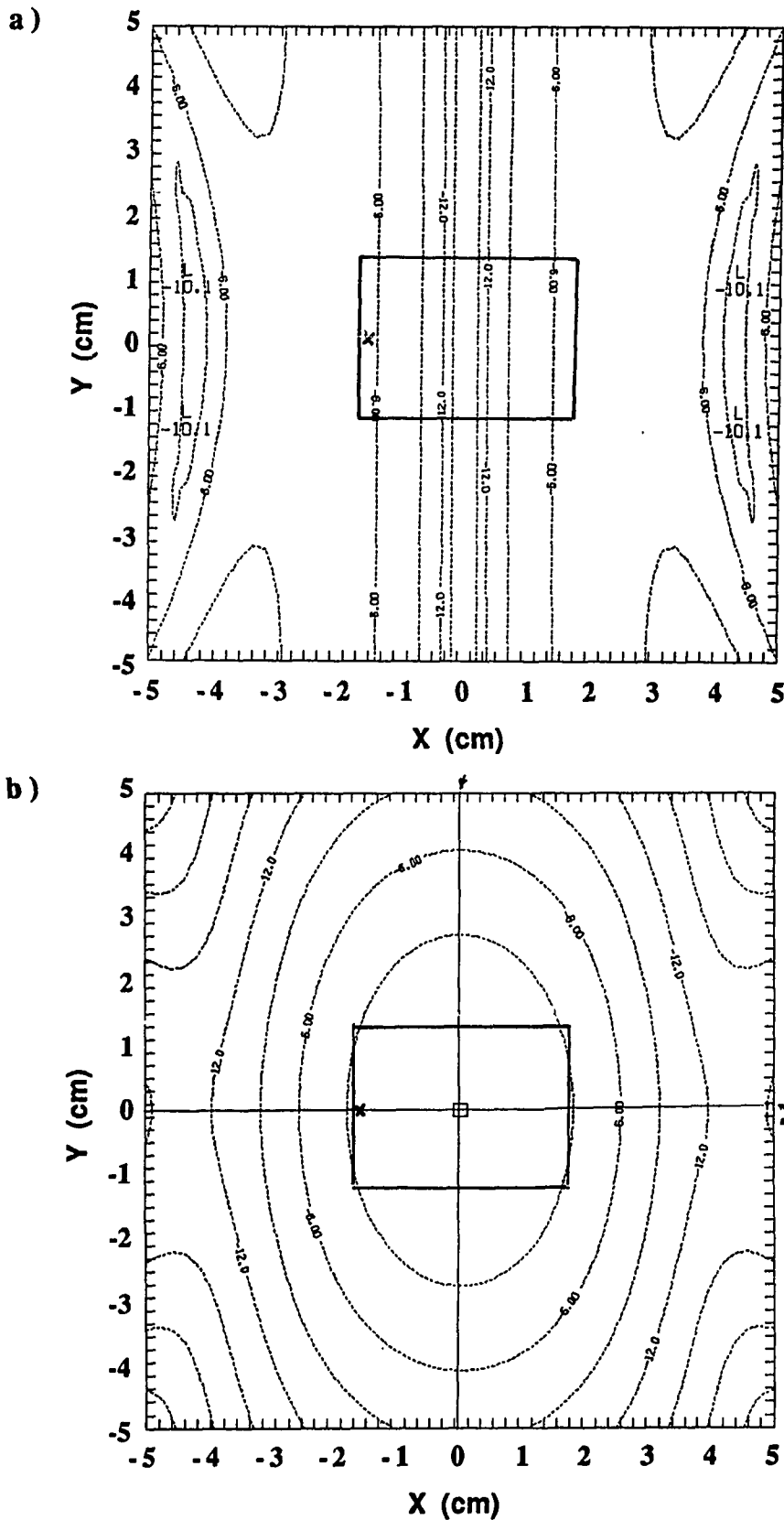


Figure C.6. Relative power (dB) contours predicted by SC model in the $z=6.0$ cm plane a) normal to transverse ratio: $R_{ZX}=10\log(|E_z|/|E_x|)$, b) total E field: $P_T \sim |E|^2 = (|E_x|^2 + |E_z|^2)$.

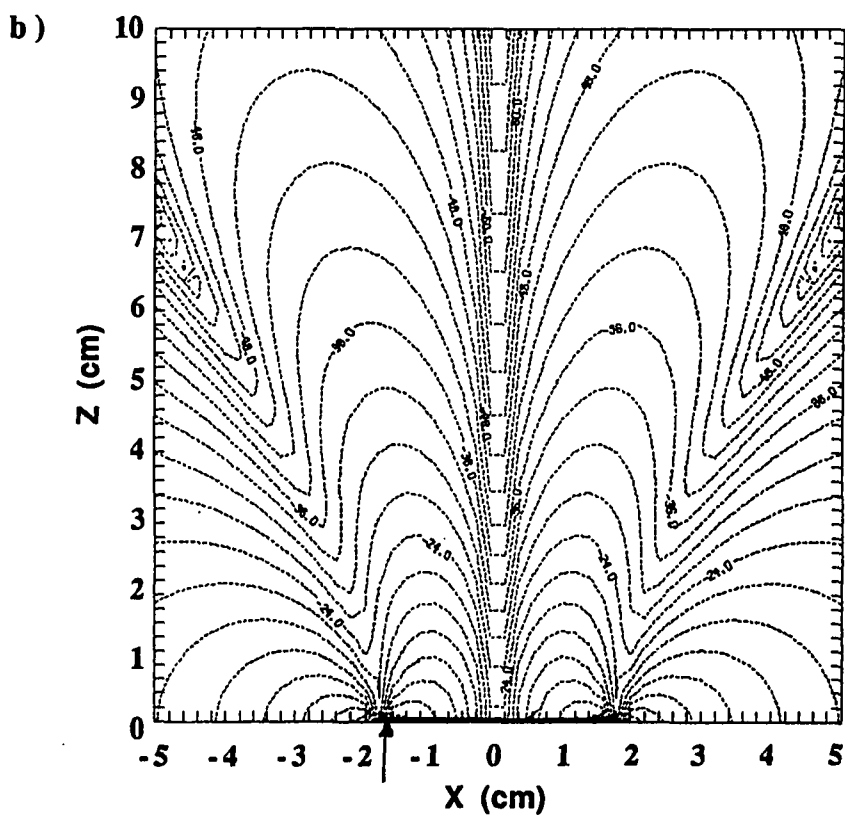
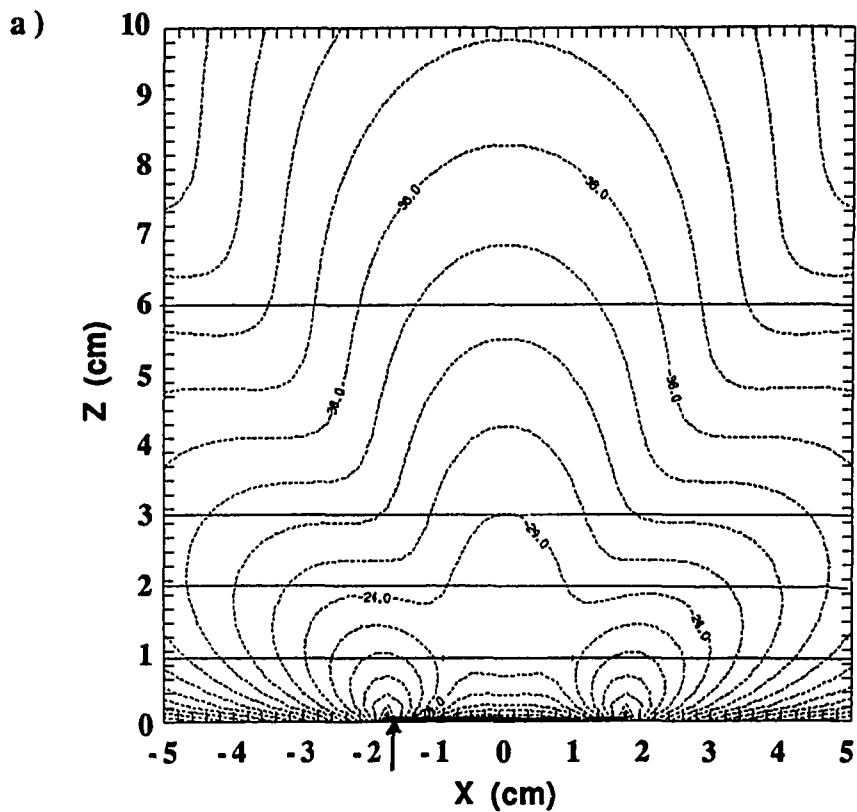


Figure C.7. Relative power (dB) contours predicted by SC model in the E-plane ($y=W/2$) a) transverse component: $P_x \sim |E_x|^2$ ($P_{xp}=+10.3\text{dB}$), b) normal component: $P_z \sim |E_z|^2$ ($P_{zp}=+2.6\text{dB}$).

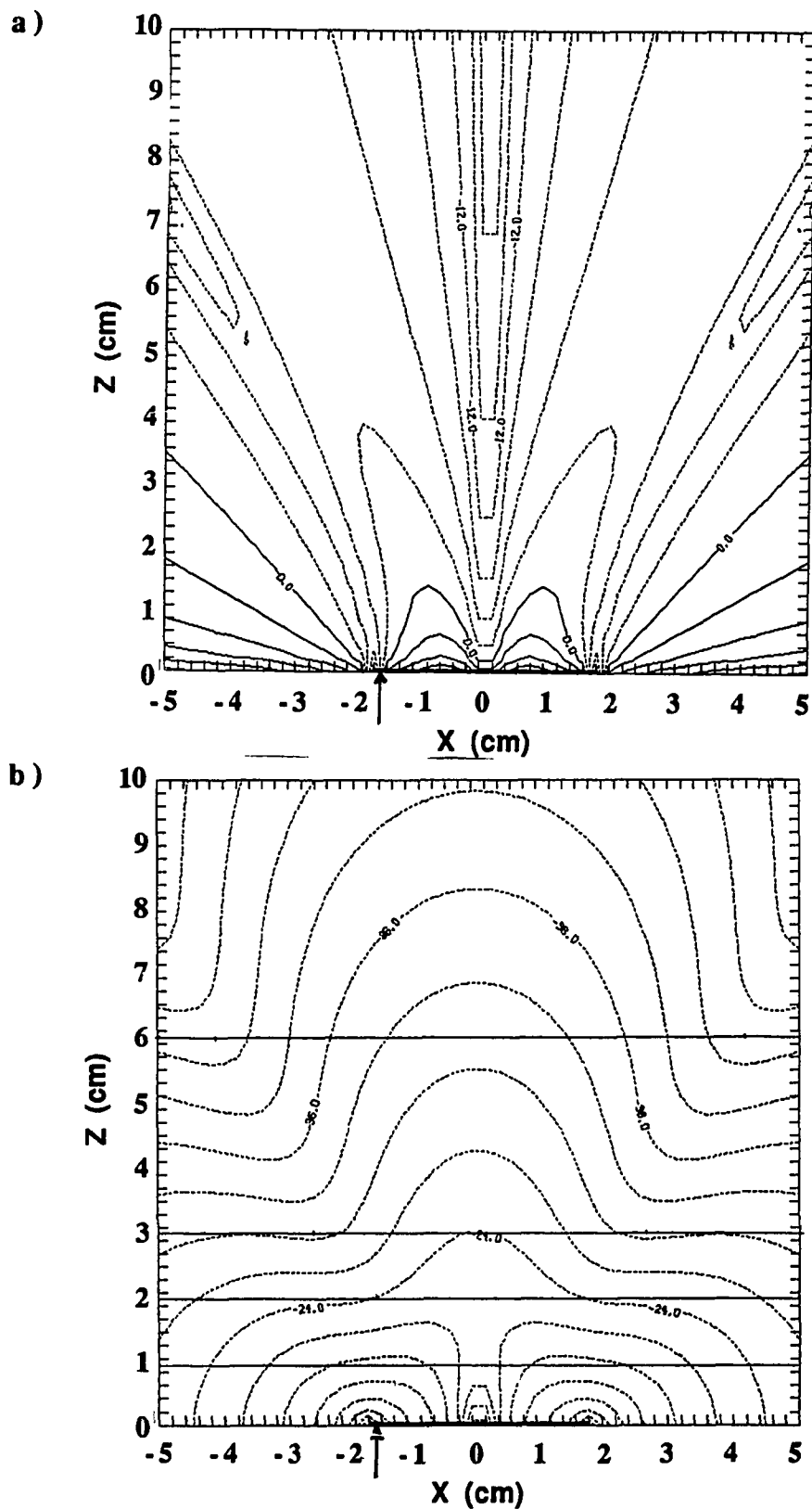


Figure C.8. Relative power (dB) contours predicted by SC model in the E-plane ($y=W/2$) a) normal-to-transverse ratio: $R_{ZX} = 10 \log(|E_z|/|E_x|)$, b) total E field: $P_T \sim |E|^2 = (|E_x|^2 + |E_z|^2)$.

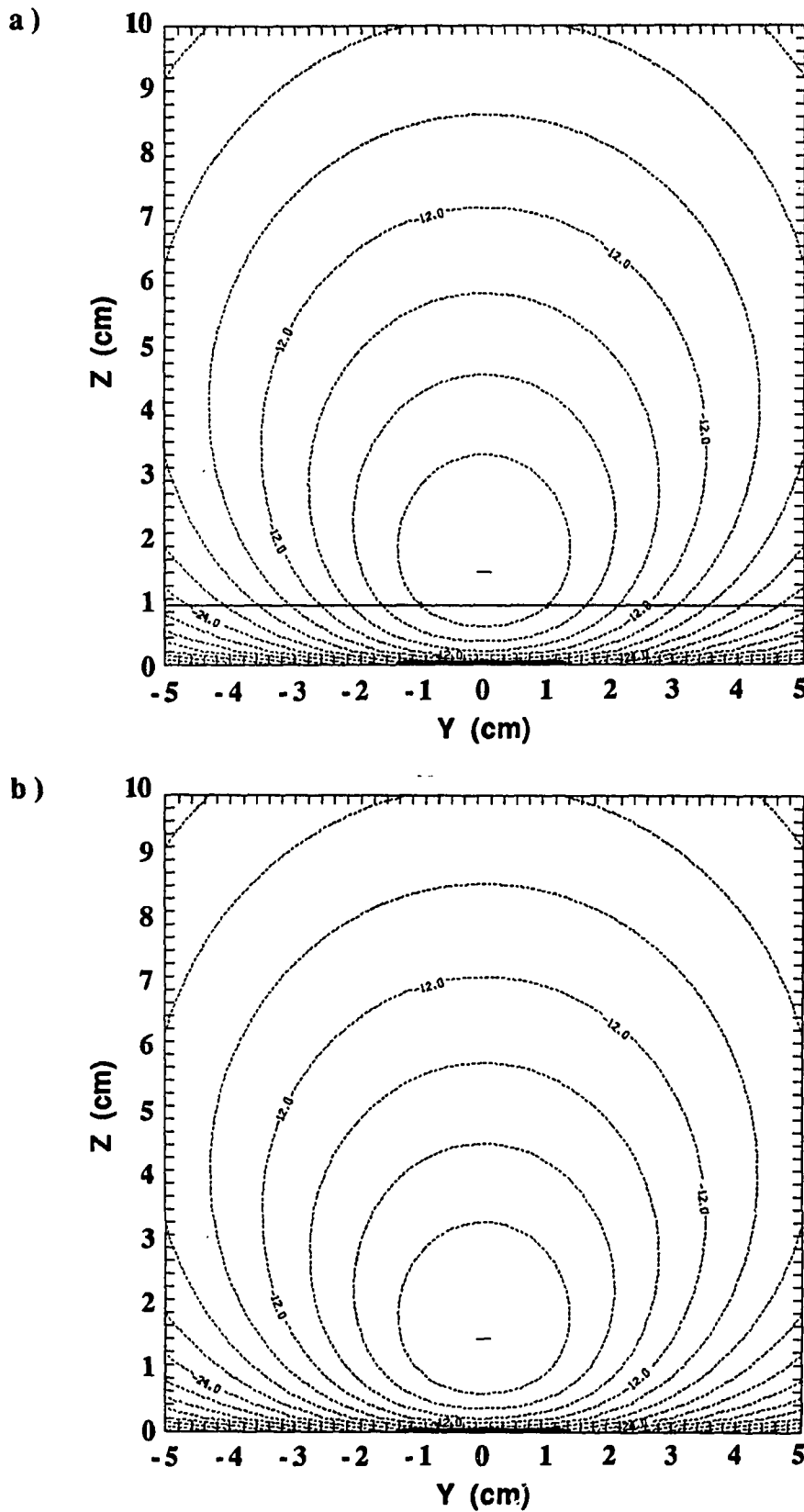


Figure C.9. Relative power (dB) contours predicted by SC model in the H-plane ($x=L/2$) a) transverse component: $P_x \sim |E_x|^2$ ($P_{xp} = -11.3$ dB), b) total E field: $P_T \sim |E|^2$.

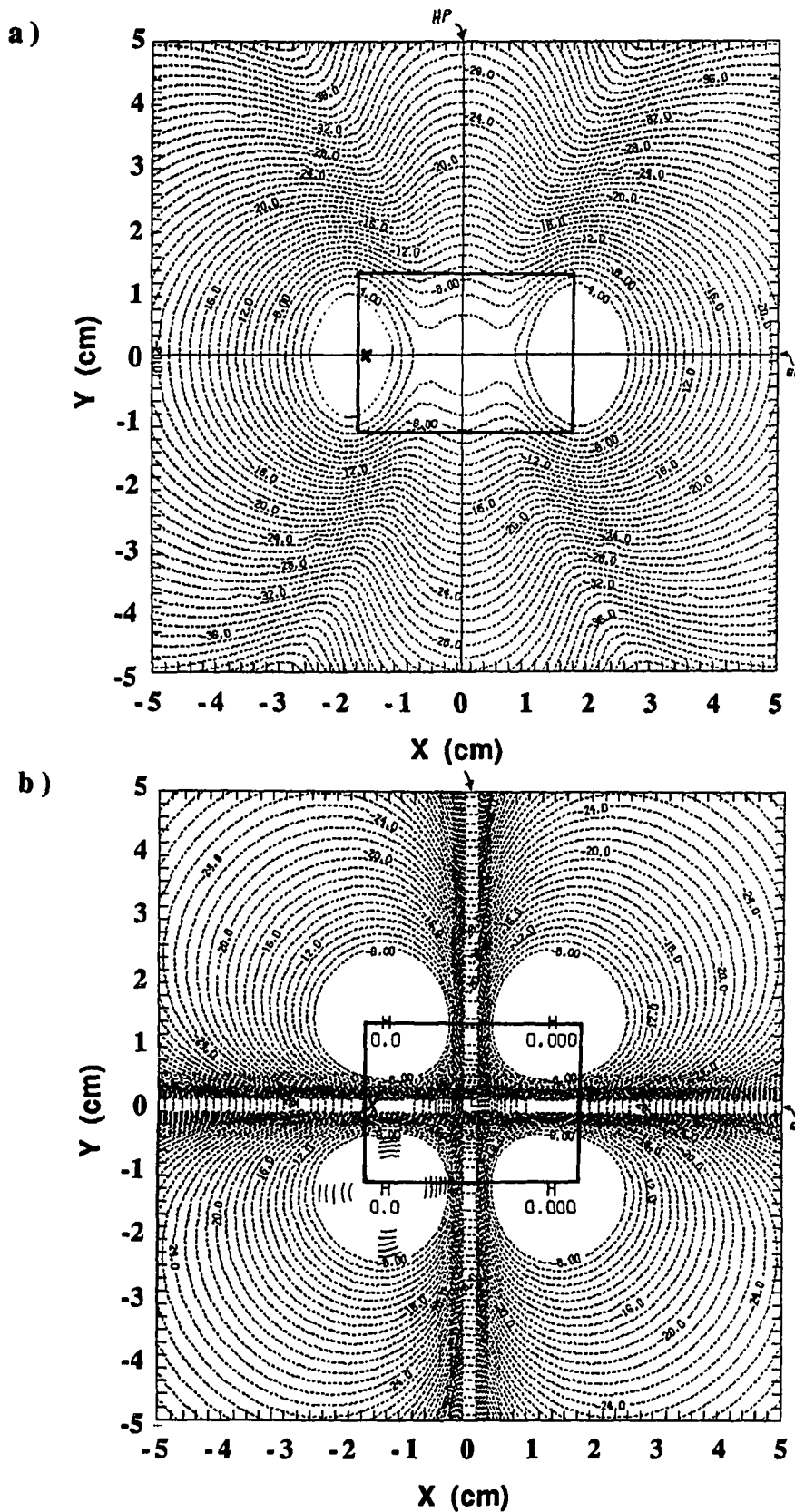


Figure C.10. Relative power (dB) contours predicted by CC model in the $z=1.0$ cm plane a) primary transverse (T1): $P_x \sim |E_x|^2$ ($P_{xp} = -7.1$ dB), b) secondary transverse (T2): $P_y \sim |E_y|^2$ ($P_{yp} = -9.2$ dB) components.

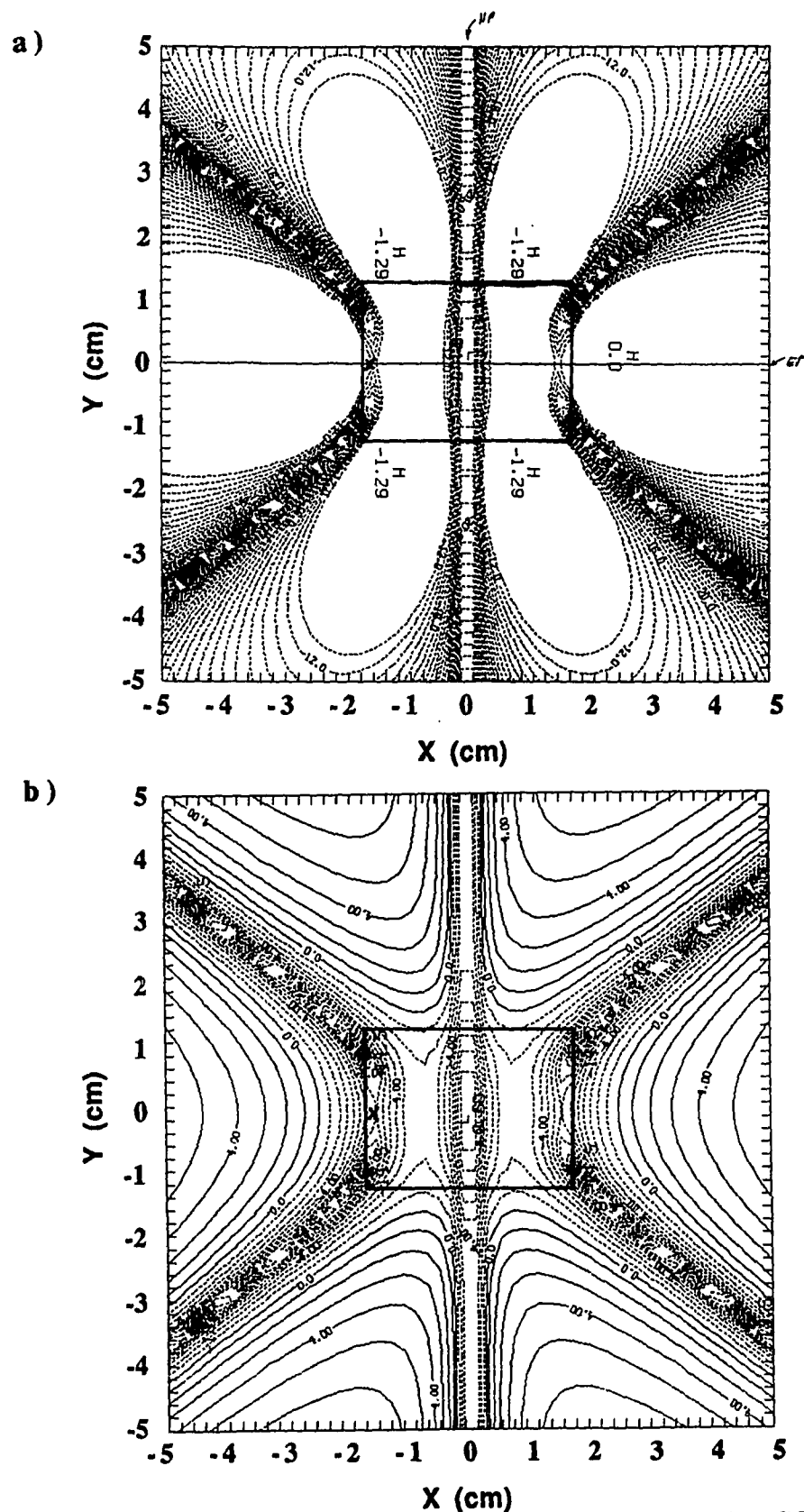


Figure C.11. Relative power (dB) contours predicted by CC model in the $z=1.0$ cm plane a) normal component: $P_z \sim |E_z|^2$ ($P_{zp} = -9.8$ dB),
 b) normal-to-transverse ratio: $R_{zt} = 10 \log(|E_z|/|E_t|)$.

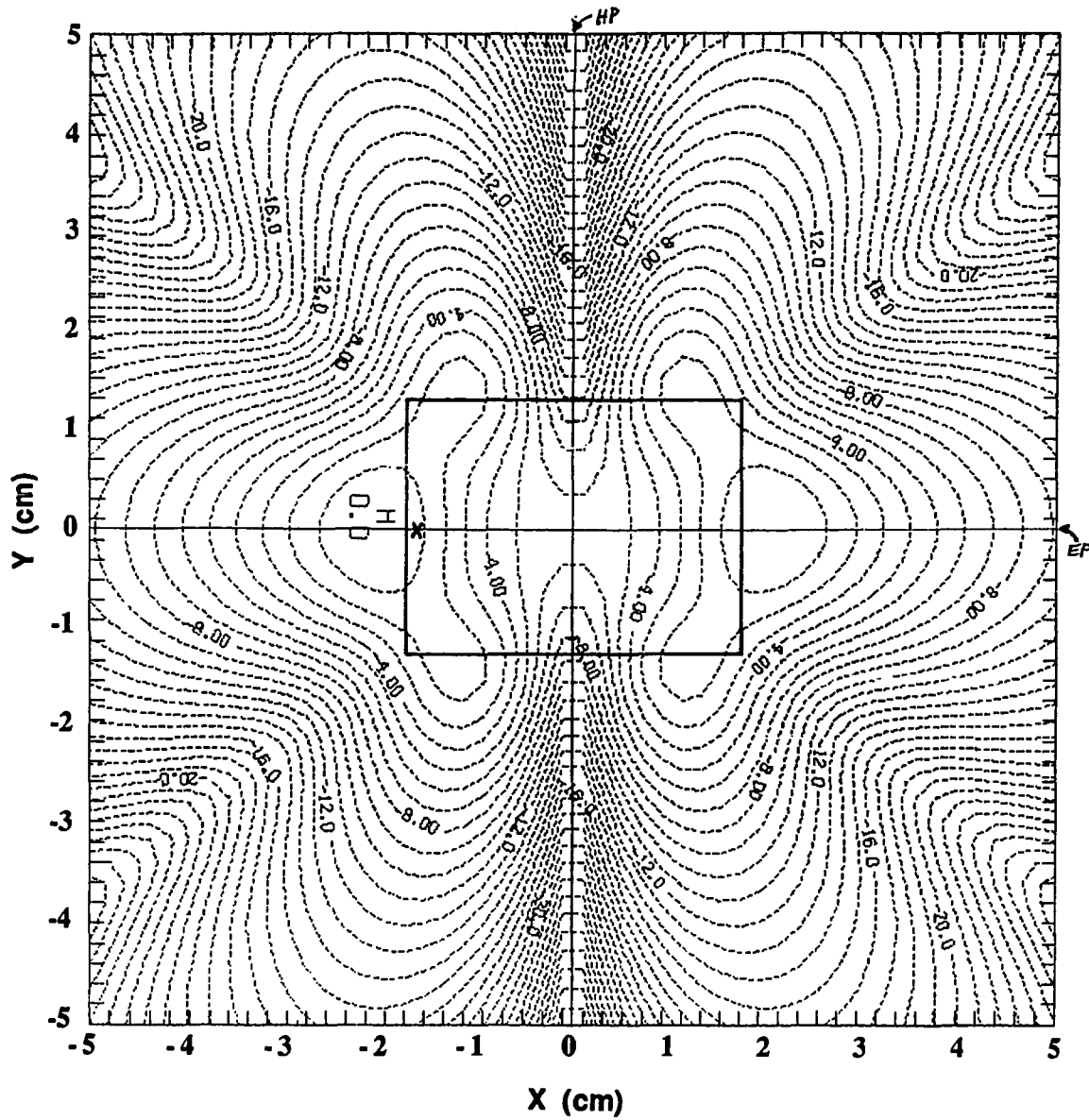


Figure C.12. Relative power (dB) contours predicted by CC model in the $z=1.0$ cm plane-total E field: $P_T \sim |E|^2 = (|E_x|^2 + |E_y|^2 + |E_z|^2)$.

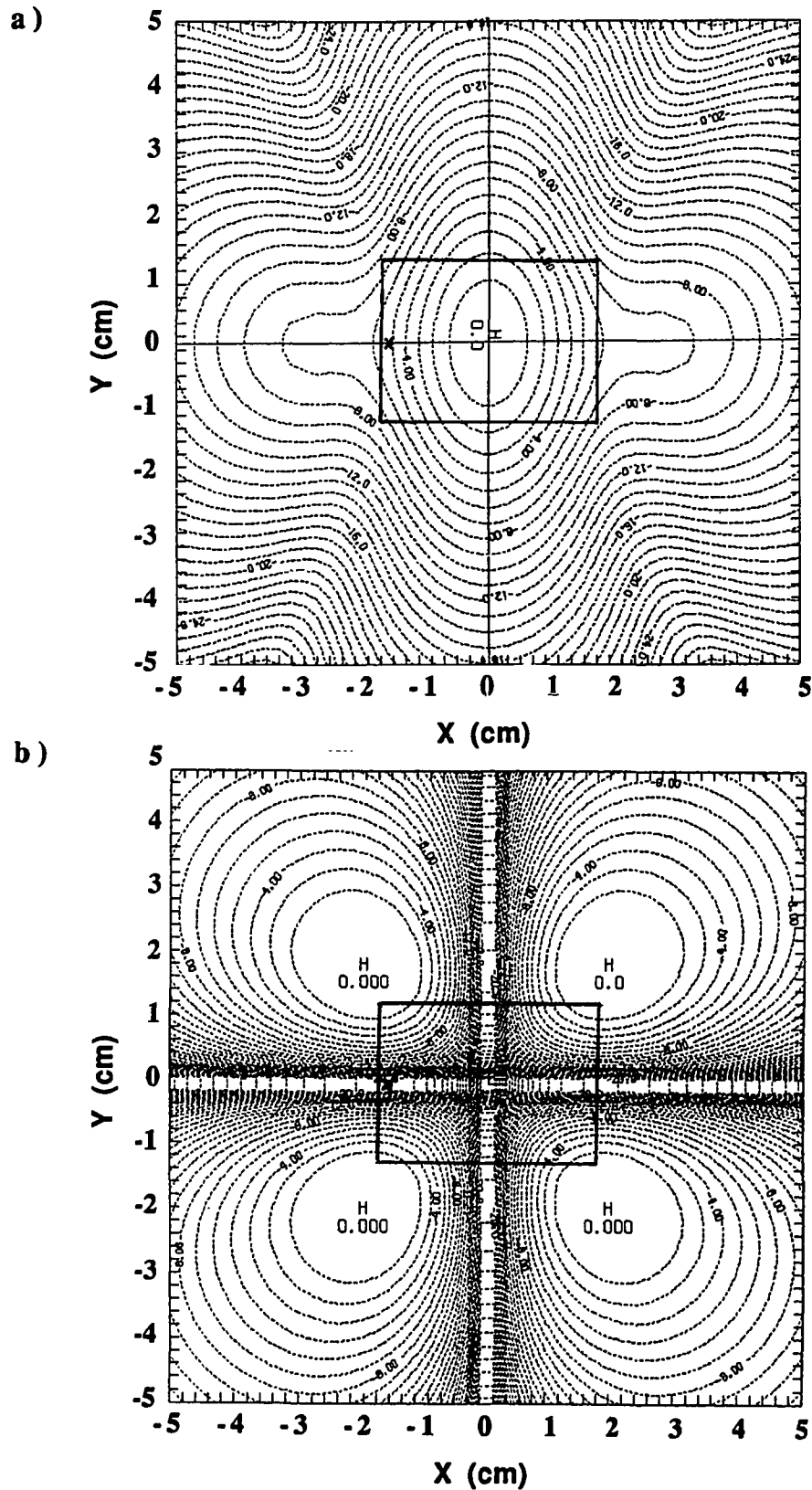


Figure C.13. Relative power (dB) contours predicted by CC model in the $z=3.0$ cm plane a) primary transverse (T1): $P_x \sim |E_x|^2$ ($P_{xp}=-13.6$ dB), b) secondary transverse (T2): $P_y \sim |E_y|^2$ ($P_{yp}=-22.2$ dB) components.

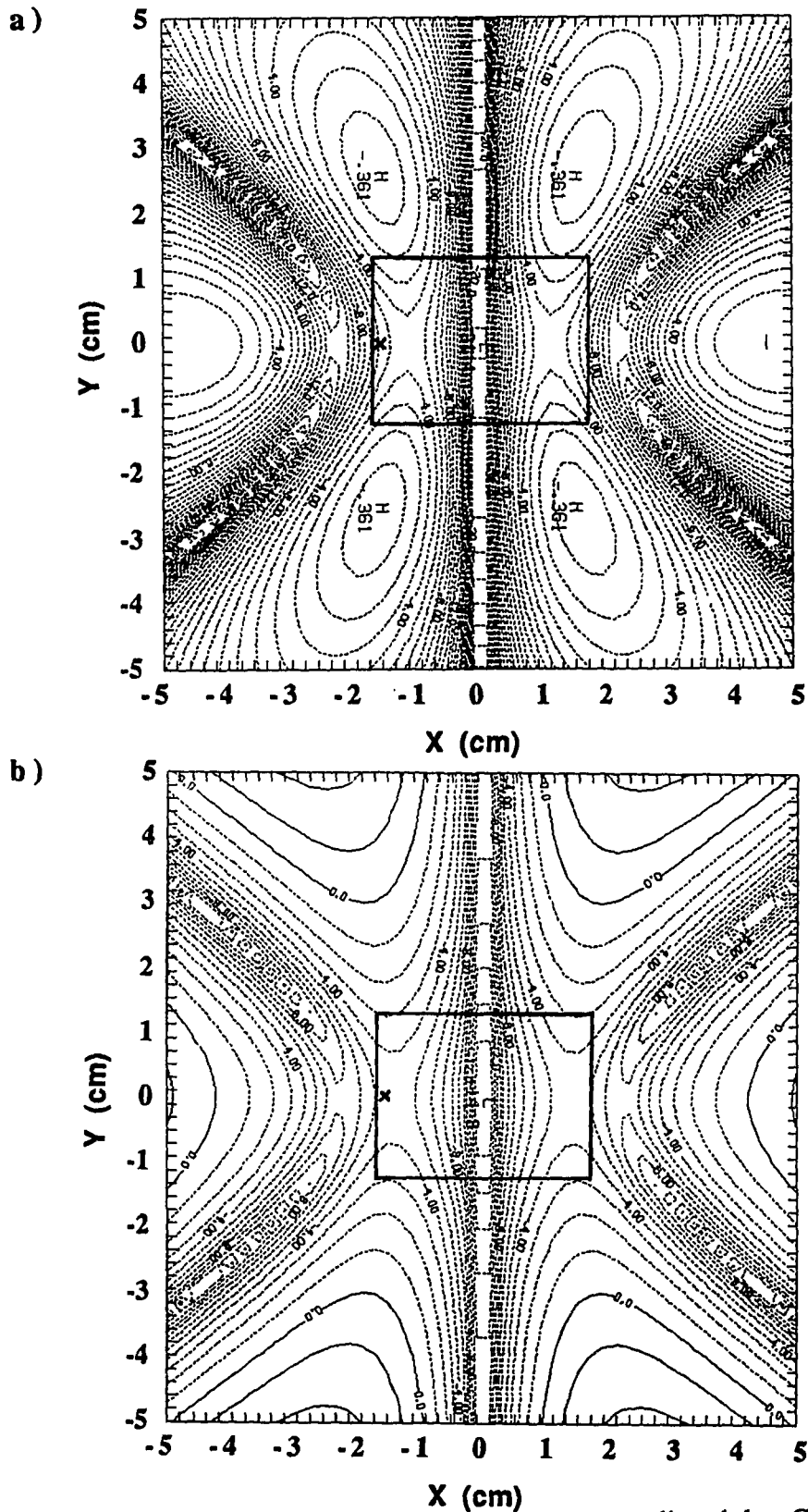


Figure C.14. Relative power (dB) contours predicted by CC model in the $z=3.0$ cm plane a) normal component: $P_z \sim |E_z|^2$ ($P_{zp} = -9.8$ dB),
 b) normal-to-transverse ratio: $R_{zt} = 10 \log(|E_z|/|E_t|)$.

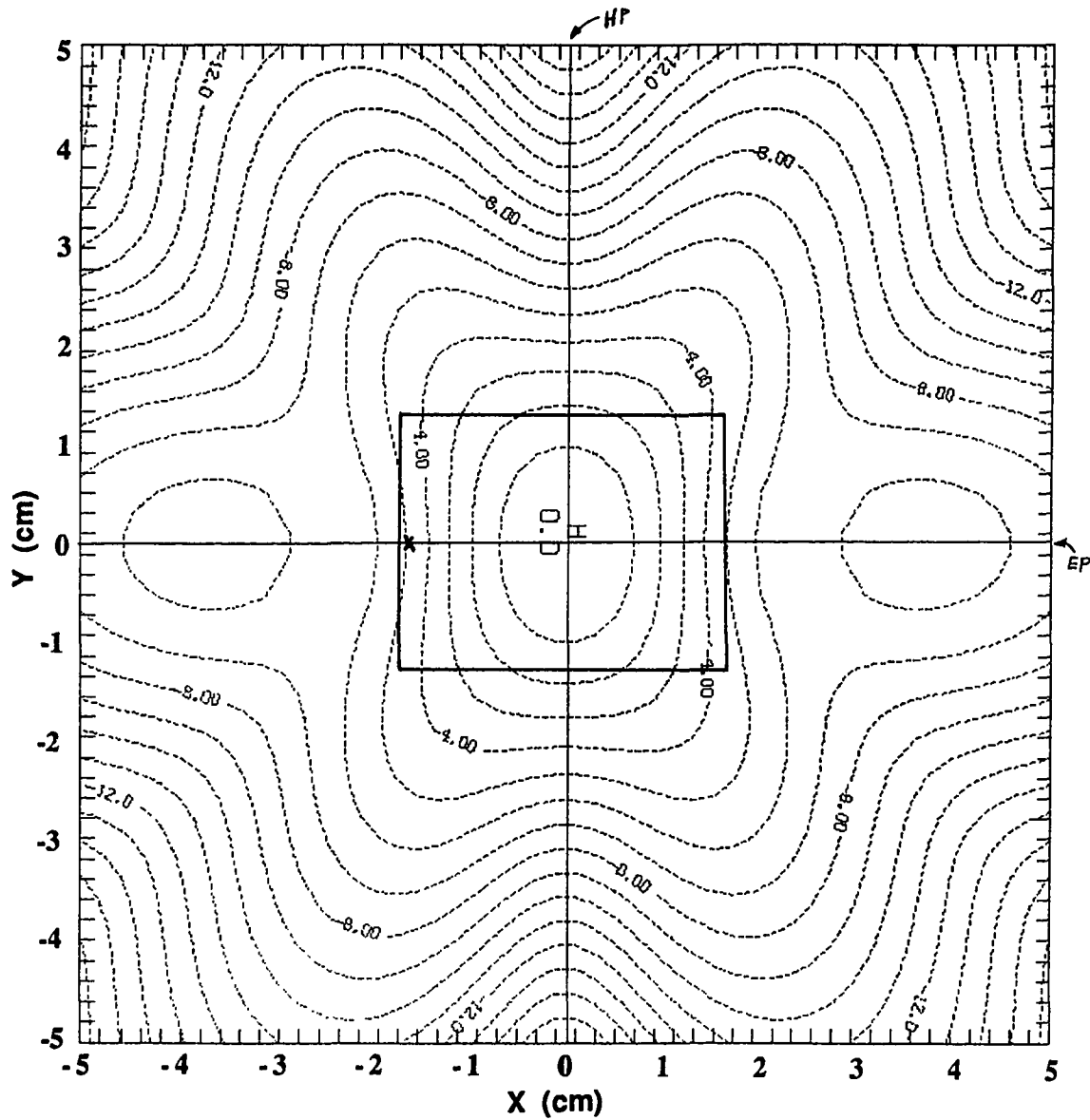


Figure C.15. Relative power (dB) contours predicted by CC model in the $z=3.0$ cm plane-total E field: $P_T \sim |E|^2 = (|E_x|^2 + |E_y|^2 + |E_z|^2)$.

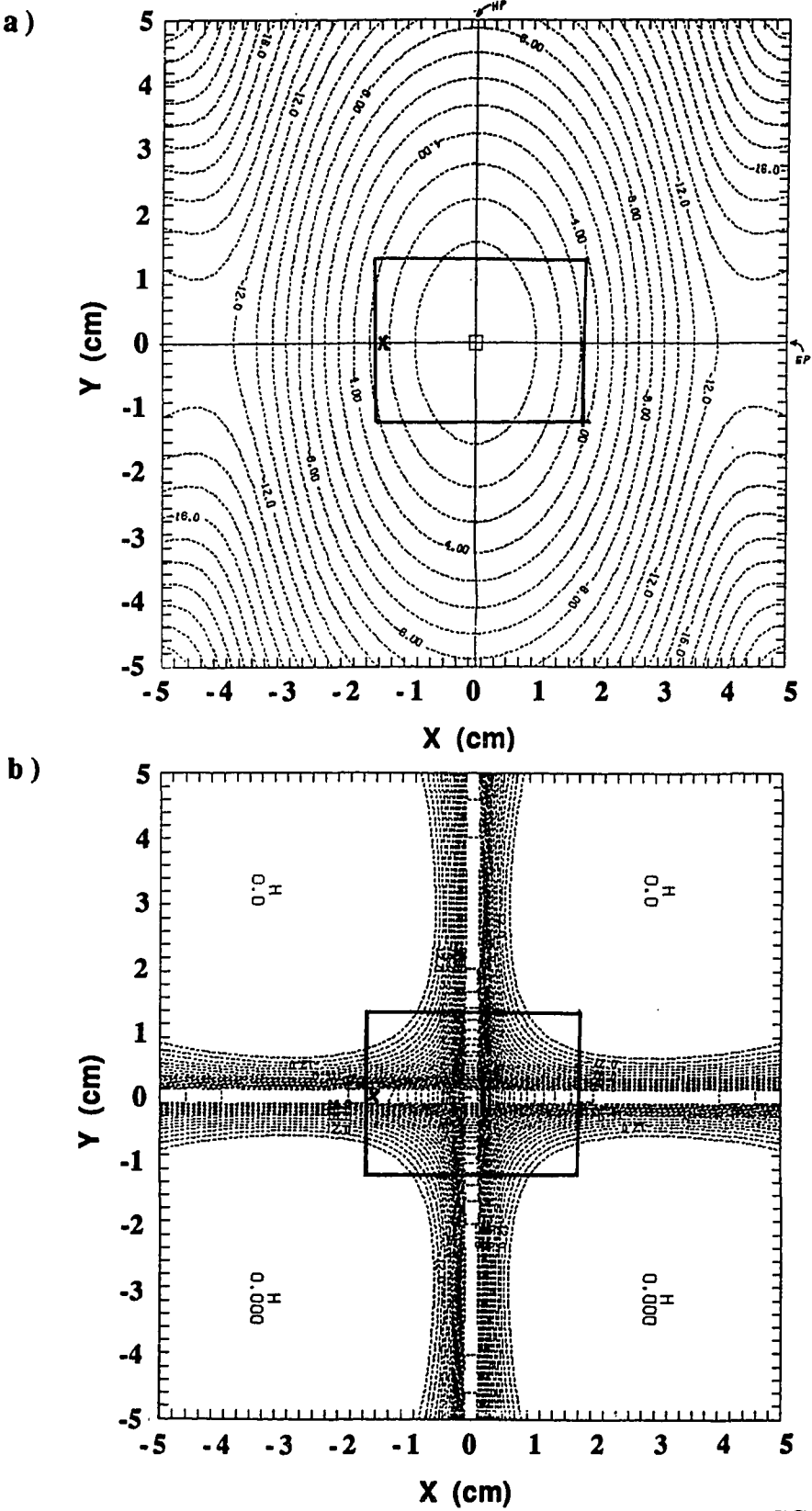


Figure C.16. Relative power (dB) contours predicted by CC model in the $z=6.0$ cm plane a) primary transverse (T1): $P_x \sim |E_x|^2$ ($P_{xp}=-20.8$ dB), b) secondary transverse (T2): $P_y \sim |E_y|^2$ ($P_{yp}=-32.2$ dB) components.

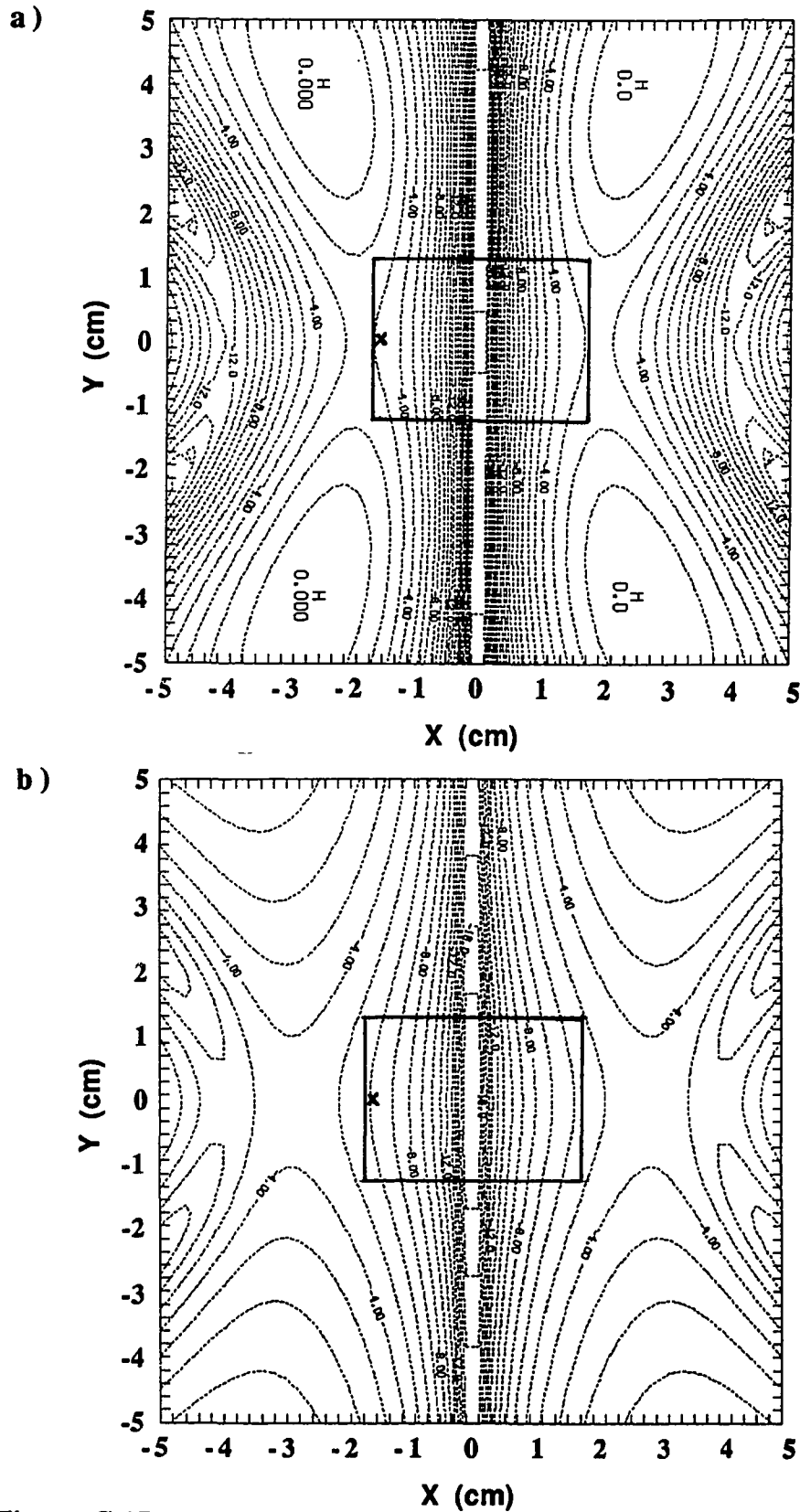


Figure C.17. Relative power (dB) contours predicted by CC model in the $z=6.0$ cm plane a) normal component: $P_z \sim |E_z|^2$ ($P_{zp} = -32.5$ dB),
 b) normal-to-transverse ratio: $R_{zt} = 10 \log(|E_z|/|E_t|)$.

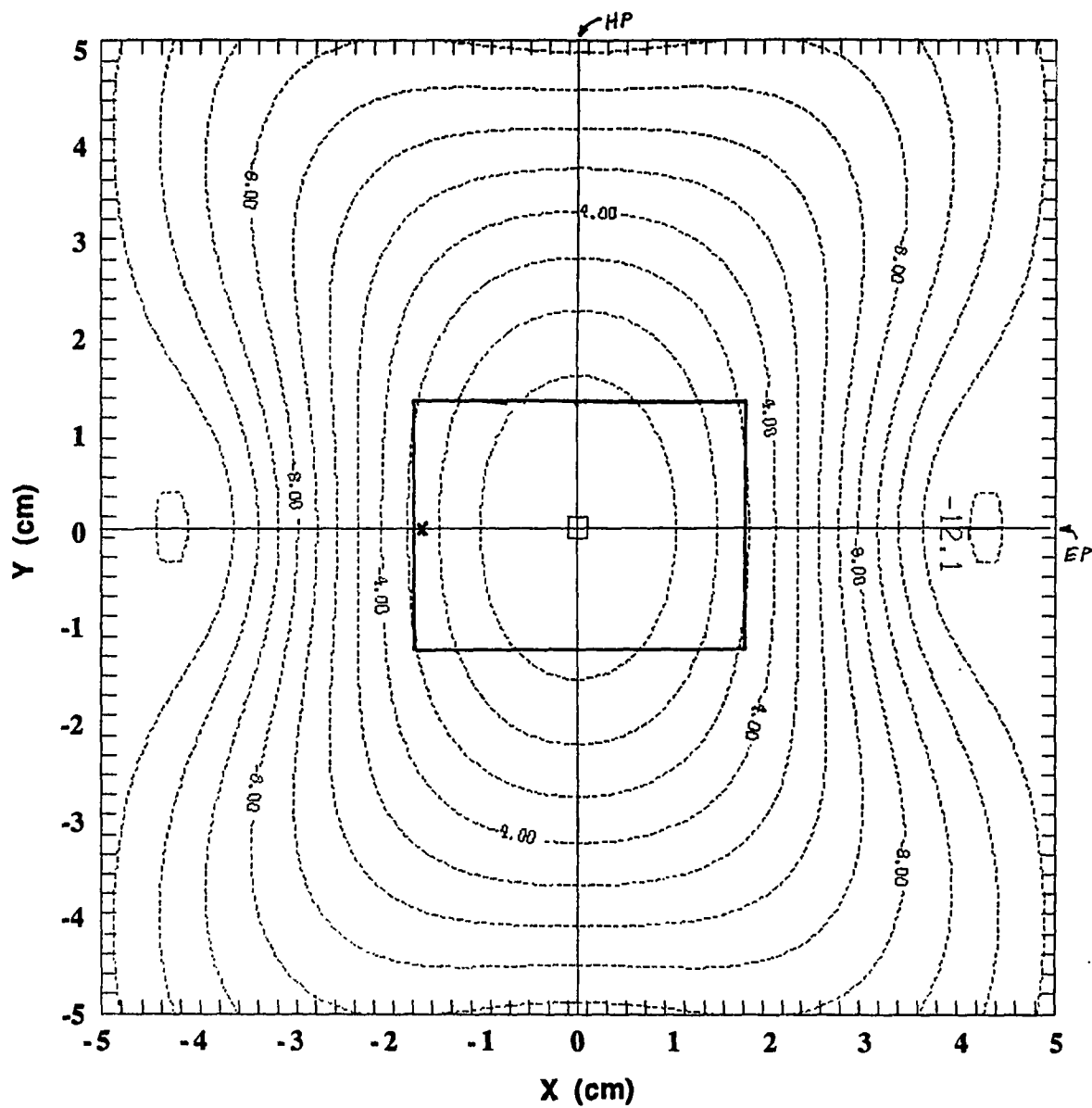


Figure C.18. Relative power (dB) contours predicted by CC model in the $z=6.0$ cm plane - total E field: $P_T \sim |E|^2 = (|E_x|^2 + |E_y|^2 + |E_z|^2)$.

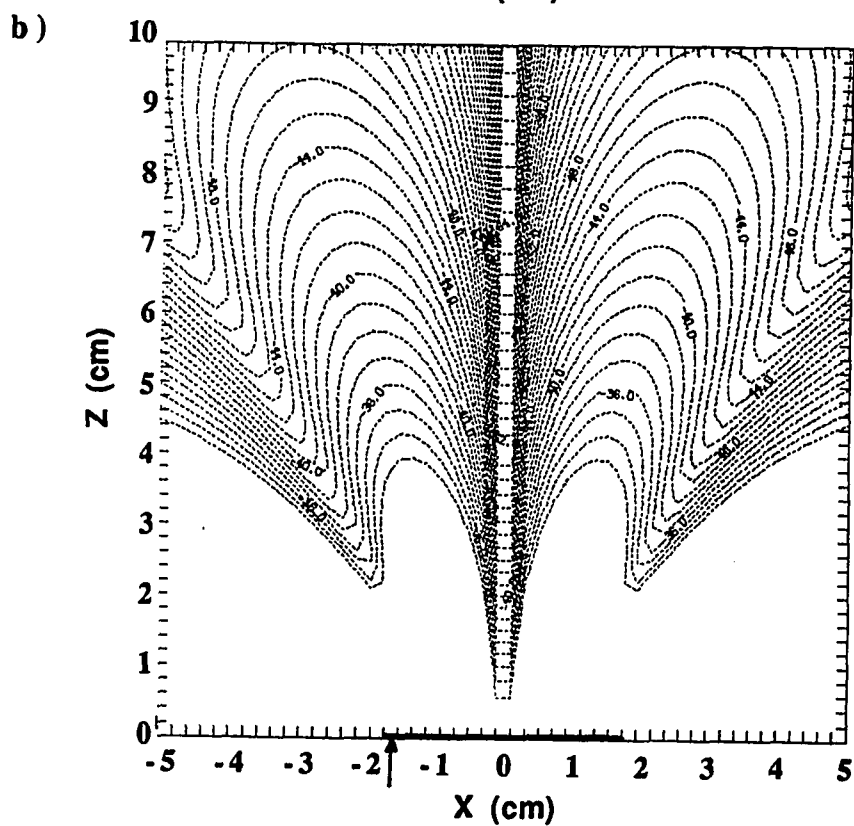
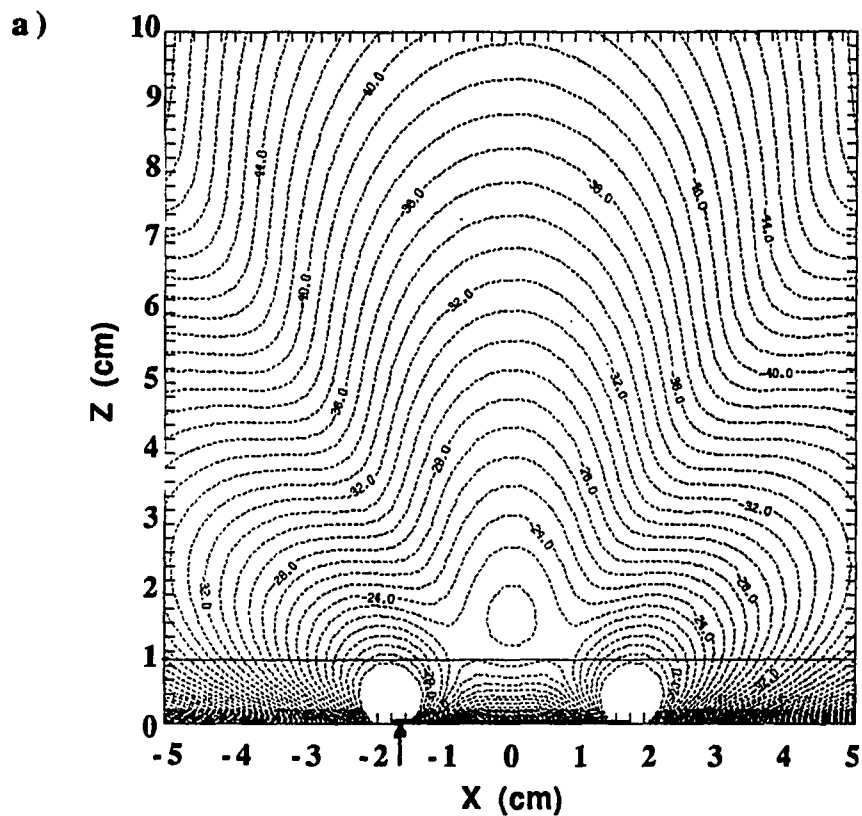


Figure C.19. Relative power (dB) contours predicted by CC model in the E-plane($y=W/2$) a) transverse component: $P_x \sim |E_x|^2$ ($P_{xp}=+10.3$ dB), b) normal component: $P_z \sim |E_z|^2$ ($P_{zp}=+3.0$ dB).

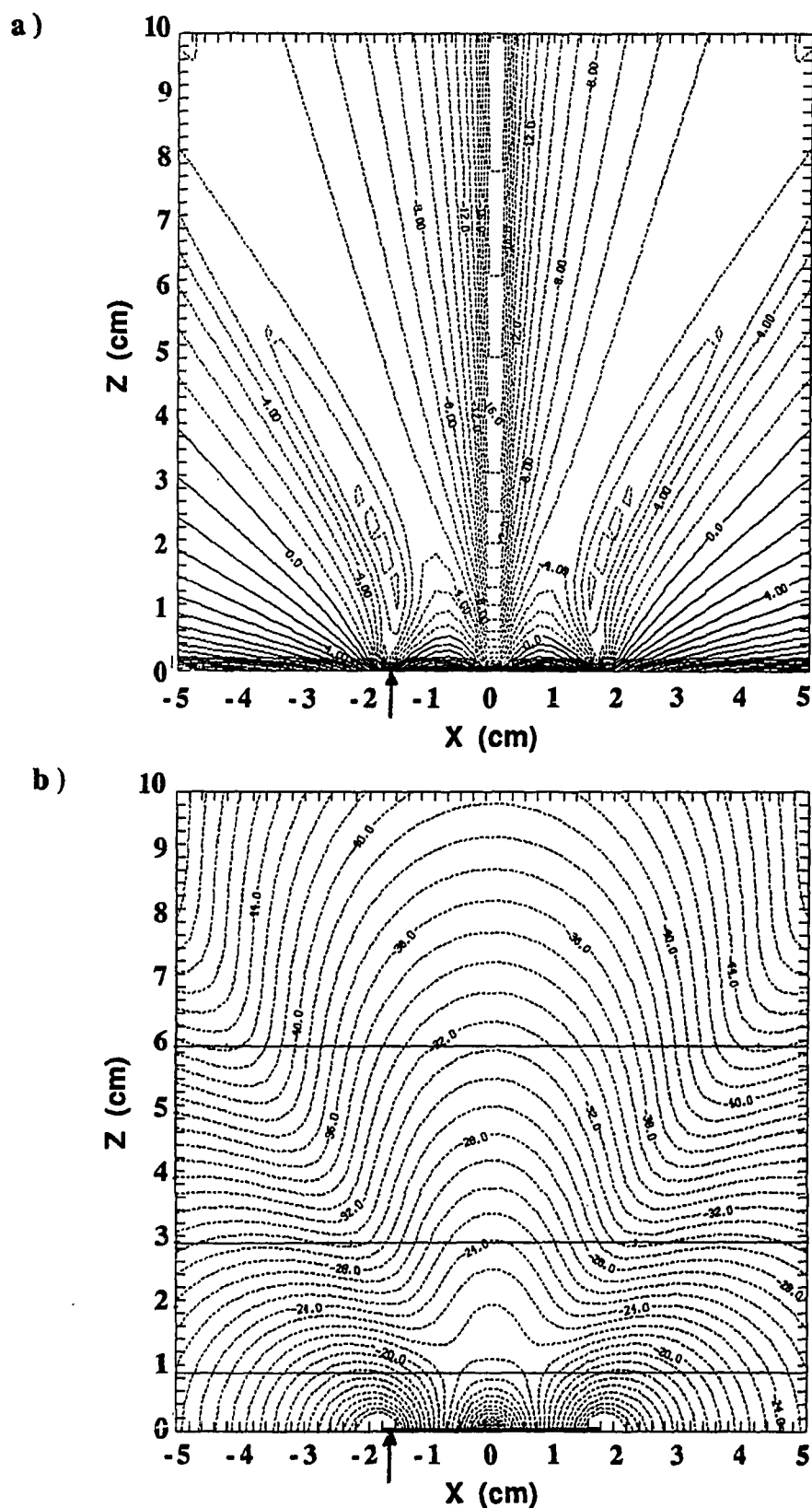


Figure C.20. Relative power (dB) contours predicted by CC model in the E-plane ($y=W/2$) a) normal-to-transverse ratio: $R_{zt}=10\log(|E_z|/|E_x|)$, b) total E field: $P_T \sim |E|^2 = (|E_x|^2 + |E_z|^2)$.

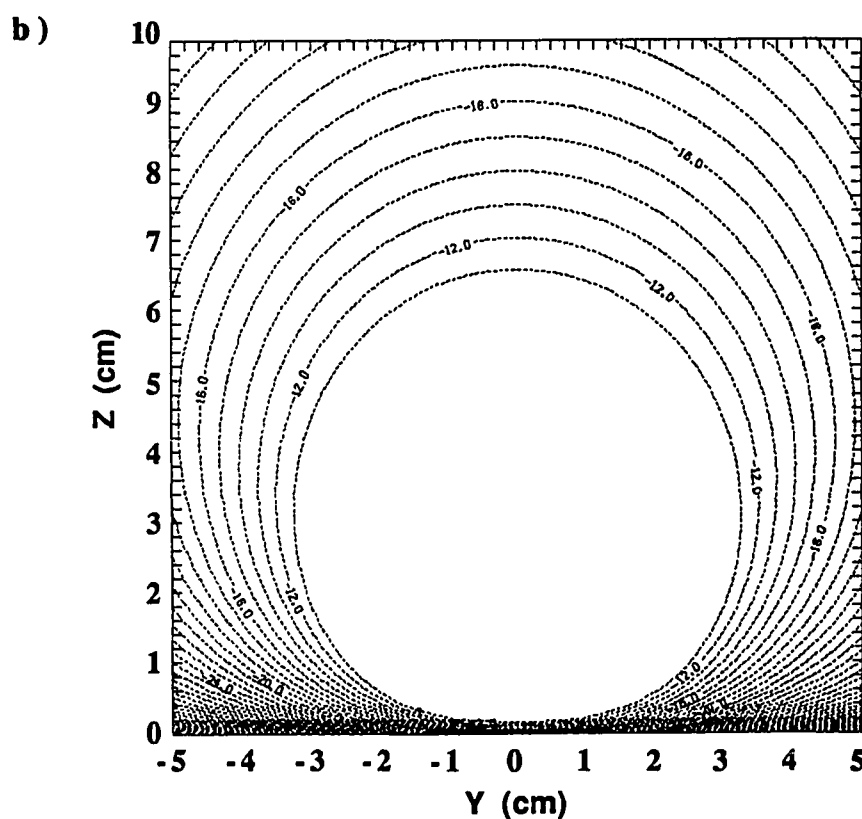
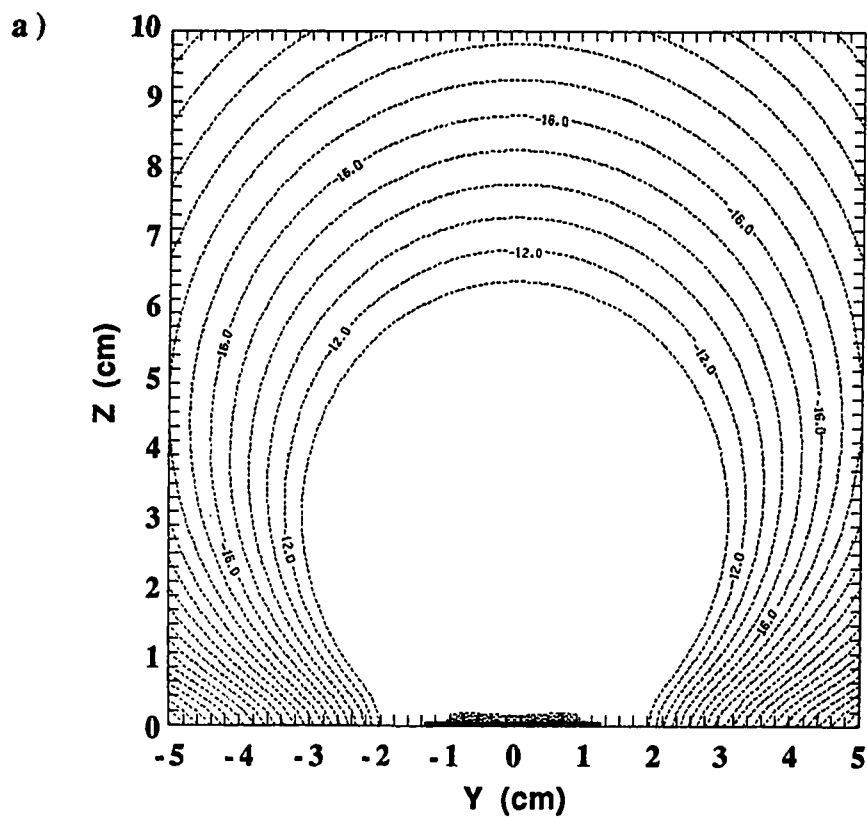


Figure C.21. Relative power (dB) contours predicted by CC model in the H-plane($x=L/2$) a) primary transverse(T1): $P_x \sim |E_x|^2$ ($P_{xp}=-11.3\text{dB}$), b) secondary transverse (T2): $P_y \sim |E_y|^2$ ($P_{yp}=-12.3\text{dB}$) components.

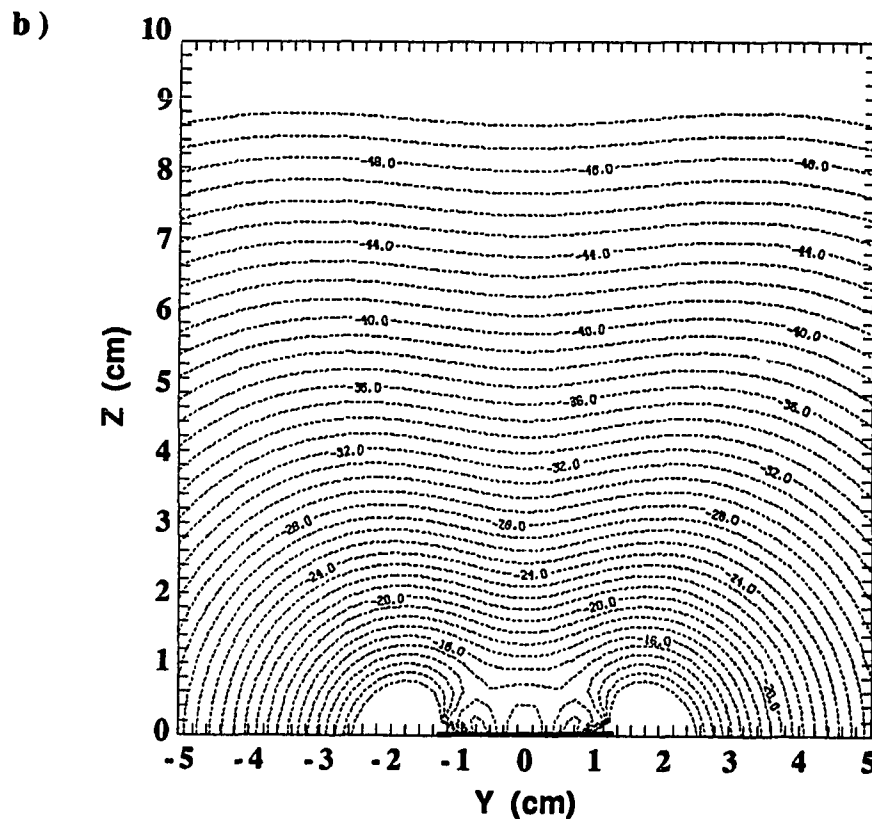
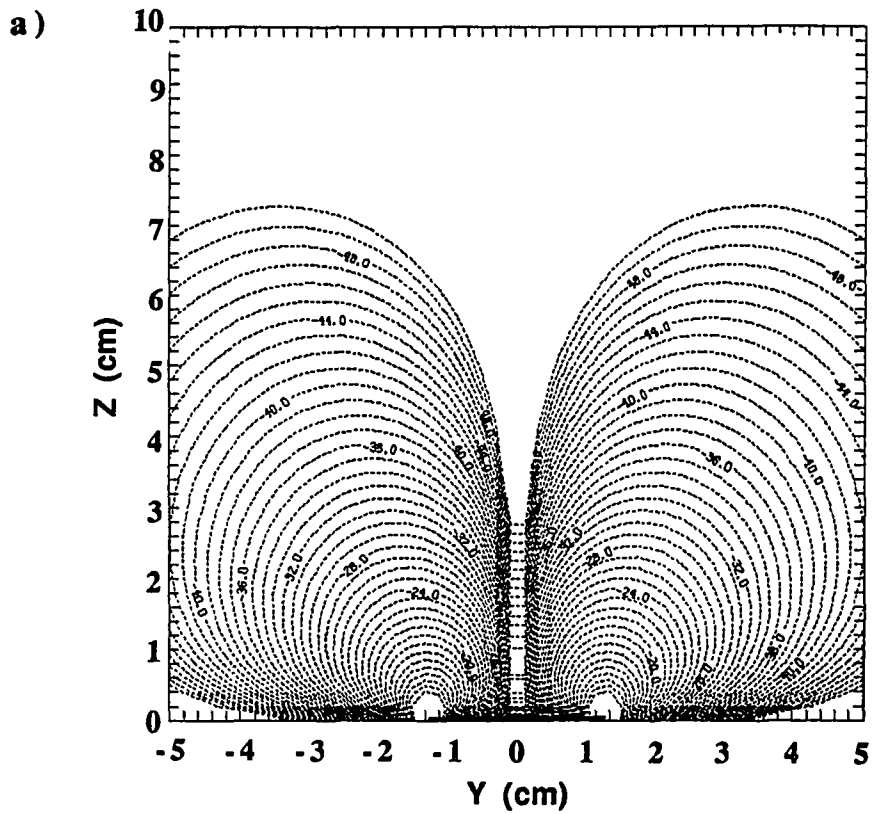


Figure C.22. Relative power (dB) contours predicted by CC model in the H-plane ($x=L/2$) a) normal component: $P_Z \sim |E_Z|^2$ ($P_{Zp} = -15.6$ dB), b) normal-to-transverse ratio: $R_{zt} = 10 \log(|E_Z|/|E_t|)$.

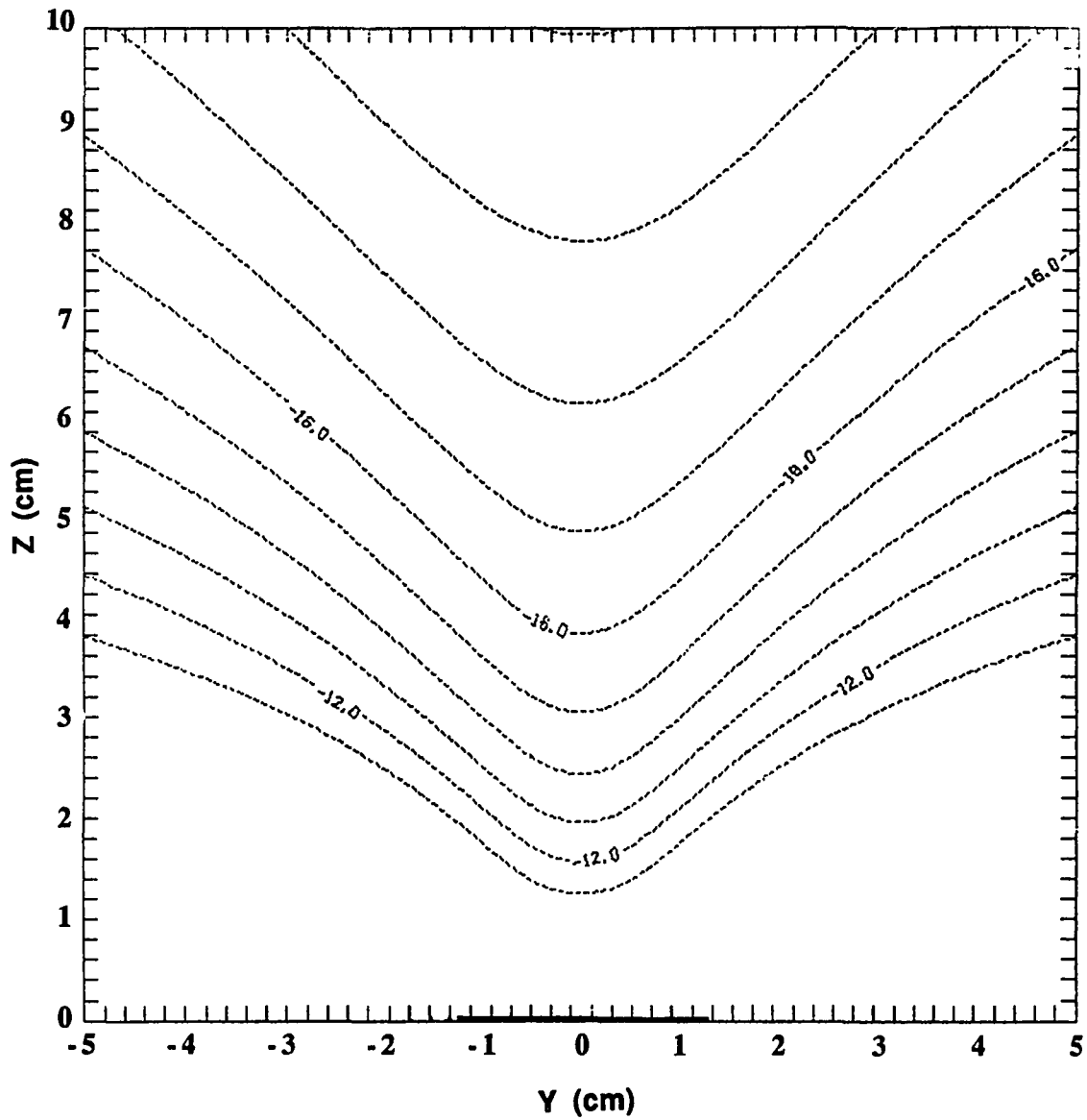


Figure C.23. Relative power (dB) contours predicted by CC model in the H-plane ($x=L/2$) - total E field: $P_T \sim |E|^2 = (|E_x|^2 + |E_y|^2 + |E_z|^2)$.

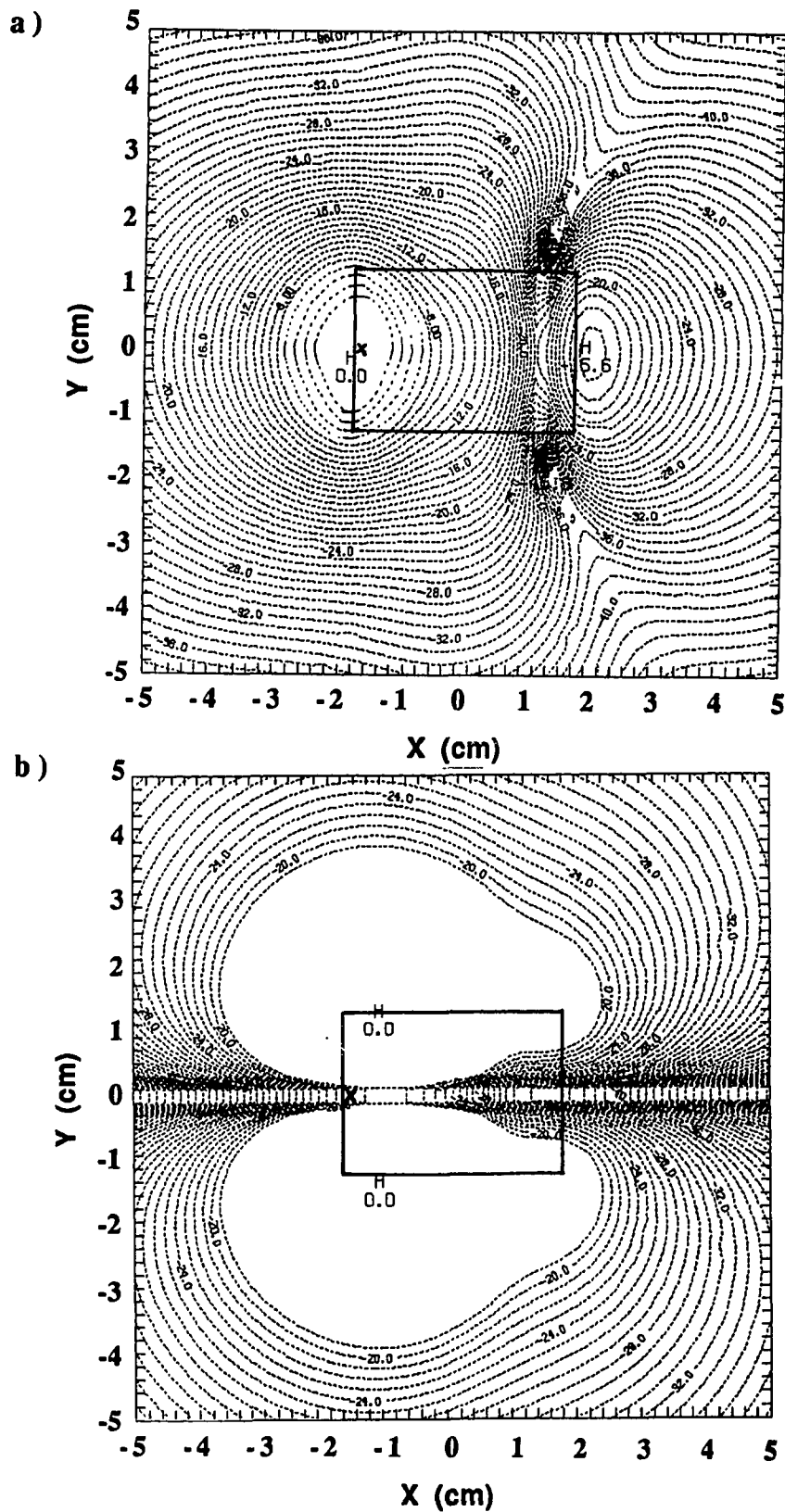


Figure C.24. Relative power (dB) contours predicted by MC model in the $z=1.0$ cm plane a) primary transverse (T1): $P_x \sim |E_x|^2$ ($P_{xp}=-2.2$ dB), b) secondary transverse (T2): $P_y \sim |E_y|^2$ ($P_{yp}=-5.5$ dB) components.

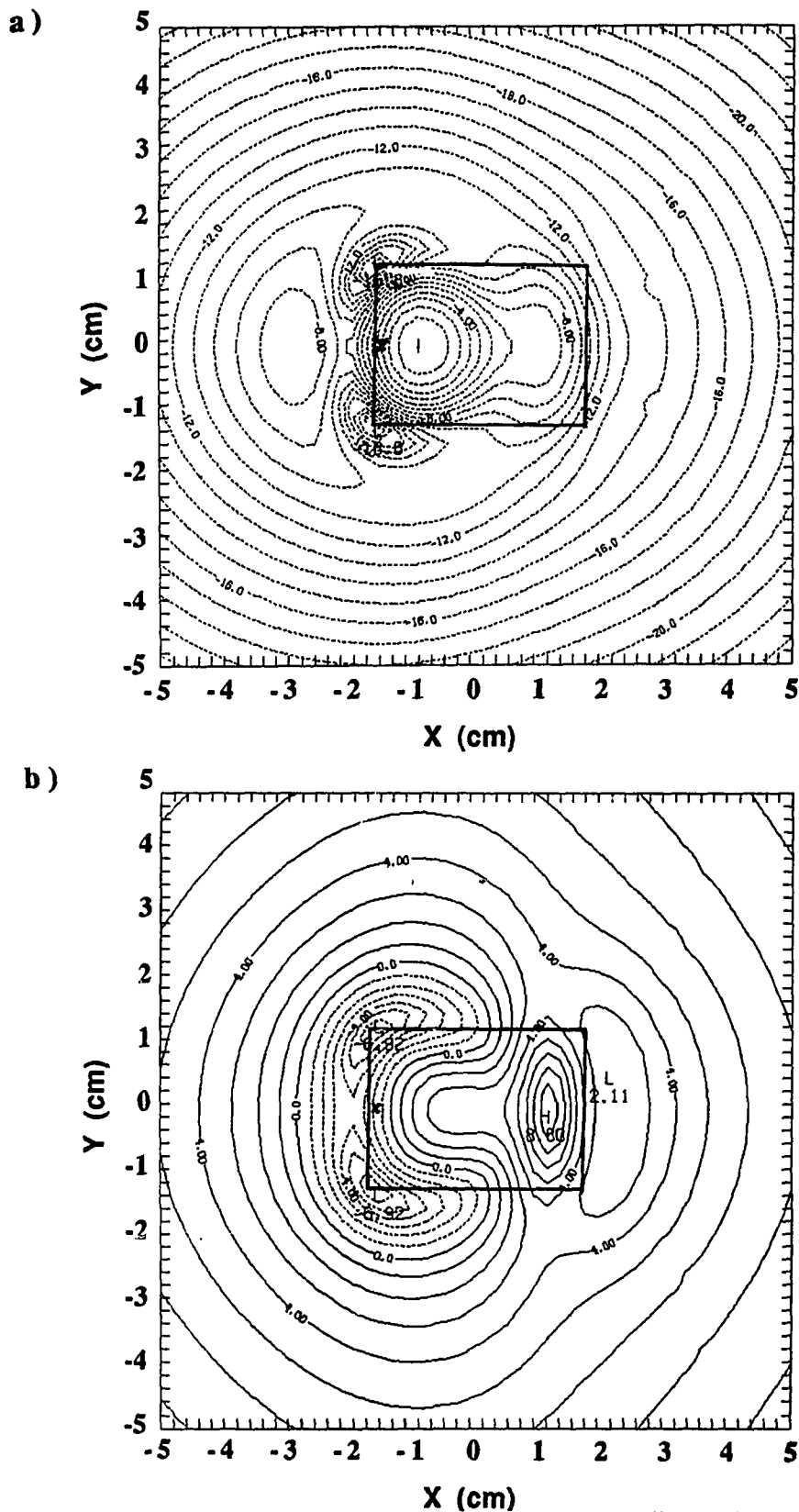


Figure C.25. Relative power (dB) contours predicted by MC model in the $z=1.0$ cm plane a) normal component: $P_z \sim |E_z|^2$ ($P_{zp} = -1.4$ dB),
 b) normal-to-transverse ratio: $R_{zt} = 10 \log(|E_z|/|E_t|)$.

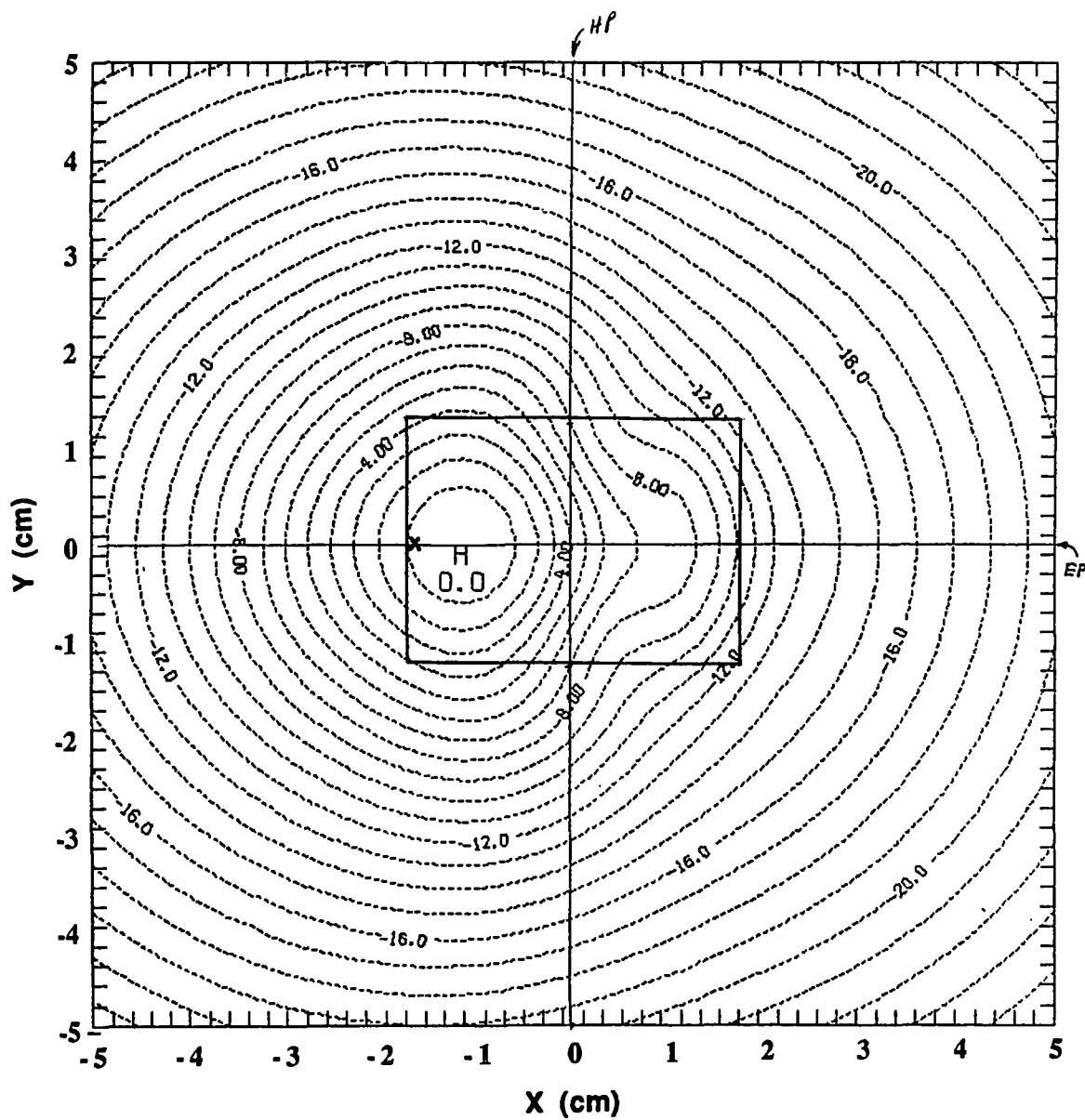


Figure C.26. Relative power (dB) contours predicted by MC model in the $z=1.0$ cm plane - total E field: $P_T \sim |E|^2 = (|E_x|^2 + |E_y|^2 + |E_z|^2)$.

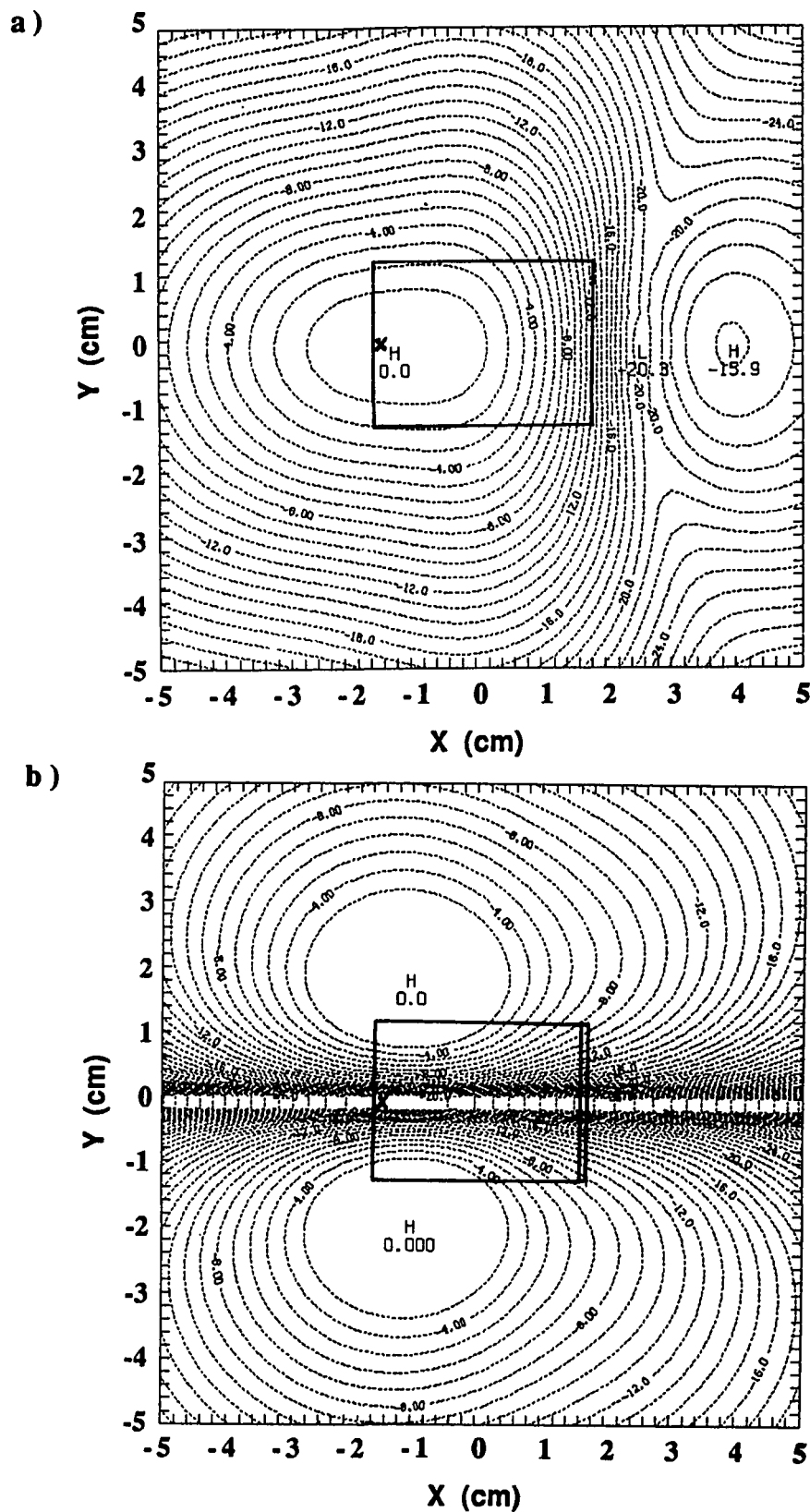


Figure C.27. Relative power (dB) contours predicted by MC model in the $z=3.0$ cm plane a) primary transverse (T1): $P_x \sim |E_x|^2$ ($P_{xp}=-12.7$ dB), b) secondary transverse (T2): $P_y \sim |E_y|^2$ ($P_{yp}=-16.4$ dB) components.

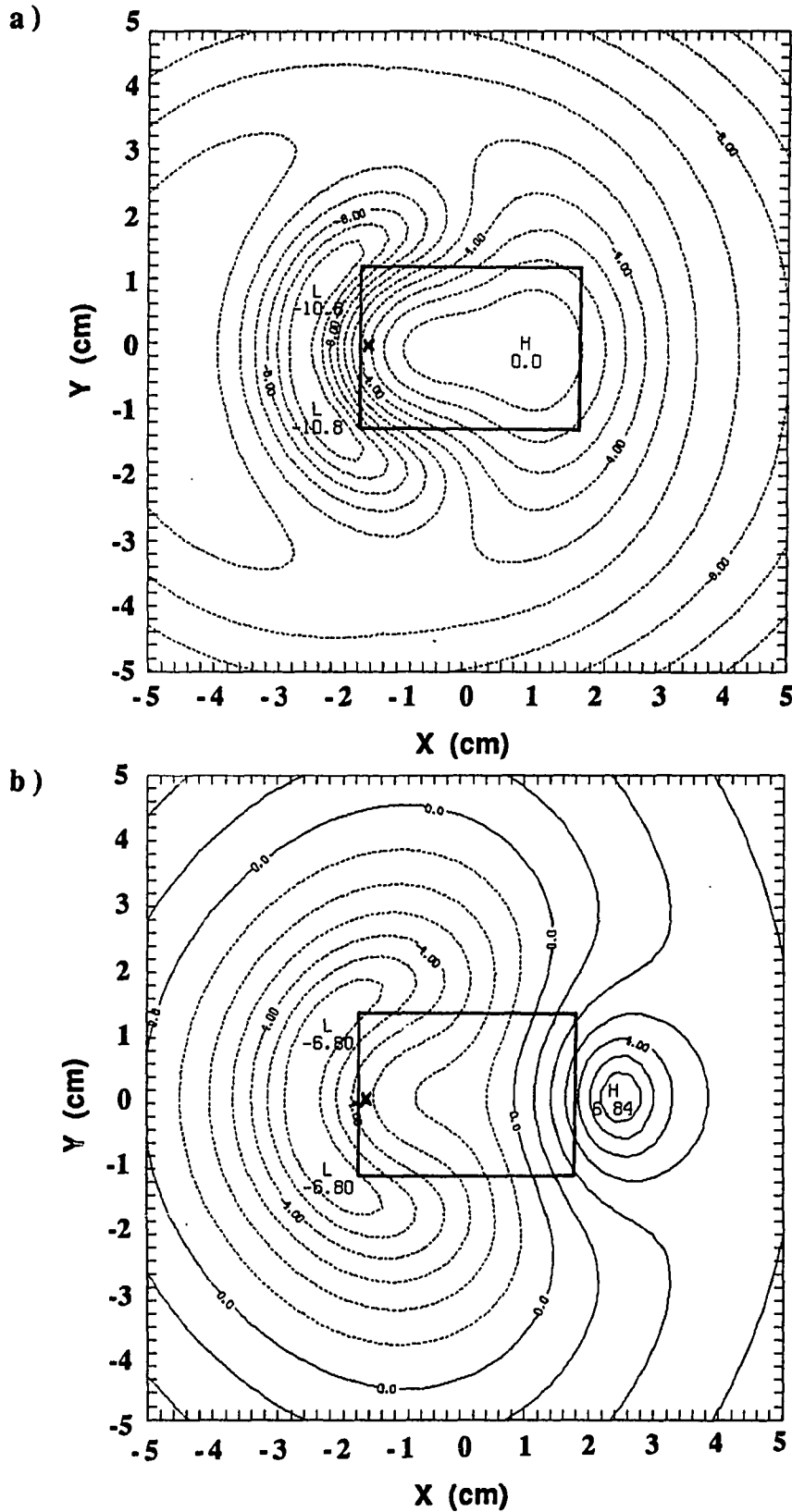


Figure C.28. Relative power (dB) contours predicted by MC model in the $z=3.0$ cm plane a) normal component: $P_{z\sim}|E_z|^2$ ($P_{zp}=-16.2$ dB),
 b) normal-to-transverse ratio: $R_{zt}=10\log(|E_z|/|E_t|)$.

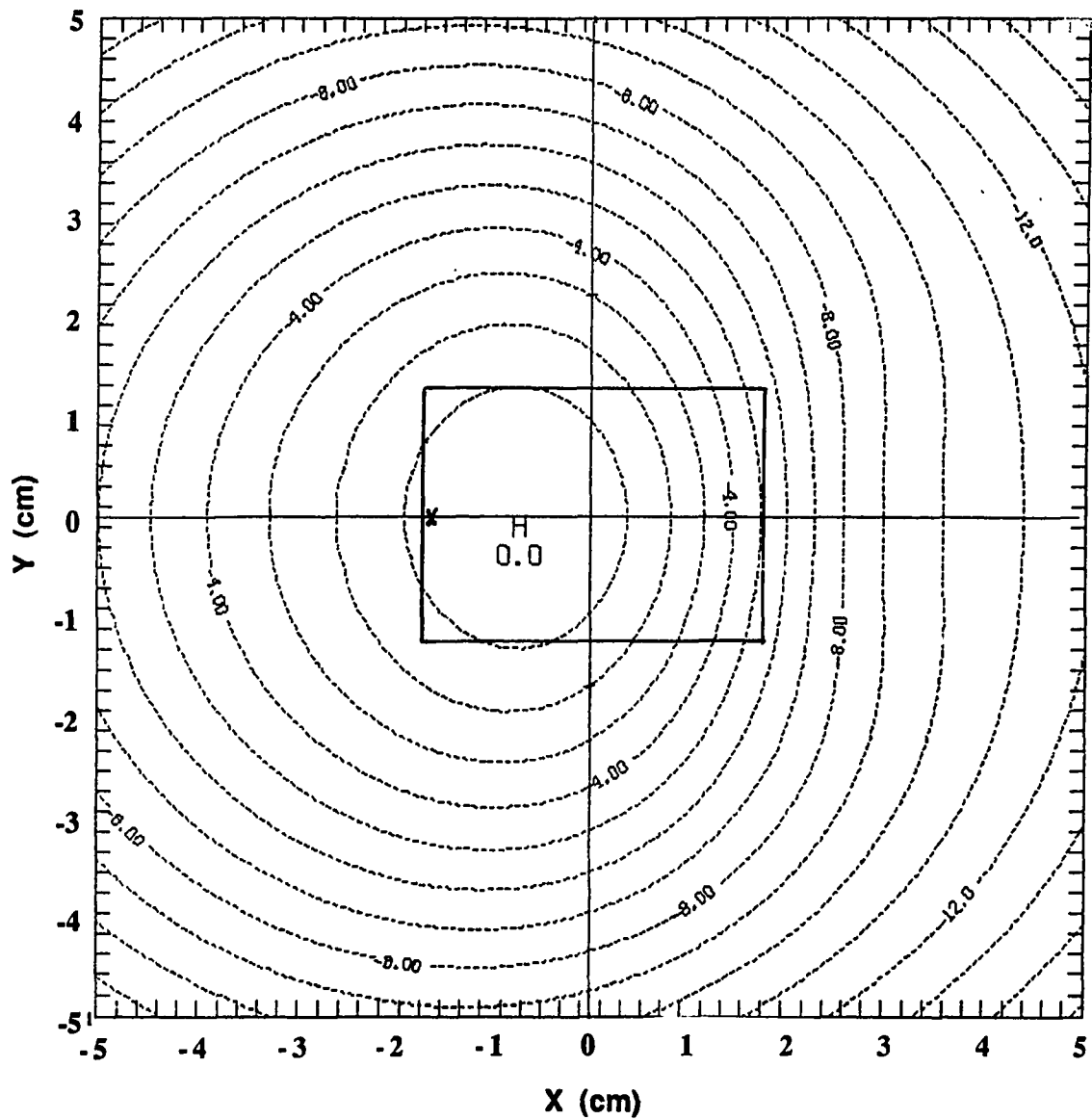


Figure C.29. Relative power (dB) contours predicted by MC model in the $z=3.0$ cm plane - total E field: $P_T \sim |E|^2 = (|E_x|^2 + |E_y|^2 + |E_z|^2)$.

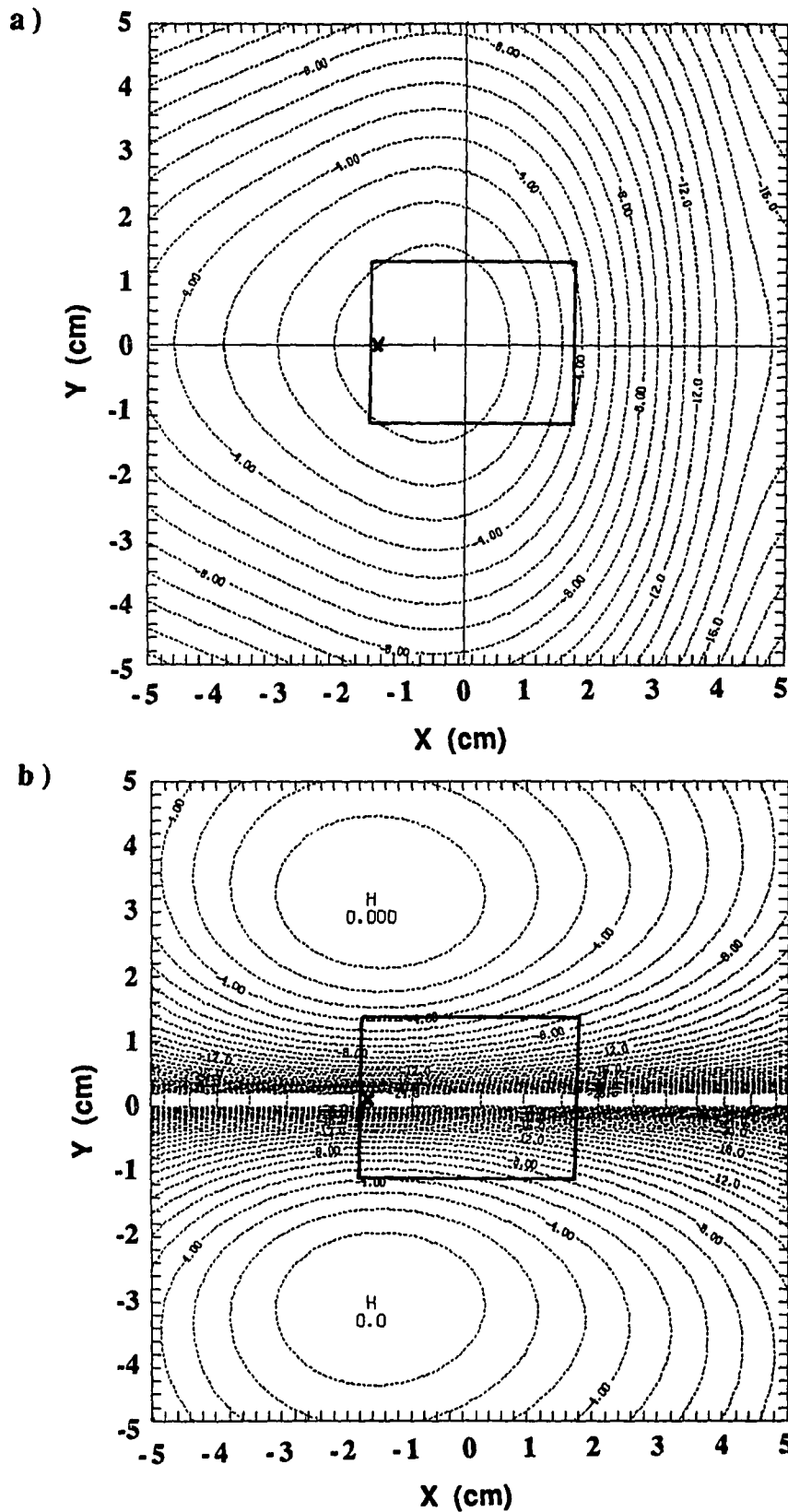


Figure C.30. Relative power (dB) contours predicted by MC model in the $z=6.0$ cm plane a) primary transverse (T1): $P_x \sim |E_x|^2$ ($P_{xp}=-20.6$ dB), b) secondary transverse (T2): $P_y \sim |E_y|^2$ ($P_{yp}=-26.3$ dB) components.

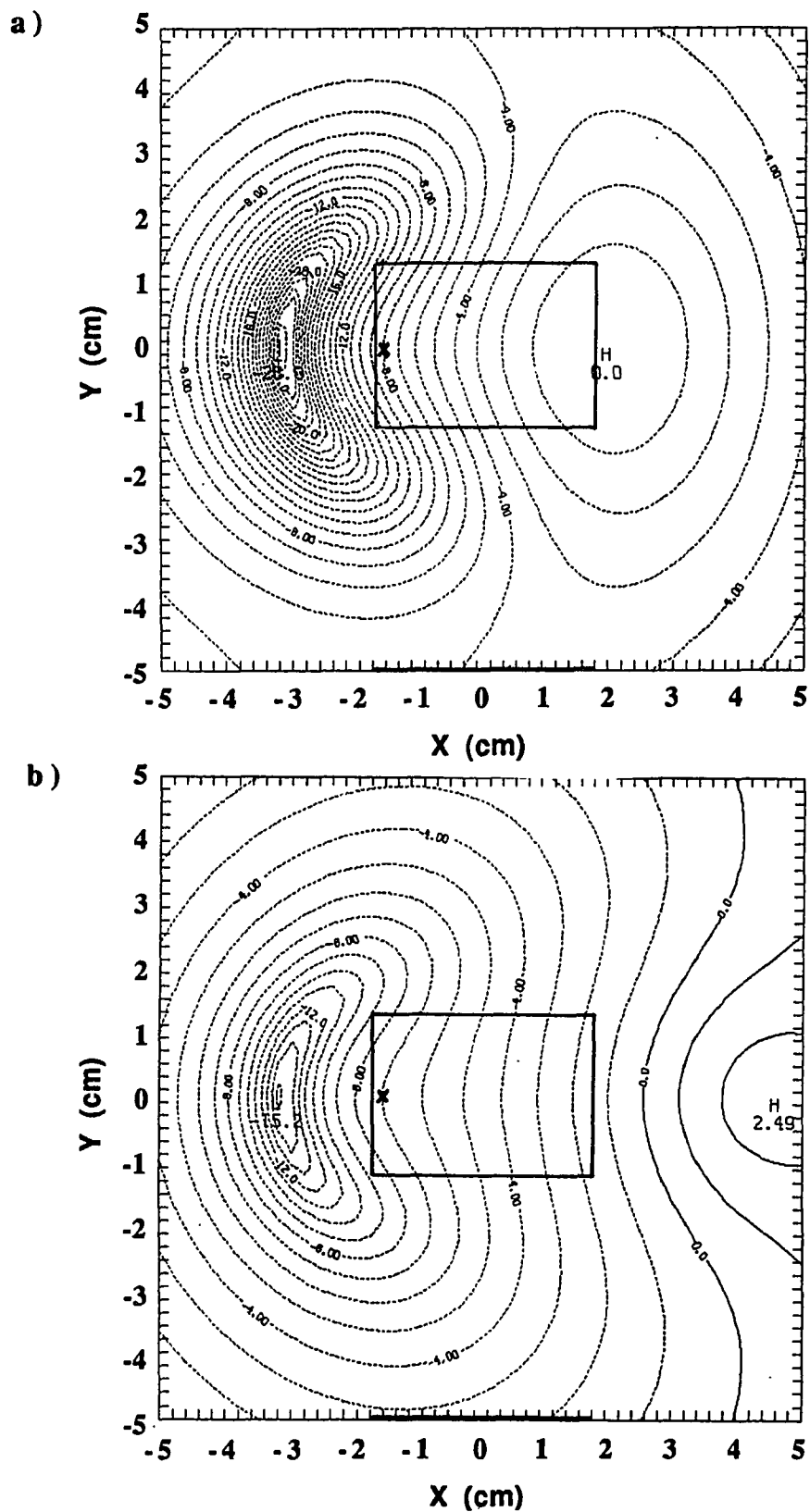


Figure C.31. Relative power (dB) contours predicted by MC model in the $z=6.0$ cm plane a) normal component: $P_z \sim |E_z|^2$ ($P_{zp} = -27.1$ dB),
 b) normal-to-transverse ratio: $R_{zt} = 10 \log(|E_z|/|E_t|)$.

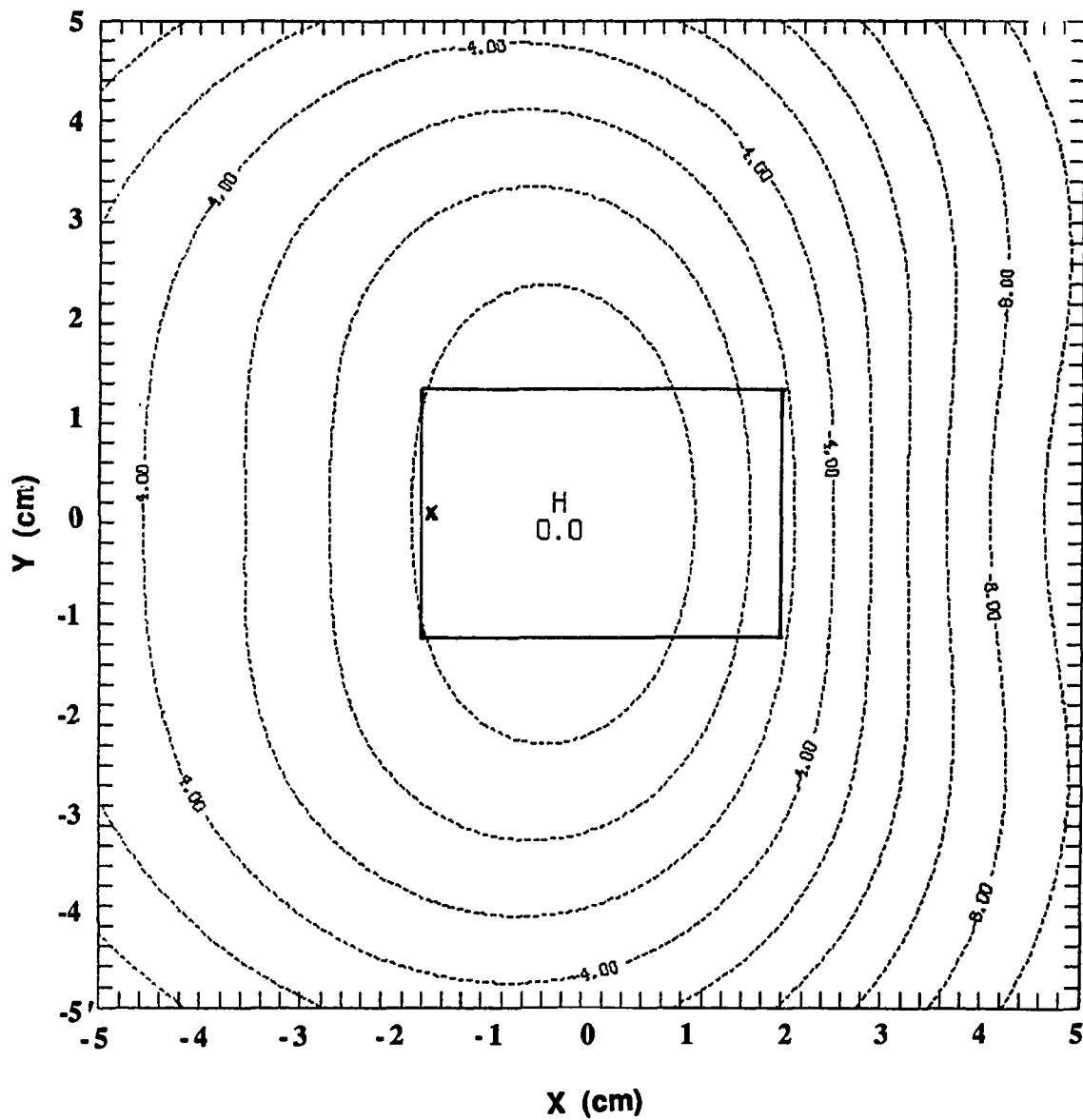


Figure C.32. Relative power (dB) contours predicted by MC model in the $z=6.0$ cm plane - total E field: $P_T \sim |E|^2 = (|E_x|^2 + |E_y|^2 + |E_z|^2)$.

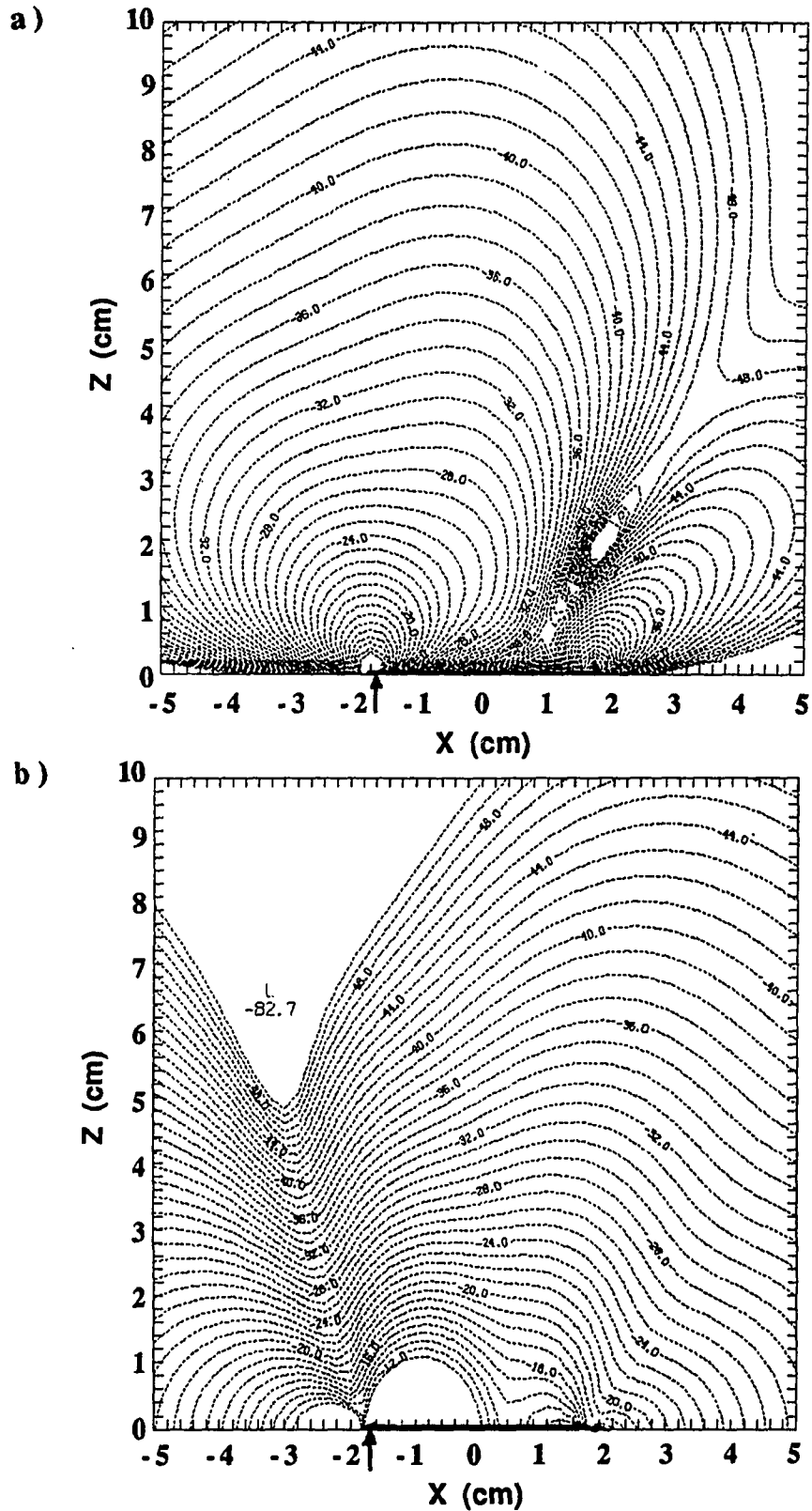


Figure C.33. Relative power (dB) contours predicted by MC model in the E-plane ($y=W/2$) a) transverse component: $P_x \sim |E_x|^2$ ($P_{xp}=+14.8\text{dB}$), b) normal component: $P_z \sim |E_z|^2$ ($P_{zp}=+8.1\text{dB}$).

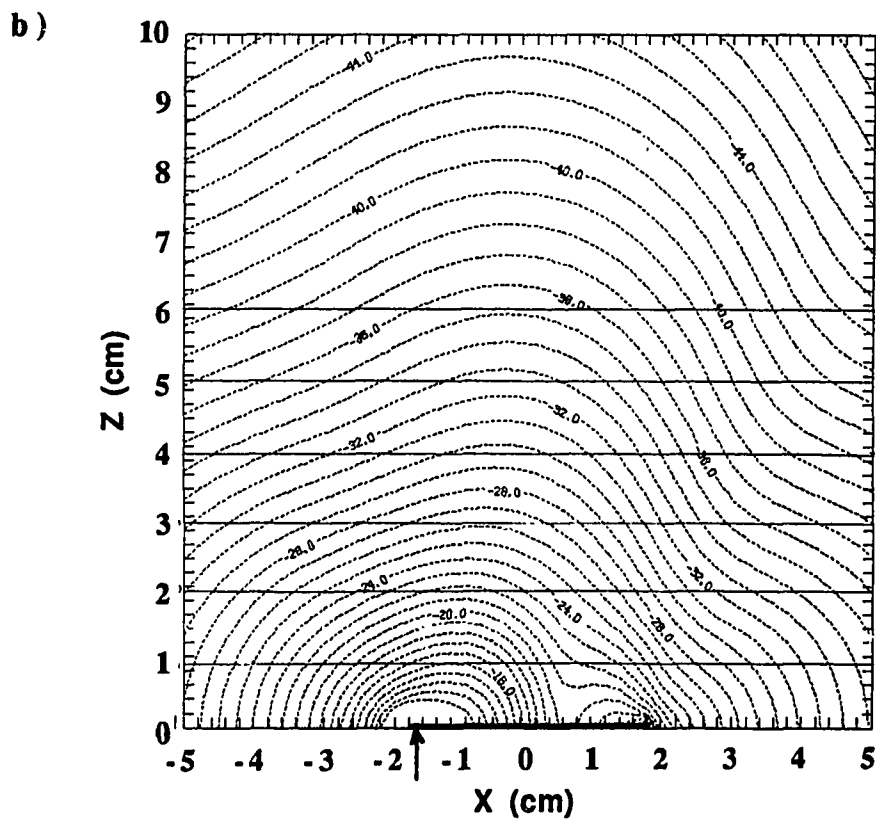
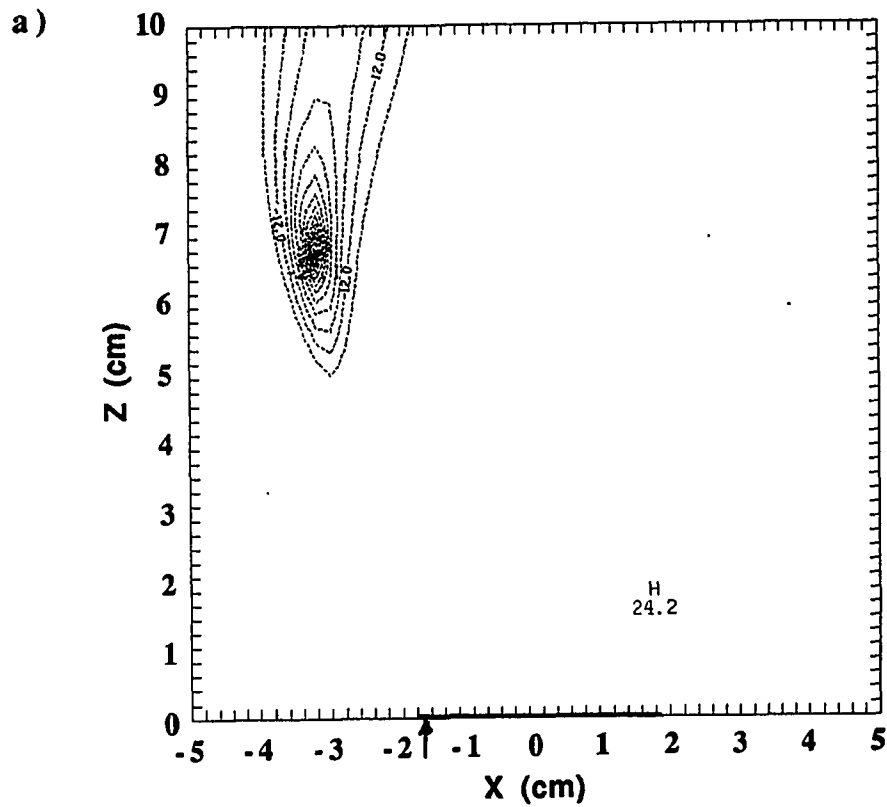
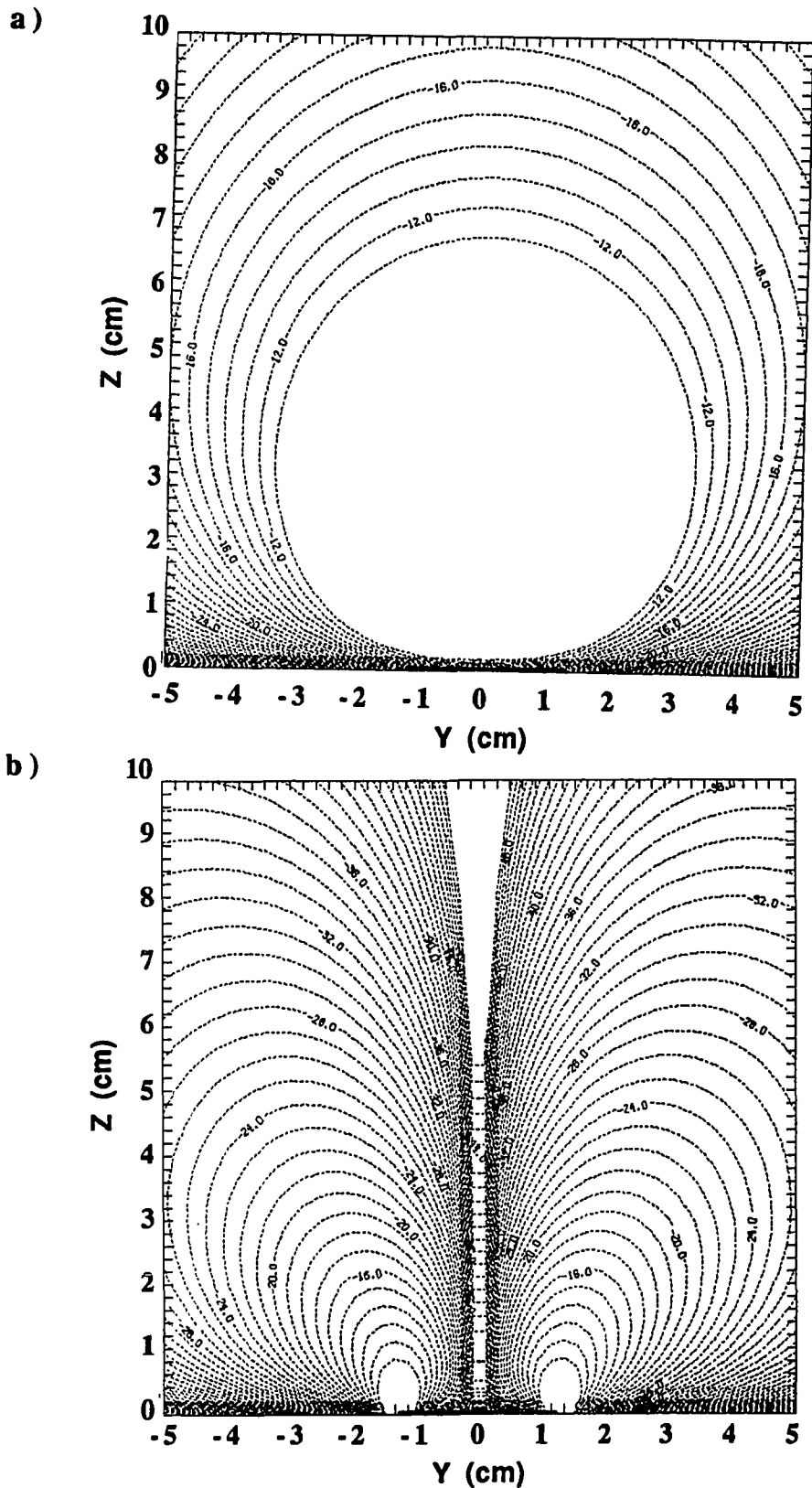


Figure C.34. Relative power (dB) contours predicted by MC model in the E-plane ($y=W/2$) a) normal-to-transverse ratio: $R_{z1}=10\log(|E_z|/|E_x|)$, b) total E field: $P_T \sim |E|^2 = (|E_x|^2 + |E_y|^2 + |E_z|^2)$.



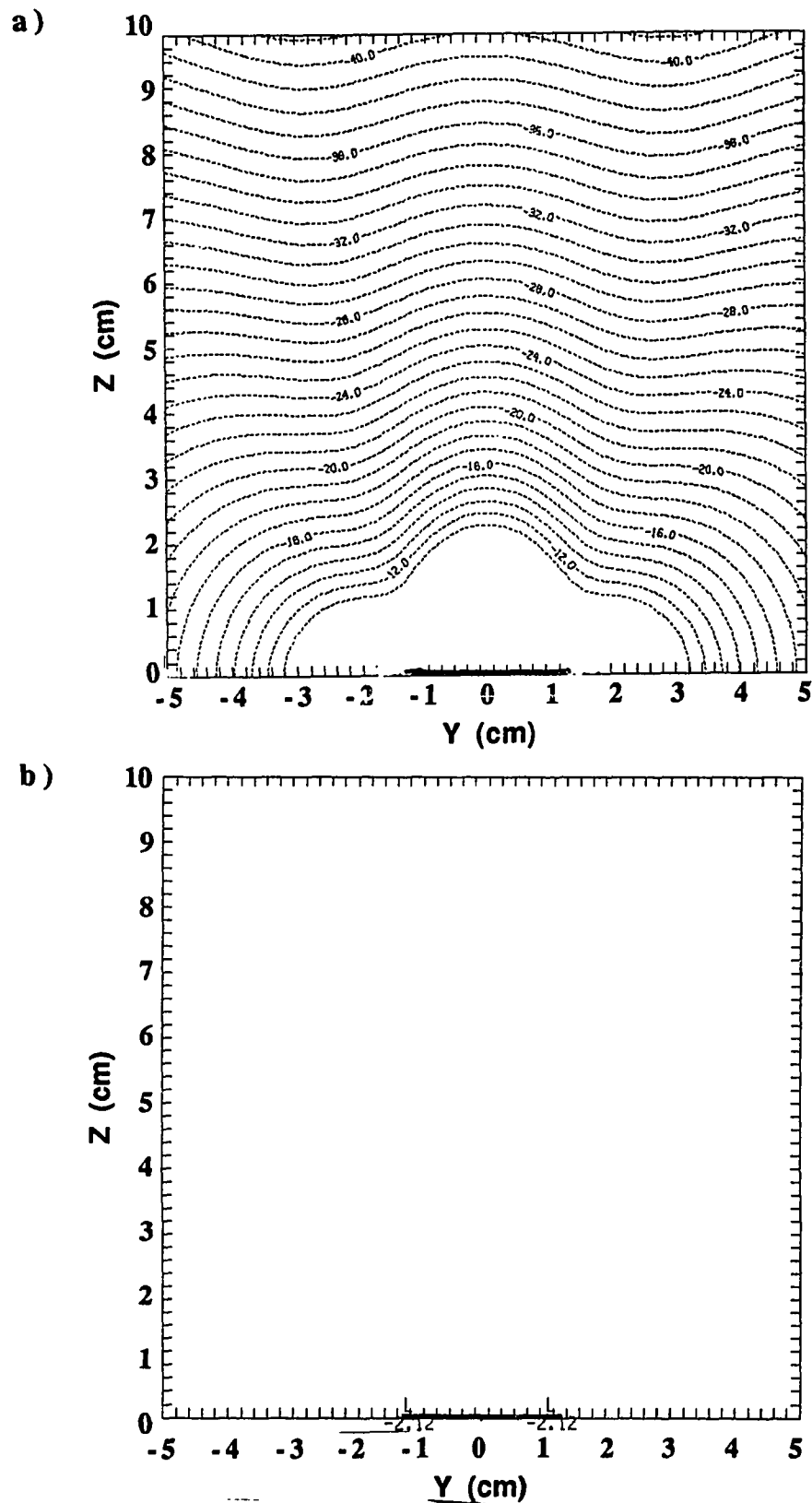


Figure C.36. Relative power (dB) contours predicted by MC model in the H-plane ($x=L/2$) a) normal component: $P_Z \sim |E_Z|^2$ ($P_{Zp} = -2.2\text{dB}$),
 b) normal-to-transverse ratio: $R_{Zt} = 10 \log(|E_Z|/|E_t|)$.

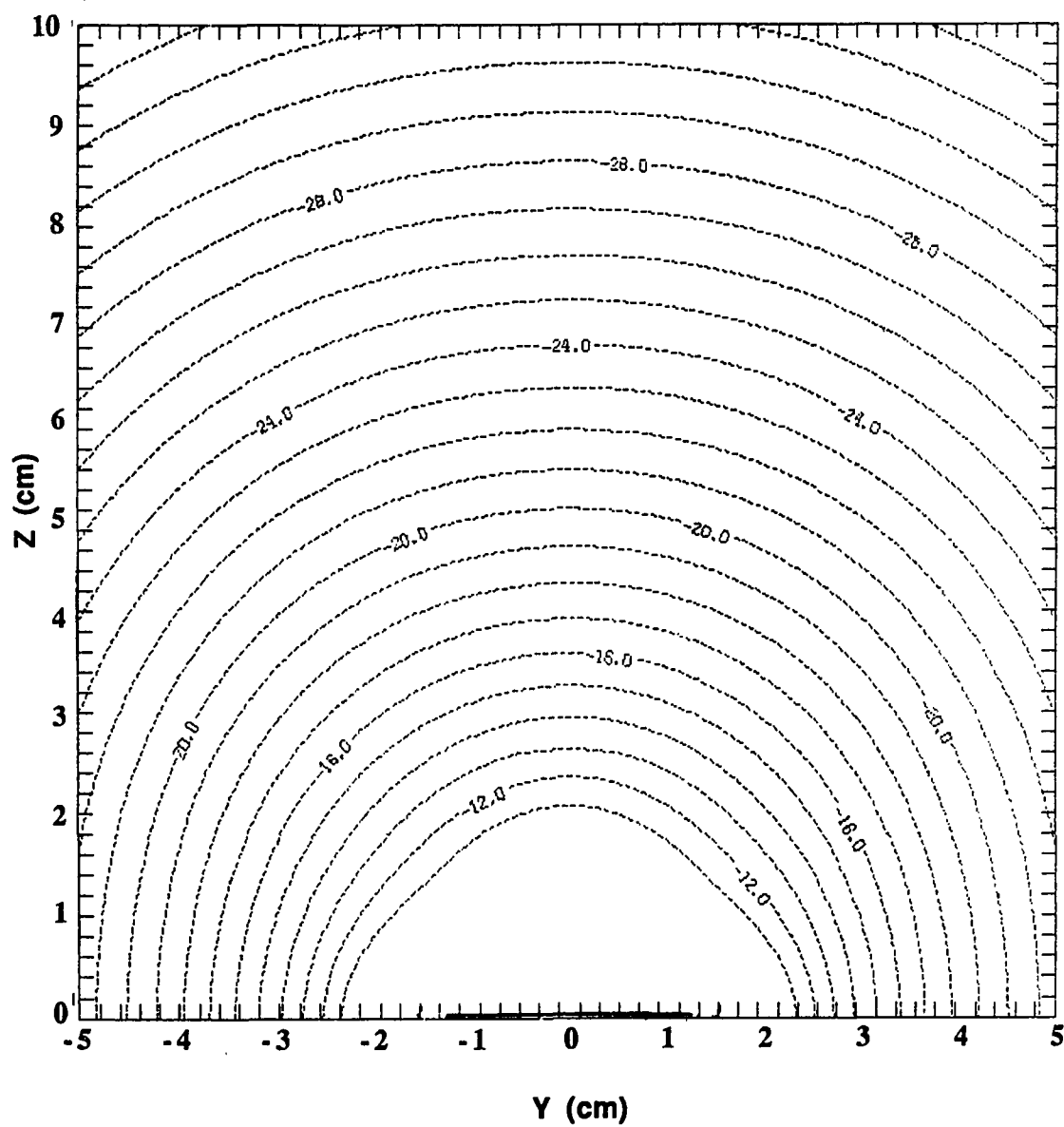


Figure C.37. Relative power (dB) contours predicted by MC model in the H-plane ($x=L/2$) - total E field: $P_T \cdot |E|^2 = (|E_x|^2 + |E_y|^2 + |E_z|^2)$.

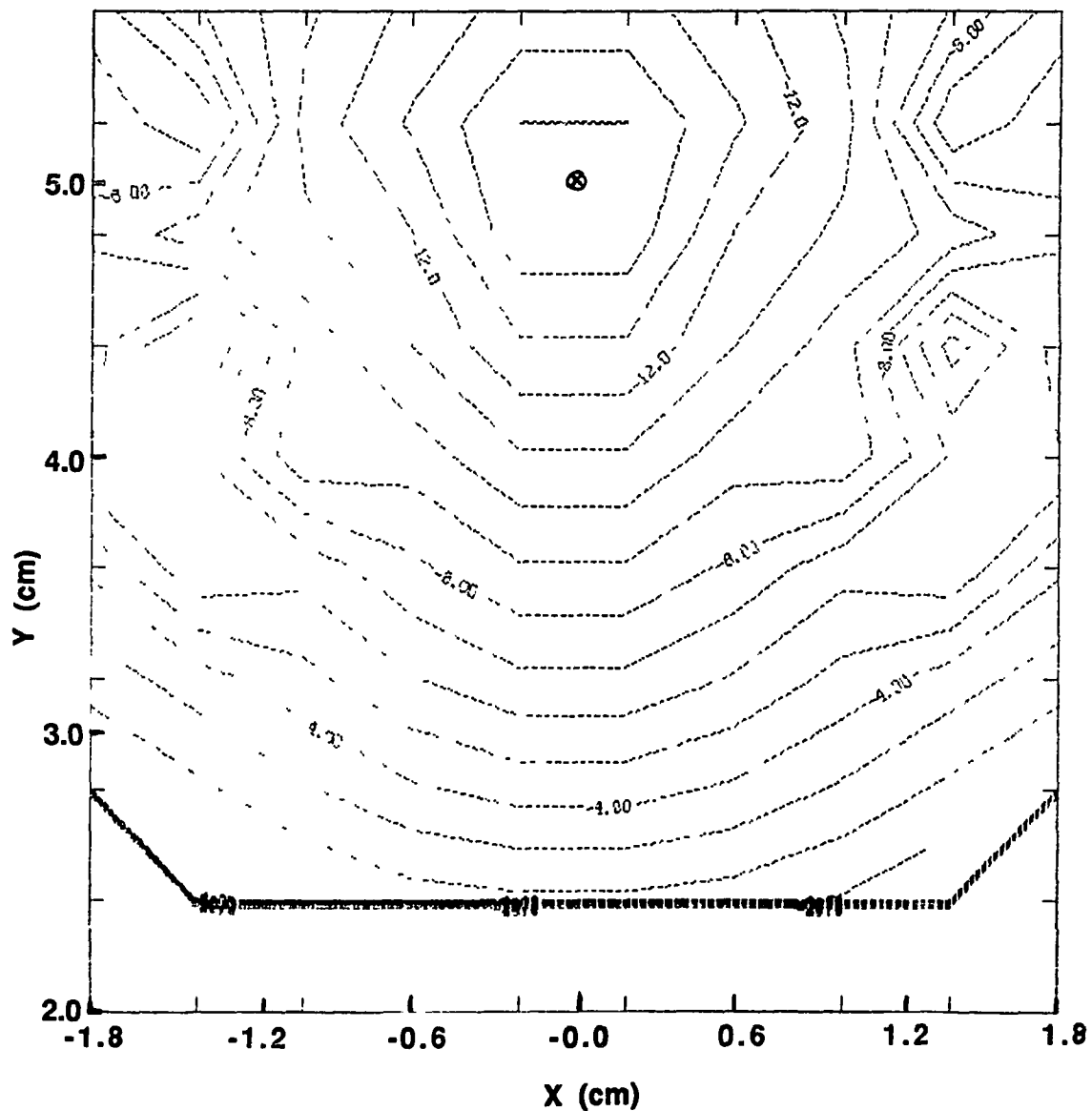


Figure C.38. Relative power (dB) contours calculated by CYLARR (CC model) in the circumferential E-plane of a single microstrip patch on a curved substrate in water – normal component: $P_{\rho} \sim |E_{\rho}|^2$ ($P_{\rho\rho} = -9.0$ dB).

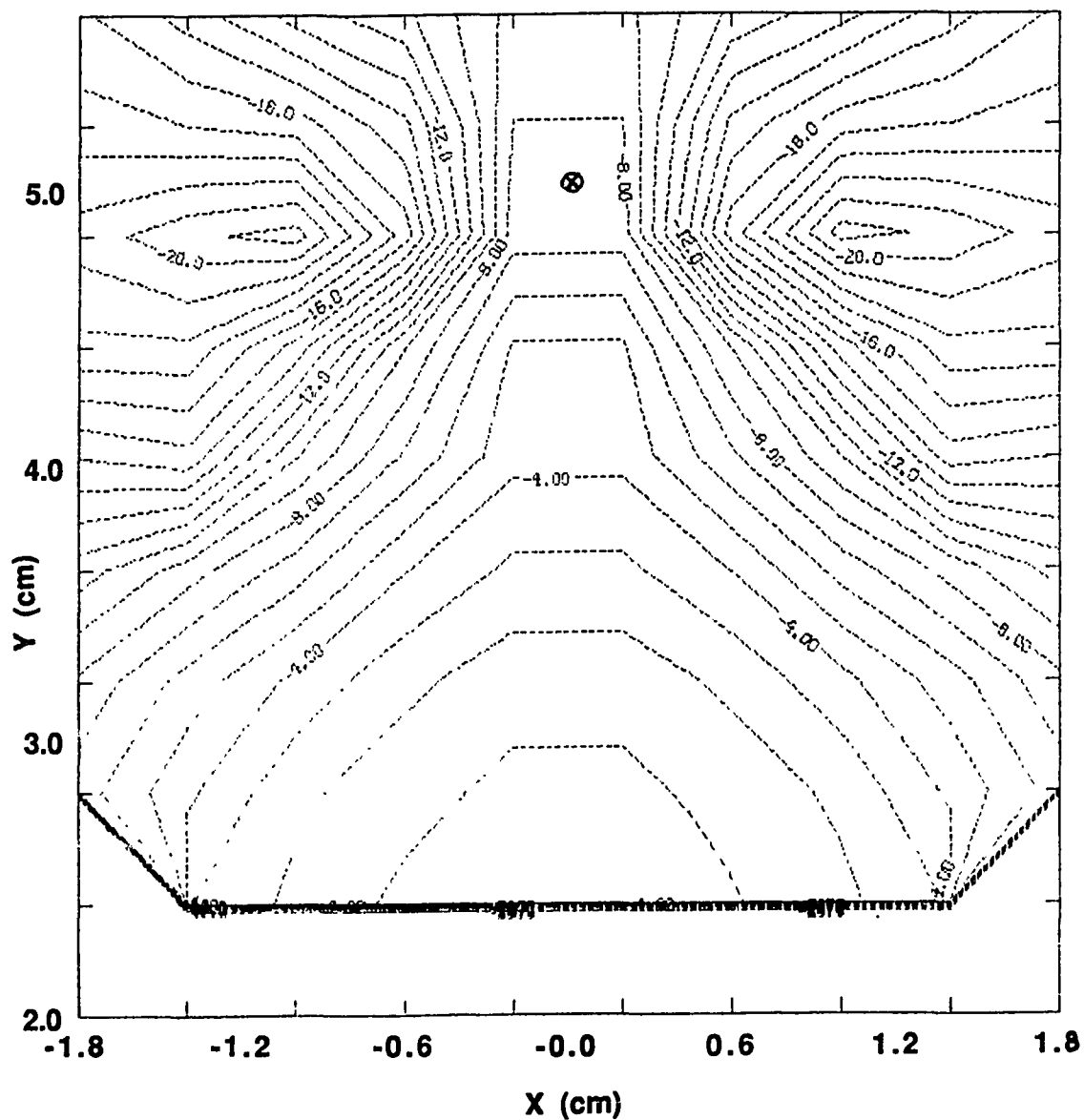


Figure C.39. Relative power (dB) contours calculated by CYLARR (CC model) in the circumferential E-plane of a single microstrip patch on a curved substrate in water – transverse (T1) component: $P_{\phi} \sim |E_{\phi}|^2$ ($P_{\phi p} = +2.4$ dB).

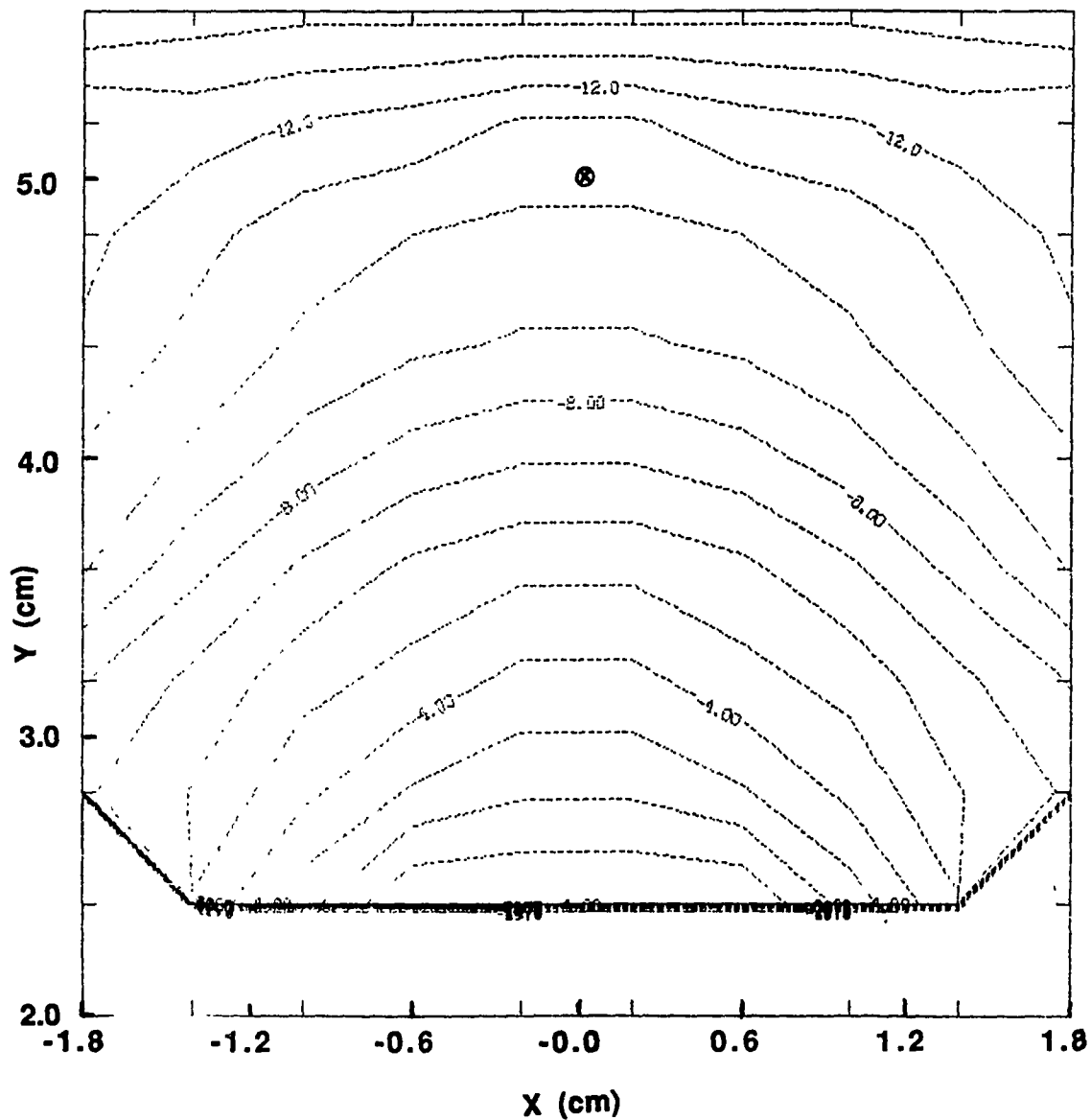


Figure C.40. Relative power (dB) contours calculated by CYLARR (CC model) in the circumferential E-plane of a single microstrip patch on a curved substrate in water — transverse (T2) component: $P_z \sim |E_z|^2$ ($P_{zp} = -6.3$ dB)

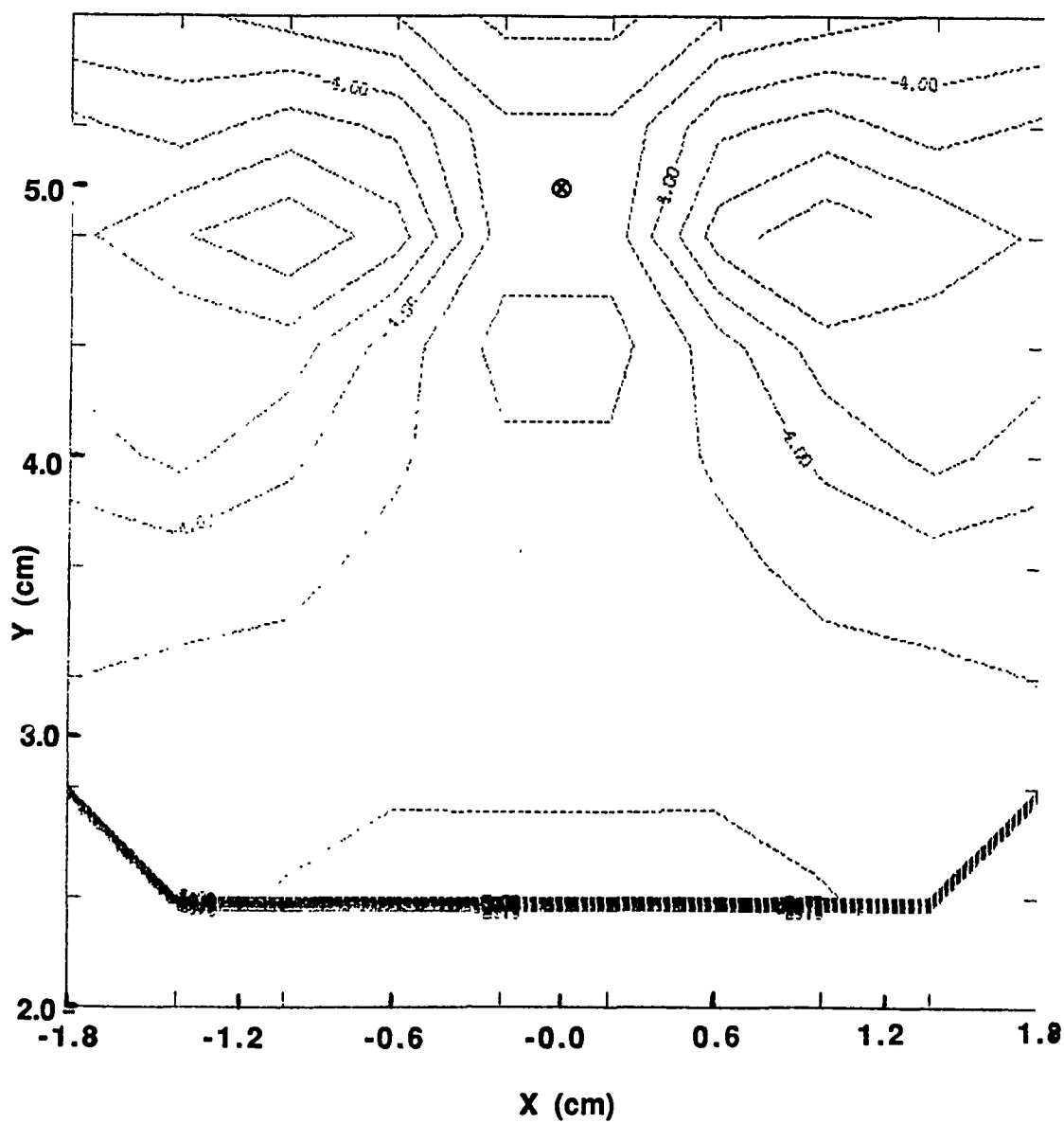


Figure C.41. Relative power (dB) contours calculated by CYLARR (CC model) in the circumferential E-plane of a single microstrip patch on a curved substrate in water – normal-to-transverse ratio:

$$R_{zt} = 10 \log \left(\frac{|E_p|}{\sqrt{|E_\phi|^2 + |E_z|^2}} \right)$$

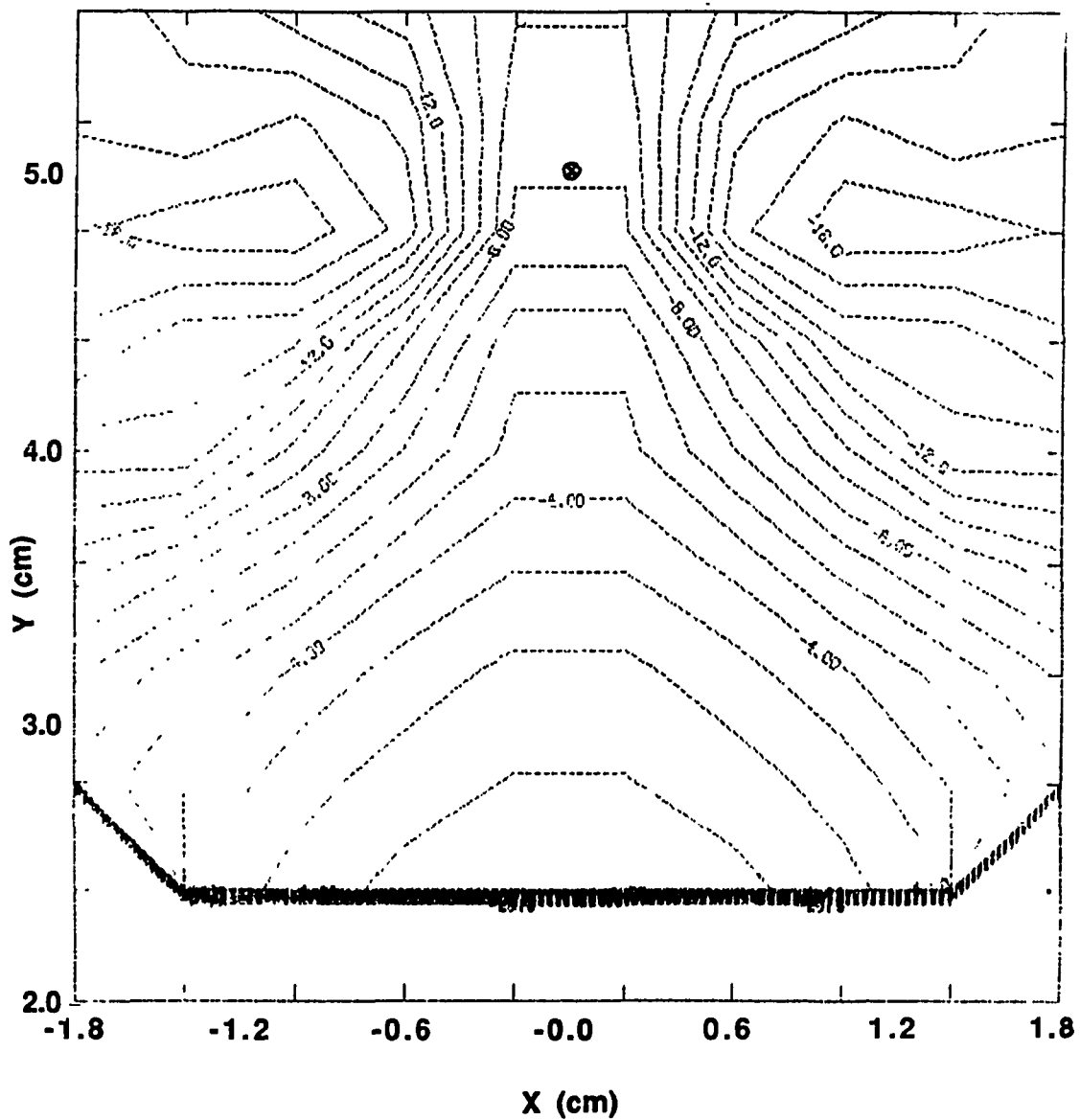


Figure C.42. Relative power (dB) contours calculated by CYLARR (CC model) in the circumferential E-plane of a single microstrip patch on a curved substrate in water—total E-field: $P_T \sim |E|^2 = (|E_\rho|^2 + |E_\phi|^2 + |E_z|^2)$

APPENDIX D
SUPPLEMENTARY MEASURED
MICROWAVE POWER PATTERNS

This appendix contains plots of the electric field component power contours detected by a miniature nonperturbing E-field probe in water radiated from a rectangular microstrip patch. The scans are along perpendicular (E,H) and parallel (P) planes away from the applicator ($z=0$) plane. Field contours in perpendicular planes are normalized to the peak power at $z=1.0$ cm.

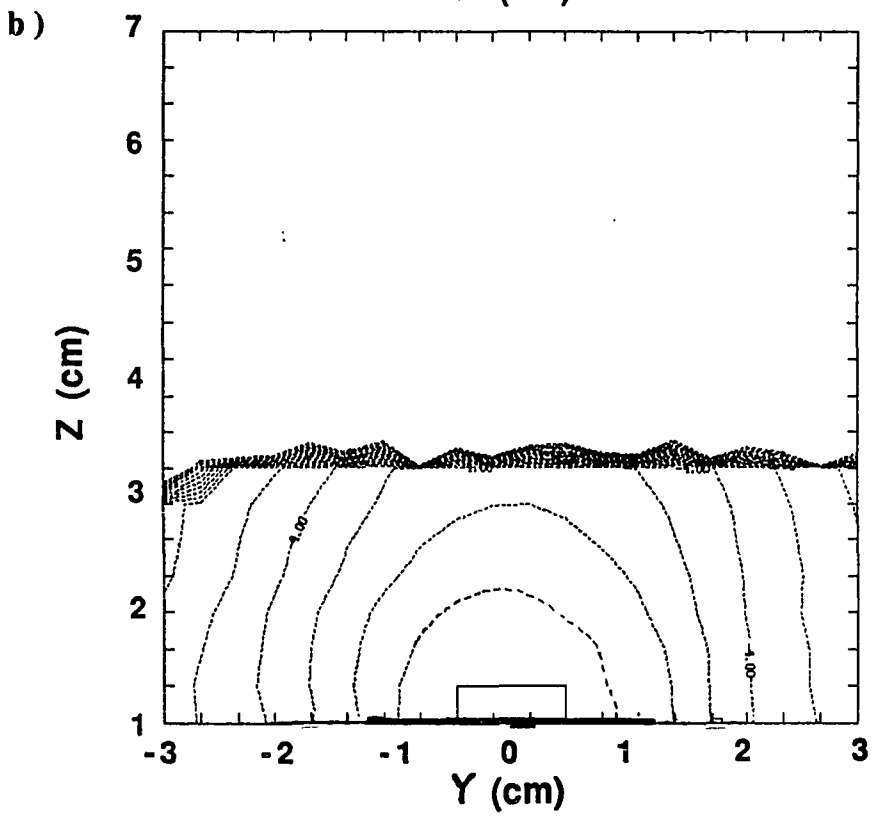
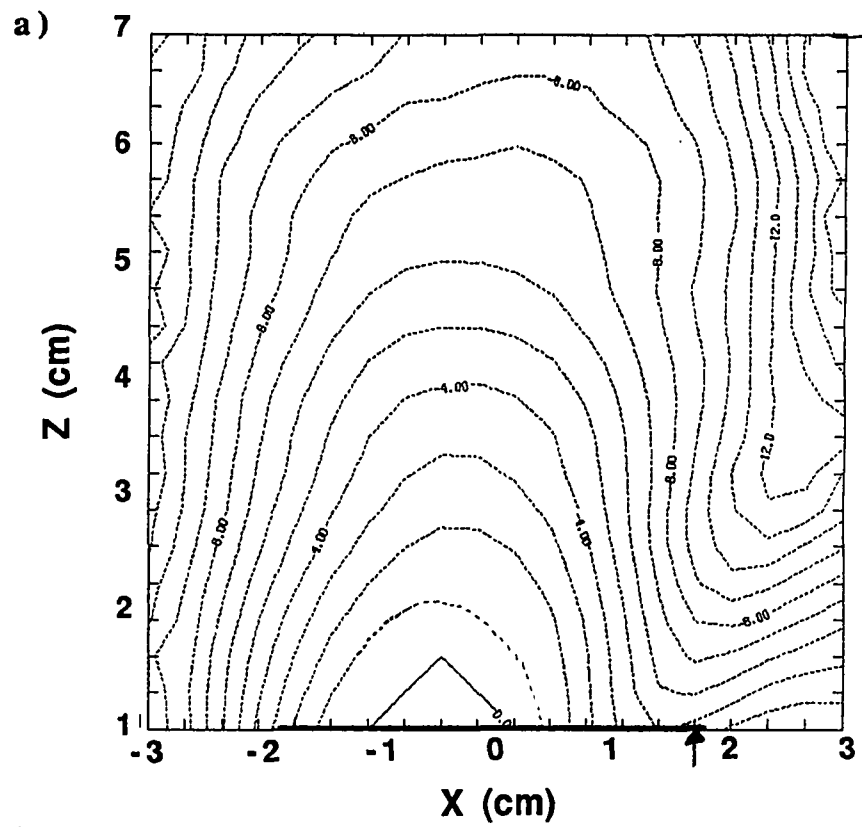


Figure D.1 Relative power (dB) contours measured in water – primary transverse (T1) component a) E-plane ($y=W/2$): $P_{xp} = +10.1$ dB ($P_i = 0.2W$) b) H-plane ($x=L/2$): $P_{xp} = +10.1$ dB ($P_i = 0.3W$)

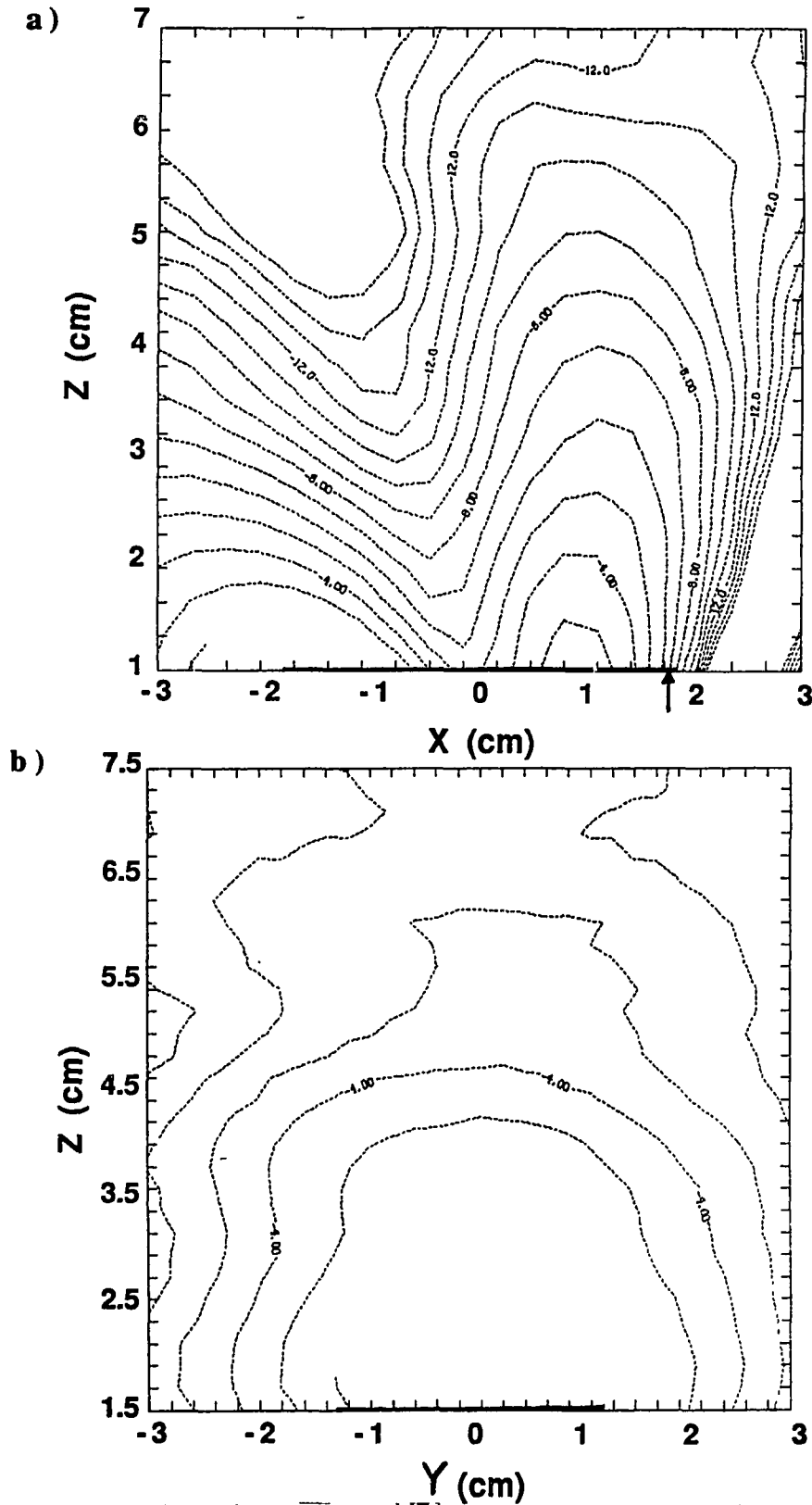


Figure D.2 Relative power (dB) contours measured in water — normal component
 a) E-plane ($y=W/2$): $P_{zp} = +8.8$ dB ($P_i = 0.2$ W)
 b) H-plane ($x=L/2$): $P_{zp} = +4.0$ dB ($P_i = 0.3$ W)

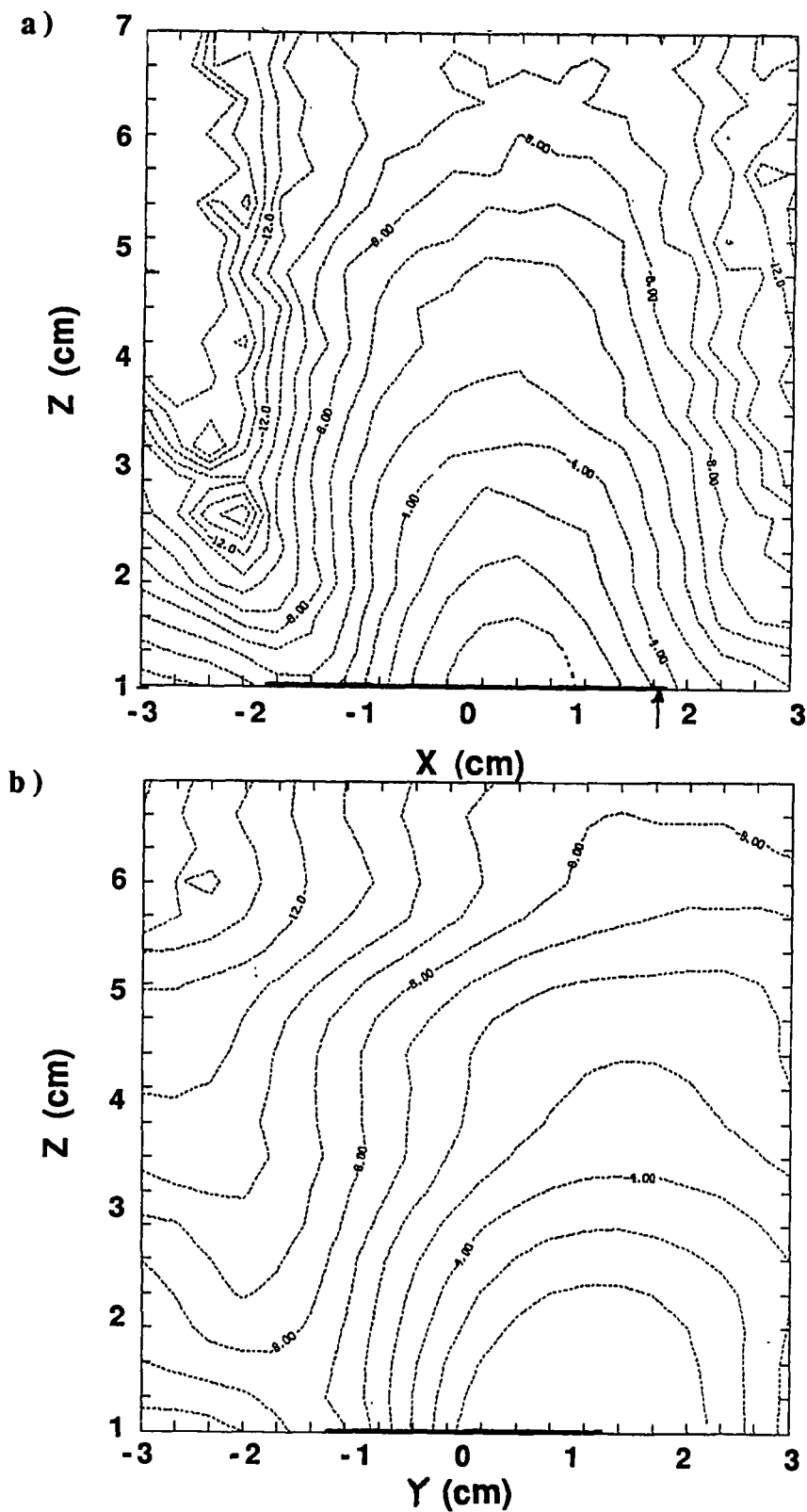


Figure D.3 Relative power (dB) contours measured in water — secondary transverse (T2) component a) E-plane ($y=W/2$): $P_{yp} = +5.4$ dB ($P_i = 0.2W$)
 b) H-plane ($x=L/2$): $P_{yp} = +6.6$ dB ($P_i = 0.3W$)

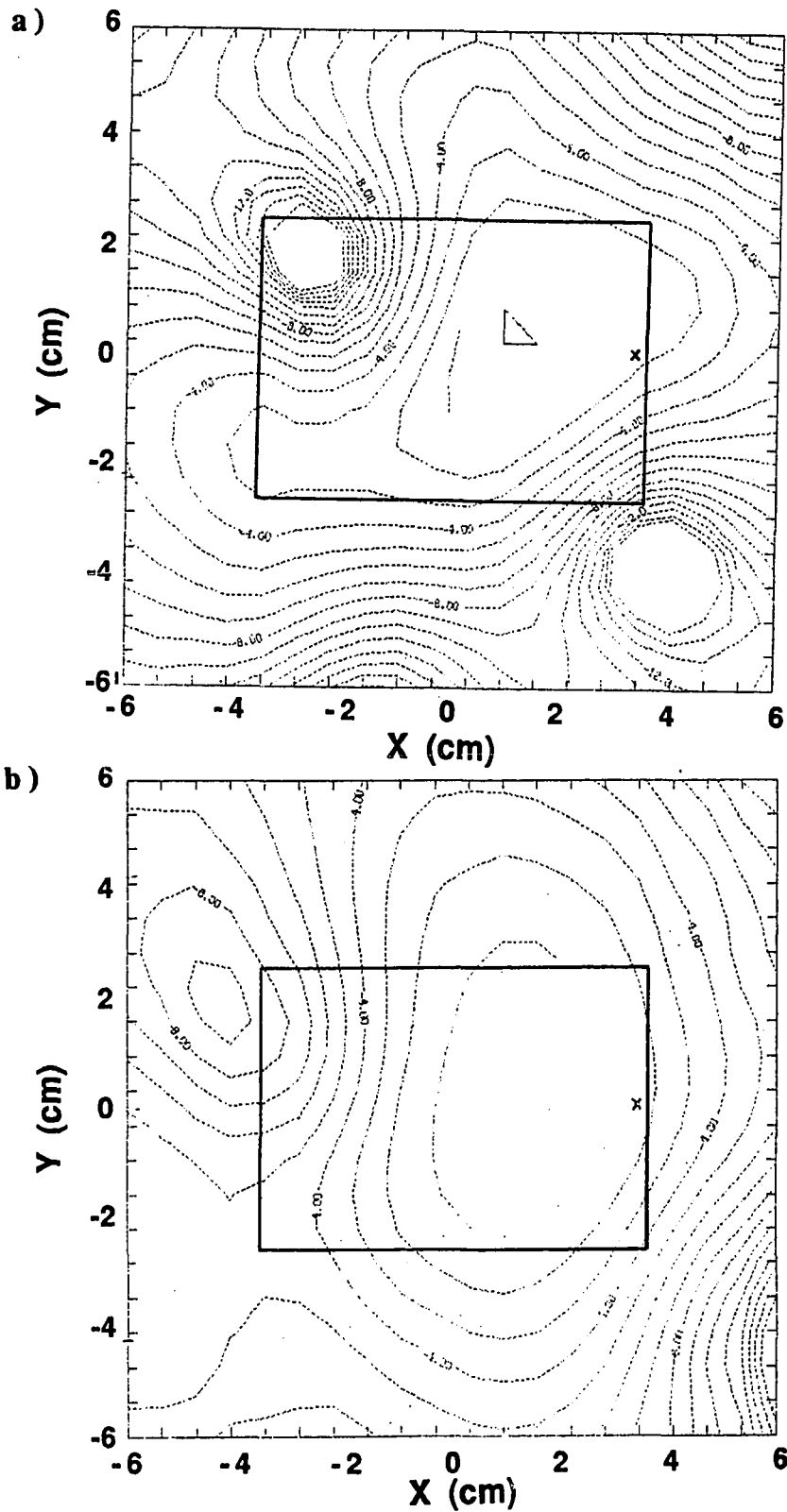


Figure D.4 Relative power (dB) contours measured in water — primary transverse (T1) component in the a) $z=1.0$ cm plane: $P_{xp}=10.1$ dB ($P_i = 0.2$ W) b) $z=3.0$ cm plane: $P_{xp}=10.0$ dB ($P_i = 0.3$ W)

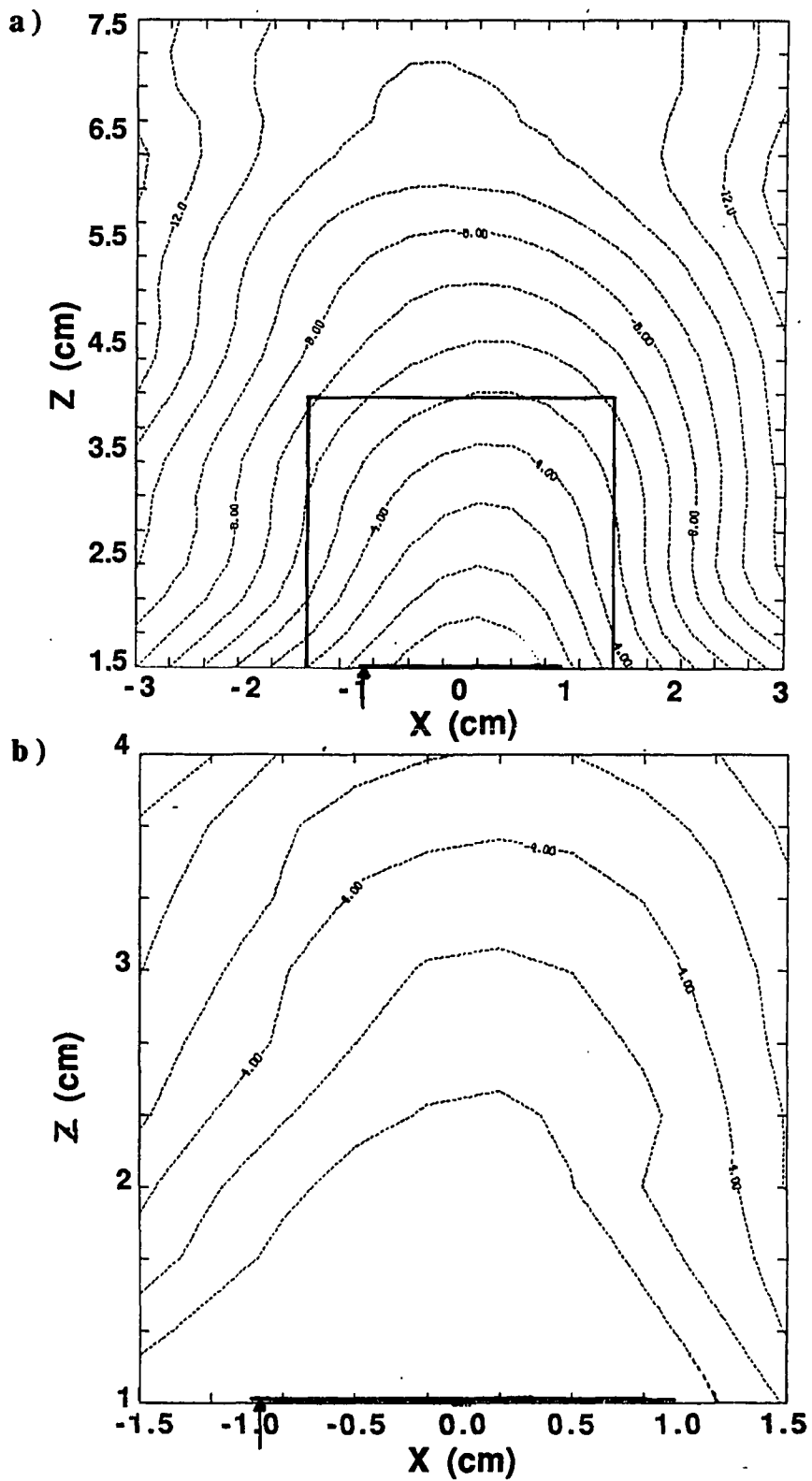


Figure D.5 Relative power (dB) contours measured in water – primary transverse (T1) component a) MIND probe: $P_{xp} = 10.1$ dB
b) DD probe: $P_{xp} = 9.7$ dB

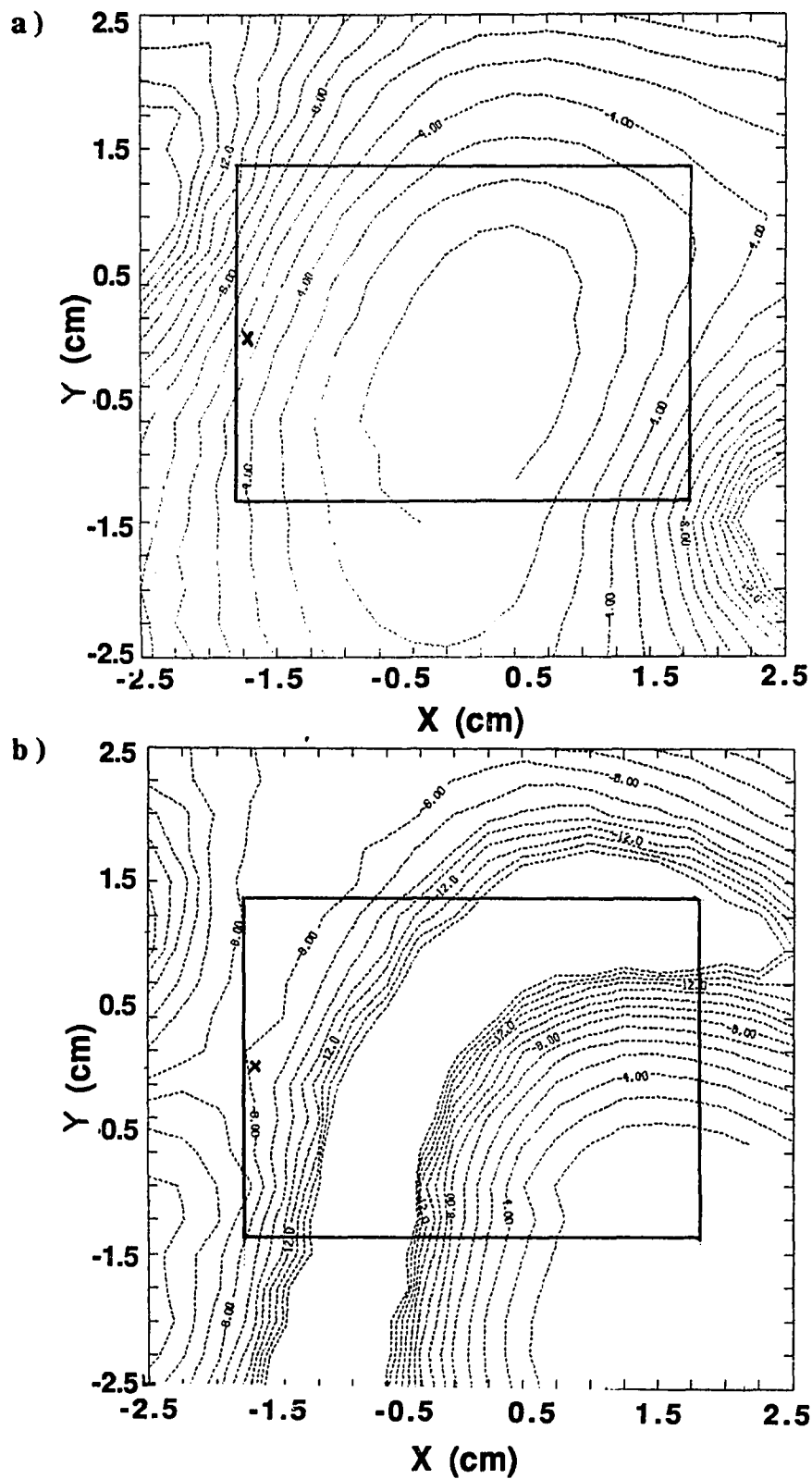


Figure D.6 Relative power (dB) contours measured in water at the $z=3.8$ cm plane
 a) primary transverse (T1) component: $P_{xp} = 8.2$ dB
 b) normal component: $P_{zp} = 2.0$ dB

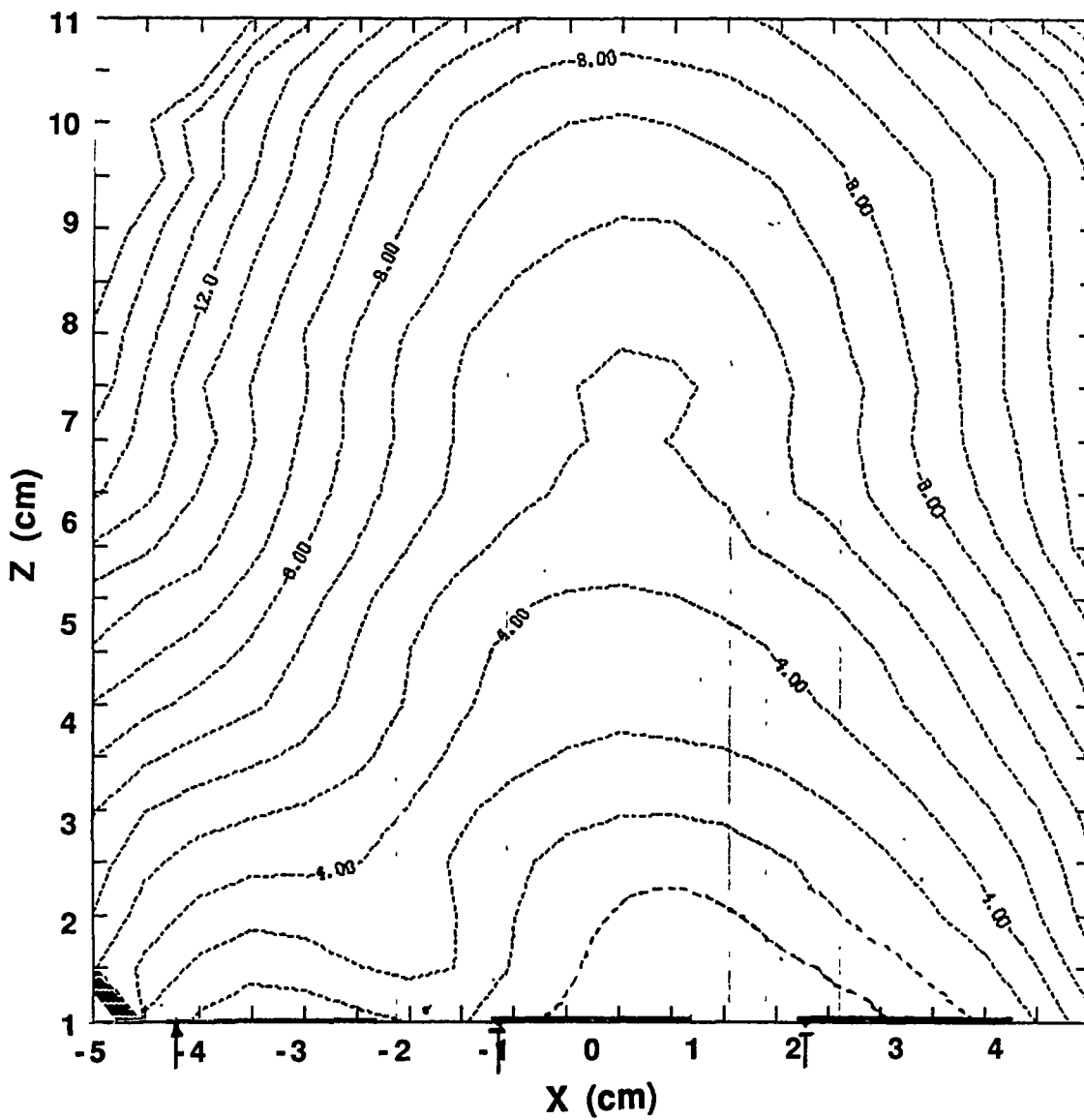


Figure D.7 Relative power (dB) contours measured in water from a 3-element linear array spaced $d=3.0$ cm apart on a MCT-85 substrate/superstrate

VITA

Harold Roger Underwood was born in Evanston, Illinois on January 22, 1961. He enrolled at Wheaton College, Wheaton, Illinois, in the Liberal Arts / Engineering program. In 1984, he finished the combined degree program with the University of Illinois at Urbana-Champaign. He received the Bachelor of Arts degree from Wheaton College and the Bachelor of Science in Electrical Engineering from the University of Illinois.

Harold spent a summer as a product engineer for Labthermics Technologies in Champaign, Illinois, where he developed an interest in ultrasound induced hyperthermia therapy. After this, he entered the graduate program at the University of Illinois with a part-time teaching and research assistantship. He joined the Bioacoustics Research Laboratory to carry out a characterization of a multielement ultrasonic square array hyperthermia applicator designed by Dr. Paul Benkeser and Dr. Leon Frizzell, developed by Dr. Stephen Goss and Labthermics Technologies. He completed the Master of Science degree in Electrical Engineering in 1986.

During his doctoral work, Harold broadened his academic training to include antennas and electromagnetics in order to have the background to assess the feasibility of a microstrip antenna array as a controlled hyperthermia applicator for superficial tumors. He received the Doctor of Philosophy degree in May 1990. Harold is a member of the Institute of Electrical and Electronics Engineers (IEEE), the IEEE Engineering in Medicine and Biology Society (EMBS) and the North American Hyperthermia Group (NAHG) of the Radiation Research Society (RRS).
